

**Analysis of Laminar-Turbulent Transition in
Time-Dependent Pipe Flows**

**A Ph.D. Thesis
in
Mechanical Engineering
University of Gaziantep**

**Supervisor
Prof. Dr. Melda Özdiñ ÇARPINLIOĞLU**

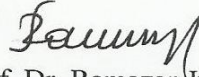
**Prof. Dr. M. Yaşar GÜNDOĞDU
Co-Supervisor**

**by
Emrah ÖZAHİ
October 2011**

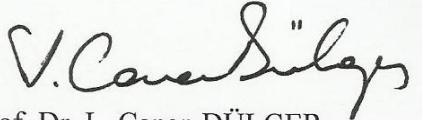
T.C.
UNIVERSITY OF GAZİANTEP
GRADUATE SCHOOL OF
NATURAL & APPLIED SCIENCES
MECHANICAL ENGINEERING DEPARTMENT

Name of the thesis : Analysis of Laminar-Turbulent Transition in Time-Dependent Pipe Flows
Name of the student : Emrah ÖZAHİ
Exam date : 14.10.2011

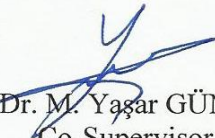
Approval of the Graduate School of Natural and Applied Sciences.

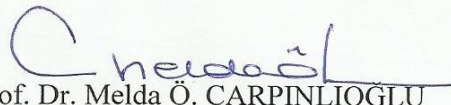

Prof. Dr. Ramazan KOÇ
Director

I certify that this thesis satisfies all the requirements as a thesis for the degree of Doctor of Philosophy.


Prof. Dr. L. Canan DÜLGER
Head of Department

This is to certify that we have read this thesis and that in our opinion it is fully adequate, in scope and quality, as a thesis for the degree of Doctor of Philosophy.


Prof. Dr. M. Yaşar GÜNDOĞDU
Co-Supervisor


Prof. Dr. Melda Ö. ÇARPINLIOĞLU
Supervisor

Examining Committee Members

signature

Prof. Dr. Kahraman ALBAYRAK



Prof. Dr. Melda ÇARPINLIOĞLU



Prof. Dr. Ali PINARBAŞI



Assist. Prof. Dr. A. İhsan KUTLAR



Assist. Prof. Dr. Vedat ORUÇ



To the memory of my grandmother

Lütfiye GÖZERİ

ABSTRACT

ANALYSIS OF LAMINAR-TURBULENT TRANSITION IN TIME-DEPENDENT PIPE FLOWS

ÖZAHİ, Emrah

Ph.D. in Mechanical Engineering

Supervisor: Prof. Dr. Melda Ö. ÇARPINLIOĞLU

Co-Supervisor: Prof. Dr. M. Yaşar GÜNDOĞDU

October 2011, 299 pages

The detection of transition to turbulence in sinusoidal pulsatile pipe flow and the flow dynamics at the onset of transition are analyzed in this study. The experimental study is conducted in the ranges of the time averaged and oscillating Reynolds numbers of $1019 \leq Re_{ta} \leq 4817$ and $107 \leq Re_{os} \leq 4261$. The velocity amplitude ratio of $0.05 \leq A_1 \leq 0.96$ and oscillation frequency of $0.1 \text{ Hz} \leq f \leq 14 \text{ Hz}$ corresponding to Womersley numbers of $2.72 \leq \sqrt{\omega'} \leq 32.21$ cover the so-called intermediate region of pulsatile flow. The generation and control of the pulsatile flow, the acquisition and processing of the measured data and the analyses of the flow dynamics are carried out by means of the devised program, *TDFC.vi* in LabView 2009-SP1 environment.

An original detection method is devised in *TDFC.vi* instead of the transition detection by visual observation in velocity waveforms, cited in the literature. Two dimensionless, dynamic turbulence detection parameters, *TDP*, of $R(dU(r,t)/dt)^2 / (\bar{U}_{ta} v \omega^2)$ for $f \leq 1 \text{ Hz}$ and $(dU(r,t)/dt)^2 / (\bar{U}_{ta}^2 \omega^2)$ for $f > 1 \text{ Hz}$ are defined. Moreover, two dimensionless, dynamic threshold parameters, *TP*, of $(1/\sqrt{\omega'})^n$ ($n = |f|$) for $f \leq 1 \text{ Hz}$ and $(1/\sqrt{\omega'})^4$ for $f > 1 \text{ Hz}$ are defined as a function of $\sqrt{\omega'}$. The detection is based on the comparison of the magnitudes of *TDP* and *TP*.

It is concluded that there is a distinct difference in flow dynamics for $\sqrt{\omega'} \leq 8.61$ and $\sqrt{\omega'} > 8.61$. Namely, at the onset of transition, despite of the noticeable influence of A_1 on Re_{ta} for $\sqrt{\omega'} \leq 8.61$, no effect of A_1 is observed for $\sqrt{\omega'} > 8.61$. There is no effect of $\sqrt{\omega'}$ on Re_{ta} for $A_1 = 0.10$ and $A_1 = 0.20$ although the significant effect of $\sqrt{\omega'}$ on Re_{ta} is observed for $A_1 > 0.30$ at the onset of transition.

Key Words: Pulsatile flow, laminar to turbulent transition, time averaged Reynolds number, oscillating Reynolds number, Womersley number, velocity amplitude ratio, oscillation frequency.

ÖZET

ZAMANA BAĞIMLI BORU AKIMLARINDA LAMINAR-TURBULENT GEÇİŞ ANALİZİ

ÖZAHİ, Emrah

Doktora Tezi, Makine Müh. Bölümü

Tez Yöneticisi: Prof. Dr. Melda Ö. ÇARPINLIOĞLU

Yardımcı Tez Yöneticisi: Prof. Dr. M. Yaşar GÜNDOĞDU

Ekim 2011, 299 sayfa

Bu çalışmada, sinüzoidal darbeli boru akımında türbülansa geçişin tespiti ve geçiş başlangıcındaki akım dinamiği incelenmiştir. Deneysel çalışma $1019 \leq Re_{ta} \leq 4817$ ve $107 \leq Re_{os} \leq 4261$ zaman ortalamalı Reynolds sayısı ve salınımlı Reynolds sayısı aralıklarında yapılmıştır. $0.05 \leq A_1 \leq 0.96$ aralığındaki hız genliği oranı ve $2.72 \leq \sqrt{\omega'} \leq 32.21$ aralığındaki Womersley sayısına denk düşen $0.1 \text{ Hz} \leq f \leq 14 \text{ Hz}$ aralığındaki salınım frekansı darbeli akışın “intermediate” bölgesini kapsamaktadır. Darbeli akışın üretimi ve kontrolü, ölçülen verinin toplanması ve işlenmesi, ve akım dinamiğinin analizleri LabView 2009-SP1 yazılım programı içerisinde tasarlanmış program, *TDFC.vi* ile gerçekleştirilmiştir.

Literatürde bahsedilen hız dalga profilleri üzerinden görsel gözlemler ile türbülansa geçişin tespiti yerine özgün bir türbülansa geçiş tespit metodu *TDFC.vi* içerisinde tasarlanmıştır. İki boyutsuz, dinamik türbülans tespit parametresi, *TDP*, $f \leq 1 \text{ Hz}$ için $R(dU(r,t)/dt)^2 / (\bar{U}_{ta} v \omega^2)$ ve $f > 1 \text{ Hz}$ için $(dU(r,t)/dt)^2 / (\bar{U}_{ta}^2 \omega^2)$ tanımlanmıştır. Bundan başka, iki boyutsuz, dinamik eşik değişkeni, *TP*, $f \leq 1 \text{ Hz}$ için $(1/\sqrt{\omega'})^n$ ($n = |f|$) ve $f > 1 \text{ Hz}$ için $(1/\sqrt{\omega'})^4$, $\sqrt{\omega'}$ parametresinin fonksiyonu şeklinde tanımlanmıştır. Türbülansa geçişin başlangıcının tespiti *TDP* ve *TP* değişkenlerinin kıyaslanması esasına dayalıdır.

$\sqrt{\omega'} \leq 8.61$ ve $\sqrt{\omega'} > 8.61$ için akım dinamiklerinde belirgin bir farkın olduğu sonucu çıkarılmıştır. Şöyle ki, türbülansa geçişin başlangıcında, $\sqrt{\omega'} \leq 8.61$ için A_1 'in Re_{ta} üzerinde fark edilir etkisinin olmasına rağmen, $\sqrt{\omega'} > 8.61$ için A_1 'in Re_{ta} üzerinde etkisi gözlemlenmemiştir. Türbülansa geçiş başlangıcında $A_1 > 0.30$ için $\sqrt{\omega'}$ 'nin Re_{ta} üzerinde kayda değer etkisinin gözlemlenmesine rağmen, $A_1 = 0.10$ ve $A_1 = 0.20$ için Re_{ta} üzerinde $\sqrt{\omega'}$ 'nin etkisi yoktur.

Anahtar Kelimeler: Darbeli akış, laminardan türbülansa geçiş, zaman ortalamalı Reynolds sayısı, salınımlı Reynolds sayısı, Womersley sayısı, hız genliği oranı, salınım frekansı.

ACKNOWLEDGEMENTS

I would like to express my deep gratitude to Prof. Dr. Melda Ö. ÇARPINLIOĞLU and Prof. Dr. M. Yaşar GÜNDOĞDU for their valuable comments, supervisions and suggestions.

I am also grateful to the members of Ph.D. thesis committee; Prof. Dr. Kahraman ALBAYRAK, Prof. Dr. Melda Ö. ÇARPINLIOĞLU, Prof. Dr. Ali PINARBAŞI, Assist. Prof. Dr. A. İhsan KUTLAR and Assist. Prof. Dr. Vedat ORUÇ for their comments, criticism and suggestions during the research study.

I especially would like to thank my wife Mrs. Didem ÖZAHİ, my mother Mrs. Zerin ÖZAHİ and Mrs. Nesrin GÖZERİ and my brother Mr. Ali ÖZAHİ for their moral supports, encouragements and patience.

My thanks are also due to my lovely daughter Defne ÖZAHİ for her great understanding and patience during my thesis.

I would like to express my sincere thanks to Research Fund of the University of Gaziantep for the research project supported under the Grant no: MF.09.09.

Lastly, I express my thanks to the personnel of the Mechanical Engineering Department and the workshop; especially to Mr. İbrahim KORKMAZ for their valuable help in the construction of the experimental set-up.

CONTENTS

ABSTRACT	i
ÖZET	ii
ACKNOWLEDGMENTS	iii
CONTENTS	iv
LIST OF FIGURES	x
LIST OF TABLES	xxi
LIST OF SYMBOLS	xxiii
CHAPTER 1: INTRODUCTION	1
1.1. Background and Motivation.....	1
1.2. Objects.....	2
1.3. Outline of the Thesis.....	2
CHAPTER 2: LITERATURE SURVEY	5
2.1. Introduction	5
2.2. Laminar to Turbulent Transition in Pulsatile Pipe Flows.....	13
2.3. Laminar to Turbulent Transition in Oscillating Pipe Flows.....	25
2.4. Conclusions.....	32
2.4.1. Conclusions on laminar to turbulent transition in pulsatile pipe flows.....	32
2.4.2. Conclusions on laminar to turbulent transition in oscillating pipe flows.....	34

CHAPTER 3: EXPERIMENTAL SET-UP AND MEASUREMENT

DEVICES.....	38
3.1. Introduction.....	38
3.2. Layout of the Experimental Set-Up.....	38
3.2.1. Screw air compressor.....	39
3.2.2. Surge tank.....	39
3.2.3. Drier.....	42
3.2.4. Air filters.....	42
3.2.5. Mass flow rate control (MFC) unit.....	43
3.2.6. Flow conditioners.....	44
3.2.7. PVC pipeline, connections and adapters.....	46
3.2.8. Probe traversing mechanism.....	48
3.2.9. Constant temperature anemometer (CTA) and hotwire probe.....	49
3.2.9.1. Working principle of CTA.....	49
3.2.9.2. Calibration of the hotwire probe.....	50
3.2.9.3. Calibration of the hotwire anemometer probe at low air speeds.....	52
3.2.9.4. Wall proximity effect on hotwire measurements	60
3.2.9.5. Wire aspect ratio effect.....	62
3.2.9.6. Overheat ratio (OHR) effect.....	62
3.2.10. Pressure transmitter.....	63
3.2.11. Oscilloscope.....	63
3.2.12. Data acquisition and processing equipment (DAQ).....	64
3.3. Conclusions.....	64

CHAPTER 4: DATA ACCUMULATION AND ACQUISITION SYSTEM

(PRESENTATION OF THE DEvised PROGRAM AND

METHODOLOGY IN LABVIEW 2009SP1[®]

ENVIRONMENT).....66

4.1. Introduction.....	66
4.2. Data Acquisition and Processing Equipment.....	66
4.3. Data Accumulation Procedure.....	67
4.3.1. Control of time dependent data accumulation.....	67
4.3.2. Procedure for velocity measurement.....	68
4.3.3. Adjustment of the position of the hotwire probe.....	68
4.3.4. Procedure for pressure measurement.....	69
4.4. Experimental Procedure.....	69
4.4.1. Adjustment of the experimental run.....	70
4.4.2. Ranges in the experimental study.....	71
4.4.3. Determination of axial velocity measurement position.....	71
4.4.4. Determination of axial locations for pressure measurement.....	73
4.4.5. Verification of the MFC unit performance.....	74
4.5. Basic Terminology Used for Data Processing in Pulsatile Pipe flows.....	76
4.6. The Devised Program, <i>TDFC.vi</i> and Methodology in LabView 2009SP1 [®] for Data Accumulation and Acquisition System.....	80
4.6.1. Background of LabView environment.....	80
4.6.2. Details of the devised program, <i>TDFC.vi</i>	81
4.6.2.1. Description of the front panel of <i>TDFC.vi</i>	81
4.6.2.2. Description of the block diagram of <i>TDFC.vi</i>	88
4.6.3. Graphical representations of sample plots generated by <i>TDFC.vi</i>	97
4.7. Conclusions.....	109

**CHAPTER 5: CHARACTERISTICS OF FLOW FIELD IN TERMS OF
PRELIMINARY TESTS AND UNCERTAINTY ANALYSIS
OF THE MEASUREMENTS.....110**

5.1. Introduction.....	110
5.2. Character of Steady Velocity Profile.....	110
5.2.1. Symmetricity of velocity field.....	110

5.2.2. Hydrodynamic development.....	111
5.3. Uncertainty Analysis.....	113
5.3.1. Uncertainty analysis for velocity measurement chain.....	117
5.3.2. Uncertainty analysis for pressure measurement chain.....	119
5.4. Conclusions.....	120
CHAPTER 6: LAMINAR FLOW CONTROL VIA UTILIZATION OF PIPE ENTRANCE INSERTS.....	122
6.1. Introduction.....	122
6.2. Velocity Flow Fields at Different X/D Locations.....	124
6.2.1. Flow nature without an entrance element (Case: WFC) with a comment on entrance length concept of White (1984).....	124
6.2.2. Flow field uniformity behind a variety of flow conditioners (Case: FC) as a function of Reynolds number	126
6.3. Performance Characteristics and Settling Distance of Pipe Inserts in Laminar Flow Range with an Approach on Entrance Length.....	129
6.3.1. Performance characteristics.....	129
6.3.2. Settling distance and entrance length in laminar flow range.....	131
6.4. Conclusions.....	140
CHAPTER 7: DETECTION METHOD AND DEvised PROGRAM FOR ONSET OF TRANSITION TO TURBULENCE IN PULSATILE PIPE FLOW.....	141
7.1. Introduction.....	141
7.2. Utilized Methodology.....	142
7.3. Utilized Detection Program.....	145
7.4. Verification of the Transition to Turbulence Detection Program.....	151
7.5. Conclusion.....	156
CHAPTER 8: PULSATILE FLOW DYNAMICS IN LAMINAR REGIME AND AT THE ONSET OF TRANSITION.....	158
8.1. Introduction.....	158
8.2. Pulsatile Laminar Regime.....	163

8.2.1. Velocity waveforms in pulsatile laminar regime.....	164
8.2.2. Velocity distributions of time averaged and oscillating components in pulsatile laminar regime.....	174
8.2.3. Mean velocity profiles in pulsatile laminar regime.....	181
8.2.4. Pressure waveforms in pulsatile laminar regime.....	183
8.2.5. Flow resistance in pulsatile laminar regime.....	186
8.2.5.1. Variations of $\Delta\bar{P}(t)/L$, $\bar{U}_m(t)$ and $\bar{\tau}_w(t)$ in pulsatile laminar regime.....	186
8.2.5.2. The variations of $\lambda_u(t)$ and $\lambda_{qL}(t)$ in pulsatile laminar regime...	188
8.3. Pulsatile Flow Regime at the Onset of Transition to Turbulence.....	191
8.3.1. Velocity waveforms in pulsatile flow regime at the onset of transition to turbulence.....	191
8.3.2. Velocity distributions of time averaged and oscillating components in pulsatile flow regime at the onset of transition to turbulence.....	205
8.3.3. Mean velocity profiles in pulsatile flow regime at the onset of transition to turbulence.....	212
8.3.4. Pressure waveforms in pulsatile flow regime at the onset of transition to turbulence.....	213
8.3.5. Flow resistance in pulsatile flow regime at the onset of transition to turbulence.....	216
8.3.5.1. Variations of $\Delta\bar{P}(t)/L$, $\bar{U}_m(t)$ and $\bar{\tau}_w(t)$ in pulsatile flow regime at the onset of transition to turbulence.....	216
8.3.5.2. The variations of $\lambda_u(t)$ and $\lambda_{qL}(t)$ in pulsatile flow regime at the onset of transition to turbulence.....	218
8.6. Conclusions.....	220
CHAPTER 9: INTERACTIVE INFLUENCES OF OSCILLATION	
FREQUENCY AND AMPLITUDE ON THE CRITICAL	
REYNOLDS NUMBERS AND FRICTION FACTORS	
AT THE ONSET OF TRANSITION.....	
	223
9.1. Introduction.....	223

9.2. Effect of A_1 on $Re_{ta,crit}$ at Constant Value of $\sqrt{\omega'}$	224
9.3. Effect of A_1 on $Re_{os,crit}$ at Constant Value of $\sqrt{\omega'}$	230
9.4. Effect of A_1 on $Re_{\delta_s,crit}$ at Constant Value of $\sqrt{\omega'}$	236
9.5. Effect of $\sqrt{\omega'}$ on $Re_{ta,crit}$ at Constant Value of A_1	237
9.6. Effect of $\sqrt{\omega'}$ on $Re_{os,crit}$ at Constant Value of A_1	244
9.7. Effect of $\sqrt{\omega'}$ on $Re_{\delta_s,crit}$ at Constant Value of A_1	250
9.8. Correlations on Critical Reynolds Numbers.....	251
9.9. Correlations on Friction Factors.....	256
9.10. Conclusions.....	258
CHAPTER 10: RECOMMENDATIONS FOR FURTHER STUDIES.....	264
REFERENCES.....	268
APPENDIX 1 SUMMARY OF THE STUDIES IN LITERATURE CONDUCTED ON PULSATILE PIPE FLOWS.....	281
APPENDIX 2 SUMMARY OF THE STUDIES IN LITERATURE CONDUCTED ON OSCILLATING PIPE FLOWS.....	286
APPENDIX 3 TECHNICAL SPECIFICATION OF THE SCREWED AIR COMPRESSOR.....	288
APPENDIX 4 TECHNICAL SPECIFICATION OF PSK TYPE PRESSURIZED AIR DRIER.....	289
APPENDIX 5 TECHNICAL SPECIFICATION OF PROBE TRAVERSING MECHANISM.....	290
APPENDIX 6 TECHNICAL SPECIFICATION OF 55P11 GENERAL PURPOSE TYPE MINIATURE PROBE.....	292
APPENDIX 7 TECHNICAL SPECIFICATIONS OF 56C17 CTA BRIDGE and 56N21 LINEARIZER.....	293
APPENDIX 8 TECHNICAL SPECIFICATION OF THE PRESSURE TRANSMITTER.....	295
APPENDIX 9 TECHNICAL SPECIFICATION OF DATA ACQUISITION AND PROCESSING EQUIPMENT.....	296
CURRICULUM VITAE.....	297

LIST OF FIGURES

	page
Figure 2.1. Centerline velocity time records of puff and slug type turbulent structures (Durst and Ünsal, 2006).....	7
Figure 2.2. Typical numerical flow visualizations of puff and slug type turbulent structures (Shan et al., 1999).....	7
Figure 2.3. Classifications of time dependent flows.....	8
Figure 2.4. Methods used for production of oscillation.....	8
Figure 3.1. A schematic layout of the experimental set-up.....	40
Figure 3.2. Photographs of the experimental set-up.....	41
Figure 3.3. A section view of connection adapters.....	47
Figure 3.4. A section view of a conical shaped adapter.....	48
Figure 3.5. A photograph of the probe traversing mechanism.....	48
Figure 3.6. High speed calibration curve using conventional method.....	52
Figure 3.7. Low speed calibration curve using laminar pipe-flow method.....	56
Figure 3.8. Cross-sectional velocity distribution at reference flow rate of $Q=29.89$ L/min in case of laminar pipe-flow method.....	56
Figure 3.9. Schematic diagram of the set-up for rotating disc method.....	57
Figure 3.10. Low speed calibration curve using rotating disc method.....	59
Figure 3.11. Comparison of the measured velocities and calculated ones from calibration equations for both laminar pipe-flow and rotating disc method.....	59
Figure 4.1. \bar{U}/\bar{U}_{CL} distributions with respect to r/R for steady state flow condition.....	70
Figure 4.2. Comparison of calculated and reference MFC unit flow rates at steady state conditions.....	75
Figure 4.3. Relative error between the reference MFC unit and calculated flow rates at steady state conditions.....	75

Figure 4.4. Comparison of the measured and predefined velocity signals with oscillation frequency of $f=0.8$ H.....	76
Figure 4.5a. <i>Analog Output</i> segment to control of MFC unit for generation of time dependent flow.....	82
Figure 4.5b. <i>Analog Input</i> segment for data acquisition.....	83
Figure 4.5c. <i>Voltage Output</i> segment to control MFC unit for generation of steady flow.....	84
Figure 4.5d. Representations of pressure and velocity waveform graphs.....	85
Figure 4.5e. Cross-sectional \bar{U}_{ta} , $ \bar{U}_{os,1} $ and their normalized value distributions with respect to r and r/R , respectively and illustrations of $\bar{U}_{m,ta}$, $ \bar{U}_{m,os,1} $, Re_{ta} and Re_{os}	86
Figure 4.5f. Cross-sectional distributions of positive and negative peak values of velocity waveforms and their normalized values through pipe cross-section.....	86
Figure 4.5g. Experimental and theoretical mean velocity, $\bar{U}_m(t)$ waveforms through pipe cross-section and tabular representation of cross-sectional velocity data.....	87
Figure 4.5h. Graphical representations of $\bar{\tau}_w(t)$, $\lambda_u(t)$, λ_{qL} , and experimental and theoretical values of $\bar{U}_m(t)$ and $\Delta\bar{P}(t)/L$ with evaluated $\bar{\tau}_w(t)$ in a combined graph.....	88
Figure 4.6a. The first part of the block diagram of <i>TDFC.vi</i> (The first part of the <i>Flat Sequence Structure</i>).....	91
Figure 4.6b. The second part of the block diagram of <i>TDFC.vi</i> (The second part of the <i>Flat Sequence Structure</i>).....	95
Figure 4.7. Velocity waveforms at different r/R at $Re_{ta}=2160$, $Re_{os}=832$, $\sqrt{\omega'}=17.22$ and $A_1=0.39$	98
Figure 4.8. Velocity waveforms at different r/R at $Re_{ta}=3018$, $Re_{os}=1610$, $\sqrt{\omega'}=2.72$ and $A_1=0.53$	98
Figure 4.9. Velocity waveforms at $r/R=0$ at $Re_{ta}=2160$, $Re_{os}=832$, $\sqrt{\omega'}=17.22$ and $A_1=0.39$	99
Figure 4.10. Velocity waveforms at $r/R=0.977$ at $Re_{ta}=2160$, $Re_{os}=832$, $\sqrt{\omega'}=17.22$ and $A_1=0.39$	99

Figure 4.11. Velocity waveforms at $r/R=0$ at $Re_{ta}=3018$, $Re_{os}=1610$, $\sqrt{\omega'}=2.72$ and $A_1=0.53$	100
Figure 4.12. Velocity waveforms at $r/R=0.977$ at $Re_{ta}=3018$, $Re_{os}=1610$, $\sqrt{\omega'}=2.72$ and $A_1=0.53$	100
Figure 4.13. Velocity waveforms at $r/R=0.977$ at $Re_{ta}=3018$, $Re_{os}=1610$, $\sqrt{\omega'}=2.72$ and $A_1=0.53$	101
Figure 4.14. Velocity waveforms at all r/R for one period at $Re_{ta}=3018$, $Re_{os}=1610$, $\sqrt{\omega'}=2.72$ and $A_1=0.53$	101
Figure 4.15. Pressure waveforms for 7 pressure transmitters at $Re_{ta}=2160$, $Re_{os}=832$, $\sqrt{\omega'}=17.22$ and $A_1=0.39$	102
Figure 4.16. Pressure waveforms for 7 pressure transmitters at $Re_{ta}=3018$, $Re_{os}=1610$, $\sqrt{\omega'}=2.72$ and $A_1=0.53$	102
Figure 4.17. \bar{U}_{ta} and $ \bar{U}_{os,1} $ distributions at $Re_{ta}=2160$, $Re_{os}=832$, $\sqrt{\omega'}=17.22$ and $A_1=0.39$	103
Figure 4.18. \bar{U}_{ta} and $ \bar{U}_{os,1} $ distributions at $Re_{ta}=3018$, $Re_{os}=1610$, $\sqrt{\omega'}=2.72$ and $A_1=0.53$	103
Figure 4.19. $\bar{U}_{ta}/\bar{U}_{m,ta}$ and $\bar{U}_{ta}/\bar{U}_{CL,ta}$ distributions with r/R at $Re_{ta}=2160$, $Re_{os}=832$, $\sqrt{\omega'}=17.22$ and $A_1=0.39$	104
Figure 4.20. $\bar{U}_{ta}/\bar{U}_{m,ta}$ and $\bar{U}_{ta}/\bar{U}_{CL,ta}$ distributions with r/R at $Re_{ta}=3018$, $Re_{os}=1610$, $\sqrt{\omega'}=2.72$ and $A_1=0.53$	104
Figure 4.21. $ \bar{U}_{os,1} / \bar{U}_{m,os,1} $ and $ \bar{U}_{os,1} / \bar{U}_{CL,os,1} $ distributions with r/R at $Re_{ta}=2160$, $Re_{os}=832$, $\sqrt{\omega'}=17.22$ and $A_1=0.39$	106
Figure 4.22. $ \bar{U}_{os,1} / \bar{U}_{m,os,1} $ and $ \bar{U}_{os,1} / \bar{U}_{CL,os,1} $ distributions with r/R at $Re_{ta}=3018$, $Re_{os}=1610$, $\sqrt{\omega'}=2.72$ and $A_1=0.53$	106
Figure 4.23. Combined graphical representation of $\bar{U}_m(t)$, $\Delta\bar{P}/L(t)$ with their FFT approximations and $\bar{\tau}_w(t)$ at $Re_{ta}=2160$, $Re_{os}=832$, $\sqrt{\omega'}=17.22$ and $A_1=0.39$	107

Figure 4.24. Combined graphical representation of $\bar{U}_m(t)$, $\Delta\bar{P}/L(t)$ with their FFT approximations and $\bar{\tau}_w(t)$ at $Re_{ia}=3018$, $Re_{os}=1610$, $\sqrt{\omega'}=2.72$ and $A_1=0.53$	107
Figure 4.25. Comparison of $\lambda_u(t)$ and $\lambda_{qL}(t)$ at $Re_{ia}=2160$, $Re_{os}=832$, $\sqrt{\omega'}=17.22$ and $A_1=0.39$	108
Figure 4.26. Comparison of $\lambda_u(t)$ and $\lambda_{qL}(t)$ at $Re_{ia}=3018$, $Re_{os}=1610$, $\sqrt{\omega'}=2.72$ and $A_1=0.53$	108
Figure 5.1. Velocity profiles at velocity measurement station ($X/D=604$) for different Reynolds numbers.....	111
Figure 5.2. Velocity profiles for $Re=2000$ at four different X/D locations along the pipeline.....	111
Figure 5.3. Velocity profiles for 10 different Re at velocity measurement station, $X/D=604$	112
Figure 6.1. Cross-sectional velocity profiles for different Re at $X/D=680$	124
Figure 6.2. Sample non-dimensional axial velocity, \bar{U}/\bar{U}_m profiles as a function of X/D for $Re=704$ for WFC case.....	125
Figure 6.3. Sample turbulence intensity u'_{rms}/\bar{U} profiles for $Re=704$, $Re=2450$ at $X/D=75$ for WFC case.....	126
Figure 6.4. Variation of $u'_{rms_{CL}}$ with Re for WFC case based on data at $X/D=680$	126
Figure 6.5. Sample non-dimensional axial velocity, \bar{U}/\bar{U}_m profiles behind flow conditioners as a function of X/D	127
Figure 6.6. Sample turbulence intensity u'_{rms}/\bar{U} profiles behind flow conditioners and WFC at $X/D=375$ and $X/D=680$	128
Figure 6.7. Variation of $\Delta\bar{P}$ with Re for the tested flow conditioners.....	130
Figure 6.8. Variation of pressure loss coefficient, K with $Re\beta$ for the tested flow conditioners.....	131
Figure 6.9. Variation of local turbulence intensity $(u'_{rms}/\bar{U})_{CL}$ at $r/R=0$ with Re	132
Figure 6.10. Variation of local turbulence intensity $(u'_{rms}/\bar{U})_{r/R=0.89}$ at $r/R=0.89$ with Re	133
Figure 6.11. Variation of local respective orders $(u'_{rms_{FC}}/u'_{rms_{WFC}})_{CL}$ at $r/R=0$ with Re	134

Figure 6.12. Variation of local respective orders $(u'_{rms_{FC}} / u'_{rms_{WFC}})_{r/R=0.89}$ at $r/R=0.89$ with Re	134
Figure 6.13. Variation of $(u'_{rms_{FC}} / u'_{rms_{WFC}})_{CL}$ at $r/R=0$ with $Re_x=(X/D)Re$	135
Figure 6.14. Variation of $[(\bar{U}/\bar{U}_m)_{FC}/(\bar{U}/\bar{U}_m)_{Blasius}]_{CL}$ at $r/R=0$ with $Re_x \beta$	137
Figure 6.15. Variation of $[(\bar{U}/\bar{U}_m)_{WFC}/(\bar{U}/\bar{U}_m)_{Blasius}]_{CL}$ at $r/R=0$ with $Re_x \beta$ for WFC Case of $\beta=1$	139
Figure 7.1. A first “True” section of the turbulence detection program for $f \leq 1$ Hz.....	146
Figure 7.2. A second “False” section of the turbulence detection program for $f > 1$ Hz.....	147
Figure 7.3. Graphical representations of TDP_1 , $TDP_2 = TDP_{Shemer}$, TDP_3 for $f \leq 1$ Hz and TDP_4 for $f > 1$ Hz, and intermittency.....	149
Figure 7.4. Illustration of “Transition Detected” indicator.....	150
Figure 7.5. Velocity waveforms at $r/R=0$ at $Re_{ta}=3018$, $Re_{os}=1610$, $\sqrt{\omega'}=2.72$ and $A_1=0.53$	152
Figure 7.6. Velocity waveforms at all r/R for one period at $Re_{ta}=3018$, $Re_{os}=1610$, $\sqrt{\omega'}=2.72$ and $A_1=0.53$	152
Figure 7.7. One period velocity waveforms at $r/R=0.977$ at $Re_{ta}=3018$, $Re_{os}=1610$, $\sqrt{\omega'}=2.72$ and $A_1=0.53$	153
Figure 7.8. Velocity waveforms at $r/R=0.977$ at $Re_{ta}=3018$, $Re_{os}=1610$, $\sqrt{\omega'}=2.72$ and $A_1=0.53$	153
Figure 7.9. Variation of the dynamic TDP_4 at $r/R=0.977$ at $Re_{ta}=2160$, $Re_{os}=832$, $\sqrt{\omega'}=17.22$ and $A_1=0.39$	154
Figure 7.10. Variation of TDP_3 at $r/R=0$ at $Re_{ta}=3018$, $Re_{os}=1610$, $\sqrt{\omega'}=2.72$ and $A_1=0.53$	155
Figure 8.1. Available data for the onset and the end of transition in pulsatile pipe flows in terms of $Re_{m,crit}$	161
Figure 8.2. Available data for the onset and the end of transition in pulsatile pipe flows in terms of $Re_{ta,crit}$	162

Figure 8.3. Velocity waveforms in laminar and at the onset of transition at $r/R=0.977$ and $r/R=0$ for $\sqrt{\omega'} = 2.72$	165
Figure 8.4. Velocity waveforms in laminar and at the onset of transition at $r/R=0.977$ and $r/R=0$ for $\sqrt{\omega'} = 3.85$	166
Figure 8.5. Velocity waveforms in laminar and at the onset of transition at $r/R=0.977$ and $r/R=0$ for $\sqrt{\omega'} = 5.44$	167
Figure 8.6. Velocity waveforms in laminar and at the onset of transition at $r/R=0.977$ and $r/R=0$ for $\sqrt{\omega'} = 6.67$	168
Figure 8.7. Velocity waveforms in laminar and at the onset of transition at $r/R=0.977$ and $r/R=0$ for $\sqrt{\omega'} = 7.70$	169
Figure 8.8. Velocity waveforms in laminar and at the onset of transition at $r/R=0.977$ and $r/R=0$ for $\sqrt{\omega'} = 8.61$	169
Figure 8.9. Velocity waveforms in laminar and at the onset of transition at $r/R=0.977$ and $r/R=0$ for $\sqrt{\omega'} = 12.17$	171
Figure 8.10. Velocity waveforms in laminar and at the onset of transition at $r/R=0.977$ and $r/R=0$ for $\sqrt{\omega'} = 17.22$	171
Figure 8.11. Velocity waveforms in laminar and at the onset of transition at $r/R=0.977$ and $r/R=0$ for $\sqrt{\omega'} = 27.22$	172
Figure 8.12. Velocity waveforms in laminar and at the onset of transition at $r/R=0.977$ and $r/R=0$ for $\sqrt{\omega'} = 32.21$	173
Figure 8.13. Cross-sectional distributions of \bar{U}_{ta} and $ \bar{U}_{os,1} $ for runs 26, 46 and 62.....	175
Figure 8.14. Cross-sectional distributions of $\bar{U}_{ta} / \bar{U}_{m,ta}$ with r/R for runs 26, 46 and 62.....	176
Figure 8.15. Cross-sectional distributions of $ \bar{U}_{os,1} / \bar{U}_{m,os,1} $ with r/R for runs 26, 46 and 62.....	176
Figure 8.16. Cross-sectional distributions of \bar{U}_{ta} and $ \bar{U}_{os,1} $ for runs 92, 110, 128, 147, 174, 186 and 206.....	179
Figure 8.17. Cross-sectional distributions of $\bar{U}_{ta} / \bar{U}_{m,ta}$ with r/R for runs 92, 110, 128, 147, 174, 186 and 206.....	180
Figure 8.18. Cross-sectional distributions of $ \bar{U}_{os,1} / \bar{U}_{m,os,1} $ with r/R for runs 92,	

110, 128, 147, 174, 186 and 206.....	180
Figure 8.19. Cross-sectional mean velocity profiles obtained experimentally and their FFT approximations for runs 3, 59, 106, 149, 170 and 188.....	183
Figure 8.20. Pressure waveforms acquired from each pressure transmitters for runs 3, 42, 62, 90, 110, 128, 149, 174, 190 and 207.....	185
Figure 8.21. Variations of $\Delta\bar{P}(t)/L$, $\bar{U}_m(t)$ with their FFT approximations and $\bar{\tau}_w(t)$ for runs 3, 47, 112, 156, 168, 186.....	188
Figure 8.22. Variations of $\lambda_u(t)$ and λ_{qL} for runs 3, 47, 133, 156, 168 and 186.....	190
Figure 8.23. Velocity waveforms at the onset of transition and transition to turbulence method at $r/R=0.977$ and $r/R=0$ for run 14.....	192
Figure 8.24. Variation of TP_1 with f in the range of $2.72 \leq \sqrt{\omega'} \leq 8.61$	193
Figure 8.25. Laminar velocity waveforms and graphical representations of the detection method at $r/R=0.977$ and $r/R=0$ for run 26.....	194
Figure 8.26. Velocity waveforms at the onset of transition and transition to turbulence method at $r/R=0.977$ and $r/R=0$ for runs 50, 64 and 88....	196
Figure 8.27. Laminar velocity waveforms and graphical representations of the detection method at $r/R=0.977$ and $r/R=0$ for run 86.....	197
Figure 8.28. Velocity waveforms at the onset of transition and transition to turbulence method at $r/R=0.977$ and $r/R=0$ for runs 113 and 123.....	198
Figure 8.29. Variation of TP_2 with f in the range of $12.17 \leq \sqrt{\omega'} \leq 32.21$	199
Figure 8.30. Velocity waveforms at the onset of transition and transition to turbulence method for $\sqrt{\omega'} > 8.61 (f > 1 \text{ Hz})$ at $r/R=0.977$ and $r/R=0$ for runs 146, 164, 185, 214.....	201
Figure 8.31. Velocity profiles at all r/R at the onset of transition to turbulence for runs 50, 64, 88, 113, 123, 146, 164, 185 and 214.....	203
Figure 8.32. Cross-sectional distributions of \bar{U}_{ta} and $ \bar{U}_{os,1} $ for runs 14, 50 and 64.....	206
Figure 8.33. Cross-sectional distributions of $\bar{U}_{ta}/\bar{U}_{m,ta}$ with r/R for runs 14, 50 and 64 at the onset of transition.....	206
Figure 8.34. Cross-sectional distributions of $ \bar{U}_{os,1} / \bar{U}_{m,os,1} $ with r/R for runs 14, 50 and 64 at the onset of transition.....	207

Figure 8.35. Cross-sectional distributions of \bar{U}_{ta} and $ \bar{U}_{os,1} $ for runs 88, 113, 123, 146, 164, 185 and 214.....	210
Figure 8.36. Cross-sectional distributions of $\bar{U}_{ta}/\bar{U}_{m,ta}$ with r/R for runs 88, 113, 123, 146, 164, 185 and 214 at the onset of transition.....	210
Figure 8.37. Cross-sectional distributions of $ \bar{U}_{os,1} / \bar{U}_{m,os,1} $ with r/R for runs 88, 113, 123, 146, 164, 185 and 214 at the onset of transition.....	211
Figure 8.38. Cross-sectional mean velocity profiles obtained experimentally and theoretically for runs 14, 64, 113, 146, 164 and 185.....	213
Figure 8.39. Pressure waveforms acquired from each pressure transmitters for runs 14, 50, 64, 88, 113, 123, 146, 164, 185 and 214.....	216
Figure 8.40. Variations of $\Delta\bar{P}(t)/L$, $\bar{U}_m(t)$ with their FFT approximations and $\bar{\tau}_w(t)$ for runs 14, 57, 113, 146, 164, 185.....	218
Figure 8.41. Variations of $\lambda_u(t)$ and λ_{qL} for runs 14, 50, 113, 146, 164, 185.....	220
Figure 9.1. Effect of A_1 on $Re_{ta,crit}$ in the range of $2.72 \leq \sqrt{\omega'} \leq 32.21$	224
Figure 9.2. Effect of A_1 on $Re_{ta,crit}$ at $\sqrt{\omega'} = 2.72$	225
Figure 9.3. Effect of A_1 on $Re_{ta,crit}$ at $\sqrt{\omega'} = 3.85$	226
Figure 9.4. Effect of A_1 on $Re_{ta,crit}$ at $\sqrt{\omega'} = 5.44$	226
Figure 9.5. Effect of A_1 on $Re_{ta,crit}$ at $\sqrt{\omega'} = 6.67$	227
Figure 9.6. Effect of A_1 on $Re_{ta,crit}$ at $\sqrt{\omega'} = 7.70$	227
Figure 9.7. Effect of A_1 on $Re_{ta,crit}$ at $\sqrt{\omega'} = 8.61$	228
Figure 9.8. Effect of A_1 on $Re_{ta,crit}$ at $\sqrt{\omega'} = 12.17$	229
Figure 9.9. Effect of A_1 on $Re_{ta,crit}$ at $\sqrt{\omega'} = 17.22$	229
Figure 9.10. Effect of A_1 on $Re_{ta,crit}$ at $\sqrt{\omega'} = 27.22$	230
Figure 9.11. Effect of A_1 on $Re_{ta,crit}$ at $\sqrt{\omega'} = 32.21$	230
Figure 9.12. Effect of A_1 on $Re_{os,crit}$ in the range of $2.72 \leq \sqrt{\omega'} \leq 32.21$	231

Figure 9.13. Effect of A_1 on $Re_{os,crit}$ at $\sqrt{\omega'} = 2.72$	231
Figure 9.14. Effect of A_1 on $Re_{os,crit}$ at $\sqrt{\omega'} = 3.85$	232
Figure 9.15. Effect of A_1 on $Re_{os,crit}$ at $\sqrt{\omega'} = 5.44$	232
Figure 9.16. Effect of A_1 on $Re_{os,crit}$ at $\sqrt{\omega'} = 6.67$	233
Figure 9.17. Effect of A_1 on $Re_{os,crit}$ at $\sqrt{\omega'} = 7.70$	233
Figure 9.18. Effect of A_1 on $Re_{os,crit}$ at $\sqrt{\omega'} = 8.61$	234
Figure 9.19. Effect of A_1 on $Re_{os,crit}$ at $\sqrt{\omega'} = 12.17$	234
Figure 9.20. Effect of A_1 on $Re_{os,crit}$ at $\sqrt{\omega'} = 17.22$	234
Figure 9.21. Effect of A_1 on $Re_{os,crit}$ at $\sqrt{\omega'} = 27.22$	235
Figure 9.22. Effect of A_1 on $Re_{os,crit}$ at $\sqrt{\omega'} = 32.21$	235
Figure 9.23. Effect of A_1 on $Re_{\delta_s,crit}$ in the range of $2.72 \leq \sqrt{\omega'} \leq 32.21$	236
Figure 9.24. Effect of $\sqrt{\omega'}$ on $Re_{ta,crit}$ in the range of $0.10 \leq A_1 \leq 0.90$	238
Figure 9.25. Effect of $\sqrt{\omega'}$ on $Re_{ta,crit}$ at $A_1 = 0.10$	238
Figure 9.26. Effect of $\sqrt{\omega'}$ on $Re_{ta,crit}$ at $A_1 = 0.20$	239
Figure 9.27. Effect of $\sqrt{\omega'}$ on $Re_{ta,crit}$ at $A_1 = 0.30$	240
Figure 9.28. Effect of $\sqrt{\omega'}$ on $Re_{ta,crit}$ at $A_1 = 0.40$	240
Figure 9.29. Effect of $\sqrt{\omega'}$ on $Re_{ta,crit}$ at $A_1 = 0.50$	241
Figure 9.30. Effect of $\sqrt{\omega'}$ on $Re_{ta,crit}$ at $A_1 = 0.60$	241
Figure 9.31. Effect of $\sqrt{\omega'}$ on $Re_{ta,crit}$ at $A_1 = 0.70$	241
Figure 9.32. Effect of $\sqrt{\omega'}$ on $Re_{ta,crit}$ at $A_1 = 0.80$	242
Figure 9.33. Effect of $\sqrt{\omega'}$ on $Re_{ta,crit}$ at $A_1 = 0.90$	242

Figure 9.34. Comparison of the experimental data with the data available in the literature in terms $Re_{ta,crit}$ with $\sqrt{\omega'}$ in pulsatile pipe flows at the onset of transition.....	244
Figure 9.35. Effect of $\sqrt{\omega'}$ on $Re_{os,crit}$ in the range of $0.10 \leq A_1 \leq 0.90$	245
Figure 9.36. Effect of $\sqrt{\omega'}$ on $Re_{os,crit}$ at $A_1 = 0.10$	245
Figure 9.37. Effect of $\sqrt{\omega'}$ on $Re_{os,crit}$ at $A_1 = 0.20$	246
Figure 9.38. Effect of $\sqrt{\omega'}$ on $Re_{os,crit}$ at $A_1 = 0.30$	247
Figure 9.39. Effect of $\sqrt{\omega'}$ on $Re_{os,crit}$ at $A_1 = 0.40$	247
Figure 9.40. Effect of $\sqrt{\omega'}$ on $Re_{os,crit}$ at $A_1 = 0.50$	248
Figure 9.41. Effect of $\sqrt{\omega'}$ on $Re_{os,crit}$ at $A_1 = 0.60$	248
Figure 9.42. Effect of $\sqrt{\omega'}$ on $Re_{os,crit}$ at $A_1 = 0.70$	249
Figure 9.43. Effect of $\sqrt{\omega'}$ on $Re_{os,crit}$ at $A_1 = 0.80$	249
Figure 9.44. Effect of $\sqrt{\omega'}$ on $Re_{os,crit}$ at $A_1 = 0.90$	249
Figure 9.45. Effect of $\sqrt{\omega'}$ on $Re_{\delta_s,crit}$ in the range of $0.10 \leq A_1 \leq 0.90$	250
Figure 9.46. Flow map showing laminar regime and onset of transition in terms of Re_{ta} and Re_{os}	252
Figure 9.47. Flow map showing laminar regime and onset of transition in terms of $Re_{ta,crit}$ with respect to $\sqrt{\omega'}$	253
Figure 9.48. Relationship between $Re_{ta,crit}$ and $A_1 \sqrt{\omega'}$ at the onset of transition....	254
Figure 9.49. Relationship between $Re_{os,crit}$ and $\sqrt{\omega'}$ at the onset of transition.....	254
Figure 9.50. Relationship between $Re_{os,crit}$ and $A_1 \sqrt{\omega'}$ at the onset of transition....	255
Figure 9.51. Relationship between $\sqrt{\omega'}/\sqrt{Re_{ta}^{3/4}}$ and $\lambda_{sL}/\lambda_{u,ta}$ in the laminar regime.....	256
Figure 9.52. Relationship between $\sqrt{\omega'}/\sqrt{Re_{ta}^{3/4}}$ and $\lambda_{sL}/\lambda_{u,ta}$ at the onset of	

transition.....257

Figure 9.53. Relationship between $\sqrt{\omega'}/\sqrt{\text{Re}_{ta}^{3/4}}$ and $\lambda_{sL}/\lambda_{u,ta}$ in the laminar regime and at the onset of transition.....258

LIST OF TABLES

	page
Table 2.1. Pulsatile pipe flow studies with critical values of proposed parameters; utilized validity ranges of $\sqrt{\omega'}$ and comments.....	13
Table 2.2. Oscillating pipe flow studies with critical values of proposed parameters; utilized validity ranges of $\sqrt{\omega'}$ and comments.....	26
Table 3.1. Utilized flow conditioners.....	46
Table 5.1. Uncertainty analysis of velocity measurement in the experimental study based on the method in (ANSI/ASME, 1986), (Coleman and Steele, 1989)and (Wheeler and Ganji, 1996).....	117
Table 5.2. Uncertainty analysis of velocity measurement in the experimental study based on the method in (Jorgensen, 2002).....	118
Table 5.3. Uncertainty analysis of pressure measurement in the experimental study based on the method in (ANSI/ASME, 1986), (Coleman and Steele, 1989) and Wheeler and Ganji, 1996).....	119
Table 5.4. Evaluated uncertainty values of the experimental study ranges.....	120
Table 6.1. Settling distances of the flow conditioners calculated in reference to Eq. (6.6).....	136
Table 6.2. Calculated parameters of Re_x , Re and X/D for the covered range of β in reference to Eq. (6.10).....	139
Table 8.1. Characteristic parameters of the experimental study.....	159
Table 9.1. Linear relations between $Re_{\delta_{os,crit}}$ and A_1 in the range of $2.72 \leq \sqrt{\omega'} \leq 32.21$	235
Table 9.2. Linear relations between $Re_{\delta_s,crit}$ and A_1 in the range of $2.72 \leq \sqrt{\omega'} \leq 32.21$	237
Table 9.3. Relations between $Re_{\delta_s,crit}$ and $\sqrt{\omega'}$ in the range of $0.10 \leq A_1 \leq 0.90$	251

Table 9.4. Relations between $\text{Re}_{os,crit}$ and $A_1\sqrt{\omega'}$ in the range of 0.1 Hz $\leq f \leq$ 14 Hz.....	255
---	-----

LIST OF SYMBOLS

a	acceleration, m/s^2
a_{cal}	constant of relative standard uncertainty, %
a^*	amplitude of the fluid oscillation defined by Sergeev (1966), m
A, B, A', B'	empirical constants of King's law
A_{CM}	amplitude defined by Clamen and Minton (1977), $A_{CM} = 2X_A \sqrt{\omega'} / R$
A_{cross}	pipe cross-sectional area, m^2
A_E	amplitude defined by Eckmann and Grotberg (1991), $A_E = V_T / \pi R^3$
A_M	characteristic parameter defined by Merkli and Thomann (1975), $A_M = 2 U_{os} _r / \sqrt{v\omega}$
A_1	velocity amplitude ratio, $A_1 = \bar{U}_{m,os,1} / \bar{U}_{m,ta}$
A^*	amplitude number defined by Sergeev (1966), $A^* = 4a^* \sqrt{\omega'} / D$
b_{cal}	constant contribution used in uncertainty analysis, m/s
B_x	bias component of the uncertainty
c	speed of sound, m/s
c_1, c_2	empirical constants
C_u	velocity correction factor
d_t	tube diameter of tube bundle, m
d_1, d_2, d_3	hole diameters of Laws' perforated plate, m
D	pipe inner diameter, m

E	voltage read from hotwire anemometer, volt
E_{AD}	daqboard voltage input range
f	frequency of oscillation, 1/s, Hz
f_m	average friction loss coefficient defined by Einav and Sokolov (1993), $f_m = \left(\frac{dP}{dx} \right)_m / \frac{\rho U_m^2}{2D}$
F_p	plug passage frequency defined by Stettler and Hussain (1986), $F_p = fD / U_m$
I	current, amper
I	turbulence intensity, $I = u'_{rms} / \bar{u}$
J_0	first kind Bessel function of zeroth order
k	coverage factor used in the uncertainty analysis based on the method in (Jorgensen, 2002)
k_w/k	conductivity ratio
K	pressure loss coefficient, $K = \frac{\Delta \bar{P}}{1/2 \rho \bar{U}_m^2}$
K_{crit}	critical value of acceleration parameter, K defined by Iguchi and Ohmi (1984), $K = \frac{0.545}{Re^3} \left(-4\omega' Re_{os} \sin \omega t + \frac{\lambda_{q,t}}{2} Re^2 \right)$
l	amplitude of the piston defined by Merkli and Thomann (1975), m
l/d	aspect ratio of hotwire length to wire diameter
L	length of the insert, m
L	axial distance between pressure transmitters, m
L_e	development length, m
M_0	modulus of the first kind Bessel function of zeroth order
N	number of periods

$P(t)$	instantaneous local static pressure, Pa
P_{wv}	water vapor pressure, Pa
P_{x_i}	precision limit for a single measurement
$P_{\bar{x}}$	precision limit of the mean
P_0	ambient pressure, Pa
\bar{P}	ensemble-averaged static pressure, $\bar{P} = \frac{1}{1000} \left(\sum_{i=0}^{999} P_i \right)$, Pa
$ \bar{P}_{os,1} $	oscillating component of pressure, Pa
$ \bar{P}_{os,1} _6$	oscillating component of pressure at 6 th pressure transducer, Pa
$ \bar{P}_{os,1} _7$	oscillating component of pressure at 7 th pressure transducer, Pa
\bar{P}_{ta}	time-averaged component of pressure, Pa
P'_{rms}	root mean square of the fluctuating component of pressure, Pa
$\bar{P}_{6,ta}$	time-averaged component of pressure at 6 th pressure transducer, Pa
$\bar{P}_{7,ta}$	time-averaged component of pressure at 7 th pressure transducer, Pa
Q	volumetric flow rate through pipe cross-section, m ³ /s
Q_h	heat loss from the hotwire, joule
\hat{Q}	amplitude of the periodic component of volume flow defined by Yellin (1966), m ³ /s
\bar{Q}	steady component of volume flow defined by Yellin (1966), m ³ /s
r	radial position from centerline, m
R	pipe radius, m
R_w	hotwire resistance, Ω
Re	steady-state Reynolds number, $Re = UD/\nu$

$Re_{c\omega}$	modulation Reynolds number at the centerline defined by Stettler and Hussain (1986), $Re_{c\omega} = U_{c\omega} D / \nu$
Re_h	Reynolds number of harmonic flow defined by Clamen and Minton (1977), $Re_h = 2RX_A \omega / \nu = 2\sqrt{\omega'}^2 X_A / R$
Re_{ins}	instantaneous Reynolds number, $Re_{ins} = U_{ins} D / \nu$
Re_m	mean Reynolds number used in time-dependent flow, $Re_m = \bar{U}_m D / \nu$
$Re_{m\omega}$	modulation Reynolds number defined by Stettler and Hussain (1986), $Re_{m\omega} = U_{m\omega} D / \nu$
Re_{os}	oscillating Reynolds number, $Re_{os} = \bar{U}_{m,os,1} D / \nu$
Re_{peak}^F	peak Reynolds number defined by Fishler and Brodkey (1991), $Re_{peak}^F = U_{\max} D / \nu$
Re_{peak}^N	peak Reynolds number defined by Nerem et al. (1972), $Re_{peak}^N = \hat{U} \delta_b / \nu$
Re_{peak}^P	peak Reynolds number defined by Peacock et al. (1998), $Re_{peak}^P = U_{peak} D / \nu$
Re_{ta}	time-averaged Reynolds number, $Re_{ta} = \bar{U}_{m,ta} D / \nu$
Re_X	entrance length Reynolds number, $Re_X = (X / D) Re = \bar{U}_m X / \nu$
Re_{δ_b}	Reynolds number based on boundary layer thickness defined by Das and Arakeri (1998), $Re_{\delta_b} = U_e \delta_b / \nu$
Re_{δ_s}	Reynolds number based on Stokes layer thickness, $Re_{\delta_s} = \bar{U}_{m,os,1} \delta_s / \nu$
$Re_{\delta_s}^E$	Reynolds number based on Stokes layer thickness, defined by Eckmann and Grotberg (1991), $Re_{\delta_s}^E = A_E \sqrt{2\omega'}$

$Re_{\delta_s}^F$	Reynolds number based on Stokes layer thickness, defined by Fishler and Brodkey (1991), $Re_{\delta_s}^F = U_{\max} \delta_s / \nu$
Re^*	oscillating Reynolds number defined by Sergeev (1966), $Re^* = a^* D \omega / \nu$
\hat{Re}	lowest Reynolds number defined by Yellin (1966), $\hat{Re} = Re_m (1 - \hat{Q} / \bar{Q})$
S	Stokes parameter, $S = R \sqrt{\omega / 2\nu}$
S_x	standard deviation
$S_{\bar{x}}$	standard deviation of the mean
St	Strouhl number, $St = fD/U$
t	characteristic thickness, m
t	time coordinate, s
T	period of oscillation, s
$T_{w,\max}$	maximum hotwire temperature, °C
T_0	ambient reference temperature, °C
u, v	instantaneous velocity components in x- and r-axis, m/s
u^*	skin friction velocity, $u^* = \sqrt{\tau_w / \rho}$, m/s
\bar{u}_{os}	oscillating component of local velocity in x-axis, m/s
\bar{u}_{ta}	time-averaged component of local velocity in x-axis, m/s
u', v'	instantaneous fluctuating velocity components in x-and r-axis, m/s
u'_{rms}	root mean square value of axial component of instantaneous turbulent fluctuation, $u'_{rms} = \left[\sum_{i=0}^{N-1} (u_i - \bar{u})^2 / N \right]^{1/2}$, m/s
U, V	characteristic velocity, m/s

$U(r, t)$	instantaneous axial velocity, $U = \bar{U} + u'$, m/s
U_{cal}	calibrated velocity data, m/s
$U_{CL}(t)$	instantaneous velocity at pipe centerline, m/s
$U_{c\omega}$	velocity modulation amplitude of at the centerline, m/s
U_e	Maximum velocity of the basic flow at the outer edge of the boundary layer defined by Das and Arakeri (1998), m/s
U_{eff}	effective cooling velocity, m/s
U_h	harmonic velocity defined by Clamen and Minton (1977), $U_h = X_A \omega$, m/s
U_{ins}	instantaneous velocity, m/s
U_{max}	maximum velocity defined by Fishler and Brodkey (1991), $U_{max} = \pi X_{max} / T$, m/s
U_{meas}	measured velocity, m/s
$U_{m\omega}$	velocity modulation amplitude of $\bar{U}_m(t)$, m/s
$U_{neg,peak}$	negative peak value of velocity waveform, m/s
U_{peak}	peak forward velocity in pulsatile flow defined by Peacock et al. (1998), $U_{peak} = \bar{U}_m + u_{os}$, m/s
$U_{pos,peak}$	positive peak value of velocity waveform, m/s
\bar{U}	ensemble-averaged value of axial component of instantaneous velocity, $\bar{U} = \frac{1}{N} \left(\sum_{i=0}^{N-1} u_i \right)$, m/s
\bar{U}_{ave}	average velocity defined by Einav and Sokolov (1993) $\bar{U}_{ave} = \bar{U}_m + \bar{U}_{os,1} \sin(\omega t)$, m/s

\bar{U}_{CL}	ensemble-averaged value of steady flow velocity at pipe centerline, m/s
$ \bar{U}_{CL,os,1} $	oscillating component of velocity at pipe centerline, m/s
$\bar{U}_{CL,ta}$	time-averaged component of velocity at pipe centerline, m/s
\bar{U}_m	steady-state ensemble-averaged cross-sectional mean velocity, $\bar{U}_m = Q/A_{cross}$, m/s
$\bar{U}_m(t)$	time-dependent cross-sectional mean velocity, m/s
\bar{U}_{max}	axial maximum velocity at centerline, m/s
$ \bar{U}_{m,os,1} $	oscillating component of cross sectional mean velocity for the fundamental first wave in the finite Fourier expansion, m/s
$\bar{U}_{m,ta}$	time-averaged component of cross-sectional mean velocity, m/s
$ \bar{U}_{os,n} $	oscillating component of local cross sectional velocity for the fundamental wave in the finite Fourier expansion, m/s
$ \bar{U}_{os,1} $	oscillating component of local cross sectional velocity for the fundamental first wave in the finite Fourier expansion, m/s
\bar{U}_{ta}	time-averaged component of local velocity at any radial position of the probe, m/s
\hat{U}	peak systolic velocity defined by Nerem et al. (1972), m/s
U^+	normalized velocity in viscous wall region, $U^+ = U/u^*$
ν_x	degrees of freedom
$\bar{\nu}_{os}$	oscillating component of local velocity in r-axis, m/s
$\bar{\nu}_{ta}$	time-averaged component of local velocity in r-axis, m/s
V_{ratio}	velocity ratio defined by Clamen and Minton (1977), $V_{ratio} = U_h/U_m$
V_T	tidal volume defined by Eckmann and Grotberg (1991), m ³

$w_{humidity}$	humidity uncertainty
w_{lin}	linearization (conversion) uncertainty
$w_{positioning}$	positioning probe uncertainty
w_{res}	resolution uncertainty
w_R	uncertainty in result
w_{temp}	temperature uncertainty
w_{x_i}	uncertainty in variables
x_i	measured variables
x_0	amplitude of the piston producing the oscillation defined by Gerrard (1971), m
\bar{x}	mean value of measured variables
X	axial length from the end of MFC unit, m
X_A	amplitude of pipe oscillation defined by Clamen and Minton (1977),m
y^+	coordinate in viscous wall region, $y^+ = yu^* / \nu$

Greek Letters

β	open area ratio for flow conditioners, $\beta = \text{area of space} / \text{whole area of flow conditioner}$
γ	intermittency factor
δ_b	boundary layer thickness, m
δ_s	Stokes layer thickness, $\delta_s = \sqrt{2\nu/\omega}$, m
δ_{st}	Stokes-layer thickness defined by Shemer and Kit (1984), $\delta_{st} = \sqrt{\nu/\omega}$, m
∂	partial derivative

$\partial U/\partial E$	slope of the inverse calibration curve, $U = f(E)$
Δ	modulation velocity amplitude defined by Stettler and Hussain (1986), $\Delta = \text{Re}_{m\omega}/\text{Re}_m$
ΔP	ambient pressure difference, Pa
$\Delta \bar{P}(t)$	instantaneous pressure drop, Pa
$ \Delta \bar{P}_{os,1} $	oscillating component of pressure drop, Pa
$\Delta \bar{P}_{ta}$	time-averaged component of pressure drop, Pa
ΔT	temperature difference, Kelvin
ΔU_{lin}	curve fitting error
$\Delta \rho$	density difference, kg/m^3
θ	angle, deg
θ_{time}	real time spent by the fluid below $\text{Re}_{m,crit}$ defined by Yellin (1966)
θ_0	phase of the first kind Bessel function of zeroth order
λ_p	friction factor for laminar pulsatile flow defined by Hershey and Im (1968), $\lambda_p = \frac{(\Delta P)_{ave} R g_c}{U_{ta}^2 L}$
$\lambda_{qL}(t)$	laminar quasi-steady friction factor, $\lambda_{qL}(t) = \frac{64}{(\bar{U}_m(t) D/\nu)}$
$\lambda_{qT}(t)$	turbulent quasi-steady friction factor, $\lambda_{qT}(t) = \frac{0.3164}{(\bar{U}_m(t) D/\nu)^{1/4}}$
λ_{sL}	laminar steady friction factor, $\lambda_{sL} = \frac{64}{(\bar{U}_{m,ta} D/\nu)}$
λ_{sT}	turbulent steady friction factor, $\lambda_{sT} = \frac{0.3164}{(\bar{U}_{m,ta} D/\nu)^{1/4}}$
$\lambda_u(t)$	instantaneous friction factor, $\lambda_u(t) = \frac{8\bar{\tau}_w(t)}{\rho \bar{U}_m^2(t)}$

$\lambda_{u,ta}$	time averaged friction factor, $\lambda_{u,ta} = \frac{8}{\rho \bar{U}_{m,ta}^3 T} \int_0^T \bar{\tau}_w(t) \bar{U}_m(t) dt$
λ_0	amplitude of oscillation defined by Gerrard (1971), $\lambda_0 = \omega x_0 / \bar{U}_{m,ta}$
ν	kinematic viscosity, m ² /s
ρ	fluid density, kg/m ³
ρ_0	density at $t=0$
ρU	mass flux, kg/m ² s
τ	relaxation time defined by Yellin (1966), $\tau = \frac{\theta_{time} V}{2R^2} (\text{Re}_{m,crit} - \hat{\text{Re}})$
$\tau_w(t)$	instantaneous wall shear stress, Pa
ω	angular frequency of oscillation, $\omega = 2\pi f$, rad/s
ω'	dimensionless frequency of oscillation, $\omega' = R^2 \omega / \nu$
$\sqrt{\omega'}$	Womersley number, $\sqrt{\omega'} = R \sqrt{\omega / \nu}$

Subscripts and Superscripts

<i>crit</i>	critical value
<i>CL</i>	centerline
<i>m</i>	mean value
<i>os</i>	oscillating component
<i>rms</i>	root mean square value
<i>ta</i>	time-averaged component
<i>tr</i>	transitional regime
\angle	phase lag
—	ensemble-averaged value
'	turbulent component

Abbreviates and others

<i>CL</i>	centerline
<i>CTA</i>	constant temperature anemometer
<i>FC</i>	case with flow conditioner
<i>FFT</i>	fast Fourier transformation
<i>L</i>	laminar regime
<i>LDA</i>	laser Doppler anemometer
<i>LDV</i>	laser Doppler velocimeter
<i>MFC</i>	mass flow control
<i>OHR</i>	over heat ratio of hotwire probe
<i>res</i>	daqboard resolution, bits
<i>subvi</i>	sub virtual instrument
<i>OT</i>	onset of transition to turbulence regime
<i>STDV</i>	standard deviation
<i>TDFC</i>	time-dependent flow control
<i>TDP</i>	turbulence detection parameter
<i>TDP₁</i>	first kind of turbulence detection parameter, $TDP_1 = dU(t)/dt$
<i>TDP₂</i>	second kind of turbulence detection parameter defined by Shemer (1985), $TDP_2 = TDP_{Shemer} = (dU(t)/dt)^2$
<i>TDP₃</i>	third kind of turbulence detection parameter for $f \leq 1$ Hz, $TDP_3 = R(dU(r,t)/dt)^2 / (\bar{U}_{ia} v \omega^2)$
<i>TDP₄</i>	fourth kind of turbulence detection parameter for $f > 1$ Hz, $TDP_4 = (dU(r,t)/dt)^2 / (\bar{U}_{ia}^2 \omega^2)$
<i>TP₁</i>	first kind of threshold parameter for $f \leq 1$ Hz, $TP_1 = (1/\sqrt{\omega'})^n$ where $n = f $

TP_2	second kind of threshold parameter for $f > 1$ Hz, $TP_2 = (1/\sqrt{\omega'})^4$
vi, VI	virtual instrument in LabView
WFC	case without flow conditioner

CHAPTER 1

INTRODUCTION

1.1. Background and Motivation

Transition to turbulence in time dependent pipe flows is one of the major research areas by the start of 1950's to nowadays. Time dependent flow is expressed simply as a state in which the flow parameters change with time. The understanding of the onset of transition to turbulence and the subsequent fluid interactions that lead to transition to turbulence are still the gaps in this research area. Laminar to turbulent transition starts firstly in the decelerating phase of the time dependent waveforms as turbulent bursts.

Until now, the visual observation of velocity waveforms is a preferred inspection method since transition to turbulence is described by the presence of the disturbed flow with small amplitude perturbations and the growth of turbulent bursts. The observation of the first turbulent bursts in the decelerating phase and covering the whole cycle of oscillation are used to define the critical states of the onset and the end of transition, respectively.

Although, the attention to time-dependent laminar pipe flows can be extended to the early studies of Sexl (1930), Szymanski (1932), Ito (1952), Kusama (1952) and Womersley (1955), transition of laminar periodic flows has been considered as a separate research topic in 1980's (Ohmi et al., 1981; Ohmi and Iguchi, 1982; Ohmi et al., 1980's (Ohmi et al., 1981; Ohmi and Iguchi, 1982; Ohmi et al., 1982; Iguchi and Ohmi, 1982, 1984) as reviewed in (Gündoğdu and Çarpınlioğlu, 1999). In the time period of 1999 to 2010, there are a few number of experimental studies conducted on transition to turbulence in pulsatile pipe flows, major part belonging to earlier studies such as (Sarpkaya, 1966), (Yellin, 1966), (Hershey and Im, 1968), (Gerrard, 1971),

(Nerem et al., 1972), (Mizushima et al., 1973), (Clamen and Minton, 1977), (Ohmi et al., 1982), (Iguchi and Ohmi, 1984), (Shemer and Kit, 1984), (Shemer, 1985), (Stettler and Hussain, 1986), (Einav and Sokolov, 1993), (Peacock et al., 1998). Therefore, the need of updated information on the manner, the need for investigation of the flow physics effects on laminar to turbulent transition and the need of comprehensive research study in which the effects of time dependent flow parameters of Womersley number, $\sqrt{\omega'}$ and velocity amplitude ratio, A_1 on flow dynamics at the onset of transition are forming the motivation of this thesis.

1.2. Objects

The detection of laminar to turbulent transition in sinusoidal pulsatile pipe flow and the analysis of the flow dynamics at the onset of transition are mainly aimed in this thesis. The pulsatile pipe flow in the laminar intermediate region in the ranges of $2.72 \leq \sqrt{\omega'} \leq 32.21$ ($0.1 \text{ Hz} \leq f \leq 14 \text{ Hz}$) and $0.05 \leq A_1 \leq 0.96$ is generated and controlled by means of a devised program named as *TDFC.vi* (Time Dependent Flow Control) in LabView 2009 SP1 environment, with utilizing a 1 MHz, 16 bit IOtech Personaldaq 3001 A/D converter card and a desktop personal computer. The acquisition and processing of the signal is performed by the devised program, *TDFC.vi*. All the analysis of flow dynamics is also carried out by *TDFC.vi*.

The major aim of this study is to detect the onset of laminar to turbulent transition in pulsatile pipe flow by means of a detection method devised in LabView environment; instead of the conventional visual observation of velocity waveforms. In this method, two dimensionless and dynamic turbulence detection parameters and two dimensionless dynamic threshold parameters are defined for the oscillation frequency ranges of $f \leq 1 \text{ Hz}$ and $f > 1 \text{ Hz}$. The transition to turbulence is automatically detected by *TDFC.vi* if the dynamic turbulence parameter exceeds the dynamics threshold parameter at any instant and at any radial position.

1.3. Outline of the Thesis

The main body of the thesis is divided into the chapters as follows:

In chapter 2, the literature survey is presented. The basic terminology and relationships are given. The fundamental experimental studies related to laminar to turbulent transition in pulsatile and oscillating pipe flows are presented.

In chapter 3, the design and layout of the experimental set-up and its components are introduced in details. Each component of the set-up is presented with its technical specification in details. The measuring devices of Constant Temperature Anemometer (CTA) and pressure transmitter, their working principles and their calibration techniques are presented.

In chapter 4, the experimental procedure, the data acquisition and processing techniques are given. The devised program, *TDFC.vi* in LabView 2009SP1 and the methodology used in *TDFC.vi* for data acquisition and processing are presented in details including some sample plots.

In chapter 5, the preliminary tests on characteristics of flow field are given. The symmetry of the velocity field and the hydrodynamic development of velocity profile are discussed. The uncertainty analyses of the measurement chains are carried out and presented in this chapter.

In chapter 6, the control of the laminar steady flow through the pipeline is introduced. Velocity and turbulence intensity profiles over the pipe cross-section are presented at some different axial locations along the pipeline for the cases of with and without flow conditioners. Also, the performance characteristics of the flow conditioners in terms of pressure drop, $\Delta\bar{P}$ are presented.

In chapter 7, the methodology used in the sub-program embedded into *TDFC.vi* for the detection of onset of transition in pulsatile pipe flow is introduced in detail. The verification of the effectiveness and success of the turbulence detection method and the devised program are shown here by some samples.

In chapter 8, the pulsatile flow dynamics in terms of velocity and pressure waveforms, cross-sectional and mean velocity profiles, instantaneous pressure drop,

wall shear stress and friction factor profiles which are calculated/evaluated and plotted are commented. The verification of the turbulence detection method is performed for sample runs both in laminar regime and at the onset of transition.

In chapter 9, the influences of the oscillation frequency, f in other words $\sqrt{\omega'}$ and the velocity amplitude ratio, A_1 on the critical Reynolds numbers at the onset of transition are presented. Some correlations are proposed in the end of the chapter.

In chapter 10, the crucial points as a result of conclusions and the suggestions for the further studies are given.

CHAPTER 2

LITERATURE SURVEY

2.1. Introduction

Laminar to turbulent transition in pipe flows is one of the fundamental problems in fluid mechanics, which has attracted the interest of investigators for more than 100 years. There are still gaps in the understanding of the onset of instability and the subsequent fluid interactions that lead to transition to turbulence. Moreover, this phenomenon also becomes important in time dependent flows. This section presents the state of art on laminar to turbulent transition focused on experimental studies of periodic pipe flows, i.e. pulsatile and oscillating, covering the time period by the start of 1950's to nowadays, pointing out the gaps to be filled in future, and giving recent contributions of the experimental studies drawing attention to critical aspects.

The process by which a laminar flow changes to a turbulent one is called transition. In many cases, real flows in pipes diverge considerably from laminar to turbulent regime after laminar flow initially breakdown because of amplification of small disturbances (Schlichting and Gersten, 2000). The flow goes through a complex sequence of changes finally resulting in the chaotic, which is known as turbulence. The process of transition is greatly as a result of fluctuation intensity of the free stream, roughness of the surfaces, and shape of the flow entrance conditions.

Laminar to turbulent transition in steady pipe flow was studied by many scientists in early times (Hagen, 1839), (Poiseuille, 1840), (Hagen, 1854), (Reynolds, 1883), (Ekman, 1883), (Schiller, 1934), (Pfenninger, 1961). The first systematic

investigations on steady pipe flows were carried out by Reynolds (1883). He discovered the similarity principle introducing a non-dimensional parameter as mean Reynolds number, $Re_m = U_m D / \nu$. In pipe flows, it certainly is not obvious what the critical mean Reynolds number is, $Re_{m,crit}$. Barnes and Coker (1905) obtained experimentally $Re_{m,crit} = 20000$.

The oldest investigations into the mechanics of transition called the K-regime were performed at the U.S. National Bureau of Standards by Schubauer (1957), Klebanoff and Tidstrom (1959), and Klebanoff et al. (1962). Schubauer and Klebanoff (1956) showed transition to be a process involving the formation of turbulent spots, as had been postulated earlier by Emmons (1951). Experimental investigations by Hama et al. (1957), Kovasznay et al. (1962), and Hama and Nautant (1963) utilizing dye techniques in water demonstrated the occurrence of characteristic 3-D dye configurations before transition occurs. The three main stages were identified both experimentally and theoretically as receptivity, linear stability and nonlinear breakdown.

Detailed experimental studies for laminar to turbulent transition in steady pipe flows show that the flow has an “intermittent character” in a certain region of Reynolds numbers close to the critical value. The physical character of the flow is given by the *intermittency factor*, γ . This factor is the fraction of time for flow being fully turbulent, i.e., $\gamma=0$ means continuous laminar flow and $\gamma=1$ means continuous turbulent flow.

For both steady and time dependent pipe flows, some turbulent structures occur during the period of laminar to turbulent transition. For the intermediate Re_m , a localized perturbation induces turbulence in localized sections of the pipe only, named as *puff*, *slug* and *equilibrium puff* (Wyganski and Champagne, 1973), (Wyganski et al., 1975). In Fig. 2.1 and Fig. 2.2, typical centerline velocity time records (Durst and Ünsal, 2006) and numerical flow visualization (Shan et al., 1999) of puff and slug-type turbulent structures are given as their definitions, respectively. A slug in the transition has similar characteristics to the corresponding fully

developed turbulent flow having definite interfaces at their heads and tails while puff has not a clear interface at their head and their mean velocities are roughly the same as the mean flow velocity of the pipe flow. The slugs are generated at supercritical Re by the instabilities of the flow at the inlet. Puff may be considered as a natural minimal flow unit for turbulence in a pipe and the smallest volume in which a chaotic flow can be sustained. Equilibrium puff is defined as that the length of the puff is maintained at a constant rate while the puff propagates downstream, being found to neither grow, nor shrink and observed to travel downstream through the pipe (Wyganski et al., 1975). As the slugs form and grow, the increased friction due to the turbulent flow in them produces a reduction in mass flux (Sreenivasan and Ramshankar, 1986).

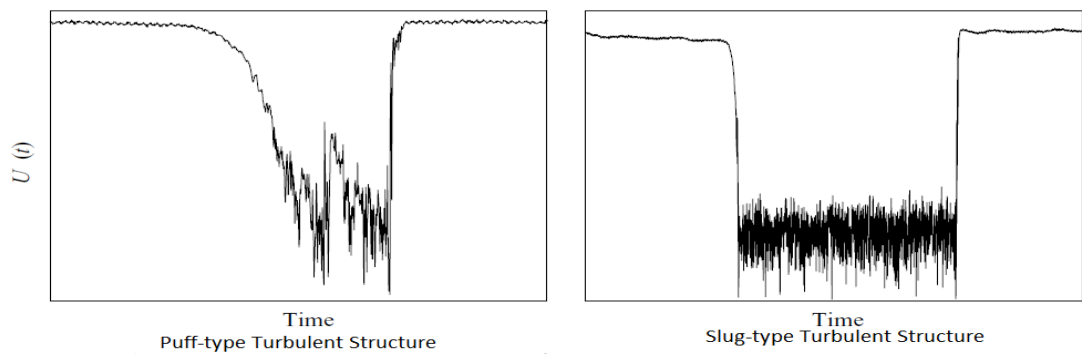


Figure 2.1 Centerline velocity time records of puff and slug type turbulent structures (Durst and Ünsal, 2006)

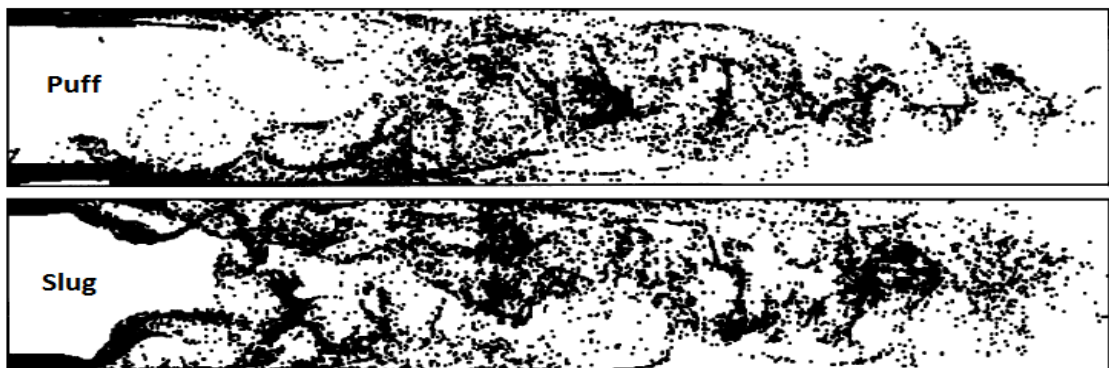


Figure 2.2 Typical numerical flow visualizations of puff and slug type turbulent structures (Shan et al., 1999)

Time dependent flow is expressed simply as a state in which the flow parameters change with time. Classification sketch of time dependent flows is shown in Fig. 2.3. Periodic flows have regular flow pattern with respect to time, i.e., in form of sinusoidal, triangular, rectangular or saw toothed waves, etc. They can be classified as pulsatile/pulsating and oscillatory/oscillating flows. Pulsatile flow is composed of a steady component and a superimposed periodical time varying component called oscillation. Oscillating flow itself is a special type of pulsatile flow which is governed by an oscillation only, with a zero steady flow component.

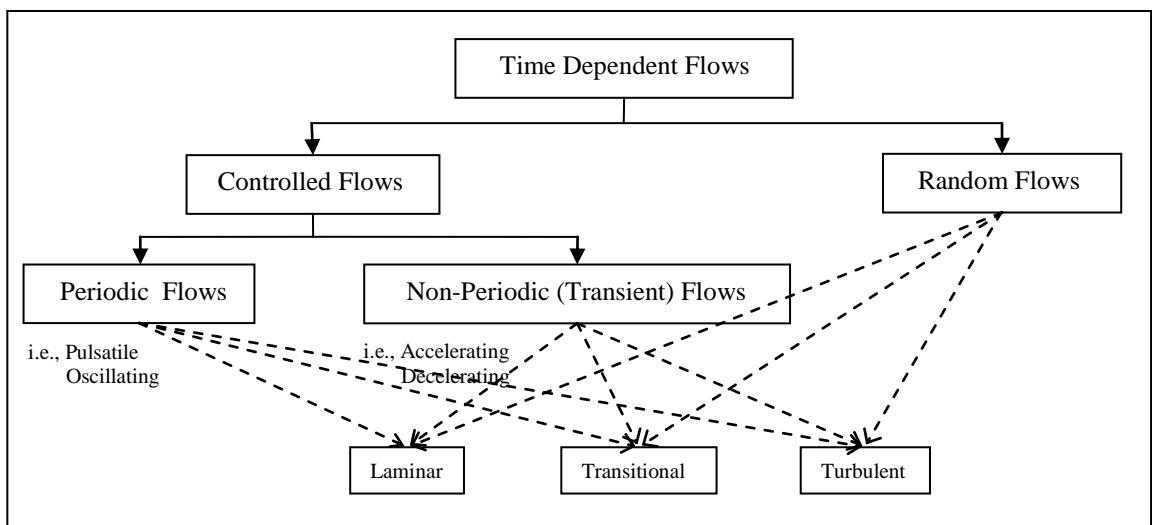


Figure 2.3 Classifications of time dependent flows

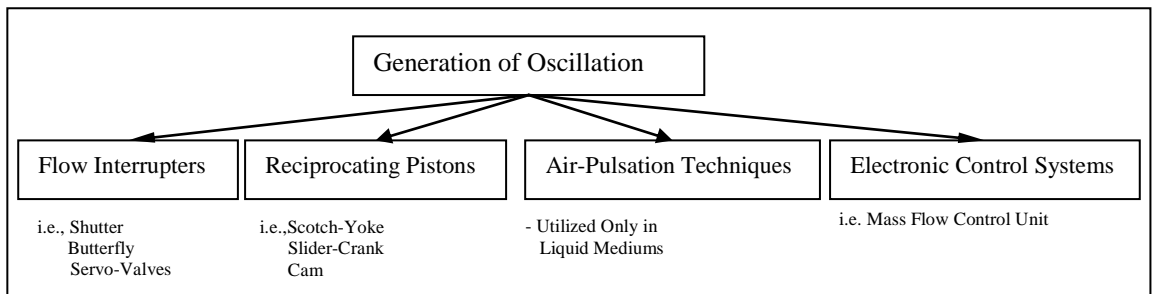


Figure 2.4 Methods used for production of oscillation

The studies of a periodic oscillation mostly in the form of a sinusoidal wave in the literature were preferred due to the simplicity in its production, control and analytical treatment. The methods used for the generation of oscillation are given in Fig. 2.4. In most of the experimental studies, pressure gradient controlling was used as a method for generation of oscillation. Currently new technologies are in use for generation and control of oscillations (Durst et al., 2003).

Let us recall the basic relations for time dependent viscous compressible pipe flow in cylindrical coordinates. The general governing equations for transitional pulsatile flows are;

a) Momentum equations:

$$\frac{\partial \bar{u}}{\partial t} + \bar{u} \frac{\partial \bar{u}}{\partial x} + \bar{v} \frac{\partial \bar{u}}{\partial r} = -\frac{1}{\rho_0} \frac{\partial \bar{P}}{\partial x} + \nu \left(\frac{\partial^2 \bar{u}}{\partial x^2} + \frac{\partial^2 \bar{u}}{\partial r^2} + \frac{1}{r} \frac{\partial \bar{u}}{\partial r} \right) + \frac{\nu}{3} \frac{\partial}{\partial x} \left(\frac{\partial \bar{u}}{\partial x} + \frac{\partial \bar{v}}{\partial r} + \frac{\bar{v}}{r} \right)$$

(x-axis) (2.1)

$$\frac{\partial \bar{v}}{\partial t} + \bar{u} \frac{\partial \bar{v}}{\partial x} + \bar{v} \frac{\partial \bar{v}}{\partial r} = -\frac{1}{\rho_0} \frac{\partial \bar{P}}{\partial r} + \nu \left(\frac{\partial^2 \bar{v}}{\partial x^2} + \frac{\partial^2 \bar{v}}{\partial r^2} + \frac{1}{r} \frac{\partial \bar{v}}{\partial r} - \frac{\bar{v}}{r^2} \right) + \frac{\nu}{3} \frac{\partial}{\partial x} \left(\frac{\partial \bar{u}}{\partial x} + \frac{\partial \bar{v}}{\partial r} + \frac{\bar{v}}{r} \right)$$

(r-axis) (2.2)

b) Continuity equation:

$$\frac{\partial \rho}{\partial t} + \rho_0 \left(\frac{\partial \bar{u}}{\partial x} + \frac{\partial \bar{v}}{\partial r} + \frac{\bar{v}}{r} \right) = 0$$

(2.3)

c) Compressibility relation:

$$\frac{\partial \bar{P}}{\partial \rho} = c^2$$

(2.4)

In the case of turbulent flow, instantaneous values of velocities and pressure are written as;

$$P = \bar{P} + P'; \quad u = \bar{u} + u'; \quad v = \bar{v} + v' \quad (2.5)$$

For pulsatile flow, ensemble-averaged value has a long time averaged value and an oscillatory component due to the pulsation, which are denoted by subscripts “*ta*” and “*os*”, respectively. Therefore, the instantaneous values in Eq. (2.5) can be rewritten for pulsatile flows as;

$$P = \bar{P}_{ta} + \bar{P}_{os} + P' \quad (2.6a)$$

$$U = \bar{U}_{ta} + |\bar{U}_{os}| + U' \quad (2.6b)$$

$$V = \bar{V}_{ta} + |\bar{V}_{os}| + V' \quad (2.6c)$$

where

$$|\bar{U}_{os}| = \sum_{n=1}^6 |\bar{U}_{os,n}| \sin(n\omega t + \angle \bar{U}_{os,n}) \quad (2.7)$$

\bar{U} is the phase averaged value, u' is the fluctuating component due to turbulent motion. The phase averaged value, \bar{U} is obtained from the data for N periods as follows;

$$\bar{U}(r,t) = \frac{1}{N} \sum_{i=0}^{N-1} U_i, \quad U_i = U(r,t+iT) \quad (2.8)$$

$$\bar{P}(t) = \frac{1}{N} \sum_{i=0}^{N-1} P_i; \quad P_i = P(t+iT) \quad (2.9)$$

The root mean square of the turbulent fluctuation velocity in axial direction u'_{rms} can be calculated as follows;

$$u'_{rms} = \left[\sum_{i=0}^{N-1} (U_i - \bar{U})^2 / N \right]^{1/2} \quad (2.10)$$

$$P'_{rms} = \left[\sum_{i=0}^{N-1} (P_i - \bar{P})^2 / N \right]^{1/2} \quad (2.11)$$

The measured values of u'_{rms} are approximated by the following finite Fourier series as follows;

$$u'_{rms} = u'_{rms,ta} + u'_{rms,os} \quad (2.12)$$

$$u'_{rms,os} = \sum_{n=1}^6 |u'_{rms,os,n}| \sin(n\omega t + \angle u'_{rms,os,n}) \quad (2.13)$$

Neglecting the radial component of motion, the axial one is approximated, as was previously done in the literature, for slightly compressible pulsatile flows as;

$$\frac{\partial \bar{U}}{\partial t} = -\frac{1}{\rho_0} + \nu \left(\frac{\partial^2 \bar{U}}{\partial r^2} + \frac{1}{r} \frac{\partial \bar{U}}{\partial r} \right) - \frac{1}{r} \frac{\partial}{\partial r} (\overline{ru'v'}) \quad (2.14)$$

$$\frac{\partial \bar{P}}{\partial t} + \rho_0 c^2 \left(\frac{\partial \bar{U}}{\partial x} + \frac{\partial \bar{V}}{\partial r} + \frac{\bar{V}}{r} \right) = 0 \quad (2.15)$$

The sub-steps and details of these relations for time dependent compressible viscous flows are given in the Ph. D. thesis of Gündoğdu (2000), and in Gündoğdu and Çarpınlioğlu (1999, Part1 & 2). The final form of the general momentum-integral equation valid for turbulent pipe flows is given as:

$$\rho \frac{d\bar{U}_m(t)}{dt} + \frac{4\bar{\tau}_w(t)}{D} = \frac{\Delta\bar{P}(t)}{L} \quad (2.16)$$

The experimental values of \bar{U}_m and $\Delta\bar{P}/L$ are approximated by the finite Fourier expansion as given by Ohmi et al. (1982):

$$\bar{U}_m = \bar{U}_{m,ta} + \sum_{n=1}^N |\bar{U}_{m,os,n}| \sin(n\omega t + \angle\bar{U}_{m,os,n}) \quad (2.17)$$

$$\Delta\bar{P}/L = \Delta\bar{P}_{ta}/L + \sum_{n=1}^N |\Delta\bar{P}_{os,n}/L| \sin(n\omega t + \angle\Delta\bar{P}_{os,n}) \quad (2.18)$$

The measured values are generally approximated by the first harmonics of the wave as follows;

$$\bar{U}_m = \bar{U}_{m,ta} + |\bar{U}_{m,os,1}| \sin(\omega t + \angle\bar{U}_{m,os,1}) \quad (2.19)$$

$$\Delta\bar{P} = \Delta\bar{P}_{ta} + |\Delta\bar{P}_{os,1}| \sin(\omega t + \angle\Delta\bar{P}_{os,1}) \quad (2.20)$$

Time average velocity can be defined as;

$$\bar{U}_{m,ta} = \frac{1}{T} \int_T U dt \quad (2.21)$$

where the instantaneous velocity at a point in the flow direction is; $U = \bar{U}_m + u'$.

As a result of the substitution of Eqs. (2.17) and (2.18) into Eq. (2.16), the following two momentum balance equations are obtained as;

$$\frac{\Delta\bar{P}_{ta}}{L} = \frac{4\bar{\tau}_{w,ta}}{D} \quad (2.22)$$

$$\begin{aligned} & -\rho_0 n\omega |\bar{U}_{m,os,n}| \sin(n\omega t + \angle\bar{U}_{m,os,n}) + (4|\bar{\tau}_{w,os,n}|/D) \cos(n\omega t + \angle\bar{\tau}_{w,os,n}) \\ & = (|\Delta\bar{P}_{os,n}|/L) \cos(n\omega t + \angle\Delta\bar{P}_{os,n}/L) \end{aligned} \quad (2.23)$$

2.2. Laminar to Turbulent Transition in Pulsatile Pipe Flows

The studies related to transitional pulsatile pipe flows are based mainly on the observations of velocity waveforms and detection of disturbance growth. Until the early 1960's there were no detailed studies. The essential studies conducted from then till now on transitional pulsatile pipe flow with their critical numbers and validity ranges are given in Table 2.1. The experimental ranges of the studies conducted on transitional pulsatile pipe flow in the literature are given in Appendix 1.

Table 2.1. Pulsatile pipe flow studies with critical values of proposed parameters; utilized validity ranges of $\sqrt{\omega'}$ and comments

Author	Critical number	Validity range	Comment
Sarpkaya (1966)	$Re_{m,crit} = 6500$	$2 \leq \sqrt{\omega'} \leq 8.5$	Onset of transition
Yellin (1966)	$\tau = \frac{\theta_{time} V}{2R^2} (Re_{m,crit} - \hat{Re})$	$4 \leq \sqrt{\omega'} \leq 13$	Neither Re_m nor \hat{Re} was sufficient for determination of transition alone
Hershey and Im (1968)	$Re_{ta,crit} = 2100$	$0 \leq \sqrt{\omega'} \leq 4.24$	Onset of transition
Gerrard (1971)	$Re_m = 3770$	$\sqrt{\omega'} = 14.4$	$Re_m = 3770$ lies in the turbulent transition range
Nerem et al. (1972)	$Re_{peak,crit}^N = 250\sqrt{\omega'}$ for descending aorta $Re_{peak,crit}^N = 150\sqrt{\omega'}$ for ascending aorta	$4 \leq \sqrt{\omega'} \leq 6$	Onset of transition
Mizushina et al. (1973)	$T > T_{crit}$ Profile I $T < T_{crit}$ Profile II $T_{crit} U_m / D \cong 0.19 Re^{2/3}$	$8.62 \leq \sqrt{\omega'} \leq 27.78$ $0.76s \leq T \leq 7.9s$	Profile I: Velocity profile is similar to the steady state Profile II: Velocity profile is different from steady state
Clamen and Minton (1977)	$Re_{m,crit} = 1500$ and up to $\sqrt{\omega'} = 16.6$	$11.2 \leq \sqrt{\omega'} \leq 34$	Onset of transition
Clamen and Minton (1977)	$A_{CM,crit} = \frac{2X_A \sqrt{\omega'}}{R} = 394$	$11.2 \leq \sqrt{\omega'} \leq 34$	Onset of transition

Table 2.1. (Cont.)

Ohmi et al. (1982)	$Re_{ta,crit} > 2240$	$\sqrt{\omega'} = 8.93$ $\sqrt{\omega'} = 16.48$	Onset of transition
Ohmi et al. (1982)	$Re_{ta,crit} = 4830$	$\sqrt{\omega'} = 8.93$	Turbulent bursts in decelerating phase
Ohmi et al. (1982)	$Re_{ta,crit} = 9690$	$\sqrt{\omega'} = 8.93$	Turbulent bursts over one cycle
Ohmi et al. (1982)	$Re_{ta,crit} = 12300$	$\sqrt{\omega'} = 16.48$	Turbulence in decelerating phase
Ohmi et al. (1982)	$Re_{ta,crit} = 24200$	$\sqrt{\omega'} = 16.48$	Turbulence over one cycle
Iguchi and Ohmi (1984)	$K_{crit} = 6 \times 10^{-7}$	$4.16 \leq \sqrt{\omega'} \leq 23.13$	Limit for occurrence of bursts in conditionally turbulent
Shemer and Kit (1984)	$\sqrt{St/Re_m} = \sqrt{2\pi f v} / U_m < 0.018$	$4.55 \leq \sqrt{\omega'} \leq 14.4$	Quasi-steady flow behavior
Shemer (1985)	$Re_{m,crit} > 3000$	$\sqrt{\omega'} = 6.5$	Fully turbulent for whole pipe
Stettler and Hussain (1986)	$Re_{m,crit} < 2540$	$1 \leq \sqrt{\omega'} \leq 70$	Fully laminar
Stettler and Hussain (1986)	$Re_{m,crit} = 2330$	$\sqrt{\omega'} = 6.25$	Onset of transition
Stettler and Hussain (1986)	$Re_{m,crit} = 2000$	$\sqrt{\omega'} \approx 70$	Onset of transition
Einav and Sokolov (1993)	$Re_{m,crit} = 1700$ and $Re_{os,crit} = 1385$	$9.89 \leq \sqrt{\omega'} \leq 21.2$	Onset of transition during decelerating phase
Peacock et al. (1998)	$Re_{peak,crit}^p = 169\sqrt{\omega'}^{0.83} St^{-0.27}$	$1.5 \leq \sqrt{\omega'} \leq 55$	Onset of transition
Çarpınlioğlu (2003)	$Re_{os,crit} = 2000$ $Re_{ta,crit} = 17929$	$7 \leq \sqrt{\omega'} \leq 28$	Onset of transition
Çarpınlioğlu (2003)	$Re_{ta,crit} = 23763$	$7 \leq \sqrt{\omega'} \leq 28$	End of transition

The first study conducted on laminar to turbulent transition in a pulsatile pipe flow by means of flow visualization is one by Gilbrech and Combs (1963). Later, Sarpkaya (1966) carried out an experimental study on determination of $Re_{m,crit}$ for pulsatile Poiseuille flow of aero hydraulic oil. The flow remained laminar up to $Re_m = 6500$ above which random 3-D bursts of turbulence were observed. Moreover, $Re_{m,crit}$ for the pulsatile flow was found to be higher than $Re_{m,crit}$ for steady pipe flow for the same mean pressure gradient clarifying that pulsatile flow was more stable than the steady flow.

Yellin (1966) investigated the development of turbulence by analyzing the dynamic characteristic parameters of the transition such as the velocity and intermittency in the case of a simple sinusoidal pulsatile pipe flow of dilute aqueous dispersion of bentonite in the range of $0 \leq Re_m \leq 3500$, $\infty \leq \hat{Q}/\bar{Q} \leq 2.2$ and $1600 \leq \hat{Re} \leq 11200$. The flow was classified by means of visual observations as laminar, disturbed and turbulent flow. It was speculated that arterial blood flow was probably disturbed but not truly turbulent. Neither Re_m nor the instantaneous Reynolds number, Re_{ins} was found to be a sufficient criterion to determine the onset of transition in a pulsatile flow. A new parameter called the relaxation time was introduced to interpret the effect of periodic flow component as:

$$\tau = \frac{\theta_{time} V}{2R^2} (Re_{m,crit} - \hat{Re}) \quad (2.24)$$

where θ_{time} is the real time spent by the fluid below $Re_{m,crit}$. It was emphasized that the relaxation time varied inversely with $\sqrt{\omega'}$ and Re_m , and directly with (\hat{Q}/\bar{Q}) where \hat{Q} is the amplitude of the periodic component of volume flow and \bar{Q} is the steady component of volume flow. The turbulence was found to persist when τ was nearly lower than 35. The disturbances were restricted to the core when transition occurred. Yellin (1966) also reported on the basis of the visual observations by photo cell the existence of three types of flows such as;

Region (i) : laminar flow

Region (ii) : disturbed flow

Region (iii) : turbulent flow.

However, Nerem et al. (1972) classified the types of flows into three regions with respect to Reynolds number as;

Region (1) : undisturbed flow

Region (2) : disturbed flow

Region (3) : highly disturbed flow.

Besides, Ohmi et al. (1979) investigated the transition to turbulence in a pulsatile flow with zero time averaged Reynolds number and classified the types of flows into five regions based on the observation of waveforms as follows;

Region (I) : laminar flow

Region (II) : small amplitude perturbations appear in the early stage of accelerating phase at the central portion of a pipe

Region (III) : small amplitude perturbations exist in the phase of higher velocity

Region (IV) : turbulent bursts occur in the decelerating phase

Region (V) : turbulent bursts occur in the accelerating phase as well as in the decelerating phase.

Later, Ohmi et al. (1982) investigated the velocity waveforms in pulsatile flows in a pipe in the experimental range of $\sqrt{\omega'} = 8.93$ and 16.48 , $0.0636 \leq A_1 \leq 1.81$, $0 \leq Re_{ta} \leq 24200$ and $1310 \leq Re_{os} \leq 19700$. They have classified pulsatile flows based on the observation of velocity waveforms into three types with regard to parameters; $\sqrt{\omega'}$, Re_{ta} , and A_1 . Velocity perturbation was observed in the phase of lower velocity above $Re_{ta} = 2240$. Turbulent bursts were seen only in the decelerating phase at $Re_{ta} = 4830$ and over one cycle at $Re_{ta} = 9690$ for pulsatile flow based on the oscillatory laminar flow. Turbulence was first observed with higher frequency in the decelerating phase at $Re_{ta} = 12300$ and then appeared over one cycle at $Re_{ta} = 24200$. Relaminarization was also observed in the accelerating phase. Their classification of the flows near the transition region is as follows;

i) laminar,

- ii) disturbed with small amplitude perturbation in the early acceleration phase of the velocity waveform,
- iii) turbulent flow with turbulent bursts occurring in the decelerating phase and over the full oscillation cycle.

Another study for sinusoidal pipe flow was performed by Hershey and Im (1968). The experimental friction factor and theoretical Fanning friction factor for laminar pulsatile flow were calculated from the following equations, respectively;

$$\lambda_p = \frac{(\Delta P)_{ave} R}{\rho U_{ta}^2 L} \quad (2.25)$$

$$\lambda_p = 16/\text{Re}_{ta} \quad (2.26)$$

Comparison of the experimental friction factors with theoretical ones has shown an excellent agreement between them. The departure from the theory was accepted as the onset of the transition from laminar to turbulence just after $\text{Re}_{ta}=2100$. $\text{Re}_{ta,crit}$ was seen to increase when ω' decreased as stated before by Sarpkaya (1966) and Gilbrech and Combs (1963).

Gerrard (1971) investigated relaminarization effects in pulsatile water pipe flow at $\text{Re}_m=3770$ defining three principal parameters as Re_m , $\sqrt{\omega'}$ and non-dimensional amplitude of oscillation, $\lambda_0 = \omega x_0 / \bar{U}_{m,ta}$. He observed that the turbulence intensity tended to decrease in the acceleration phase, known as relaminarization, and it increased in the deceleration phase. Closer to the wall, the oscillating profile was well represented by $|\bar{U}_{os,1}| / \bar{U}_{m,ta} \propto (y/R)^{1/n}$ in the turbulent phase.

Nerem et al. (1972) classified pulsatile flows as undisturbed, disturbed and highly disturbed utilizing velocity waveforms on dog's aorta through the definition

of $Re_{peak}^N = \hat{U}\delta_b / \nu$. They observed different linear relationships between Re_{peak}^N and Re_m in descending and ascending aorta as shown in Table 2.1.

Mizushina et al. (1973) measured turbulence intensity and velocity profiles for pulsatile pipe flow and classified the flow by means of a critical period of pulsation T_{crit} , which was defined to be the maximum time between bursts and introduced a parameter of $T_{crit}U_m / D \cong 0.19 Re_m^{2/3}$ valid in the range of $2300 < Re_m < 10^5$ and $0.76 \text{ sec} \leq T \leq 7.9 \text{ sec}$. In Profiles I series ($T > T_{crit}$) the velocity profiles with pulsation were found to be similar to the steady-state profile. However, in Profiles II series ($T < T_{crit}$) it was found that the pulsation did not affect the mean time between bursts, and so the turbulence intensity did not pulsate but the velocity pulsed smoothly.

Clamen and Minton (1977) measured the velocities and the intermittency of the periodic bursts of pulsatile water flow in the range of $1275 \leq Re_m \leq 2900$, $0.5 \leq V_{ratio} \leq 6.5$ and $X_A/R = 5.8$ by means of the hydrogen-bubble technique and defined Reynolds number of the harmonic flow and the stability parameter, respectively as:

$$Re_h = 2RX_A \omega / \nu = 2\sqrt{\omega'}^2 X_A / R \quad (2.27)$$

$$A_{CM} = 2X_A \sqrt{\omega'} / R \quad (2.28)$$

From the visual observation, the pulsatile flow was found to be undisturbed, disturbed or highly disturbed. The velocity distribution was found to correspond to laminar flow theory up to $Re_m = 1500$, $\sqrt{\omega'} = 10$ and $A_{CM} = 394$ with no mean flow. An increase in Re_m or amplitude of oscillation increased the intermittency, while an increase in frequency of oscillation decreased the intermittency at constant Re_m and constant amplitude of oscillation.

Two series of LDA experiments were carried out on fully developed pulsatile pipe oil flow in the range of $3.76 \leq \sqrt{\omega'} \leq 22.29$ at $Re_m = 2900$ by Ramaprian and Tu (1980). When $f = 1.75$ Hz, the flow became fully turbulent. The intermittency factor, γ , was found $\gamma = 0.2$ for the mean quasi-steady flow, $\gamma = 0.65$ for turbulent puffs of oscillating flow at $f = 0.4$ Hz. During the second half of the experiment, the unsteady flow remained nearly laminar and this half was named as laminarized unsteady flow. The structure in the flow strongly looked like the puff-type transitional structure. After this flow was oscillated at whatever frequency, laminarization was observed with the intermittency of puffs dropping almost to zero. Yellin (1966) stated that the disturbances were restricted to the core when transition occurred in pulsatile flows. However, no explanation was provided about this phenomenon by Ramaprian and Tu (1980). They concluded that periodic oscillation caused to increase in $Re_{m,crit}$ of puff-type transitional pipe flow. The extent of relaminarization was found to be dependent on the intermittency of puffs in the quasi-steady mean flow, the oscillation frequency and the residence time of the puffs in the pipe. It was suggested to perform further experiments, preferably at much higher Re_m , in order to corroborate the effects of oscillations on the time mean properties of the flow.

The instantaneous velocity distributions on flow reversal of pulsatile and oscillating pipe flows were investigated in the range of $4.29 \leq \sqrt{\omega'} \leq 16.48$, $1.06 \leq A_I \leq 1.81$, $9850 \leq Re_{os} \leq 21,800$, and $0 \leq Re_{ta} \leq 17,600$ by Iguchi and Ohmi (1982). When a flow relaminarization occurred, the time averaged distribution of axial velocity components was seen to be neither the parabolic nor one-seventh power law velocity distribution. The propagation of turbulence was seen to be starting from the vicinity of wall to the core region and the eddy viscosity, ε , influenced the whole flow field over the cross-section of the pipe. The turbulence with higher frequency decayed out when the flow changed its direction and the flow returned back to laminar. The occurrence of turbulent bursts was observed in the decelerating phase. It was declared that the velocity profile obeyed one-seventh power law in the phase when turbulence appeared and the pressure drop could be calculated readily from the momentum equation and the wall shear stress for turbulent quasi-steady flow is given by following equations:

$$\tau_w = \lambda_{q,t} \rho_0 \bar{U}_m |\bar{U}_m| / 8 \quad (2.29)$$

$$\lambda_{qT} = 0.3164 / |\text{Re}_m|^{1/4} \quad (2.30)$$

Iguchi and Ohmi (1984) have studied the transition in a pulsatile pipe flow in the range of $4.16 \leq \sqrt{\omega'} \leq 23.13$, $0.0685 \text{ Hz} \leq f \leq 2.083 \text{ Hz}$, $\text{Re}_{ta} < 10^5$ and $\text{Re}_{os} < 10^5$. They have classified pulsatile pipe flows into four categories such as; laminar, transitional, conditionally turbulent and fully turbulent flows by specifying limits between them in terms of $\sqrt{\omega'}$, Re_{ta} and Re_{os} . It was declared that the limit between the conditionally turbulent and the fully turbulent flow existed even at the lowest value of instantaneous Reynolds number, Re_{ins} of about 7000 when $f=2.083 \text{ Hz}$ or $\sqrt{\omega'}=23.13$. They have introduced an acceleration parameter, K as a criterion for the relaminarization in a pulsatile pipe flow such as;

$$K = \frac{0.545}{\text{Re}^3} \left(-4\omega' \text{Re}_{os} \sin \omega t + \frac{\lambda_{q,t}}{2} \text{Re}^2 \right) \quad \text{where } \text{Re} = \text{Re}_{ta} + \text{Re}_{os} \sin \omega t. \quad (2.31)$$

They have claimed that the limit between the conditionally turbulent and fully turbulent flow could be described by $K_{crit} = 4.5 \times 10^{-6}$. The critical limit of K for the occurrence of bursting in the conditionally turbulent flow without flow reversal was found to be $K_{crit} = 6 \times 10^{-7}$. They emphasized that further experimental studies on the applicability of K is necessary and that a greater range of experimental variables should be examined to analyze the transitional pulsatile flows.

Laminar to turbulent transition in a pulsatile pipe flow was also investigated in quasi-steady regime by Shemer (1985). The steady flow was kept laminar up to $\text{Re}_m = 20,000$. Instantaneous waveforms in transitional pulsatile flow at $\text{Re}_m = 4150$ were investigated. The intermittency coefficient was minimum at the beginning of the acceleration phase at all radial positions. When the instantaneous Reynolds number, Re_{ins} increased and exceeded 3000, intermittency coefficient grew and reached to the maximum value close to unity. It was expressed that the turbulent

slugs, once generated, were convected downstream by the mean flow. The propagation velocity of the leading edge of the slug was higher than that of the trailing edge at $Re_m > 3000$. So, the flow became fully turbulent.

Stettler and Hussain (1986) studied the pulsatile transitional water pipe flow using LDA in a wide frequency range of $1 < \sqrt{\omega'} < 70$. They have characterized the follow non-dimensional parameters such as modulation Reynolds number, $Re_{m\omega}$ and $Re_{c\omega}$, modulation velocity amplitude, $\Delta = Re_{m\omega}/Re_m$ and dimensionless plug passage frequency, F_p that are given in Table 1. Their experimentally obtained $Re_{m\omega}/Re_{c\omega}$ versus $\sqrt{\omega'}$ curve showed that $Re_{m\omega}/Re_{c\omega}$ was strongly $\sqrt{\omega'}$ -dependent only for $3 < \sqrt{\omega'} < 10$ as shown before by Uchida (1956). $Re_{m,crit}$ was observed first to increase rapidly and reach to a maximum value at $\sqrt{\omega'} = 5$, and then decrease to the steady flow value of 2000 at very high frequencies. It was emphasized that increasing pulsation amplitude destabilized the flow at high or low frequencies but stabilized the flow at intermediate frequencies. They have also found that decreasing $\sqrt{\omega'}$ progressively stabilized the flow until $\sqrt{\omega'} = 5$, below which the flow was unstable again. In pulsatile pipe flow, no plugs were observed and the flow was detected to be fully laminar at all times for $Re_{m\omega} = 1110$ and $Re_m < 2540$. Increase in mean Reynolds number, Re_m , resulted in the occurrence of small disturbances. Plugs were seen for $Re_m > 2540$. For pulsatile pipe flow, $Re_{m,crit}$ was found as 2000 for $Re_{m\omega} = 0, 250, 450$ and 674 , while $Re_{m,crit} = 2450$ for $Re_{m\omega} > 674$, and $Re_{m,crit} = 2330$ at $\sqrt{\omega'} = 6.25$. Increase of $\sqrt{\omega'}$ from 1 to 5 also observed to result in a rapid increase in $Re_{m,crit}$ for high $Re_{m\omega}$ and Δ , but more gradual increase for low $Re_{m\omega}$ and Δ . More details can be found in their paper such as neutral stability curves separating laminar-transition regions in the $(Re_{m,crit} - \sqrt{\omega'})$ plane for constant $Re_{m\omega}$ and variable Δ and vice versa.

Another experimental study on transitional pulsatile water pipe flow was carried out by Einav and Sokolov (1993) in the range of $0 < Re_m < 4000$,

$0 < \text{Re}_{os} < 4000$ and $7 < St < 15$. They have used following relations for the average velocity as:

$$\bar{U}_{ave} = \bar{U}_m + |\bar{U}_{os,1}| \sin(\omega t) \quad (2.32)$$

and the momentum conservation as:

$$\frac{\partial}{\partial t} \int_V \rho \bar{U}_{ave} dV + \pi R \Delta x \left(R \frac{dP}{dx} + 2\tau_w \right) = 0 \quad (2.33)$$

where V denotes the control volume. They have emphasized that for slowly oscillating flows τ_w could be expressed as:

$$\tau_w = f(\rho \bar{U}_m^2) / 8 \quad \text{where } f = \text{func}[\text{Re}(t)] \quad (2.34)$$

Combining the three equations given above, the following relation can be obtained as:

$$\frac{dP}{dx} = \rho \omega |\bar{U}_{os,1}| \cos \omega t + f \frac{\rho \bar{U}_m^2}{2D} \quad (2.35)$$

Then, the average friction coefficient was defined as;

$$f_m = \left(\frac{dP}{dx} \right)_m / \frac{\rho \bar{U}_m^2}{2D} \quad (2.36)$$

where

$$\left(\frac{dP}{dx} \right)_m = \frac{1}{T} \int_0^T \frac{dP}{dx}(t) dt \quad (2.37)$$

$$T = \frac{2\pi}{\omega} \quad (2.38)$$

Einav and Sokolov (1993) investigated the relationships between the experimental and theoretical results of the average friction coefficient and Re_{os} for different Re_m and St . The transition process was seen during the deceleration phase at $Re_m=1700$ and $Re_{os}=1385$. They have emphasized that an increase in the frequency parameter at a given Re_m stabilized the flow. It was stated that the higher Re_m was, the lower Re_{os} was required for transition while at higher St it was more stable.

In the study of Peacock et al. (1998), an empirical correlation for the onset of turbulence in physiological pulsatile flow was presented in the range of $450 < Re_m < 4200$, $1500 < Re_{peak}^p < 9500$, $1.5 < \sqrt{\omega'} < 55$ and $0.002 < St < 0.5$. They defined a function which was a power law in order to obtain a correlation for the onset of transition in pulsatile flow as:

$$Re_{peak,crit}^p = a' \sqrt{\omega'}^{b'} St^{c'} \quad (2.39)$$

where $a' = 169$, $b' = 0.83$ and $c' = -0.27$.

They also found that the oscillatory component stabilized pulsatile flow at higher values of $\sqrt{\omega'}$ and lower values of St . It was seen that an increase in $\sqrt{\omega'}$ tended to stabilize the flow when $\sqrt{\omega'} > 10$.

Laminar and transitional flow regime on pulsatile flow was also reviewed by Gündoğdu and Çarpınlioğlu (1999) and Çarpınlioğlu and Gündoğdu (2001). In their paper, they presented the basic terminology and relationships for pulsatile pipe flows, and also theoretical and experimental investigations in the literature related on laminar and transitional pipe flows. They discussed and compared the studies in the literature and pointed out the important fields to be fulfilled.

A test system for pulsatile pipe flow was presented by Çarpınlioğlu and Gündoğdu (2001) and Çarpınlioğlu (2003). The basics of test system and conducted experiments were introduced for pulsatile flow characteristics in the transition from

laminar to turbulent regime in the range of $1800 \leq Re_{ta} \leq 60,000$; $5 \leq \sqrt{\omega'} \leq 28$; and $0.0035 \leq A_1 \leq 0.7113$. The flow reversal was observed at $\sqrt{\omega'} = 7$ and $\sqrt{\omega'} = 12.5$. They introduced a relationship between the Re_{ta} and Re_{os} . When Re_{os} increased, Re_{ta} increased linearly as given in the following relationship with a maximum deviation of the experimental data in the order of $\pm 8\%$:

$$Re_{os} = 0.126 Re_{ta} + 738.44 \quad (2.40)$$

They suggested that $Re_{os} = 738$ seemed to be the critical value for flow reversal. They stated that oscillation superimposed to steady pipe flow resulted in a stable pulsatile flow by delaying the transition from laminar to turbulent regime.

In the study of Çarpınlioğlu (2003), an approach which consists of attempts to correlate the governing flow parameters was presented to reveal the transition process on frictional field in the range of $7 \leq \sqrt{\omega'} \leq 28$ and $0.05 \leq A_1 \leq 0.8$, respectively. The proposed correlations and determined approximate critical limits of transition were only valid in the corresponding ranges of $2000 \leq Re_{ta} \leq 60000$ and $620 \leq Re_{os} \leq 18800$. Çarpınlioğlu (2003) estimated $Re_{ta,crit} = 17929$ and $Re_{os,crit} = 23763$ for their pulsatile pipe flow in the given experimental ranges as critical limit for the onset and end of transition, respectively. It was also detected that $Re_{ta,crit} = 2000$ was the determined critical limit for the onset of transition of pulsatile flow in the range of $7 \leq \sqrt{\omega'} \leq 28$. Besides, Ohmi et al. (1982) found critical limit for the end of transition, $Re_{ta,crit} = 8330$ for $\sqrt{\omega'} = 8.93$ and $\sqrt{\omega'} = 16.48$. However, with a similar range of $7 \leq \sqrt{\omega'} \leq 28$ in the study of Çarpınlioğlu (2003), $Re_{ta,crit} = 8330$ was found to be questionable. This phenomenon can be investigated experimentally. However, there is no more available information regarding $Re_{os,crit}$ at the onset of transition and the influence of $\sqrt{\omega'}$ and A_1 on the limiting parameters Re_{ta} and Re_{os} .

The periodic pulsatile laminar pipe flows, non-periodic transient and periodic pulsatile transitional flows generated by means of mass flow control (MFC) unit

were investigated by Ertunç et al. (2003). Generally, laminar to turbulent transition was divided into two stages. The first stage is the disturbed flow with small-amplitude perturbations in the early accelerating phase of the velocity waveform and the second stage is the turbulent bursts occurring in the decelerating phase and over the full oscillation cycle. However, they observed additional types of transition scenarios in periodic pipe flows. They observed laminar to turbulent and turbulent to laminar transitions in both accelerating and decelerating phases of the velocity. They have emphasized that, the turbulent burst disappeared by keeping the mean flow rate and pulsation frequency constant, and increasing the pulsation amplitude. They have expressed that various pulsation amplitudes should be investigated in order to observe transition process at different mean flow rate and pulsation frequency in the future investigations.

In recent years, Ünsal et al. (2005) and Ünsal and Durst (2006) studied fully developed pulsatile laminar, non-periodic transient and transitional pulsatile pipe flows generated by MFC unit. They observed that acceleration delays the laminar to turbulent transition for the same starting Reynolds number. Also, it was observed that transition Reynolds number did not depend on the starting Reynolds number. Turbulent to laminar transition was delayed down to lower Reynolds numbers when the deceleration rate increased. They have essentially found that the turbulent bursts that found in the acceleration phase of sinusoidal pulsation disappeared by keeping the mean flow rate and pulsation frequency constant, and increasing the pulsation amplitude. More detailed researches such as in velocity profile, pressure drop and friction factor field may be carried out in this respect.

2.3. Laminar to Turbulent Transition in Oscillating Pipe Flows

The referred studies of transitional oscillating pipe flows are given in Table 2.2. The summary of the studies conducted on transitional oscillating pipe flow is given in detail in Appendix 2.

Sergeev (1966) studied on transition in oscillating cold and heated water flow in the range of $4 \leq \sqrt{\omega'} \leq 40$, $4000 \leq Re^* \leq 30,000$, $0.3 \text{ cm} \leq a^* \leq 30 \text{ cm}$,

$4\text{rad/s} \leq \omega \leq 25\text{rad/s}$ and $2.8 \leq S \leq 28$. Sergeev (1966) observed that $\sqrt{\omega'}$ had a significant effect on the nature of the fluid flow and laminar to turbulent transition defining the Reynolds number, amplitude number and Reynolds number based on the Stokes layer thickness for oscillating flow respectively as;

$$\text{Re}^* = \frac{a^* D \omega}{\nu} \quad (2.41)$$

$$A^* = \frac{4a^* \sqrt{\omega'}}{D} \quad (2.42)$$

$$\text{Re}_{\delta_s} = \frac{\delta_s |\bar{U}_{m,os,1}|}{\nu} \quad (2.43)$$

where

$$\delta_s = \sqrt{2\nu / \omega} \quad (2.44)$$

By means of observations, critical values for the onset of transition corresponding to the first occurrence of turbulent bursts were found to be approximately:

$$\text{Re}^*_{crit} = 700\sqrt{\omega'}, A^*_{crit} = 700 \text{ and } \text{Re}_{\delta_s,crit} = 495.$$

Table 2.2. Oscillating pipe flow studies with critical values of proposed parameters; utilized validity ranges of $\sqrt{\omega'}$ and comments

Author	Critical number	Validity range	Comment
Sergeev (1966)	$\text{Re}^*_{crit} = 700\sqrt{\omega'}$ $\text{Re}_{\delta_s,crit} = 500$ for $\sqrt{\omega'} > 5$	$4 \leq \sqrt{\omega'} \leq 40$	Onset of transition
Hino and Takasu (1974)	$\text{Re}_{\delta_s,crit} = 550$	$1.91 \leq \sqrt{\omega'} \leq 8.75$	Onset of transition
Merkli and Thomann (1975)	$\text{Re}_{\delta_s,crit} = 280$ $\text{Re}_{os,crit} = 400\sqrt{\omega'}$	$42 \leq \sqrt{\omega'} \leq 71$	Onset of transition

Table 2.2. (Cont.)

Hino et al. (1976)	$Re_{\delta_s, crit} = 550$ $Re_{os, crit} = 780\sqrt{\omega'}$	$1.91 \leq \sqrt{\omega'} \leq 8.75$	Onset of transition
Ohmi et al. (1982)	$Re_{os, crit} = 800\sqrt{\omega'}$	$2.6 \leq \sqrt{\omega'} \leq 41$	Onset of transition
Ohmi and Iguchi (1982)	$Re_{os, crit} = 2450$ $Re_{os, crit} = 882\sqrt{\omega'}$	for $\sqrt{\omega'} \leq 1$ for $\sqrt{\omega'} \geq 7$	Onset of transition
Ohmi and Iguchi (1982)	$Re_{os, crit} = 1800$ $Re_{os, crit} = (211\sqrt{\omega'})^{8/7}$	for $\sqrt{\omega'} < 5.02$ for $\sqrt{\omega'} > 7$	End of transition
Fishler and Brodkey (1991)	$650 \leq Re_{\delta_s, crit}^F \leq 1000$	$6.6 \leq \sqrt{\omega'} \leq 16.6$	No turbulent events were observed
Akhavan et al. (1991)	$Re_{\delta_s, crit} = 500 \sim 550$	$7 \leq \sqrt{\omega'} \leq 14$	Onset of Transition
Eckmann and Grotberg (1991)	$Re_{\delta_s, crit}^E = 500$	$9 \leq \sqrt{\omega'} \leq 33$	Onset of transition
Eckmann and Grotberg (1991)	$500 \leq Re_{\delta_s, crit}^E \leq 1310$	$9 \leq \sqrt{\omega'} \leq 33$	Conditionally turbulent in which the core flow is laminar whereas Stokes layer is unstable during decelerating phase
Das and Arakeri (1998)	$Re_{\delta_s, crit} = 300$	$\sqrt{\omega'} = 10$	Onset of Transition

Merkli and Thomann (1975) investigated transition in a Stokes layer for air flow through a pipe in the range of the amplitude of the piston, $2.85\text{mm} \leq l \leq 13.8\text{mm}$, $30 \leq S \leq 50$ and $0 \leq f \leq 130\text{ Hz}$. Turbulent bursts which are always followed by relaminarization were observed during the deceleration phase of the cycle. They have defined the amplitude as;

$$A_M = \frac{2|u_{os}|_{r=0}}{\sqrt{v\omega}} \quad (2.45)$$

Transition in a Stokes layer was investigated and the critical number $A_{M, crit} = 400$ was found. The transitions were observed to take place for $f = 86\text{--}88\text{ Hz}$ by means of flow visualization and $f = 82\text{--}84\text{ Hz}$ measured with the hot-wire probe. They

found the critical $Re_{\delta_s} = 280$ using the disappearance of the vortices as the criterion of transition to turbulence. They defined the critical Reynolds number, $Re_{os,crit} = 400\sqrt{\omega'}$.

Another experiment on transition in a purely oscillating pipe flow was carried out by Hino et al. (1976) in ranges of $1.35 \leq S \leq 6.19$, $19 \leq Re_{\delta_s} \leq 1530$, and $1/6 \text{ Hz} \leq f \leq 1 \text{ Hz}$. They have defined three types of turbulent flow regimes as;

- Regime (I) : weakly turbulent flow
- Regime (II) : conditionally turbulent flow in only decelerating phase
- Regime (III) : fully turbulent flow.

They have also classified the flows into four types with respect to Reynolds number as follows;

- Region (I) : laminar flow
- Region (II) : small amplitude perturbations appear in the early stage of accelerating phase at the central portion of a pipe
- Region (III) : small amplitude perturbations exist in the phase of higher velocity
- Region (IV) : turbulent bursts occur in the decelerating phase.

In weakly turbulent flow regime, $Re_{\delta_s} = 128$ at $S = 2.76$, the velocity distribution profiles began to deviate slightly from the laminar theoretical profile at the central position of the pipe. The same type of transition was observed at Re_{δ_s} of 180 when $S = 3.9$. In conditionally turbulent flow, when the value of Re_{δ_s} was increased further to $Re_{\delta_s} = 568$, a different type of turbulence was observed. They have identified the critical Re_{δ_s} as a value of 550 for $S > 1.6$. The critical Reynolds number $Re_{os,crit}$ specifying the limit between Region (II).(III) and Region (IV) was given as $Re_{os,crit} = 780\sqrt{\omega'}$ in the range of $2.3 \leq \sqrt{\omega'} \leq 8.8$.

Ohmi et al. (1982) studied experimentally on transition to turbulence in an oscillating pipe flow over ranges of $600 \leq Re_{os} \leq 65,000$, $0.0527 \text{ Hz} \leq f \leq 6.24 \text{ Hz}$ and

$2.6 \leq \sqrt{\omega'} \leq 41$. In addition to the classification of Hino et al., 1976, a fifth region was observed as;

Region (V) : turbulent bursts occur in the accelerating phase as well as in the decelerating phase.

The critical value was found as $Re_{os,crit} = 800\sqrt{\omega'}$ when the occurrence of turbulent bursts was firstly seen. The limit between Region (I) and Region (II).(III) agreed well with derived from experiments of Merkli and Thomann (1975) ($Re_{os,crit} = 400\sqrt{\omega'}$).

An evaluation method of the proposed critical Reynolds number was performed by Ohmi and Iguchi (1982) by assuming that the generation region of turbulence was the same as that in a steady flow. By means of velocity waveforms, turbulence was observed in most phases in a cycle except the early stage of accelerating and the latest stage of decelerating phases. Their assumption for oscillating pipe flow resulted in $Re_{os,crit} = 2450$ for $\sqrt{\omega'} \leq 1$ and $Re_{os,crit} = 882\sqrt{\omega'}$ for $\sqrt{\omega'} \geq 7$ when the generation region of turbulence was built up as a criteria of the occurrence of first turbulent bursts. They have also numerically found the critical value of Re_{os} at which generation region of turbulence disappeared such as; $Re_{os,crit} = 1800$ for $\sqrt{\omega'} < 5.026$; and $Re_{os,crit} = (211\sqrt{\omega'})^{8/7}$ for $\sqrt{\omega'} > 7$ by using the Blasius' friction law. The comparison of theoretical and experimental results gave good agreement.

Transitional and turbulent oscillating pipe flow was studied in the range of Re number based on maximum oscillatory velocity; ($Re_{peak}^F = U_{max} D / \nu$) of $7200 \leq Re_{peak}^F \leq 22,000$ and $6.65 \leq \sqrt{\omega'} \leq 16.4$ by Fishler and Brodkey (1991). They stated that the transition to turbulence for oscillating flow occurred during the deceleration phase and relaminarization occurred at acceleration phase. For $Re_{peak}^F = 22000$ and $\sqrt{\omega'} = 11.6$, they observed some structural events in flow field. The first event was the local deceleration near the wall. Just following the local deceleration, the local acceleration took place near the core region. The other

observed event was excitation-transverse vortex (random chaotic radial motion) which occurred either simultaneously with or directly after the local acceleration event. The transverse vortex appeared at the end of a local acceleration. The other event was the ejection which was characterized by a large amount of radial motion, observed always directed downstream away from the wall, as opposed to local accelerations which were directed towards the wall. The ejection was defined as a low speed element of fluid. They have also investigated the effects of $\sqrt{\omega'}$ and Re_{peak}^F on aforementioned flow structures. They stated that the level of turbulence tended to decrease when $\sqrt{\omega'}$ increased and noted that increasing $\sqrt{\omega'}$ should lead to a stable state of the flow. Critical Reynolds number based on Stokes' layer thickness, $Re_{\delta_s, crit}^F$ was found to be in a range from 650 to 1000 using the existence of flow structures as a critical Reynolds number. They stated that the oscillating flow structures were a good indicator of transition to turbulence.

A LDA experimental study for turbulent oscillating pipe flow in the range of $550 \leq Re_{\delta_s} \leq 2,000$ and $5 \leq S \leq 10$ was conducted by Akhavan et al. (1991) - Part 1. Ensemble-averaged values of the wall friction velocity, $u^{*2}(\omega t)$, were calculated from the following equation, using experimental $\partial \bar{P} / \partial x$ measurements and $\bar{u}_{av}(\omega t)$ calculated from LDA measurements of velocity.

$$\frac{\tau_w}{\rho} = u^{*2} = \frac{1}{2} R \left(-\frac{1}{\rho} \frac{\partial \bar{P}}{\partial x} - \frac{\partial \bar{u}_{av}}{\partial t} \right) \quad (2.46)$$

$$\bar{u}_{av}(\omega t) = \frac{2}{R^2} \int_0^R \bar{u}(r, \omega t) r dr = U_m \sin \omega t \quad (2.47)$$

They have observed that during the early part of the acceleration phase, production of turbulent stopped and the flow relaminarized. Turbulence restricted to the wall region of the pipe was observed explosively at the end of the acceleration phase and was sustained throughout the deceleration phase. The transition to turbulence has been observed at Re_{δ_s} of about 500 to 550, independent of the particular flow

geometry. They introduced also two non-dimensional groups as $u^*/R\omega$ and $u^{*2}/\omega\nu$ as critical parameters for determination of the flow structure. They introduced four cases, i.e., in the Case I ($u^*/R\omega \gg 1$ and $u^{*2}/\omega\nu \gg 1$), the universal log-law applied and the flow behaved as quasi-steady, and in Case 2 ($u^*/R\omega \approx 1$ and $u^{*2}/\omega\nu \gg 1$), the velocity profiles obeyed a logarithmic law with the same slope as the universal log-law but with an intercept that varied with ωt . In Case 3 ($u^*/R\omega \ll 1$ and $u^{*2}/\omega\nu \gg 1$), the usual law of the wall was assumed to be valid. In Case 4 ($u^*/R\omega \ll 1$ and $u^{*2}/\omega\nu \approx 1$), the effect of oscillation was confined to the near-wall region.

Another experimental study on oscillating transition to turbulent pipe flow was conducted by Eckmann and Grotberg (1991) in the range of amplitude ($A_E = V_T / \pi R^3$), $2.4 \leq A_E \leq 21.6$, $9 < \sqrt{\omega'} < 33$ and $500 < \text{Re}_{\delta_s}^E < 854$ where $\text{Re}_{\delta_s}^E = A_E \sqrt{2\omega'}$. Transition to turbulence was observed during the deceleration phase of the cycle. Transition from laminar to turbulent flow occurred at $\text{Re}_{\delta_s}^E = 500$. The flow was found to be laminar in the range of $8.9 \leq \sqrt{\omega'} \leq 32.2$ and $\text{Re}_{\delta_s}^E < 500$. For $500 < \text{Re}_{\delta_s}^E < 1310$, the core flow remained laminar, however, the Stokes layer became unstable during the deceleration phase of the cycle.

The study of Das and Arakeri (1998) related on the stability and transition to turbulence in oscillating pipe with reverse flow using water as a working fluid in the range of $250 \leq \text{Re}_{\delta_b} \leq 3000$. The flow was observed to be unstable with the formation of a helical vortex from flow visualization. They stated that Re_{δ_b} was found theoretically 82 for oscillating pipe flow, whereas experimentally it was found to be in the range of 300 to 500. They said that, generally, turbulent bursts are observed during the deceleration phase. At low Reynolds number such as $\text{Re}_{\delta_b} < 500$, instability was not observed and transition to turbulence was observed only for $\text{Re}_{\delta_b} \geq 1200$. In part of the analytical analyses, linear stability theory was

conducted. They have emphasized from the literature that Re_{δ_b} for the disturbed laminar flow and transition to intermittent turbulent flow were independent of Stokes parameter, S , for $S > 2$. The flow in a pipe where $S > 2$ should be investigated in the future studies.

2.4. Conclusions

2.4.1. Conclusions on laminar to turbulent transition in pulsatile pipe flows

Although the first study conducted on transitional pulsatile pipe flows goes back to 1960's, the studies in this field are still inadequate. There are no more details about the flow dynamics and no more correlations as criteria in pulsatile pipe flow for transition regime. Generally, the most common parameter, frequency of oscillation is seen to be used in studies on transitional pulsatile pipe flow as in the form of Womersley number, $\sqrt{\omega'}$. There are some studies on the effect of frequency in any manner on the critical values of Reynolds number and flow stability in this field.

There are both consistent and conflicting results in the early studies on the effect of oscillation frequency on stability and transition. According to some studies, $Re_{m,crit}$, $Re_{ta,crit}$ and stability of pulsatile flow were found to be increased when $\sqrt{\omega'}$ decreased (Sarpkaya, 1966), (Hershey and Im, 1968) contradictory to some other studies (Stettler and Hussain, 1986), (Clamen and Minton, 1977), (Einav and Sokolov, 1993), (Peacock et al., 1998) who have claimed that the increase of $\sqrt{\omega'}$ was seen to stabilize the flow.

The effect of pulsation amplitude on flow stability in addition to the effect of oscillation frequency was also studied by Çarpınlioğlu and Gündoğdu (2001). Superimposed oscillation to steady flow was pointed to stabilize the flow. Similarly, Ertunç et al. (2003) and Ünsal and Durst (2006) found that turbulent bursts in accelerating phase of sinusoidal pulsation disappeared by increasing the pulsation amplitude and keeping the mean flow rate and pulsation frequency constant.

There are also some suggested critical numbers for determining transition in pulsatile pipe flows. However, these critical numbers vastly differ from each other, i.e., $Re_{m,crit}$ was found to be as 6500, 1500, 2540, 1700, 3000 by Sarpkaya (1966), Clamen and Minton (1977), Stettler and Hussain (1986), Einav and Sokolov (1993) and Shemer (1985) respectively. Instead of Re_m , some other criteria were also proposed to detect transition such as relaxation time, τ , by Yellin (1966), critical pulsation period, T_{crit} , by Mizushina et al. (1973, 1975), stability parameter, A_{CM} , by Clamen and Minton (1977). The differences between the critical values of Re_m proposed by researchers are predicted as results of inlet configurations of pipes, existence or absence of flow conditioners, roughness of pipe wall and different experimental ranges. So, it is not rational to investigate only the effect of Re_m on flow regime and stability. The effects of pulsation amplitude and frequency of oscillation are also important parameters for determination of critical Re numbers. Unfortunately, it can be said that there is no common correlation proposed including the all parameters which affect the flow stability and transition to turbulence. All proposed critical values are numeral which differs from each other, not consist of oscillation parameters.

As an unusual contribution is given by Peacock et al. (1998) in the form of a new correlation for detecting the onset of transition in pulsatile pipe flows as $Re_{peak,crit}^p = 169\sqrt{\omega'}^{0.83} St^{-0.27}$ instead of using Re_m , Re_{ta} and Re_{os} . A new approach which was not expressed previously was introduced by Çarpınlioğlu and Gündoğdu (2001) giving a relationship between Re_{ta} and Re_{os} .

According to the previous studies, many researchers defined their own classifications of pulsatile pipe flows, especially observing the velocity waveforms. Yellin (1966) classified the pulsatile pipe flow as laminar, disturbed and turbulent flow, in which disturbance was restricted to the core flow when transition occurred similar to the observation of turbulence generation in the core by Ohmi and Iguchi (1982) and Ohmi et al. (1982). On the other hand, Iguchi and Ohmi (1982) declared that turbulent burst occurred near the wall propagating from the wall to the core region. Nerem et al. (1972) classified the regimes near transition as undisturbed,

disturbed and highly disturbed flow, similar as Clamen and Minton (1977). In the study of Ohmi et al. (1981), the flow pattern for a pulsatile laminar pipe flow were classified into three types as quasi-steady ($\sqrt{\omega'} < 1.32$), intermediate ($1.32 < \sqrt{\omega'} < 28$) and inertia dominant ($\sqrt{\omega'} > 28$) with respect to the dimensionless frequency parameter, $\sqrt{\omega'}$. Ohmi et al. (1982) classified regimes near transition as laminar, disturbed and turbulent flow. Later Iguchi and Ohmi (1984) classified pulsatile flow into four regimes as laminar, transitional, conditionally turbulent and fully turbulent although they previously classified into three regimes of laminar, transitional and turbulent in their first report.

There are both consistent and conflicting results according to previous studies on transitional pipe flows. Recently, there are some studies related on both frequency of oscillation and pulsation amplitude. However, it is necessary for more detailed studies with extended Re numbers, pulsation amplitude and frequency ranges covering all the previously conducted ones. The number of previous studies has been carried out by means of the observation of velocity waveforms, in which the transition phenomena was tried to determine by these observations even though there are few studies related to the measurements of velocity profile and turbulence intensity. On the other hand, pulsatile and oscillating pipe flows were seen to be classified via observation of velocity waveforms.

2.4.2. Conclusions on laminar to turbulent transition in oscillating pipe flows

The effect of frequency on transition to turbulence in oscillating pipe flow was also investigated by some researchers. On contrary to the studies on transition to turbulence in pulsatile pipe flows, there are some proposed correlations of Re_{os} and Re_{δ_s} as functions of $\sqrt{\omega'}$. All these correlations are listed in Table 2.2.

All these correlations are in the same characteristics and consistent with each other in which the critical number tended to increase when $\sqrt{\omega'}$ increased. However, it is necessary to verify these correlations covering larger range of $\sqrt{\omega'}$, especially in

smaller $\sqrt{\omega'}$ ($\sqrt{\omega'} < 1.32$) range where it is so hard to find more detailed study for quasi-steady regime.

In view of the classification of oscillating pipe flow, there are some specified regimes. Hino et al. (1976) defined three types of turbulent regimes near the transition as weakly turbulent, conditionally turbulent and fully turbulent in oscillating pipe flow. They also classified the oscillating flow with respect to Re number as laminar, small amplitude perturbation appeared in the early stage of accelerating phase of the core, small amplitude perturbation in the phase of higher velocity and turbulent bursts occurred in decelerating phase. In addition to the classification of Hino et al. (1976), a fifth region was observed by Ohmi et al. (1982) as turbulent bursts occurred in the accelerating phase as well as the decelerating phase. However, all these classifications have been done according to velocity waveforms as a result of observation of velocity-time records on oscilloscope. So, it is necessary to verify and define these regimes as well as onset and end of transition using velocity profiles through the cross-section of the pipe. There is very little known about the velocity distribution near the transition regime of oscillating pipe flow in terms of proposed any correlation covering all regimes of quasi-steady, intermediate and inertia-dominant.

As in the studies of transitional pulsatile pipe flows, there are also some studies conducted on transitional oscillating pipe flows. Contrary to the studies on pulsatile ones, there are some consistent results on determination of $Re_{os,crit}$ as a function of $\sqrt{\omega'}$. However, the results are inadequate since there is no more study covering the extended $\sqrt{\omega'}$ range, especially for $\sqrt{\omega'} < 1.32$ and $\sqrt{\omega'} > 28$.

As a result of a comprehensive literature survey, these deductions given below are expressed as follows;

1. The studies are generally based on observation of velocity waveforms to detect turbulent structures in transition regime. Furthermore pulsatile and oscillating pipe flows are also classified via the observations of velocity waveforms. However

there are few studies related to the measurements of cross sectional velocity profiles and turbulence intensity profiles in transitional pulsatile pipe flows. There is almost no information regarding the cross sectional velocity and turbulence intensity profiles in the transitional period of oscillating pipe flows.

2. There are consistent and conflicting results on the effect of oscillation frequency on flow stability and transition. $Re_{m,crit}$ and $Re_{ta,crit}$ are increased stabilizing the flow when either $\sqrt{\omega'}$ is decreased (Sarpkaya, 1966), (Hershey and Im, 1968) or is increased (Clamen and Minton, 1977), (Stettler and Hussain, 1986), (Einav and Sokolov, 1993), (Peacock et al., 1998).

3. Generally, transition to turbulence and the fact of relaminarization are detected at the decelerating and accelerating phases of oscillation, respectively.

4. Disturbance growth and turbulence generation are either observed in the core region (Ohmi et al., 1981), (Ohmi et al., 1982) or in the near wall region (Iguchi and Ohmi, 1982). Therefore, there is need for further confirmation in terms of critical cross-sectional position for disturbance or turbulence generation.

5. In comparison with the stability and transition of steady flow, presence of oscillation is found to stabilize the time dependent flow.

6. As can be seen from Table 2.1 and Table 2.2, there is a variety of non-dimensional parameters proposed to define critical state of transition.

7. On contrary to the studies on transitional pulsatile pipe flows, there are proposed correlations of Re_{os} and Re_{δ_s} as functions of $\sqrt{\omega'}$ to determine the transition to turbulence in oscillating pipe flows. All these correlations are in terms of the same characteristics and almost consistent with each other. However, it is necessary to verify these correlations in smaller ($\sqrt{\omega'} < 1.32$) and higher ($\sqrt{\omega'} > 28$) ranges of $\sqrt{\omega'}$.

8. The number of studies conducted on non-periodic flows is found to be inadequate. The available studies are generally carried out by means of observation of velocity waveforms.

9. Therefore, in this study;

i) The cross sectional velocity profiles and flow resistance in terms of friction factor should be measured in transitional period of time dependent pipe flows.

ii) The cross sectional position in which the first turbulence generation will occur should be determined.

iii) The validity of the critical numbers proposed in the literature in the specified $\sqrt{\omega'}$ ranges for determination of transition should be verified or refuted.

iv) The relationships among the non-dimensional parameters should be specified for the determination at the onset of transition in time dependent pipe flows in terms of $Re_{os,crit} = Re_{os,crit}(\sqrt{\omega'}, A_1)$ and $Re_{ta,crit} = Re_{ta,crit}(\sqrt{\omega'}, A_1)$.

v) In reference to i) and ii), a method for the determination of critical state (onset) of transition should be devised and should be compared with the previous observations on velocity waveforms.

CHAPTER 3

EXPERIMENTAL SET-UP AND MEASUREMENT DEVICES

3.1. Introduction

In this chapter, the design and the construction details of the experimental set-up together with the calibration procedures of the measurement devices and technical specification of each component are presented. Operation principles of constant temperature hotwire anemometer (CTA), its calibration at moderate and low speeds and the calibration of the pressure transmitter are also presented in this chapter.

3.2. Layout of the Experimental Set-Up

The experimental set-up is planned to determine the velocity field and the pressure drop characteristics of pulsatile pipe flow in laminar to turbulent transition regime. The design and the construction of the set-up are based on the review of the recent experimental studies available in the literature and the fundamental principles of the fluid mechanics. However, despite the wide usage of conventional pulse generator systems such as Scotch-Yoke pressure driven pistons in the literature, a new digital mass flow rate control (MFC) unit is preferred in order to generate well-controlled time dependent flow through the pipe.

A schematic layout and a photograph of the experimental set-up are given in Fig. 3.1 and Fig. 3.2, respectively. In the experiment, air is used as a working fluid. The experimental set-up consists of the following basic components:

1. Screw air compressor
2. Surge tank
3. Drier
4. Air filters

5. Mass flow rate control (MFC) unit
6. Flow conditioners
7. Polyvinyl chloride (PVC) pipeline, connections & adapters
8. Probe traversing mechanism
9. Constant temperature anemometer (CTA) and hotwire probe
10. Pressure transmitters
11. Oscilloscope
12. Data acquisition and processing equipment (DAQ board + PC)

3.2.1. Screw air compressor

LKV 30/8 type of Lupamat screw air compressor is used in order to supply air flow through the pipeline system. The compressor operates at 8 bar with a volumetric flow rate of 4.85 m³/min (80.83 L/s). It has a 30 kW motor. This compressor is adequate to supply air to MFC unit which has a maximum flow rate of 3 L/s. The screw air compressor has many components in itself such as air suction filter, suction control valve, suction control valve piston, screw block, air/oil separation tank, air cooling, oil cooling, oil filter, compressor motor, fan motor, minimum pressure valve, pressure transmitter at the exit of screw, system pressure transmitter, resistance thermometer, air filter optic blockage indicator, 3/2 solenoid valve etc. The compressor is driven by a 3-phase, closed (IP 54), F-isolated, termic, AC motor. The fan motor is assembled into the compressor unit to supply cooling air for air cooled typed compressor. The technical specification of the drive unit of the compressor is given in Appendix 3.

3.2.2. Surge tank

The surge tank is used for air storage at a certain pre-specified pressure to supply air uniformly through the pipeline during the experiment. The air is supplied by the screw compressor to the surge tank until the pressure inside the tank becomes 7 bar. Then, the compressor automatically switches to standby mode. The pressurized air at 7 bar is then supplied to the pipeline. Because of the MFC unit operating pressure range limitation of 3-6 bar, the air inlet pressure to it is reduced to 4.5 bar by means of a pressure relief valve situated just before the MFC unit. During the experiment the intermittent operation of the compressor is realized automatically

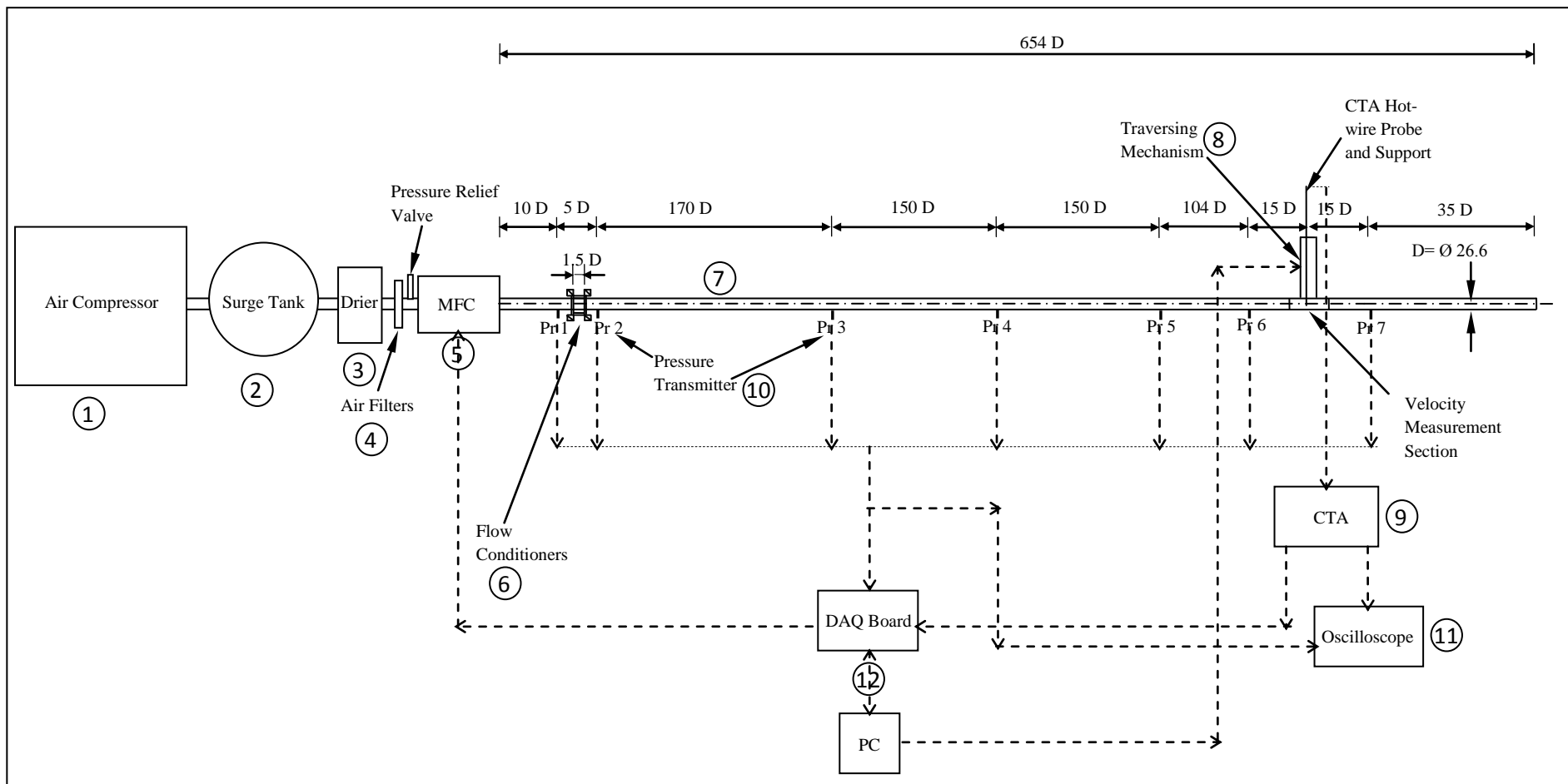


Figure 3.1. A schematic layout of the experimental set-up

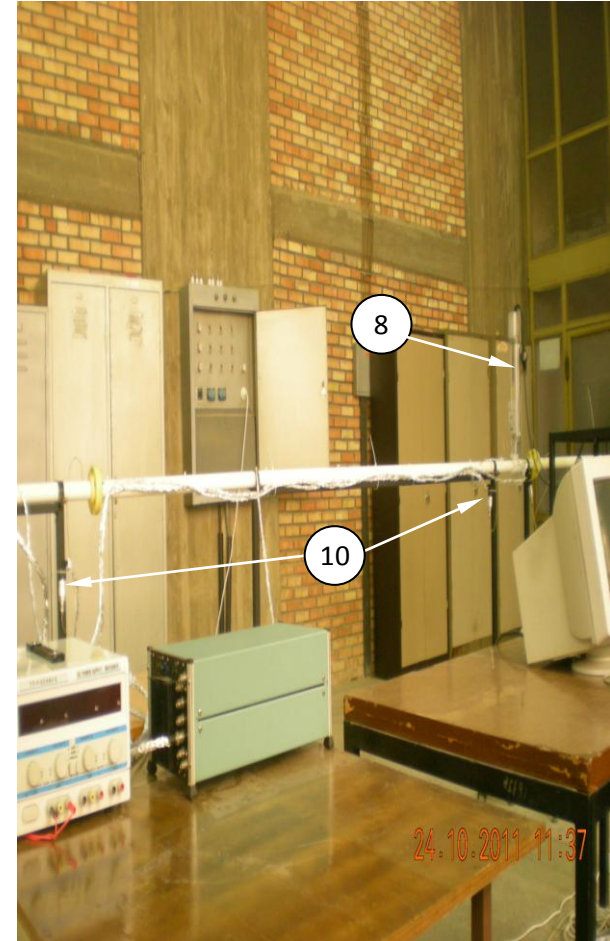
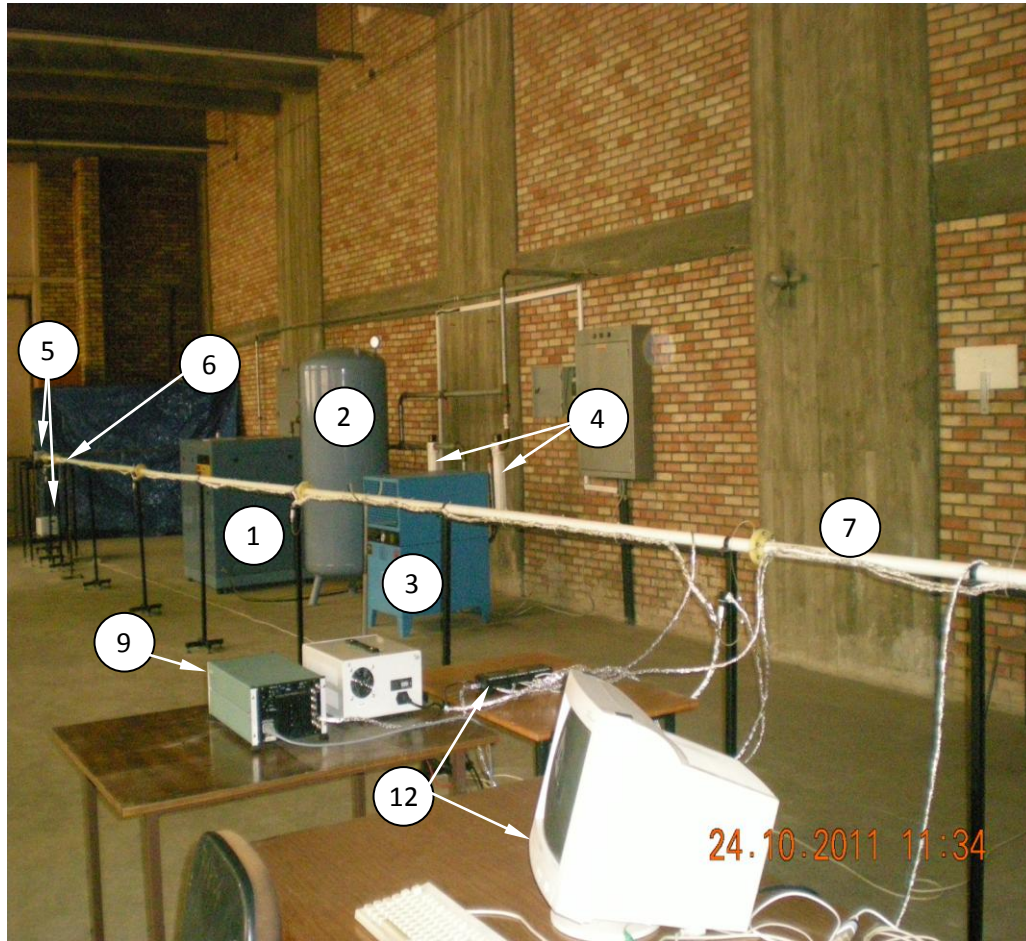


Figure 3.2. Photographs of the experimental set-up

to secure the compressed air pressure inside the surge tank always between 5-7 bar. The surge tank is also used for the purpose of preventing and removing non-uniformities and unsteadiness of air flow in the pipe caused by fluctuations of electricity supply or any other unaccounted reasons. The tank was constructed by the manufacturer according to TS 1203. It has a height of 1.8 m and diameter of 0.85 m.

3.2.3. Drier

In order to prevent the measurement devices from the damage caused by the dust, humidity and waste oil in the unconditioned air, a drier is used in the experiment. In the present set-up, Pnöso Type-S PSK-6000F air drier whose technical specifications are given in Appendix 4 is used. In the drier, air firstly enters into an air-to-air heat exchanger. By means of the cooler air, pre-cooling of the pressurized air is provided. After the air-to-air heat exchanger, the compressed air enters into refrigerator, resulting a temperature drop of the air to +3°C. Then, the condensed vapor of the air is drained off. The dry air then enters to another air-to-air heat exchanger again and the warmed up air leaves the drier. The air drier used in the set-up has a maximum volumetric flow rate capacity of 6 m³/min.

3.2.4. Air filters

The unconditioned pressurized air may contain some particles worn out from the compressor, the carbonized oil wastes due to the effect of temperature, any rust and dust. These are undesirable particles for any pneumatic applications and especially for laboratory studies.

For that reason, PS 1 and PS 2 air filters are used. PS 1 is the front filter which does not permit particles of having sizes greater than 1 micron to pass. Also in this filter, the amount of oil in the air is reduced to the amounts less than 0.5 mg/m³. The second filter PS 2 used in the set-up is more sensitive which does not permit the particles of sizes greater than 1 micron to pass. After PS 2 filter, the amount of oil in the air becomes less than 0.01 mg/m³. The pressure loss at each filter is about 80 mbar. The filters must be renewed when the pressure loss is seen to reach 0.7 bar.

3.2.5. Mass flow rate control (MFC) unit

The mass flow control (MFC) unit has been designed and constructed by Durst F. and his co-workers in LSTM Erlangen. The complexity and difficulties involved in conventional pressure driven instruments when especially used in time dependent flows have led to the design of mass flow control (MFC) units. Many experimental investigations in the literature have been carried out under steady-state flow conditions (more than 90% of the experimental investigations). The major reason of this is that there was a lack of experimental studies to impose well-controlled time dependent flows.

The MFC unit is used to generate and control both steady and time dependent flows. In the present study, the MFC unit is used to generate the pulsatile pipe flow at desired velocity amplitudes and oscillation frequencies in the range of experiments. The MFC unit used is capable of providing 0 to 180 L/min (3 L/s) flow rate with supply of compressed air pressures between 3 and 6 bar. The MFC unit works with 230 Volts and 50 Hz connection. The flow can be controlled in steps of 0.5 L/min from 0 to 70 L/min and in steps of 1 L/min from 70 to 180 L/min. The MFC can be controlled manually, over an analog port (0 to 10 V) or digitally through the parallel port. It is designed to operate up to frequencies of 125 Hz (Durst et al. 2003). The air supply to the MFC unit should be dry, oil and dust free and satisfying DIN 13260 requirements. Air drier and filters are used in the experiment to prevent the damaging of MFC unit.

The system is sensitive to any zero offset in the coil rod displacement. Therefore, the displacement sensor needs to be zeroed regularly. This zeroing is done automatically with a resolution of about 0.1 μm at each opportunity where the mass flow is zero. The valve can also be recalibrated on demand by an external input or simply by pushing a recalibration button. For safety reasons, there is a button and an input line for a logic “vent off” signal to prevent any damage to delicate laboratory equipment.

Due to the high speed of the electro-dynamic coil system of the MFC unit, the valve can provide mass flow variations very rapidly (Durst et al. 2003). The response

time of the displacement controller is about 2 ms. Also, the temperature effect, compared with the high-pressure influences, on the mass flow rate is less significant: it has only square root influence. The temperature variation in any laboratory is usually small. Therefore, there is no temperature sensor in the MFC. It is recommended to run experiment at around usual room temperature of about 20 °C.

Calibration curves of the MFC unit have been provided by Durst et al. (2003). It has been shown that the MFC unit not only works well but can also be operated in a very simple way with an accuracy of $\pm 1\%$ of supplied volumetric flow rate for sinusoidal variations of the input voltage. The details of the uncertainty analysis of the MFC unit can be found in the paper by Durst et al. (2003).

Also, the repeatability of MFC flow conditions has been checked and by repeating experiments it has been shown that the Re number range at which the laminar to turbulent transition occurred has been highly repeatable within $\pm 2\%$ of the nominal Re number setting (Durst and Ünsal 2006).

To control operation of the MFC unit, there are 3 possibilities;

- 1) a digital sensor signal
- 2) an analogue input (0-10 V)
- 3) manually by simply turning on the potentiometer of the MFC control unit.

In the present set-up, pulsatile air flow is generated and controlled by the MFC unit. By means of triggering the MFC unit via analogue volt inputs between 0 and 10 V sinusoidal pulses with any value of amplitude and oscillation frequency is generated.

3.2.6. Flow conditioners

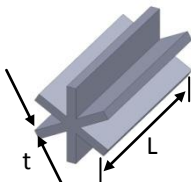
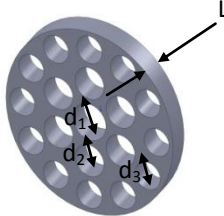
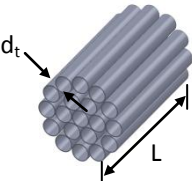
The flow characteristic is affected by swirl symmetry and distortions because of the valves, bends and other pipe fittings. The non-uniformity of flow also breaks down the measurements of flow characteristics. All these phenomena affect the

accuracy of measured data greatly. A flow conditioner capable of removing swirl and asymmetry in approaching flow conditions is thus necessary to provide an acceptable flow profile. A flow conditioner is used extensively in experimental studies because it is cheap to manufacture, simple and convenient to install and it has a remarkable success in improving the structure of flow profile. Tube bundles in the shape of honeycomb can effectively reduce the transverse components of mean velocity along with any upstream turbulence. Lumley (1964) found that for equal pressure drops, a honeycomb is more efficient than a screen in reducing turbulence intensity. Bradshaw and Pankhurst (1964) and Loehrke and Nagib (1976) have reviewed various previous studies and recommended a value of 6-8 for the cell length-to-diameter ratio of honeycombs. Farell and Youssef (1996) concluded that in order to use a relatively short honeycomb to reduce large scale swirling motions and turbulence levels, it is best to install an upstream coarse screen so that the flow reaching the honeycomb is as uniform as possible. Some experimental studies were conducted based on the measurements of turbulence characteristics behind the flow conditioner in (Loehrke and Nagib, 1976), (Groth and Johansson, 1988), (Xia et al., 1990), (Farell and Youssef, 1996).

In the present study, flow conditioners of a tube bundle, an etoile and a perforated plate have been designed to be used at high Re and tested separately in the Reynolds number range of $Re \leq 9000$ at steady state conditions. The utilized and designed flow conditioners with their schematic representations and technical specifications are given in Table 3.1. The details of the study are given in Çarpınlioğlu and Özahi (2011). The utilization of etoile has provided experimental confirmation to the recent numerical study of Frattolillo and Massarotti (2002) who suggested that etoile has been more efficient in terms of its minimum settling length. The cross-sectional axial velocity profiles at three downstream X/D locations behind flow conditioners are measured with pressure losses, ΔP . The methodology proposed for the analysis of the experimental data is presented in terms of settling length, flow uniformity, pressure loss characteristics of flow conditioners and entrance length concept for the control of laminar pipe flow in the other chapter of the thesis. In the experiment, a couple of the flow conditioners consisted of a tube bundle and a

perforated plate is used in order to provide symmetricity of the flow through the pipe cross-section and to remove the swirl and turbulence intensity.

Table 3.1. Utilized flow conditioners

Flow Conditioner	Schematic Presentation	Open Area Ratio, β	Geometrical Characteristics
Etoile (Frattolillo and Massarotti, 2002)		0.57	# of radial vanes=6 $L/D=2$ $t=3 \text{ mm}$ (0.113 D)
Laws' Perforated Plate (Laws and Chesnoy, 1993; Laws, 1990)		0.49	# of holes=19 (1:6:12) $L/D=0.123$ $d_1=5.32 \text{ mm}$ (0.200 D) $d_2=4.65 \text{ mm}$ (0.175 D) $d_3=4 \text{ mm}$ (0.150 D)
Tube Bundle (Bradshaw and Pankhurst, 1964; Loehrke and Nagib, 1976)		0.74	# of tubes=19 $L/D=1.5$ $d_t=5 \text{ mm}$ (0.188 D)

3.2.7. PVC pipeline, connections and adapters

Deciding of a pipe diameter before the experimental study is very important. Some systematic steps have to be taken to decide the pipe diameter. The MFC unit used in the set-up has the maximum flow rate of $0.003 \text{ m}^3/\text{s}$. Hence there is a limitation for pipe diameter in the experiment imposed by the MFC unit. In order to investigate the laminar to turbulent transition, especially the onset of transition in pulsatile pipe flows, the most feasible and logical pipe diameter should have been selected. The other important limitation is the spatial intrusion of hotwire probe. Because of these reasons, the pipe diameter should be big enough to neglect blockage effect of the probe, and should be small enough to provide adequate

velocity for higher Re numbers. Hence, a pipe diameter of 25 mm is decided. But, instead of an exact pipe diameter of 25 mm, a readily available standard pipe of 26.6 mm inner diameter is selected. With this pipe, the maximum mean velocity is estimated to be around 5.3 m/s at the maximum flow rate of 0.003 m³/s. Hence the corresponding maximum steady flow Re number is calculated to be 9573.

In the present set up, the pipeline is composed of the smooth, rigid, polyvinyl chloride (PVC) pipe sections which have a length of 4 m and an outer diameter of 40 mm. The pipeline has a total length of 17.4 m ($X/D=654$). The custom-designed connection adapters with key slots are used to connect the pipes. By using these connections, the smooth and continuous flow through the pipeline is obtained by preventing the surface blanks between the pipe joints (Fig. 3.3). The MFC unit is connected to the pipe line with a conical adapter (Fig. 3.4). In order to provide a smooth passage of flow from the MFC unit to the pipeline, a conical shaped adapter has been designed and manufactured as described by Clancy (1975), Rae and Pope (1984) and Anderson (1991).

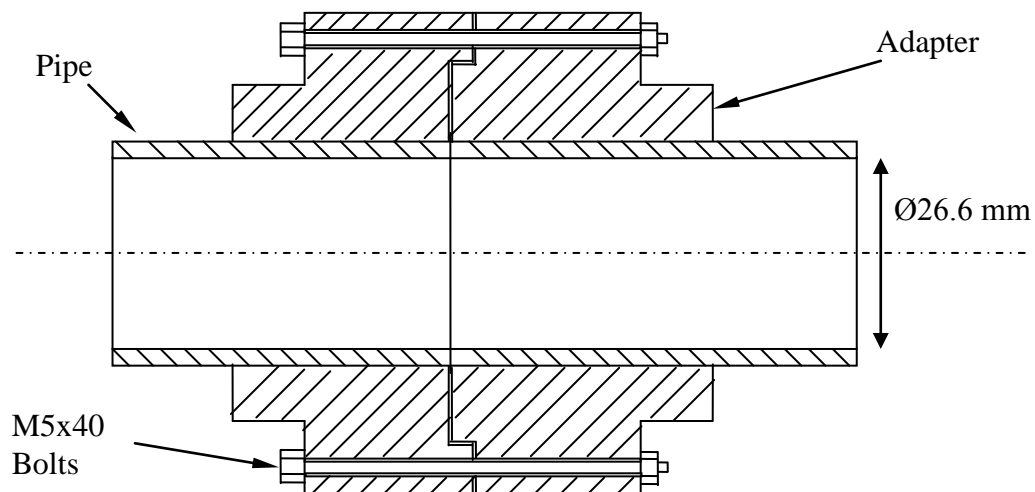


Figure 3.3. A section view of connection adapters

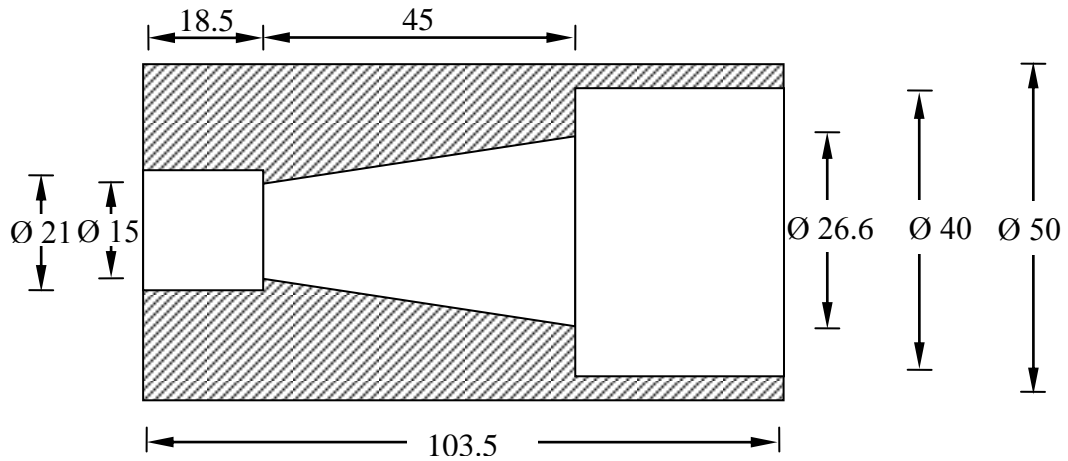


Figure 3.4. A section view of a conical shaped adapter

3.2.8. Probe traversing mechanism

RCP2-SA6-I-PM-6-200-P1-SBE Robocylinder and RCP2-CGA-SA6-I-PM-0-P Robocylinder Positioning Unit are used as a traversing mechanism to traverse the hotwire probe for the measurement of the axial flow velocity over the pipe cross-section. By means of this traversing mechanism, the location of the hotwire probe is automatically adjusted for any radial position in the pipe cross-section using PC interface software supplied by the manufacturer, whose photograph is shown in Figure 3.5.

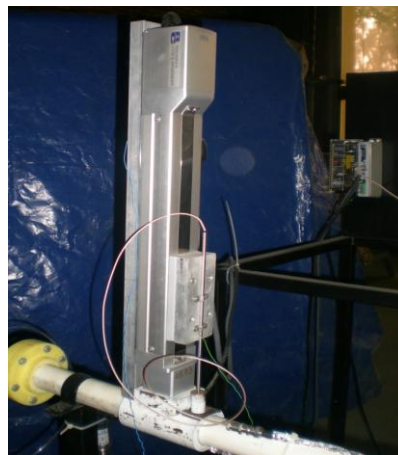


Figure 3.5. A photograph of the probe traversing mechanism

The robocylinder has a maximum stroke of 200 mm, which is suitable for the present set-up in order to traverse the hotwire probe over the 26.6 mm-diameter pipe. It has a high repeatability of 0.02 mm. It has an incremental encoder. Its power supply is a 24 V DC. The traverse mechanism is controlled by the PC using the software program supplied by the manufacturer. By means of the high accuracy and positioning repeatability of 0.02 mm, very small increment as low as 0.1 mm can be provided for traversing the hotwire probe. The technical specifications of the traversing mechanism are given in Appendix 5.

3.2.9. Constant temperature anemometer (CTA) and hotwire probe

In the present experiment, the velocity $U = U(r, t)$ measurements are performed at the axial station of $X/D=604$ by using a constant temperature hotwire anemometer (CTA) unit comprising of a general purpose miniature type hotwire probe. The measurement started with the hotwire probe, which is connected via a bridge to the CTA main unit. Signals received from sensing probe by the CTA main unit is transferred to daqboard and subsequently to PC as raw data. In PC, the raw data are processed using the devised software program.

The CTA main unit used in the set-up is manufactured by DANTEC, 56C01 CTA main unit. Plug-in 56C17 CTA Bridge, 56N21 linearizer are used in the 56C01 CTA main unit. The 55P11 type hotwire probe is supplied by DANTEC. The technical specification of 55P11 miniature hotwire anemometer probe is given in Appendix 6. The working principle of CTA is also given in the next section. 56N21 linearizer is used for linearizing the output signals from the 56C01 main unit. Offset compensation and amplifier are provided in the input, making it possible to amplify the signal to a normalized level of 0-10 V. The technical specifications of 56C17 CTA Bridge and 56N21 linearizer are given in Appendix 7.

3.2.9.1. Working principle of CTA

Hotwire anemometer is the standard and until recently one of the satisfactory method of measuring instantaneous fluid velocity. CTA is a point-measuring technique appropriate for the measurement of time series in 1, 2 or 3-dimensional

flows. CTA is particularly suitable for flow measurements with very fast fluctuations at a point (high turbulence) and the study of flow micro structures, where there is a need to resolve small flow eddies down to the order of tenths of a mm. By using CTA, velocities can be measured from a few cm/s to supersonic.

The working principle is based on the cooling effect of a flow on a heated body. The CTA measures velocity at a point and provides continuous velocity time series, which can be processed into amplitude and time domain statistics. This technique depends on the convective heat loss from an electrically heating sensing element or probe to the surrounding fluid. The heat loss depends on the temperature and geometry of the sensor and on the velocity, temperature, pressure, density and thermal properties of fluid. The working principle of the hotwire anemometer is based on the convective heat loss from the electrically heated sensor caused by flow about the sensor. This cooling causes a change in the probe resistance, which results in an increase in amplifier output current. In this manner, due to the temperature coefficient of resistance of the sensor, the operating resistance and thus the temperature of the probe is maintained. Therefore, it may be assumed that the instantaneous value of electric power applied to the sensor is equal to the instantaneous thermal loss of the sensor to its surroundings.

Assuming that only one of the fluid parameters varies, the heat loss can be interpreted as a direct measure of the quantity, usually the velocity or temperature. The wire, R_w , is connected to one arm of a Wheatstone bridge and heated by an electrical current. A servo amplifier keeps the bridge in balance by controlling the current to the sensor so that the resistance and hence temperature is kept constant, independent of the cooling imposed by the fluid. The bridge voltage, E , represents the heat transfer and is thus a direct measure of the velocity. The combination of the sensor's low thermal inertia and the high gain of the servo loop amplifier give a very fast response to fluctuations in the flow.

3.2.9.2. Calibration of the hotwire probe

Many techniques for the calibration of hotwire probes are described in the literature. Calibration of the CTA for velocity measurements in incompressible,

isothermal flows is based on the early work of L.V. King on the heat transfer of infinite, circular cylinders in a uniform flow normal to the cylinder axis. It is known as King's Law, which affords a reasonable approximation to the overall shape of a hotwire calibration curve:

$$Q_h = RI^2 = A + BU^{0.5} \quad (3.1)$$

where Q_h is the rate of heat loss by convection from the sensor, RI^2 is the electric power dissipated in the sensor, A and B are calibration constants to be determined.

The calibration curve of a hotwire anemometer is the so-called generalized King's Law:

$$E^2 = A' + B'U_{eff}^{n'} \quad (3.2)$$

where E is the output voltage of the anemometer, A' , B' and n' are empirical constants and U_{eff} is the so-called effective cooling velocity. For most hotwire probes, n' is approximately 0.45 for a velocity range in air between 0.3 m/s and 80 m/s. Effective cooling velocity can in most cases be taken as the velocity component normal to the wire. However for more accurate measurements, the directional sensitivity of the wire should be taken into account. Details of the calibration techniques and their comparisons can be found in (Bruun et al., 1988).

In the present study, two calibration methods for a CTA probe for low speeds covering a range of $0.029 \text{ m/s} \leq U \leq 1.79 \text{ m/s}$ and in-situ calibration method for high speeds $U > 1 \text{ m/s}$ are performed. For low air speeds, in situ laminar pipe-flow method and a new proposed method of rotating disc are used. These techniques are discussed in next sections.

The theoretical approach based on the fluid flow over a heated cylindrical body is used (Hinze, 1975), (Bruun, 1995) in terms of the utilization of the well-known equation;

$$\frac{I^2 R_w}{R_w - R_g} = \frac{E^2}{R_w(R_w - R_g)} = A + BU^n \quad (3.3)$$

where I is current through the hot wire, R_w is resistance of the hot wire and R_g is resistance of the wire at gas temperature, E^2 is square of the output of the hot-wire anemometer bridge, A and B are constants, U is calibration velocity and n is an exponent, usually found to be between 0.45 and 0.5. The most commonly used relationship is the modified King's Law;

$$E^2 = A + BU^n \quad (3.4)$$

For high air speeds, the in-situ calibration of hotwire probe is performed using an inclined alcohol manometer, a pitot-tube and a static tapping at the velocity measurement section. The calibrator which is a pitot-static tube has an uncertainty of maximum $\pm 1.5\%$ for high air speeds. In the velocity measurements, the curve fitting in the form of modified King's Law with corresponding values of the parameters; $A=2.176$, $B=0.966$ and $n=0.55$ is found to be compatible with the velocity data with deviation of $\pm 0.5\%$. The calibration curve for the high air speeds is given in Fig. 3.6.

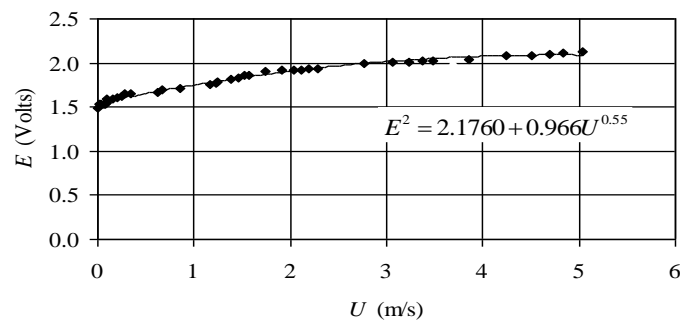


Figure 3.6. High speed calibration curve using conventional method

3.2.9.3. Calibration of the hotwire anemometer probe at low air speeds

Until recently, an accurate calibration of hotwire anemometer at low velocity (0-1 m/s) has been a major problem. The accuracy of calibration of hotwire probes at velocities below 1 m/s is often in doubt. Generally, hotwire probes have been

calibrated using a calibration nozzle or a wind tunnel. The velocity is evaluated by using pitot-static tube in the wind tunnel, based on the technique of the pressure difference. However, when the flow velocity becomes smaller, the pressure drop in airflow becomes so small that it is difficult to obtain an accurate velocity measurement using these conventional methods. For this reason, several methods for calibration of hot-wire anemometers for low velocities have been investigated and proposed. Moreover, it is expressed that conventional calibration methods are not sufficiently accurate below about 0.6 m/s (Pratt and Bowsher, 1978), (Aydın and Leutheusser, 1980).

Accurate calibration of hotwire probes at low velocities (about lower than 1 m/s) is difficult, as standard pitot-tubes cannot be used. Recently, the calibration of hotwire probe for low velocities is carried out by moving the hotwire relative to the stationary fluid or by placing the hotwire at the centre of a long pipe in which fully developed flow is established.

Collis and Williams (1959) are the first to report a detailed effort in the area of low-velocity hotwire calibration. They only investigated the flow normal to a horizontal wire and mainly interested in showing the effect of buoyancy in flows with small Reynolds numbers. Chua et al. (2000) have designed and constructed a hotwire calibrator which can travel at a constant and low speed ranging from 0 to 350 mm/s with an accuracy of ± 1 mm/s. The measurement principle is based on the hotwire probe mounted on a travelling belt whose speed is pre-known. Al-Garni (2007) used the calibration technique based on moving hotwire probes in stagnant air. In the study, the motor speed could be adjusted to any desired velocity in its range. The results showed that the relationship between E^2 and U^n is linear in the range of $U \approx 3-15$ cm/s when fitted to the modified King's law. Aydın and Leutheusser (1980) used a special calibration technique. The probe was moved at a prescribed velocity through a quiescent fluid medium. The results showed that the calibration equipment must not be used at velocities of less than 0.5 m/s. A method for the calibration of hotwire probes by means of a free jet facility, including the calibration at low velocities was expressed by Seifert and Graichen (1982). The calibration was based on the measurements of the flow rate and corresponding

profiles of the anemometer output voltage in the exit cross-section of the nozzle. Another study based on the calibration of hotwire anemometer at very low velocities in air was expressed by Tewari and Jaluria (1990). The desired flow was simulated by moving the probe at a precisely known velocity in a stationary medium. A hotwire was successfully calibrated using apparatus for the flow velocities as low as 0.1 cm/s, with an estimated error of $\pm 1\%$ in the measured velocity range. A rig for the hotwire anemometer probe calibration at velocities below 1 m/s was described in the study of Heikal et al. (1988). The hotwire probe was fixed to the carriage that moved with a known speed by means of a stepping motor. The maximum error of $\pm 0.8\%$ occurred at a velocity of 1 m/s. Details about the hotwire calibration can be found in the review article of Lekakis (1996). Kohan and Schwarz (1973) used shedding-frequency method and calibrated a hotwire at low speeds using the Roshko's (1954) Strouhal-Reynolds number (SR) relationship for flow Reynolds number ranged between 50 and 150. The velocity was obtained by measuring the vortex-shedding frequency and then using the SR relationship. Christman and Podzimek (1981) calibrated a hotwire using the nozzle of a DISA 55D41/42 calibrator. Tsanis (1987) used laminar plane Couette flow and towing tanks as calibration devices to calibrate a hot-wire anemometer at very low velocities capable of operating down to 0.1-0.5 m/s. Bruun et al. (1989) carried out a swing-arm apparatus to calibrate hotwire at low speeds. Guellouz and Tavoularis (1995) used a probe mounted on a pendulum arm for calibration of low speeds. Yue and Malmström (1998) used laminar-pipe flow method for hotwire anemometer in the low speed range of 0.1 m/s and above. Johnstone et al. (2005) used the same method to calibrate a hotwire in the velocity range of 0.125-13.78 m/s. Durst et al. (2008) calibrated hotwire anemometer by using special calibration test rig including a mass flow control unit and a pressurized container in the range of the mass flow rates per unit area, ρU , of 0.1-25 kg/m²s.

Lee and Budwig (1991) used laminar pipe-flow method in the exit plane of fully-developed laminar pipe flow for hotwire anemometer calibration. In the laminar pipe-flow method, a hotwire probe is located at the centre of the pipe in the exit plane of the tube. But, the flow in the pipe must be fully-developed laminar flow. If the flow rate, Q , is known, the mean velocity can be calculated. And the maximum velocity at the centre of the pipe is twice of mean velocity for fully-developed

laminar pipe flow. Now, the maximum velocity at the center of the pipe can be detected via measured voltage from hotwire anemometer. Repeating this procedure for several low-speeds, the calibration curve can be obtained.

In this study, low-speed calibration is performed by using two methods; (i) using laminar pipe-flow method and (ii) a new method based on rotating of a disc with known angular velocity, ω in stagnant air, named as rotating disc calibration method. The overheat ratio value, OHR of 1.8 is chosen as suggested by Bruun (1995) in both methods. This recommended value results the maximum wire temperature $T_{w,max}$ as being equal to about 290 °C which is below the oxidization temperature. Since the probe used is a single normal wire type, the wire element is placed perpendicularly to the mean flow direction. The perpendicularity of the probe to the flow direction in both calibration methods is secured by rotating the probe around its axis until the maximum voltage is seen as described by Bruun (1995). The temperature of the laboratory was always kept constant at 21±1 °C during all the experiments.

In laminar pipe-flow method, the hotwire probe is located at the center of the pipe. The minimum permissible flow rate produced by MFC unit is 0.49 L/min (8.17×10^{-6} m³/s) with a corresponding mean velocity of 0.0147 m/s. Therefore the calibration velocity at the pipe center is 0.029 m/s being twice the mean velocity of 0.0147 m/s. The calibration procedure is carried out to the maximum flow rate of 29.89 L/min (4.98×10^{-4} m³/s) corresponding to the mean velocity of 0.89 m/s, with a calibration velocity of 1.79 m/s at the pipe center. The validity of the method is also checked in terms of the cross-sectional velocity profile measurements for all test cases. The range is covered for 50 different flow rates with an increment of 8.17×10^{-6} m³/s. A typical calibration curve is given in Fig. 3.7. As it can be seen from Fig. 3.7, the calibration curve is in good agreement with the modified King's law in which the constants A and B and exponent n are found as 2.676, 0.749 and 0.75, respectively, resulting in a maximum error margin of velocities ±1 %. In general, exponent n varies in between 0.45 and 0.5 for $U \geq 1$ m/s while this exponent increases as the velocity falls to a few centimeters per second (Bruun et al., 1989), (Guellouz and Tavoularis, 1995), (Al-Garni, 2007). The exponent n is claimed to be changing up to

the value of 1 for low speed flows according to Tsanis (1987), Chua et al. (2000), Al-Garni (2007). Here, in the present study, it is found to be 0.75 for the speed range of 0.029-1.79 m/s.

The fully-developed laminar character of the flow at the measurement stations of $X/D=146$ and 604 is also verified by means of the cross-sectional velocity distribution at 35 radial positions for the covered calibration test cases. A typical normalized distribution of \bar{U}/\bar{U}_{CL} as a function of r/R at the flow rate of 29.89 L/min is given in Fig. 3.8. The well-known parabolic velocity profile of Blasius is also given in the same figure by the dashed lines. The cross-sectional velocity distribution is in good agreement with the parabolic velocity profile displaying a maximum error margin of $\pm 5\%$.

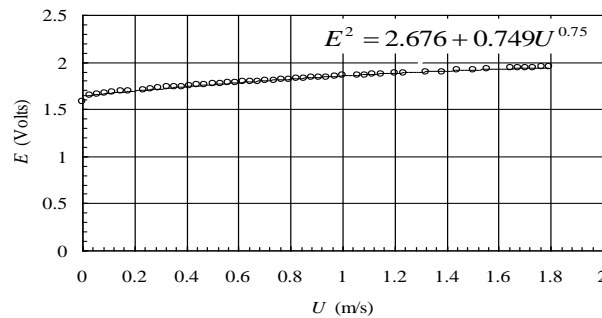


Figure 3.7. Low speed calibration curve using laminar pipe-flow method

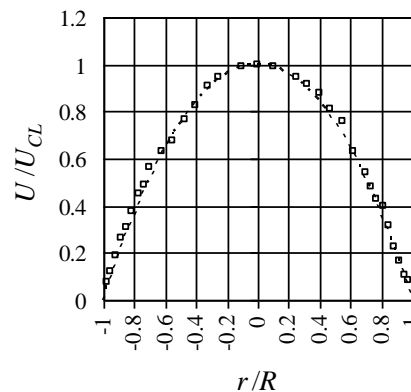


Figure 3.8. Cross-sectional velocity distribution at reference flow rate of $Q=29.89$ L/min in case of laminar pipe-flow method

For rotating disc calibration, a simple system is constructed and used for hotwire calibration at low speeds similar to the methods described in (Bruun et al., 1989), (Guellouz and Tavoularis, 1995), (Al-Garni, 2007). The calibration set-up comprised of a disc rotated at known angular velocities, ω , in stagnant air as shown in Fig. 3.9.

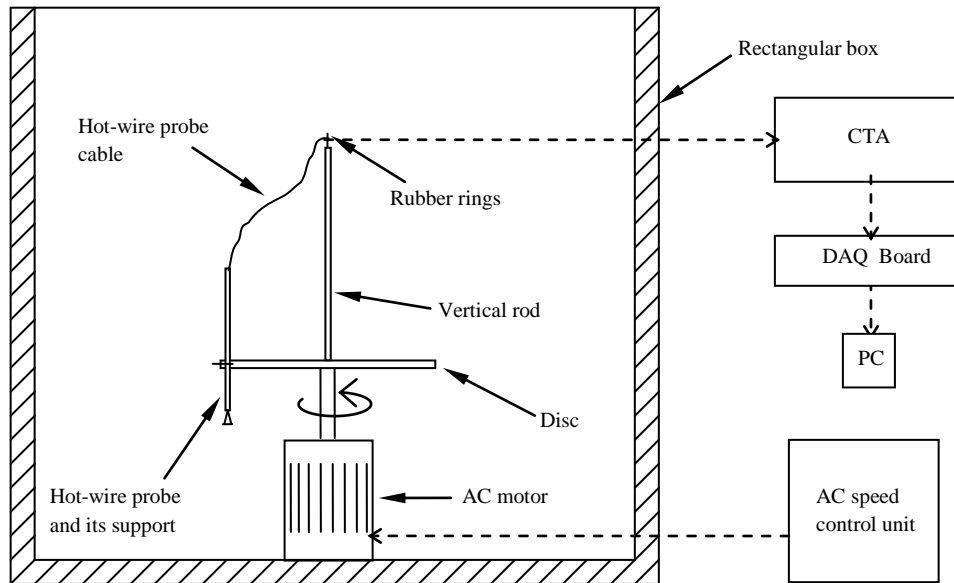


Figure 3.9. Schematic diagram of the set-up for rotating disc method

The disc is made of steel having a radius of 9 cm and a thickness of 5 mm. It is driven by a 1.5 kW variable-speed AC motor. The motor is controlled by a SIEMENS micromaster speed control unit (code: 6SE3018-8BC00) operatable in the angular frequency range of $0 \text{ Hz} \leq f \leq 650 \text{ Hz}$. A 4-mm diameter hole is drilled on the disc at 8 cm far from the disc center in order to mount the hotwire probe support. The distance between the disc center and the probe support is selected as 8 cm in order to eliminate the probability of wind effect caused by the disc rotation itself. The probe is placed into the hole and its angular position is adjusted by rotating the probe around its axis and recording the anemometer signal until the maximum voltage signal is obtained as expressed in (Bruun, 1995). The probe cable is attached to the vertical rod on the center of the disc to prevent twist of the cable. In order to

disconnect the interaction between the metal support cable end and the vertical rod, rubber rings are used. The calibration set-up is sealed by means of a rectangular box with a volume of 0.94 m^3 having a length of 1.2 m, a width of 1.2 m and a depth of 0.65 m so that the air inside the box is stagnant. The hotwire probe location is at 0.52 m from the walls of the box eliminating end effects. The probe calibration is free from the effects of rotation in terms of the generated centrifugal force and the probe wake. Since the direction of the centrifugal force is parallel to the axes of 1.25 mm-length of wire which is also between the rigid prongs. Therefore, stretch of hotwire is negligible and probe wake is prevented by means of balanced disc rotation through insulated driving motor via use of rubber sleeves during the calibration tests. During the calibration, the disc is rotated at angular velocities, ω of ranging from 0.63 rad/s to 13.19 rad/s by adjusting the angular frequency, f , of the motor between 0.1 Hz and 2.1 Hz, correspondingly. The angular velocities are also cross-checked by using a mechanic tachometer. The angular velocities both calculated from the angular frequency of the motor and the tachometer are in agreement within a margin of ± 1 %. At each run, the hotwire output voltage signal is transferred through a Daq3001 USB board into PC environment and saved into a file. The air speeds sensed by the hotwire probe are calculated by multiplying the angular velocities by the radius of the probe location. Hence the calibration range covers the speeds of 0.05-1.05 m/s. Calibration of the probe for velocities above 1.05 m/s is unsuitable by this method since effects of vibration at high angular velocities of rotating disc start to dominate.

The rotating disc method is used for 21 test cases with an incremental increase of 0.0502 m/s. The calibration curve is shown in Fig. 3.10. As can be seen from Fig. 3.10, the calibration equation is found to be in good agreement with the modified King's law in which the A and B constants and n exponent are found as 2.625, 0.847 and 0.75, respectively with a maximum error margin of ± 5 %.

In order to compare the proposed calibration methods, the velocities are calculated using the calibration equations and the relationships between the calculated and measured velocities are compared for both laminar pipe-flow and rotating disc method as shown in Fig. 3.11.

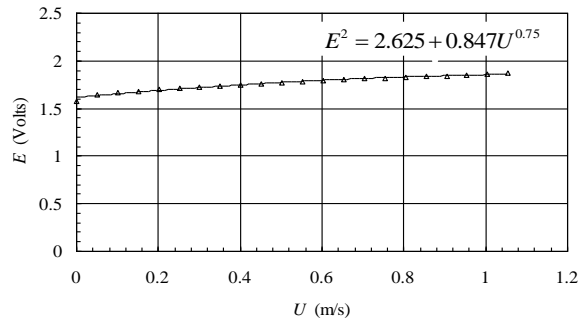


Figure 3.10. Low speed calibration curve using rotating disc method

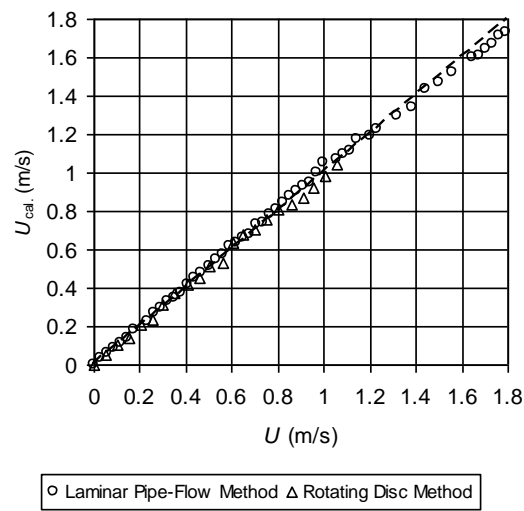


Figure 3.11. Comparison of the measured velocities and calculated ones from calibration equations for both laminar pipe-flow and rotating disc method

Two calibration methods have an acceptable confirmation with a maximum deviation of $\pm 7\%$. The maximum deviation of $\pm 7\%$ corresponding to $U \geq 0.8$ m/s may be the result of the aforementioned effects of high angular velocities of rotating disc. Rotating disc method contributes to the literature as a new and original low speed calibration method besides in situ laminar pipe-flow method. Both methods are seen to be compatible with each other in an acceptable error margin. The n exponent of modified King's Law, Eq. (3.4) which can be seen up to the value of 1 for low speeds in the literature is found to be 0.75. It can be declared that the well-known King's law is convenient also for low speed calibration part of hotwire probes as well

as its usage for high speed calibration sides. The details of these calibration methods can be found in Özahi et al. (2010).

3.2.9.4. Wall proximity effect on hotwire measurements

When the hotwire anemometer provides data in the region very close to a wall, there is a need for correction to be applied to velocity readings which are influenced by the presence of the wall. The velocity measurements in boundary layer may reach a minimum value and then increase as the hotwire probe is moved toward the wall. Hotwire probe displays signs of additional heat transfer when it is traversed into wall proximity and therefore, the indicated velocity is larger than the true value. There is an additional conduction heat transfer to the wall over and above the convective heat transfer due to the local flow velocity. In addition to this there is an increasing aerodynamic blockage effect due to the proximity of the wire and prongs to the wall. A method of correction is based on extending Wills' laminar correction (Wills, 1962). In general, the wall influence depends on the distance between the wall and hot-wire sensor, the flow velocity, the wall material, the overheat ratio, the wall roughness and the geometry of probe (Hebbar, 1980). The wall material can be conducting or non-conducting. The conducting walls affect the heat transfer more than the others. Turan et al. (1987) described all walls for which $k_w/k > 100$ as conducting.

Hebbar K. S. (1980) observed that the wall proximity effects cease beyond $y^+ = 5$. The scatter was observed to be largely in the region $y^+ < 1.5$. Oka and Kostic (1972) studied on the wall proximity effect. They found that the wall effect ceases at $y^+ > 5$. The distance at which the wall influence was detected was about 1 mm. The wall correction of the hotwire anemometer was also expressed by Gibbings et al. (1995). In the study of Durst et al. (2001) and Durst and Zanoun (2002), the results showed typical deviations from the linear velocity distribution $U^+ = y^+$ for wall distances of $y^+ < 3.5$ as a result of the increased heat transfer from the presence of the aluminum wall. Therefore, they claimed that corrections for hotwire measurements in near-wall region were needed for all values of $y^+ \leq 3.5$. Hutchins and Choi (2002) studied experimentally the local skin friction coefficient using hotwire anemometry. They have observed that deviations from the linear region occurred at wall distances

less than $y^+ \approx 3.5$. The voltage rise occurring near the wall without flow was characterized with respect to wire position by Vagt and Fernholz (1979) and Bhatia et al. (1982). The thermal characteristics of a hotwire in near-wall flow were investigated by Wenzhong et al. (2006). Velocity correction factor was introduced as;

$$C_u = \frac{U_{eff}}{U} \quad (3.5)$$

Bhatia et al. (1982) concluded from their computations that no correction was needed in the case of an insulating wall. In another study related with wall effects by Lange et al. (1999), a new correction factor was proposed for all temperature loadings with a good approximation as follows:

$$C_u = 1.0 - \exp(-0.4y^{+2}) \quad (3.6)$$

It was claimed that no correction to the measured velocity would be needed if the wire is more than $y^+ = 4$ away from the wall. Another correction factor was also introduced for insulating walls as:

$$C_u = 1.0 + 0.363 \exp(-0.22y^{+2.5}) \quad (3.7)$$

Bruun (1995) expressed that experimental investigations of the velocity correction needed in the case of non-conducting wall materials showed an increase in the measured velocity for $y^+ \leq 2$. Most applications of the hotwire anemometer are in the forced convection domain where the velocity past the probe is large, so that the natural convection effects in the heat transfer from the sensor are negligible (Tewari and Jaluria, 1990). In the present study, the wall proximity effect is not seen during the experiment due to no undesirable, unexpected hotwire signal near the pipe wall. None of the velocity graphs contains any unexpected data near the wall. To verify it theoretically, $y^+ = yu^*/\nu$ is considered for the experimental range of the instantaneous wall shear stress $\bar{\tau}_w(t)$. The value of y^+ is found to be minimum 2.31 for $r/R=0.977$

and $\bar{\tau}_w(t)=0.015$ Pa, which is above expressed value of $y^+=2$ which is deduced by Bruun (1995).

3.2.9.5. Wire aspect ratio effect

Another important parameter for the hotwire probe is the ratio of wire length to wire diameter, l/d . The lengths of wires should be short for anemometry considerations of spatial resolution. Most hotwire probes are in the range of aspect ratio of $100 < l/d < 600$. The length of the wire should be short to maximize spatial resolution and to minimize aerodynamic loading. On the other hand, the length of the wire should be long enough to minimize end conduction losses and to provide a more uniform temperature distribution. In general, for $l/d < 200$, end conduction effects are important and l/d ratio must be retained as a parameter. More detailed information can be found in (Ligrani and Bradshaw, 1987), (Turan and Azad, 1989), (Collis and Williams, 1959). In the present experimental set-up, l/d ratio of the used 55P11 probe is 250. Hence there is no end conduction effect.

3.2.9.6. Overheat ratio (OHR) effect

In the hotwire measurements, overheat ratio of the hotwire anemometer is one of the very important parameters. Care is necessary to take into account the effect due to the ambient fluid temperature variation, to keep the overheat ratio, with respect to sensor resistance at the new ambient temperature, constant. Therefore, it is important to maintain the temperature difference between the sensor and the fluid constant. In literature (Johnstone et al., 2005), (Christman and Podzimek, 1981), (Yue and Malmström, 1998), (Durst and Zanoun, 2002), (Durst et al., 2008), (Khoo et al., 1998), (Bruun et al., 1988), (Bruun, 1995), OHRs used can be seen to be in the range of 0.7 and 1.8 depending on the character of their studied case according to different study characteristics.

In the present study, the OHR value of 1.8 is used as suggested by Bruun (1995). The resulting the maximum wire temperature $T_{w, \max}$ was about 290 °C which is below the oxidization temperature of the wire material.

3.2.10. Pressure transmitter

Pressure transmitters convert pressure into a proportional electrical standardized output. In the present experiment, WIKA SL-1 pressure transmitters for low pressure applications are used to measure static pressures along the pipe at 7 downstream locations of $X/D=10, 15, 185, 335, 485, 589, 619$ as can be seen from Fig. 3.1. The operating range of the transmitter is in between -20 mbar and +20 mbar. Its analog output signal and power supply are 0-10 V and 14-30 VDC, respectively. Its response time is 1 μ s. So, the time resolution is 1 kHz. Its accuracy is less than 0.5 % and its operating temperature is between -30 °C and +80 °C. The linearity and repeatability uncertainties are less than 0.2 % and 0.1 %, respectively. The technical specification of the pressure transmitter is also given in Appendix 8.

In order to secure highly accurate pressure measurements, it is necessary to calibrate the WIKA SL-1 pressure transmitters. The calibration of the pressure transmitter is performed by the manufacturer and its one-year stability is given less than 0.3 %. The calibration curve of the pressure transmitter is linear ($P=cst.E$) between 0 and 10 volt corresponding to -20 mbar and +20 mbar. Pressure transmitters are more accurate than transducers such that the accuracy, linearity and repeatability of the WIKA SL-1 pressure transmitter are given less than 0.5 %, 0.2 % and 0.1 %, respectively.

3.2.11. Oscilloscope

An oscilloscope is a type of electronic test instrument that allows signal voltages to be viewed, usually as a two-dimensional graph of one or more electrical potential differences (vertical axis) plotted as a function of time or of some other voltage (horizontal axis). Although an oscilloscope displays voltage on its vertical axis, any other quantity that can be converted to a voltage can be displayed as well. In most instances, oscilloscopes show events that repeat with either no change or change slowly. In addition to the amplitude of the signal, an oscilloscope can measure the frequency, show distortion, show the time between two events (such as pulse width or pulse rise time), and show the relative timing of two related signals. Some better modern digital oscilloscopes can analyze and display the spectrum of a

repetitive event. Special-purpose oscilloscopes, called spectrum analyzers, have sensitive inputs and can display spectra well into the GHz range. A few oscilloscopes that accept plug-ins can display spectra in the audio range.

In the present experimental study, Tektronix 5403 type Oscilloscope is used for preliminary test and the pre-calibration of CTA. It is a general-purpose, plug-in oscilloscope type at 60 MHz. The 5403 type oscilloscope provides 5 mV sensitivity at 60 MHz and 1 mV/division sensitivity at 25 MHz.

3.2.12. Data acquisition and processing equipment (DAQ)

In the experimental set-up, a 16-bit, 1-MHz A/D converter IOtech Daq3001 USB board is used for the acquiring of velocity and pressure data, to trigger the MFC unit analogously. Sampling frequency of 100 Hz is used for the data acquisition in all cases. The details of the data acquisition are given in the next chapter. The technical specification of the converter IOtech Daq3001 USB board is given in Appendix 9.

To pre-calibrate the daqboard, a high precision digital voltmeter and ampermeter, the software program of the daqboard, DaqView supplied by the IOtech and the utilized program in LabView 2009SP1[®] are used. Signals acquired by the hotwire probe are controlled by means of a digital voltmeter by connecting the output of the CTA directly to the digital voltmeter. The same signal acquired by means of the daqboard is also visualized in the utilized program in LabView and the DaqView program on PC. All the results are found to same with each other with a high precision up to 5 digits after point.

3.3. Conclusions

The experimental set-up is designed and constructed in order to investigate the flow dynamics of laminar to turbulent transition in pulsatile air flow through the pipeline of 26.6 mm diameter and of 17.4 m length. The screw air compressor and a surge tank are used in the experiment to supply air through the pipeline. In order to generate pulsatile pipe flow through the pipeline system, the MFC unit is used. The

flow conditioners, a tube bundle and a perforated plate, whose effects have been investigated previously, are used in order to provide fully developed and swirl-free flow in the pipeline. To achieve a smooth passage between the 4-m pipes and MFC unit, the designed conical adapter and connection adapters are used in the experiment.

The measurement devices for the velocity and the pressure measurement are selected as DANTEC CTA with miniature probe, and WIKA SL1 pressure transmitters, respectively. The CTA pre-calibration and internal switch adjustments are performed and the overheat ratio OHR of the hotwire probe is adjusted. The hotwire probe calibration for low speeds is conducted using the in-situ laminar pipe-flow and rotating disc method. The calibration of the hotwire probe for high speeds is performed with the well-known in-situ calibration method by means of an inclined leg alcohol manometer, a pitot-static tube and a static tapping. The calibration of the pressure transmitters is carried out by means of the linear calibration curve supplied by the manufacturer. The pre-calibration of the daqboard is conducted using the high precision digital voltmeter, DaqView and the devised program in LabView.

CHAPTER 4

DATA ACCUMULATION AND ACQUISITION SYSTEM (PRESENTATION OF THE DEvised PROGRAM AND METHODOLOGY IN LABVIEW 2009SP1[®] ENVIRONMENT)

4.1. Introduction

In this chapter, data accumulation and processing techniques are presented. The experimental procedure and the devised program in LabView 2009SP1 environment are discussed in details. The methodology used in the devised program, the automated measurement, and the control of pulsatile pipe flow are described.

4.2. Data Acquisition and Processing Equipment

In the experimental study, a 16-bit, 1-MHz A/D converter IOtech Daq3001 USB Board with 16 single-ended, 8 differential analog inputs and 4 analog outputs is used in order to accumulate the raw velocity and pressure data. It is easily connected to the computer by means of USB connector. IOtech Daq3001 USB daqboard is compatible with LabView software program.

The analog output signals from the PC are sent from the analog output channel of the daqboard to the MFC unit to generate and control the pulsatile pipe flows. The signals from the hotwire anemometer and 7 pressure transmitters are acquired by means of the analog input channels of the daqboard and accumulated in the PC simultaneously.

The accumulation of the data is performed using the devised program in LabView 2009SP1 environment. The accumulated data are then processed by the devised program in terms of the desired physical flow parameters. The processed

data are analyzed and necessary plots are formed and saved into the file in PC. During the accumulation process of the velocity data throughout the pipe cross-section, an automatically controlled traverse mechanism is used. The software of the data acquisition system is the devised program, *TDFC.vi* using LabView 2009SP1.

4.3. Data Accumulation Procedure

All instantaneous signals from the hotwire anemometer at $X/D=604$ together with the instantaneous static pressures at 7 downstream locations along the pipeline are accumulated in the PC by means of the IOtech Daq3001 USB daqboard and the devised program, *TDFC.vi* in LabView. For cross-sectional velocity distribution throughout the pipe cross-section, instantaneous velocity signals from the hotwire anemometer are taken at 13 different radial positions between the pipe wall and pipe center line at the half of the cross-sectional pipe section due to the symmetry of the flow. The sampling frequency is adjusted to 100 Hz in order to take 5000 samples of hotwire signals at each radial position and 5000 samples of pressure signals.

4.3.1. Control of time dependent data accumulation

The time dependent data control and accumulation are performed by the measurement chain consisted of the devised program in LabView, CTA, hotwire probe, pressure transmitters, daqboard, MFC unit, traverse mechanism and PC. The data control and accumulation during all instances are performed automatically by means of PC, daqboard and the devised program, *TDFC.vi* in LabView 2009-SP1. The details of the devised program are given in the next sections.

The MFC unit is controlled by the devised program in order to generate the steady and time dependent flow through the pipeline. The analog voltage signal is sent to the MFC unit from the analog output channel of the daqboard in order to generate time dependent pipe flow for any amplitude and oscillation frequency. On the other hand, the voltage signals from the hotwire anemometer and seven pressure transmitters throughout the analog input channels of the daqboard are accumulated simultaneously on the PC by means of the devised program, *TDFC.vi*.

4.3.2. Procedure for velocity measurement

The experimental study is carried out to analyze the flow dynamics of transitional pulsatile flow in the pipeline. Hence the axial velocity field of the flow in the pipe is also time dependent and dependent on the radial positions, r , throughout the pipe cross-section as $U = U(r, t)$. Therefore, the time dependent axial velocity measurements are repeated at different radial positions, r , throughout the pipe cross-section to determine the cross-sectional velocity profiles.

Pipe flow is considered as being independent from the axial flow direction if flow is fully developed. The velocity measurements are always performed at the station where the flow is fully developed. Hence, in the experiment, the velocity measurements are performed at the axial position of the pipeline, $X/D=604$, where the flow is fully developed.

4.3.3. Adjustment of the position of the hotwire probe

The radial position of the hotwire probe throughout the pipe cross-section is controlled and changed by means of the traverse mechanism, RCP2-SA6-I-PM-6-200-P1-SBE Robocylinder and RCP2-CGA-SA6-I-PM-0-P Robocylinder Positioning Unit. The traverse mechanism has an electro-mechanic cylinder motor, incremental encoder and positioning unit with a high repeatability of 0.02 mm. The traversing mechanism is controlled by means of PC interface software for robocylinder supplied by the manufacturer through a serial protocol and RS-232 connection cable.

In the experiment, for a preliminary test of the determination of the reference position of the hotwire probe, a custom-designed wall contact indicator is used in order to position the hotwire probe to the closest radial position near the pipe wall as near as possible. To determine the reference radial position of the probe, a copper sheet of 0.01 mm thickness is covered on the pipe wall and electrical circuit is constructed between the copper sheet and the hotwire probe. When the prongs of the hotwire probe touch to the copper sheet, the lamp lights and the reference position of the hotwire probe is fixed as 0.01 mm at this location. The thickness of the copper

sheet is measured by the micrometer. Then considering the wall proximity effect, the closest position of the hotwire probe to the pipe wall is adjusted as $r/R=0.977$.

The traversing route used in the experiment, r/R , is adjusted as 0, 0.165, 0.278, 0.391, 0.504, 0.617, 0.692, 0.767, 0.842, 0.880, 0.917, 0.955, 0.977. The traversing unit has sensitivity less than 0.02 mm so that these radial positions can be provided successfully. In the experiment, the actual radial position of the hotwire probe seen in the PC interface software program supplied by the manufacturer is exactly as same as the given radial positions above. The electro-mechanic cylinder motor with incremental encoder satisfies the accurate probe positioning with the defined r/R positions.

4.3.4. Procedure for pressure measurement

The pressure signals from 7 pressure transmitters are accumulated through the 7 analog input channels of the daqboard by means of the *TDFC.vi* to process and analyze them. The pressure measurement is performed at 7 axial downstream locations along the pipe at $X/D=10, 15, 185, 335, 485, 589, 619$. During the accumulation of the velocity data for 13 radial positions, the static pressure data at each pressure transmitter are accumulated 13 times. The pressure data acquired from each pressure transmitter, which are taken for 13 times in one run are found to be same with an accuracy of $\pm 0.8\%$. This verifies the accuracy of pressure measurement for each pressure transmitter.

The last two pressure transmitters located at $15D$ downstream and at $15D$ upstream of the hotwire probe in the test section, $X/D=589$ and 619 , are used to evaluate the pressure drop through the test section. In the devised program, *TDFC.vi*, the instantaneous pressure drop per unit length, $\Delta P(t)/L$ is evaluated.

4.4. Experimental Procedure

In the present study, two characteristic time dependent parameters of oscillation frequency, f , and the velocity amplitude ratio, A_1 , are changed

systematically in order to investigate the resulting flow dynamics of the pulsatile air flow through the pipeline at the onset of the transition to turbulence and also reveal their effects on the flow dynamics.

4.4.1. Adjustment of the experimental run

The experimental study is based on velocity measurement over the cross-section of the pipe and static pressure measurements at 7 different locations along the pipe length. These measurements are planned to carry out for different flow conditions by means of adjusting the flow parameters of $\sqrt{\omega'}$ and A_1 . The control and the adjustment of $\sqrt{\omega'}$ and A_1 are realized by means of *TDFC.vi*. The methodology and the details of *TDFC.vi* are given in the next sections.

Before the pulsatile flow analyses, steady state flow measurements are performed as preliminary axial velocity and pressure measurements. *TDFC.vi* has capabilities to generate and analyze steady state flow. Hence steady state axial velocity measurements are performed to obtain the information about the velocity distribution character of the steady state pipe flow in the experimental set-up. The cross-sectional velocity distributions are obtained by measuring velocities at 19 different radial positions for 48 different runs covering the Reynolds number range of $547 \leq Re \leq 9000$. Some of the velocity distributions in the covered range are given in Fig. 4.1.

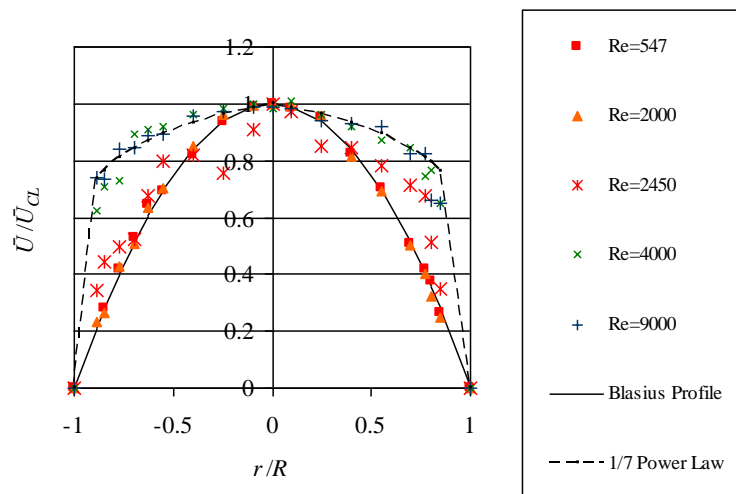


Figure 4.1. \bar{U}/\bar{U}_{CL} distributions with respect to r/R for steady state flow condition

4.4.2. Ranges in the experimental study

The time dependent axial velocity measurements at 13 radial positions at the half of the pipe cross-section and the time dependent static pressure measurements at 7 downstream locations are performed by means of the hotwire probe connected to the CTA and 7 pressure transmitters, respectively by changing systematically the characteristic flow parameters of f and A_1 in order to investigate the flow dynamic in transitional pulsatile pipe flow and to detect the onset of the transition to turbulence in pulsatile pipe flow. All velocity measurements are carried out for the fully developed flow conditions at $X/D=604$. The measurements are reduced to the ones at the standard temperature and pressure, STP condition.

The experiments are carried out in the ranges of the time averaged Reynolds number of $1019 \leq Re_{ta} \leq 4817$, oscillating Reynolds number of $107 \leq Re_{os} \leq 4261$, velocity amplitude ratio of $0.05 \leq A_1 \leq 0.96$ and the pulsation frequencies of $0.1 \text{ Hz} \leq f \leq 14 \text{ Hz}$ (the corresponding Womersley numbers of $2.72 \leq \sqrt{\omega'} \leq 32.21$).

4.4.3. Determination of axial velocity measurement position

The present experimental set-up is designed to study pulsatile pipe flows in transitional flow regime. In order to obtain the accurate velocity measurement, the fully developed pipe flow should be provided due to the development of the pipe flows requiring a certain axial distance from the pipe inlet. In the literature, there are some empirical correlations for estimating the flow development length under steady state conditions such as given by Durst et al. (2007) as follows;

$$\frac{L_e}{D} = \left[0.619^{1.6} + (0.0567 \text{Re})^{1.6} \right]^{1/1.6} \quad (4.1)$$

This equation is derived for steady state flow conditions but it can be applied for pulsatile flows to estimate the required length since $L_{e \text{ pulsatile}} / L_{e \text{ steady}} < 1$ (Durst et al., 2005).

Moreover, for laminar pulsatile, laminar oscillating, turbulent pulsatile and turbulent oscillating pipe flows, experimental investigations were performed. The development length of laminar oscillating pipe flow was found to be shorter than that of a steady laminar pipe flow at the same mean Re number (Gerrard and Hughes, 1971), (Eckmann and Grotberg, 1991) and given as;

$$\frac{L_e}{D} = 0.03\text{Re}_{os} \quad (4.2)$$

The development length of turbulent oscillating pipe flow was represented by Ohmi et al. (1982) as;

$$\frac{L_e}{D} = 1.3\text{Re}_{os}^{1/4} \quad (4.3)$$

The theoretical and experimental studies were performed for the determination of the development length for laminar pulsatile pipe flow and showed that the development length for laminar pulsatile pipe flow did not differ so much from that of a steady pipe flow at the same mean Re number, contrary to the case of laminar oscillating pipe flow. The development length for laminar pulsatile pipe flow was expressed as (Ohmi et al., 1976), (Florio and Mueller, 1968), (Fargie and Martin, 1971);

$$\frac{L_e}{D} = 0.049\text{Re}_{ta} \quad (4.4)$$

The development length for turbulent pulsatile pipe flow was expressed as (Iguchi et al., 1987), (Ohmi et al., 1980), (Kirmse, 1979);

$$\frac{L_e}{D} = 1.3\text{Re}_{ta}^{1/4} \quad (4.5)$$

In view of the above mentioned expressions, the X/D ratio for the present set-up is taken as 654 and the pipe length is 654D. For the pipe of 26.6 mm diameter, the

pipe length is found as 17.4 m to obtain fully-developed pipe flow. The velocity measurements are performed at $X/D=604$ at 16 m downstream location from the MFC unit. The detailed investigation of the laminar entrance length concept can be found in the next chapters.

4.4.4. Determination of axial locations for pressure measurement

Deciding on the axial locations of pressure measurements plays an important role in any design of the experimental set-up. In the experiment, the locations of the pressure measurement stations are adjusted at downstream locations in view of the literature (Durst and Ünsal, 2006). At 7 downstream locations along the pipeline, 7 pressure transmitters are installed, which allow one to carry out the instantaneous pressure measurements along the pipe. These particular locations along the pipe provide the local resolution, which turns out to be sufficient for the investigations of transition to turbulence.

The next important decision is to specify the locations of the last two pressure transmitters at the test section. The distance between these two pressure measurement stations should be estimated very accurately. In that, the shorter the distance between two static pressure measurement stations, the more closely will the approximation $\Delta P(t)/L$ approach the pressure gradient $\partial P/\partial x$. However, with very small distance L , the arising differential pressure may be too weak to be measured. If the distance between them is great, the effect of propagation time L/c that a pressure wave takes to pass through the distance cannot be neglected.

A criterion to determine the distance between pressure measurement stations for pulsatile pipe flows was given by Fargie and Martin (1971). By an analytical approach, it was shown that if v/R^2 is very small ($v/R^2 \leq 1$), the ratio of $\Delta P(t)/L$ and $\partial P/\partial x$ could be written as;

$$\frac{\Delta P / L}{\partial P / \partial x} = \frac{\sin\left(\frac{\omega L}{2c}\right)}{\frac{\omega L}{2c}} \quad (4.6)$$

Moreover, the criterion for L was drawn from the above Eq. (4.6) as that;

$$\frac{\omega L}{c} < 0.5 \quad \text{for accuracy better than 99\% and} \quad (4.7)$$

$$0.5 < \frac{\omega L}{c} < 1.1 \quad \text{for accuracy better than 95\%} \quad (4.8)$$

In the present study, in order to provide the more closely will the approximation $\Delta P(t)/L$ approach the pressure gradient $\partial P/\partial x$, the shorter the distance is used. Because of using the static pressure transmitters, all pressures can be measured in the covering range of ± 2 kPa. The natural frequency of the pressure transmitters is 1 kHz that is big enough to transfer the maximum frequency of pulsation ($f=125$ Hz) generated by means of MFC unit. Away from the pipe entrance, the pressure gradient needed is obtained from 7 different pressure locations distributed along the pipe as shown in Fig. 3.1. In view of the above mentioned representation, the distance between the two pressure transmitters at the velocity measurement station is determined to be $30D$ for the pressure measurement accuracy's ranging between 95% and 99% with respect to the obtainable angular frequency of the pulsation provided by the MFC unit; $0.628 \text{ rad/s} \leq \omega \leq 88 \text{ rad/s}$.

Observations, made by Patel and Head (1974), showed that the mean pressure gradients illustrated an earlier state of full development at distances between $10D$ and $20D$ from the pipe inlet test section. So, the first pressure location of $10D$ downstream of the MFC unit is found to be sufficient to ensure fully developed of flow pressure. The locations of the next four pressure transmitters are located at $15D$, $185D$, $335D$ and $485D$ downstream of the MFC unit. The first two pressure transmitters are also used for the determination of the pressure drop caused by the flow conditioners.

4.4.5. Verification of the MFC unit performance

In order to verify the performance of the MFC unit, series experiments are performed under both steady and pulsatile pipe flow. For preliminary experiments in

steady state, the cross-sectional velocities are measured in steady state and corresponding flow rates are calculated by numerically integrating the data over the cross-section of the pipe by using the well-known Simpson's rule. The calculated flow rates and the corresponding ones read from the MFC unit led screen are compared and found to be compatible within $\pm 1.2\%$. The comparison of the reference MFC unit and calculated values of flow rates and their relative errors are illustrated in Figs. 4.2 and 4.3, respectively.

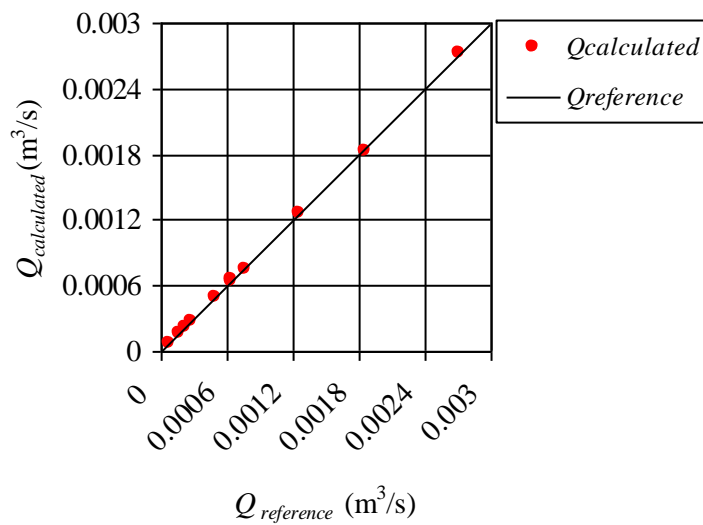


Figure 4.2. Comparison of calculated and reference MFC unit flow rates at steady state conditions

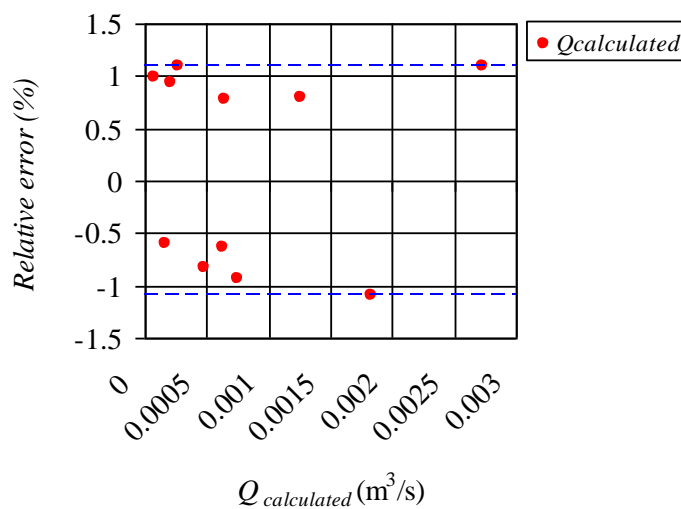


Figure 4.3. Relative error between the reference MFC unit and calculated flow rates at steady state conditions

Also, the MFC unit accuracy has been previously checked by the manufacturers using an air mass flow rate meter (AWM 700) from the company Honeywell and this check enabled a flow rate measurement accuracy lower than $\pm 1\%$ (Durst et al., 2007).

Moreover, the verifications of the MFC unit are performed for the pulsatile pipe flow. The predefined signals that trigger the MFC unit are compared with the measured velocity signals and they are also found to be very compatible with mean error margin of $\pm 1.2\%$ as can be seen from the sample plot for $f=0.8$ Hz in Fig.4.4.

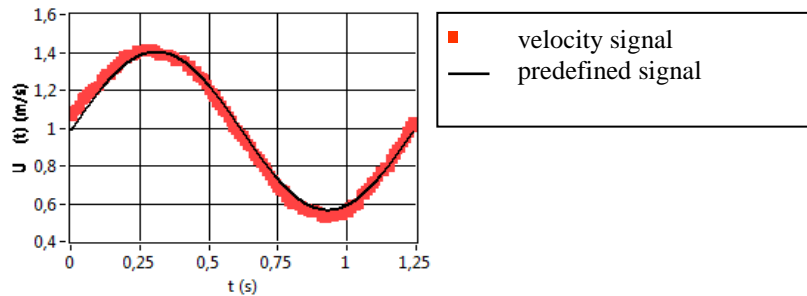


Figure 4.4. Comparison of the measured and predefined velocity signals with oscillation frequency of $f=0.8$ Hz

Figure 4.4 shows the comparison between the predefined signal given to the MFC unit and the corresponding measured velocity at the centerline of the pipe. The amplitudes of the predefined and measured velocity signals are found in good agreement.

4.5. Basic Terminology Used for Data Processing in Pulsatile Pipe flows

The most common data processing techniques available in the literature are performed for the analysis of the pulsatile pipe flow. All these data processing techniques are carried out automatically by means of the devised program, *TDFC.vi* in LabView 2009SP1 environment. The procedure of used data processing techniques are given in details as follows.

The measured data in the experiment are the time dependent axial velocity, $U(r,t)$ and the static pressures, $P(t)$ on the pipe wall along the different axial locations. The velocity and pressure data are ensemble averaged in the devised program. According to the available literature survey, there is a little difference among the ensemble averaged of velocity and pressure data obtained over 200, 1000 and 2000 pulsation cycles of the flow (Iguchi et al., 1987), (Iguchi et al., 1989). The ensemble averaged values are therefore obtained from the data accumulated over 5000 data with a sampling rate of 100 Hz resulting, i.e. 50 periods for $\sqrt{\omega'}=8.61$, 200 periods for $\sqrt{\omega'}=17.22$, 500 periods for $\sqrt{\omega'}=27.22$, 700 periods for $\sqrt{\omega'}=32.21$. It is not meaningful to increase the accumulation time for many hours being too long time for conducting the experiments at stable atmospheric pressure and temperature. Moreover, the devised program in LabView environment has capacity to analyze the signal accurately for very low periods as a comparison of the data accumulation for 5 and 50 periods with less than 2% mean deviation. The program evaluated the ensemble averaged value of velocity and pressure data.

The cross-sectional mean velocities, $\bar{U}_m(t)$, for each phase of the cycle are evaluated by numerically integrating the ensemble averaged data over the cross-section of the pipe by means of the well-known Simpson's rule. The evaluated values of $\bar{U}_m(t)$ are approximated by the finite Fourier series expansion (Eq. 2.17). The time averaged value of $\bar{U}_{m,ta}$ and the amplitude $|\bar{U}_{m,os,n}|$ are then represented by the first harmonics of the sine-wave which well fitted the data by using Eq. (2.19).

In order to evaluate the time averaged and the oscillating components of the pressure data, \bar{P}_{ta} and $|\bar{P}_{os}|$, the following finite Fourier series expansion is used.

$$\bar{P} = \bar{P}_{ta} + \sum_{n=1}^N |\bar{P}_{os,n}| \sin(n\omega t + \angle \bar{P}_{os,n}) \quad (4.9)$$

The time averaged value of \bar{P}_{ta} and the amplitude $|\bar{P}_{os}|$ are then presented by the first harmonics of the sine-wave which well fitted the data as follows;

$$\bar{P} = \bar{P}_{ta} + |\bar{P}_{os,1}| \sin(\omega t + \angle \bar{P}_{os,1}) \quad (4.10)$$

The time averaged and the oscillating values of the pressure drop evaluated by means of the pressure data taken from the 6th and 7th pressure transmitters are calculated using the following equations.

$$\Delta \bar{P}_{ta} = \bar{P}_{ta_6} - \bar{P}_{ta_7} \quad (4.11)$$

$$|\Delta \bar{P}_{os,1}| = |\bar{P}_{os,1}|_6 - |\bar{P}_{os,1}|_7 \quad (4.12)$$

The values of the instantaneous wall shear stress, $\bar{\tau}_w(t)$, for different phases of the cycle are then evaluated by substituting the evaluated values of $\Delta \bar{P}(t)/L$ and $d\bar{U}_m(t)/dt$ into the well-known time dependent momentum integral equation which gives the relationship between the pressure gradient term, $\Delta \bar{P}(t)/L$, the inertial term, $d\bar{U}_m(t)/dt$, and the viscous term $4\bar{\tau}_w(t)/D$ for fully developed pulsatile pipe flows.

The instantaneous friction factor, $\lambda_u(t)$, and the time averaged friction factor, $\lambda_{u,ta}$, are also important parameters for the time dependent pipe flows. They are evaluated using the following definitions given in the literature (Ohmi and Iguchi 1980).

$$\lambda_u(t) = \frac{8\bar{\tau}_w(t)}{\rho \bar{U}_m^2(t)} \quad (4.13)$$

$$\lambda_{u,ta} = \frac{8}{\rho \bar{U}_{m,ta}^3 T} \int_0^T \bar{\tau}_w(t) \bar{U}_m(t) dt \quad (4.14)$$

In order to compare the friction factor of the time dependent flow with steady one, the following definition of the instantaneous laminar quasi-steady friction factor, $\lambda_{qL}(t)$ is also used.

$$\lambda_{qL}(t) = \frac{64}{\left(\frac{\bar{U}_m(t)D}{\nu} \right)} \quad (4.15)$$

The steady friction factor for laminar pulsatile flow λ_{sL} is also evaluated using the Fanning's formula but by using the time averaged component of mean velocity, $\bar{U}_{m,ta}$ as follows;

$$\lambda_{sL} = \frac{64}{\left(\frac{\bar{U}_{m,ta}D}{\nu} \right)} \quad (4.16)$$

The details of the basic terminology of the pulsatile pipe flows can also be found in the literature (Çarpınlioğlu and Gündoğdu 2001), (Gündoğdu and Çarpınlioğlu, 1999). The other parameters of the time dependent pipe flows are dimensionless frequency of oscillation, ω' , Womersley number, $\sqrt{\omega'}$, Stokes parameter, S , velocity amplitude ratio, A_1 , time averaged Reynolds number, Re_{ta} and oscillating Reynolds number, Re_{os} as follows;

$$\omega' = R^2 \omega / \nu \quad (4.17)$$

$$\sqrt{\omega'} = R \sqrt{\omega / \nu} \quad (4.18)$$

$$S = R \sqrt{\omega / 2\nu} \quad (4.19)$$

$$A_1 = \frac{|\bar{U}_{m,os,1}|}{\bar{U}_{m,ta}} \quad (4.20)$$

$$Re_{ta} = \frac{\bar{U}_{m,ta}D}{\nu} \quad (4.21)$$

$$\text{Re}_{os} = \frac{|\bar{U}_{m,os,1}|D}{\nu} \quad (4.22)$$

4.6. The Devised Program, *TDFC.vi* and Methodology in LabView 2009SP1® for Data Accumulation and Acquisition System

In this section, the devised program, *TDFC.vi* and the used methodology in this program for data accumulation and acquisition system are discussed in details. The background of the program, *TDFC.vi* describing its front panel and block diagram in details and the sample graphical representations as direct outputs of *TDFC.vi* are expressed in the following sections.

4.6.1. Background of LabView environment

It is essential to introduce a basic concept/terminology of the used LabView program. LabView is one of the widely used visual programming languages since 1986 (Whitley et al., 2006). It is designed to facilitate development of data acquisition, analysis, display and control applications. LabView program has been chosen for several reasons. Unlike other text-based programs, LabView is a graphical program and based on the dataflow paradigm. Many common data processing or mathematical functions are already built-in and available. It is also possible for researchers to incorporate the algorithm into their existing or modified LabView programs. LabView contains a comprehensive set of tools for acquiring, analyzing, displaying and saving data as well as tools to help the user troubleshoot code user write. Using LabView, all measurement processes covered in this study have been performed such as; controlling the daqboard, sending the signal to trigger the mass flow control (MFC) unit, acquiring the velocity and the pressure signals, saving the measured data to the files, analyzing, processing and post-processing of the experimental data.

The program is consisted of functions which are called virtual instruments (VIs). LabView VIs contain three main components such as *Front Panel*, *Block Diagram* and *Icon/Connector Pane*. *Front Panel* is an interactive environment and

used for operations and to specify the inputs and outputs of the program. *Block Diagram* defines an actual data flow between the inputs and the outputs, which is a source code of a LabView program. *Icon/Connector Pane* graphically represents a virtual instrument (VI) in the block diagram and allows to use and to view a VI in another VI. Each VI also consists of three basic components of *terminals*, *nodes* and *wires*. *Terminals* are VI's data values which are input, output and constant values. *Nodes* are VI's operators, function calls and structure nodes. *Operators and function calls* are computations built into LabView and mathematical expressions. The examples of the *structure nodes* are *Flat Sequence Structure*, *Case Structure*, *For Loop* and *While Loop*. LabView is a form of structured dataflow. Data values travel on wires and pass through functions. The flow of data is controlled by structures. *While Loop* and *For Loop* are structures that repeat the execution of a sub diagram. *Case Structure* is analogue to case If-Then-Else used in text-based programs. *Sequence Structure* executes diagrams sequentially in the order in which they appear (Wells, 1995), (Johnson, 1997), (Wells and Travis 1997), (Beyon, 2001).

4.6.2. Details of the devised program, *TDFC.vi*

In order to generate time dependent air flow in the sinusoidal, square or triangular waveforms, MFC unit is used and controlled by a devised program named as *Time Dependent Flow Control.vi (TDFC.vi)*. The program has two main parts. One of them is the front panel which is an interactive interface used by program users to control the measurement devices and to acquire and to process any signal. The other part is the block diagram of the program, which is prepared and constructed by the authors.

4.6.2.1. Description of the front panel of *TDFC.vi*

The front panel of *TDFC.vi* and separately each segment are the user interfaces which contain controls and indicators that are the interactive input and output terminals of the VI, respectively. In the front panel of *TDFC.vi*, there are five categories such as controls, indicators, arrays, waveform charts and graphs. The controls are used to select the type of dashboard, scan rate, total scan to acquire and to

generate any steady or time dependent pipe flows of any frequency in the range of $0.1 \text{ Hz} \leq f \leq 100 \text{ Hz}$, amplitude and offset value in the range of the MFC unit capacity. The device name of the controlled dashboard is shown as *PersonalDaq3001* in the left corner of the front panel (Fig. 4.5a). *Scan rate* and *total scan to acquire* can be adjusted by the users on the front panel. There are 3 segments labeled as *Analog Input*, *Analog Output* and *Voltage Output* as controls (Fig. 4.5a).

Analog Output segment is for generation and control of time dependent air flow for any type of waveforms, frequency, amplitude and offset in the range of the MFC unit capacity. Using the *Analog Output* segment of *TDFC.vi*, the execution of the analog output signal is generated through the dashboard to trigger the MFC unit. As can be seen from the front panel of *Analog Output* segment (Fig. 4.5a), there are four analog output channel controls. In the present study, only *Channel 1* is used to trigger the MFC unit for generation and control of pulsatile air flow.

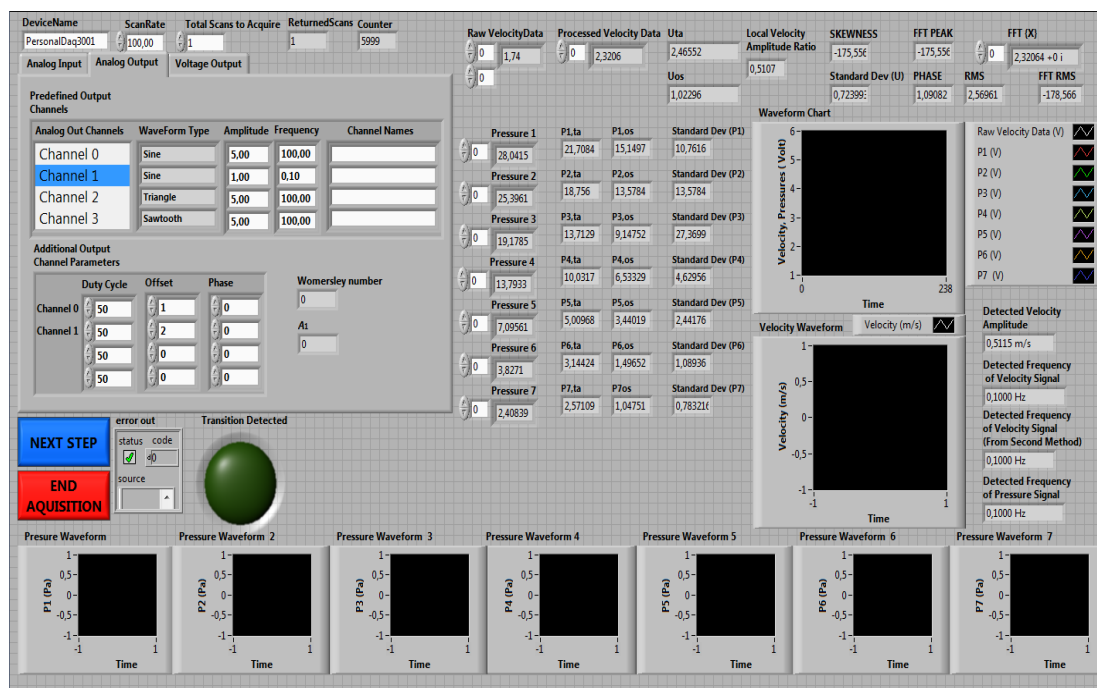


Figure 4.5a. *Analog Output* segment to control of MFC unit for generation of time dependent flow

From *Additional Output Channel Parameters* section (Fig. 4.5a), offset of the waveform is adjusted. If offset value is zero, oscillating air flow which is a special type of pulsatile flow with zero mean value is generated. Changing the offset value from zero, the pulsatile air flow is generated through the pipeline.

In Fig. 4.5b, the front panel of the *Analog Input* segment is seen. *Analog Input* segment is used to acquire the data from the hotwire anemometer and 7 pressure transmitters. Though there are 16 analog input channels, only 8 channels are used for the hotwire anemometer signal and 7 pressure transmitters' signal. The channel minimum and maximum voltage values are between -10 V and 10 V. However, the hotwire and pressure transmitters' signal are in 0-10 V analog in the present study.

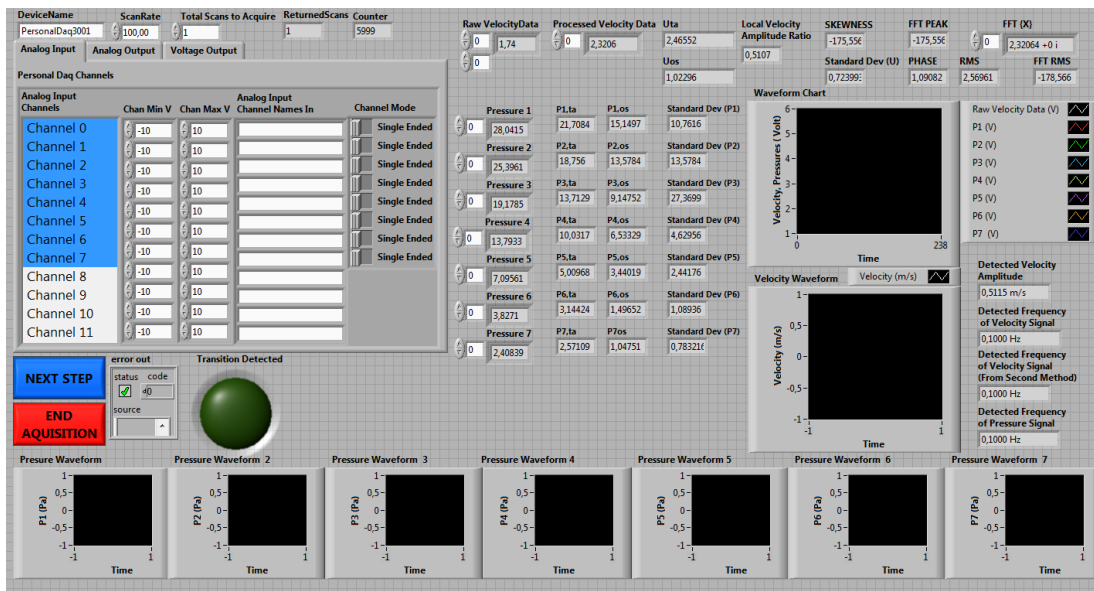


Figure 4.5b. *Analog Input* segment for data acquisition

In the front panel of *Voltage Output* segment (Fig. 4.5c), there are four voltage output channels. *Voltage Output* segment is used only for steady flow adjusting the voltage between 0 and 10 V corresponding to the flow rate values of 0 and 0.003 m³/s. In order to produce steady air flow through pipeline system, any value between 0-10 V can be selected in “Channel 0” port.

On the front panel, there are also many indicators which show the results of the experimental data as numerical and graphical representations. The raw and processed velocity and pressure data are shown with indicators, (Figs. 4.5a-4.5c) which are then saved in their corresponding file. These indicators in the program show the values of the instantaneous raw and processed $U(r,t)$, \bar{U}_{ta} and $|\bar{U}_{os,l}|$, the local amplitude ratio for each radial position of the hotwire probe, $P(t)$, \bar{P}_{ta} and $|\bar{P}_{os,l}|$, f detected from two different methods for velocity waveforms, $\sqrt{\omega'}$, f detected for pressure waveforms, A_1 , and the statistical analyses of skewness, RMS and standard deviations of velocity and pressure data. All these values are also saved into the corresponding file. There are many waveform charts on the front panel of the program, which illustrate the instantaneous raw and processed velocity and pressure waveforms (Figs. 4.5a-4.5c). To obtain continuous waveforms of any experimental or evaluated data, *While Loop* structures are used in the program.

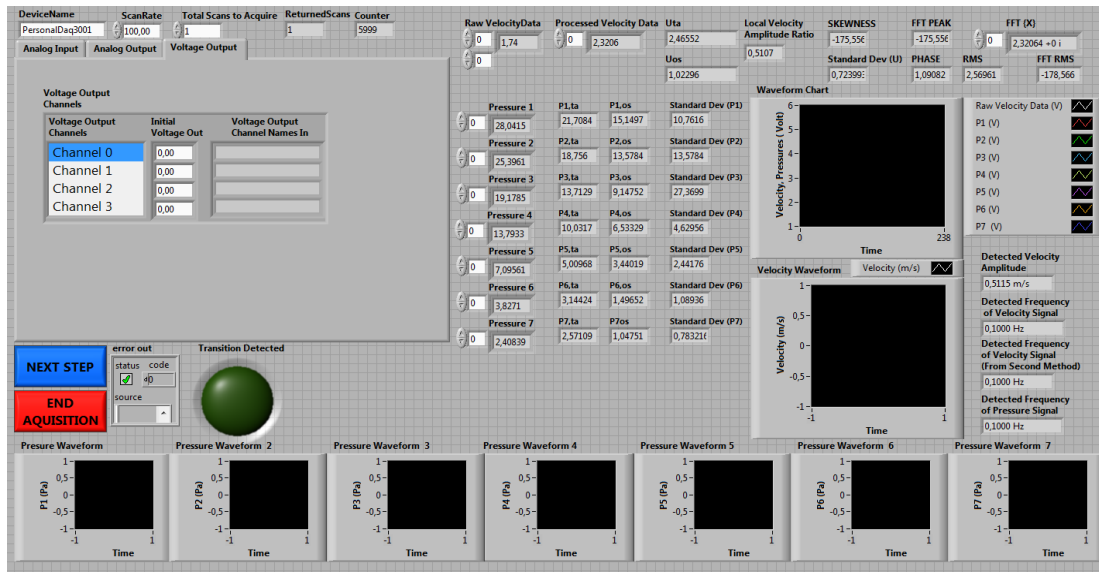


Figure 4.5c. *Voltage Output* segment to control MFC unit for generation of steady flow

The velocity graphs at the pipe centerline and near the wall, $U_{CL}(t)$ and $U_{r/R=0.977}(t)$ for whole and one period, the pressure waveform graphs acquired from

all pressure transmitters for whole and one period, the velocity waveform graph corresponding to all normalized radial positions, r/R and the velocity waveform graphs corresponding to some specified r/R are shown as waveform graphs in Fig. 4.5d.

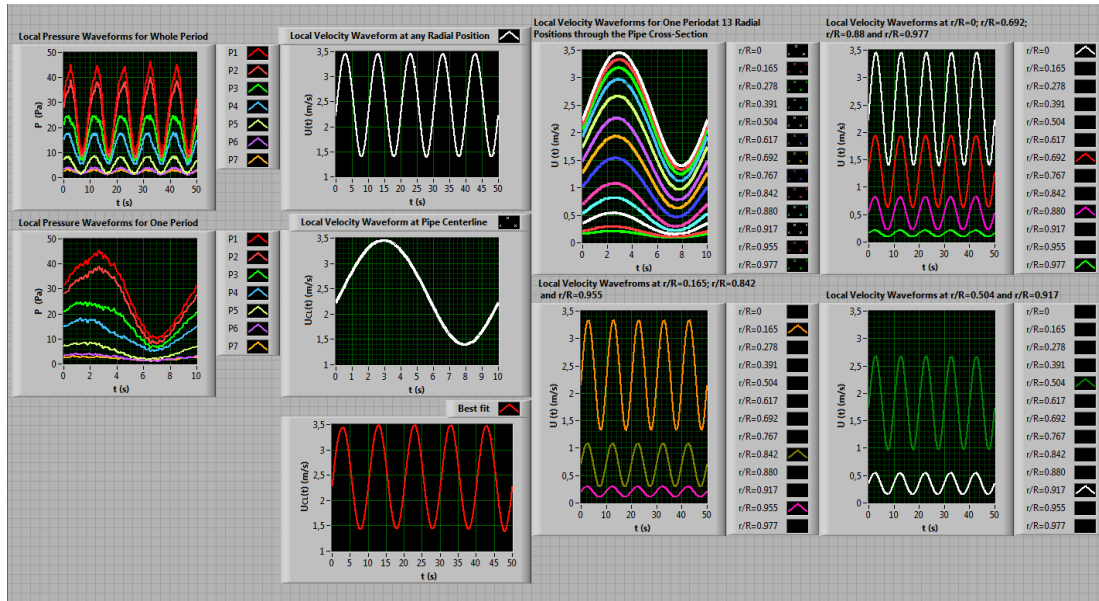


Figure 4.5d. Representations of pressure and velocity waveform graphs

The cross-sectional distributions of the time averaged and the oscillating components of the velocity (\bar{U}_{ta} vs. r and $|\bar{U}_{os,1}|$ vs. r) and their normalized value distributions with respect to normalized radius ($\bar{U}_{ta}/\bar{U}_{m,ta}$ vs. r/R , $|\bar{U}_{os,1}|/|\bar{U}_{m,os,1}|$ vs. r/R , $\bar{U}_{ta}/\bar{U}_{CL,ta}$ vs. r/R and $|\bar{U}_{os,1}|/|\bar{U}_{CL,os,1}|$ vs. r/R) are shown in the graphs and the tables on the front panel of *TDFC.vi* (Fig. 4.5e). For each run, \bar{U}_{ta} and $|\bar{U}_{os,1}|$ data are recorded near to the corresponding radial position value in the arrays of *Cross-Sectional Time Averaged Velocity Distribution* and *Cross-Sectional Oscillating Velocity Distribution*.

The cross-sectional distributions of the positive and the negative peak values of the velocity waveforms at each radial position of the hotwire probe through the

pipe cross-section ($U_{pos,peak}$ vs. r and $U_{neg,peak}$ vs. r) and their normalized values with respect to normalized radius ($U_{pos,peak}/\bar{U}_{ta}$ vs. r/R , $U_{pos,peak}/|\bar{U}_{os,1}|$ vs. r/R , $U_{neg,peak}/\bar{U}_{ta}$ vs. r/R and $U_{neg,peak}/|\bar{U}_{os,1}|$ vs. r/R) are evaluated by the program and then represented as graphs on the front panel as shown in Fig. 4.5f.

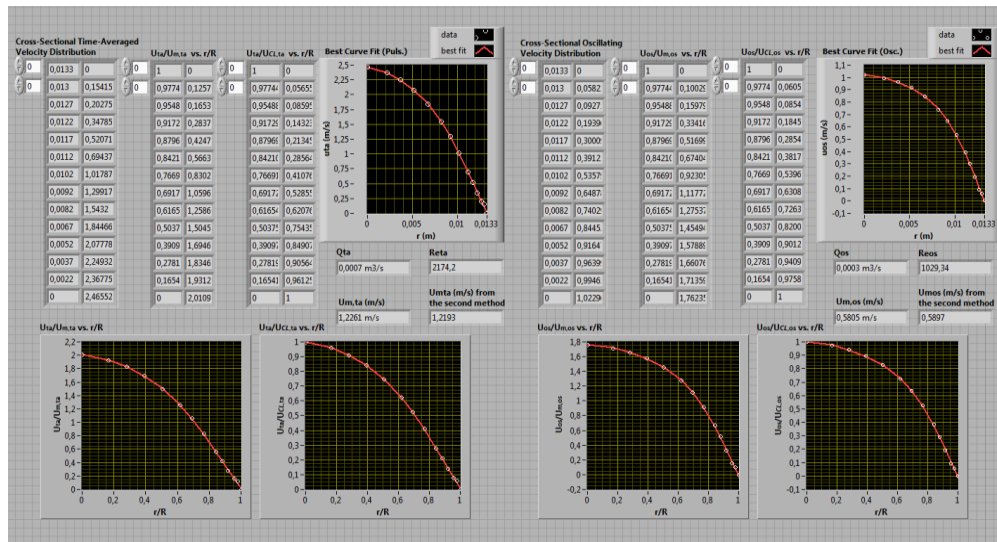


Figure 4.5e. Cross-sectional \bar{U}_{ta} , $|\bar{U}_{os,1}|$ and their normalized value distributions with respect to r and r/R , respectively and illustrations of \bar{U}_{mta} , $|\bar{U}_{mos,1}|$, Re_{ta} and Re_{os}

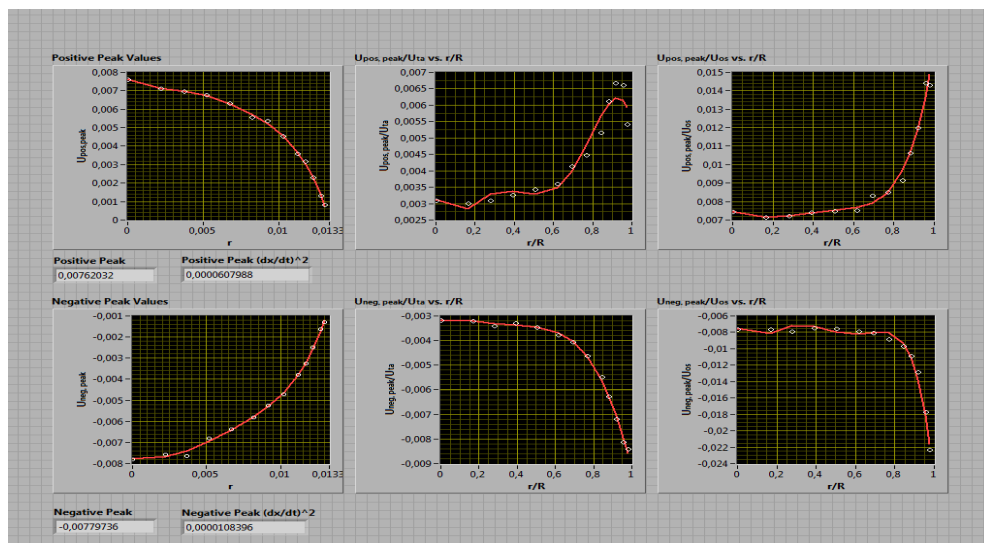


Figure 4.5f. Cross-sectional distributions of positive and negative peak values of velocity waveforms and their normalized values through pipe cross-section

The mean velocity waveform through the pipe cross-section, $\bar{U}_m(t)$ evaluated using two different methods together with the fast Fourier transformation, FFT of $\bar{U}_m(t)$ for whole and one period are graphed on the front panel (Fig. 4.5g). Also, the tabular representations of the instantaneous velocity data, $U(t)$ at each radial position of the hotwire probe are given for one and whole period as preliminaries of the second method analysis in [14x5001] matrix forms.

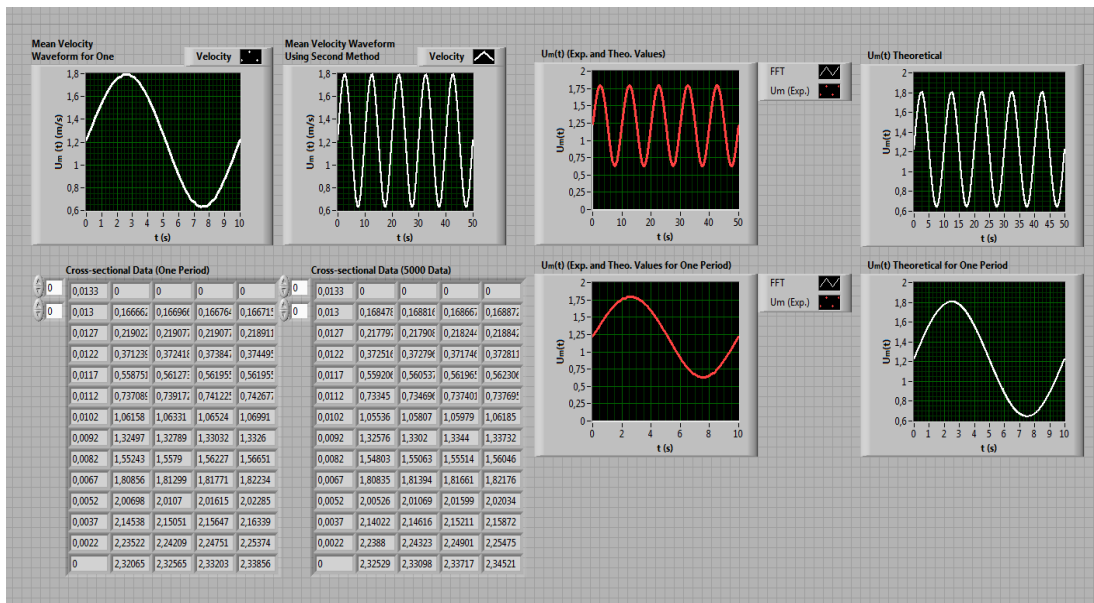


Figure 4.5g. Experimental and theoretical mean velocity, $\bar{U}_m(t)$, waveforms through pipe cross-section and tabular representation of cross-sectional velocity data

The evaluated instantaneous wall shear stress, $\bar{\tau}_w(t)$, the instantaneous friction factor of pulsatile pipe flow, $\lambda_u(t)$ and its comparison with the instantaneous laminar quasi-steady friction factor, $\lambda_{qL}(t)$ are illustrated as graphs on the front panel in Fig. 4.5h. The combined presentation of $\bar{U}_m(t)$, FFT of $U_m(t)$, $\Delta\bar{P}(t)/L$, FFT of $\Delta\bar{P}(t)/L$ and $\bar{\tau}_w(t)$ together for whole and one period are given as waveform graphs on the front panel (Fig. 4.5h).

After the execution is completed at each radial position of the hotwire probe, the probe is sent to the next radial position and the program is run again without exiting from the program for the measurements at the next radial positions, only clicking on the NEXT STEP button as shown in Figs. 4.5a-4.5c. After the measurements are completed for all radial positions of the hotwire probe through the half cross-section of the pipe, the program users click on the END ACQUISITION button and the program execution is ended giving a name to the file in which all data, relating the charts, the graphs and the evaluated mean values are saved in the corresponding file in the PC folder.

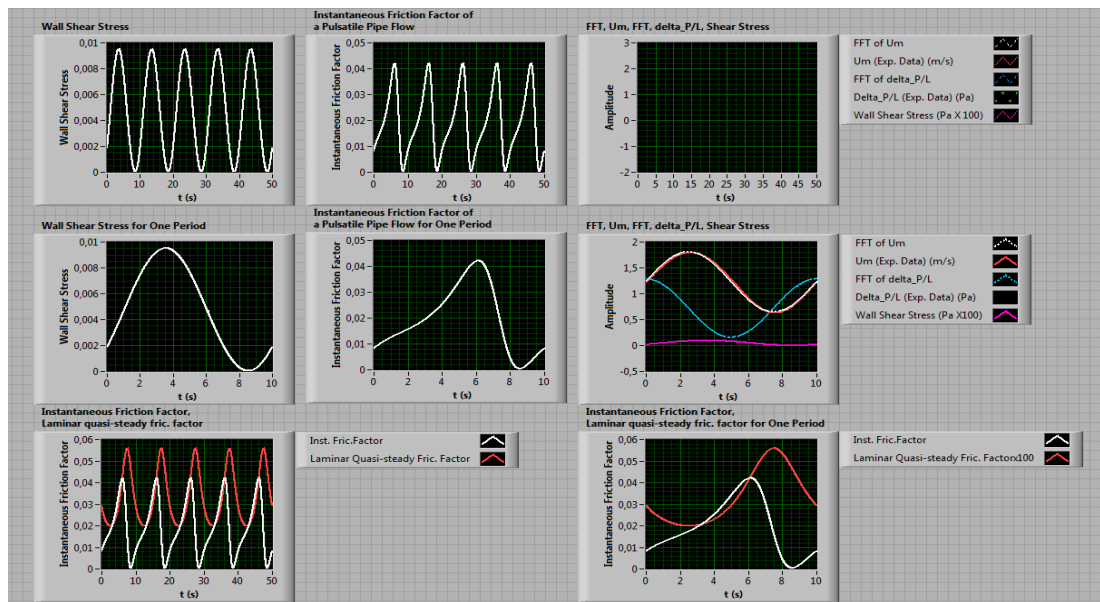


Figure 4.5h. Graphical representations of $\bar{\tau}_w(t)$, $\lambda_u(t)$, λ_{qL} , and experimental and theoretical values of $\bar{U}_m(t)$ and $\Delta\bar{P}(t)/L$ with evaluated $\bar{\tau}_w(t)$ in a combined graph

4.6.2.2. Description of the block diagram of *TDFC.vi*

The *functions* and *mathematical operators* to control the front panel objects are in the block diagram of the program. The block diagram of *TDFC.vi* is composed of two main parts using a *Flat Sequence Structure* (1a, 1b) as given in Figs. 4.6a and 4.6b. *Flat Sequence Structure* is used for the arrangement of the sequence of events. The input of the Part 1b depends on the output of the Part 1a. The first part of the *Flat Sequence Structure* is used for the control of the MFC unit and for acquisition,

accumulation, processing and saving the data taken from the measurement devices (1a). The second part is used for post-processing the acquired data, i.e. for evaluations of $\bar{U}_{m,ta}$, $|\bar{U}_{m,os,1}|$, Re_{ta} , Re_{os} and A_1 using two different methods, and for calculations of $\bar{v}_w(t)$, $\Delta\bar{P}(t)/L$, $\lambda_u(t)$, $\lambda_{u,ta}$, $\lambda_{qL}(t)$ and λ_{sL} and dimensionless parameters of S , ω' , δ_s and Re_{δ_s} (1b).

In the first part of the *Flat Sequence Structure*, there are four main structures as two *While Loops* (2, 3) and two *Case Structures* (4, 5). The *While Loops* are executed to repeat the same operations for many times until the desired count of data are satisfied. The *While Loop* (3) is used in order to repeat the acquisition process 6000 times. Due to the data accumulation starting always from the zero value, 6000 data are taken for the velocity and the pressure signals and the first 1000 data are deleted and 5000 velocity and pressure data are then used for processing. The *Case Structures* are used to determine which case is executed as If-Then-Else structure in a text-based program.

Before *While Loop* execution, in order to save all velocity and pressure data, a new file is opened (6). In the *Case Structure* (4), there is a subvi named as *Acquiring Signal.vi* (7). In this subvi, the *total scan to acquire*, the *scan rate* of the signal and the *buffer size* of the daqboard are adjusted.

To generate the time dependent flow in any sinusoidal, triangular or rectangular form with any value of amplitude, frequency and offset, or to generate steady flow, the MFC unit is triggered and controlled by means of this subvi (7). Firstly, the analog signal between 0 and 10V is sent to the MFC unit in order to generate any periodic flow through the pipe. There are three control panels for this operation so that the amplitude, the offset value and the oscillation frequency parameter are adjusted. In *Acquiring Signal.vi* (7), the *scan rate* is adjusted as 100 Hz. According to the chosen f , $\sqrt{\omega'}$ is evaluated and illustrated on the front panel.

In order to acquire the data from the hotwire anemometer and 7 pressure transmitters converting the digital value to the analog ones in the voltage unit, the

DAQIO READ SCAN.vi is used (8). The velocity and pressure waveforms as raw data in voltage can be seen in the front panel adding the *waveform charts* to this subvi (8). To process the raw velocity and pressure data, it is firstly essential to separate all data from each other. For this reason, *Index Array* palette is used (9). Hence the raw velocity data in voltage are wired to *King's Law.vi* (10) to convert into the processed velocity data in m/s unit. All other raw pressure data in voltage are wired to the *Pressure Transducers' Calibration.vi* (11) to convert into the processed pressure data in Pa unit. As a result of *While Loop* (3) execution, the continuous acquisition of the raw velocity and pressure data are performed.

As a next step, the statistical measurements and FFT analysis of the processed data are carried out. Using the prepared *Statistics of Velocity.vi* (12), the time averaged and the oscillating component of velocity waveform, \bar{U}_{ta} and $|\bar{U}_{os,1}|$ are evaluated for each radial position of the hotwire probe through the cross-section of the pipe. Also, the standard deviation, RMS value, skewness, range, FFT peak of the velocity data are estimated in this subvi. Using the evaluated \bar{U}_{ta} and $|\bar{U}_{os,1}|$, the local velocity amplitude ratio is also calculated. These processes are repeated at all 13 radial positions of the hotwire probe without exiting from the program. Beside this, the frequency of oscillation, f , is detected in this subvi. It is observed that the detected frequency of the velocity waveform is exactly same as one sent to the MFC unit at the start of the program execution in the *Analog Output* segment.

The time averaged and the oscillating components of the pressure waveform, \bar{P}_{ta} and $|\bar{P}_{os,1}|$ are evaluated in *Statistics of Pressures.vi* (13) and *Tone Meas. of Pressures.vi* (14) for all pressure data acquired from 7 pressure transmitters. The standard deviations of the pressure data are also evaluated using *Statistics of Pressure.vi*. The frequencies of the pressure waveforms are detected using the *Frequency and Amplitude Detection of Pressure Signal.vi* (15). The frequencies of the pressure waveforms are found to be as same as that of velocity waveforms.

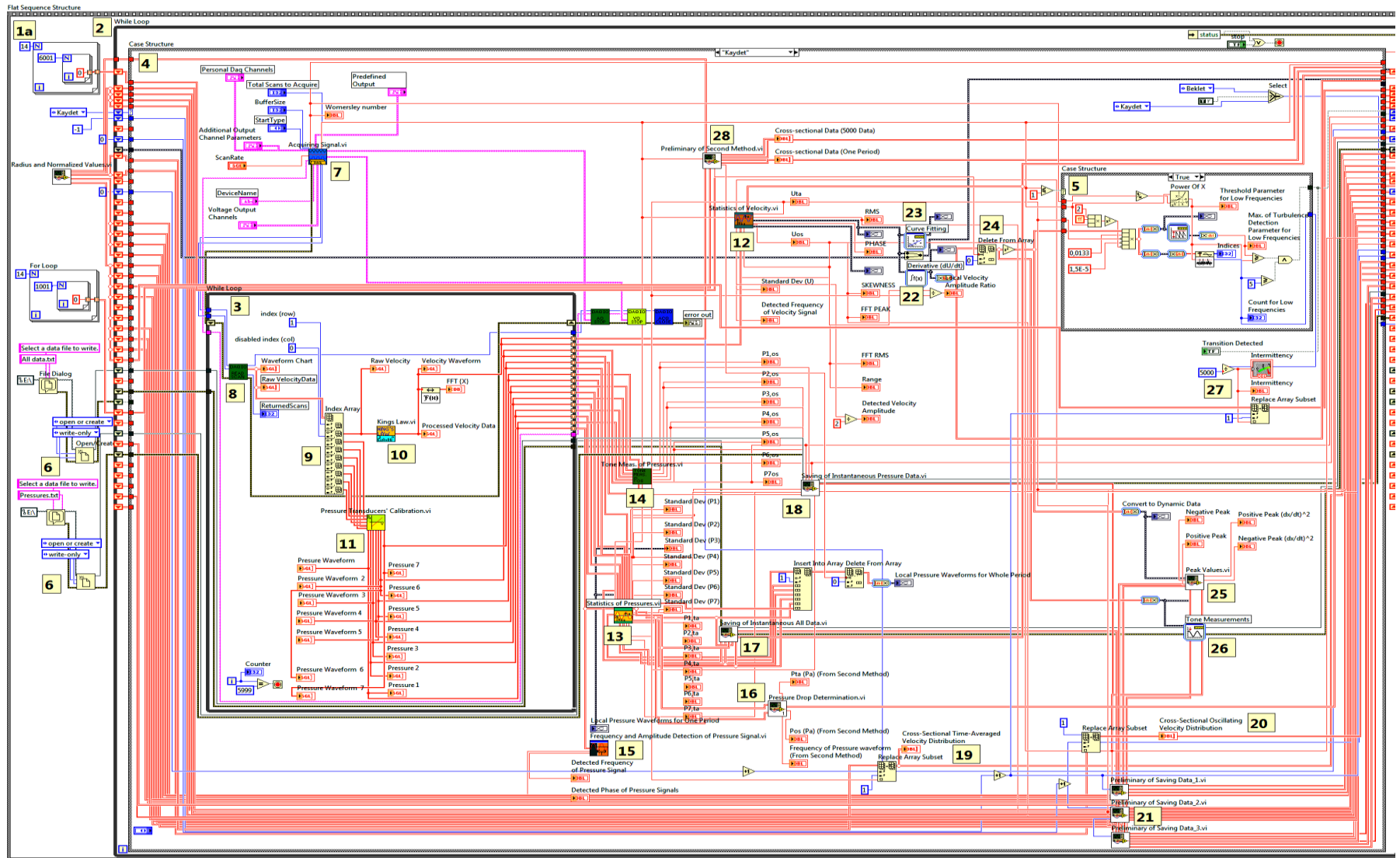


Figure 4.6a. The first part of the block diagram of *TDFC.vi* (The first part of the *Flat Sequence Structure*)

Pressure Drop Determination.vi (16) is used in order to calculate the pressure drop per unit length at the test section, $\Delta\bar{P}(t)/L = (\bar{P}_6 - \bar{P}_7)/L$. The time averaged and the oscillating components of pressure drop per unit length, $\Delta\bar{P}_{ta}/L$ and $|\Delta\bar{P}_{os,1}|/L$ are evaluated in this subvi. All $P(t)$, \bar{P}_{ta} , $|\bar{P}_{os,1}|$, $\Delta\bar{P}_{ta}/L$ and $|\Delta\bar{P}_{os,1}|/L$ acquired from each pressure transmitter are saved into the file using *Saving of Instantaneous All Data.vi* (17) and *Saving of Instantaneous Pressure Data.vi* (18).

In order to acquire and process the velocity data at each radial position of the hotwire probe, the *Case Structure* (4) is used for 13 times without exiting from the main program, clicking on the “Next Step” button on the front panel. After each step, the same procedures are repeated for all other radial positions of the hotwire probe. Besides, the pressure data are always taken for all execution of velocity measurements at 13 radial positions. The pressure data acquired from each pressure transmitter, which are taken for 13 times in one run are found to be same with an accuracy of $\pm 0.8\%$.

\bar{U}_{ta} and $|\bar{U}_{os,1}|$ data evaluated for each radial position of the hotwire probe are used separately to obtain the cross-sectional \bar{U}_{ta} and $|\bar{U}_{os,1}|$ distributions with radial position, r by means of *Replace Array Subset* palettes (19, 20). These velocity distributions are later used for estimation of Re_{ta} and Re_{os} . This method is denoted as *First Method* in this study.

Preliminary of Saving Data_1.vi, *Preliminary of Saving Data_2.vi* and *Preliminary of Saving Data_3.vi* (21) are used for the organization of the corresponding file to save later all raw, processed and post-processed data into the specified folder in PC.

For further steps, in order to detect the onset of transition to turbulence in the flow, the first derivative of $U(r,t)$ is taken for each radial position of the hotwire probe as a preliminary process of the turbulence detection method (22).

Curve Fitting.vi (23) is used to fit a curve to $U(r,t)$. The curve fit is found to be very compatible with the experimental data of $U(r,t)$ satisfying the best sinusoidal fitting. *Delete From Array* palette is used in order to delete the first 1000 data from 6000 experimental data (24). *Peak Values.vi* (25) is used to determine the positive and the negative peak values of the velocity waveforms and the square of their first derivative. Using *Tone Measurements.vi* (26), the amplitude of velocity waveform is also estimated for checking it with that found by FFT analysis.

In the second *Case Structure* (5), the detection of the onset of transition is performed. The process is different for low frequency ($f \leq 1$ Hz) and high frequency ($f > 1$ Hz) ranges. The dynamic threshold parameters and the dynamic turbulence detection parameters are derived for low and high frequency ranges by means of the dimensional analysis. If the transition is detected at any time of the velocity waveform and any radial positions of the hotwire probe, the green lamp lights and it gives an alert on the front panel. Then, all data are saved into the file named automatically as “(Transitional Regime) $Re_{ta} = \dots$; $Re_{os} = \dots$; $fre = \dots$; $wom = \dots$ ”. The intermittency of the velocity waveform is also detected and saved into the folder (27).

In order to evaluate $\bar{U}_{m,ta}$, $|\bar{U}_{m,os,1}|$, Re_{ta} and Re_{os} by means of the *Second Method*, the preliminaries are performed in *Preliminary of Second Method.vi* (28). In this subvi, [14x5001] matrix form is constructed. All $U(r,t)$ data at all radial positions of the hotwire probe are recorded to the corresponding row in this matrix.

In the second part of the *Flat Sequence Structure*, the post-processing and saving of the waveform charts and graphs are carried out. In order to calculate the mean value of time averaged and oscillating component of velocity through cross-section of the pipe, $\bar{U}_{m,ta}$ and $|\bar{U}_{m,os,1}|$, two different methods are used in the program. In the first method, each time averaged and oscillating component of velocity, \bar{U}_{ta} and $|\bar{U}_{os,1}|$ are evaluated at each radial position of the hotwire probe through the cross-section of the pipe. \bar{U}_{ta} and $|\bar{U}_{os,1}|$ distributions are then plotted separately with

respect to the corresponding radial positions and curve fittings are applied for both \bar{U}_{ta} and $|\bar{U}_{os,1}|$ distributions. Using the equation of $Q = 2\pi \int_0^R u(r)rdr$, the curves are integrated and then, $\bar{U}_{m,ta}$ and $|\bar{U}_{m,os,1}|$ are evaluated using the expression of $\bar{U}_m = Q / \pi R^2$. The curve fitting to each plot is performed in *First Method (Determination of $\bar{U}_{m,ta}$ and $\bar{U}_{m,os}$).*vi (29). Hence Re_{ta} and Re_{os} are calculated in the same subvi (29). The velocity amplitude ratio, A_1 , is also evaluated by the definition of $A_1 = |\bar{U}_{m,os,1}| / \bar{U}_{m,ta}$.

In *First Method (Determination of $\bar{U}_{m,ta}$ and $\bar{U}_{m,os}$).*vi, the palettes of *Index Array, Real/Imaginary To Complex, Build Cluster Array* and *Insert Into Array*, and the subvis of *General Polynomial Fit.vi, Ramp Pattern.vi, Polynomial Evaluation.vi* and *1D Numeric Integration.vi* are used in order to construct the cross-sectional \bar{U}_{ta} and $|\bar{U}_{os,1}|$ distributions, to fit curves for these distributions and to evaluate the equations of these curve fits. *Transpose 2D Array* palettes are used to adjust the axes of the graphs of the distributions.

Using $\bar{U}_{m,ta}$ and $|\bar{U}_{m,os,1}|$, the theoretical mean velocity distribution, $\bar{U}_m(t)$ is also expressed by using Eq. (2.19) (30). The theoretical $\Delta\bar{P}(t)/L$ is also expressed using the evaluated values of $\Delta\bar{P}_{ta}/L$ and $|\Delta\bar{P}_{os,1}|/L$ (31). Then, the evaluated waveforms of $\bar{U}_m(t)$ and $\Delta\bar{P}(t)/L$ theoretically are compared with their experimental waveforms in the same graph (32). They found to be in a good conformity with mean deviations of $\pm 1.5\%$ and $\pm 3\%$, respectively.

The local velocity waveforms at each 13 radial position for one period are plotted in the velocity graphs as a group plot and separate plots (33). The positive and negative peak values of the velocity waveform and their normalized values are also determined and evaluated in *Positive Negative Values.vi* (34).

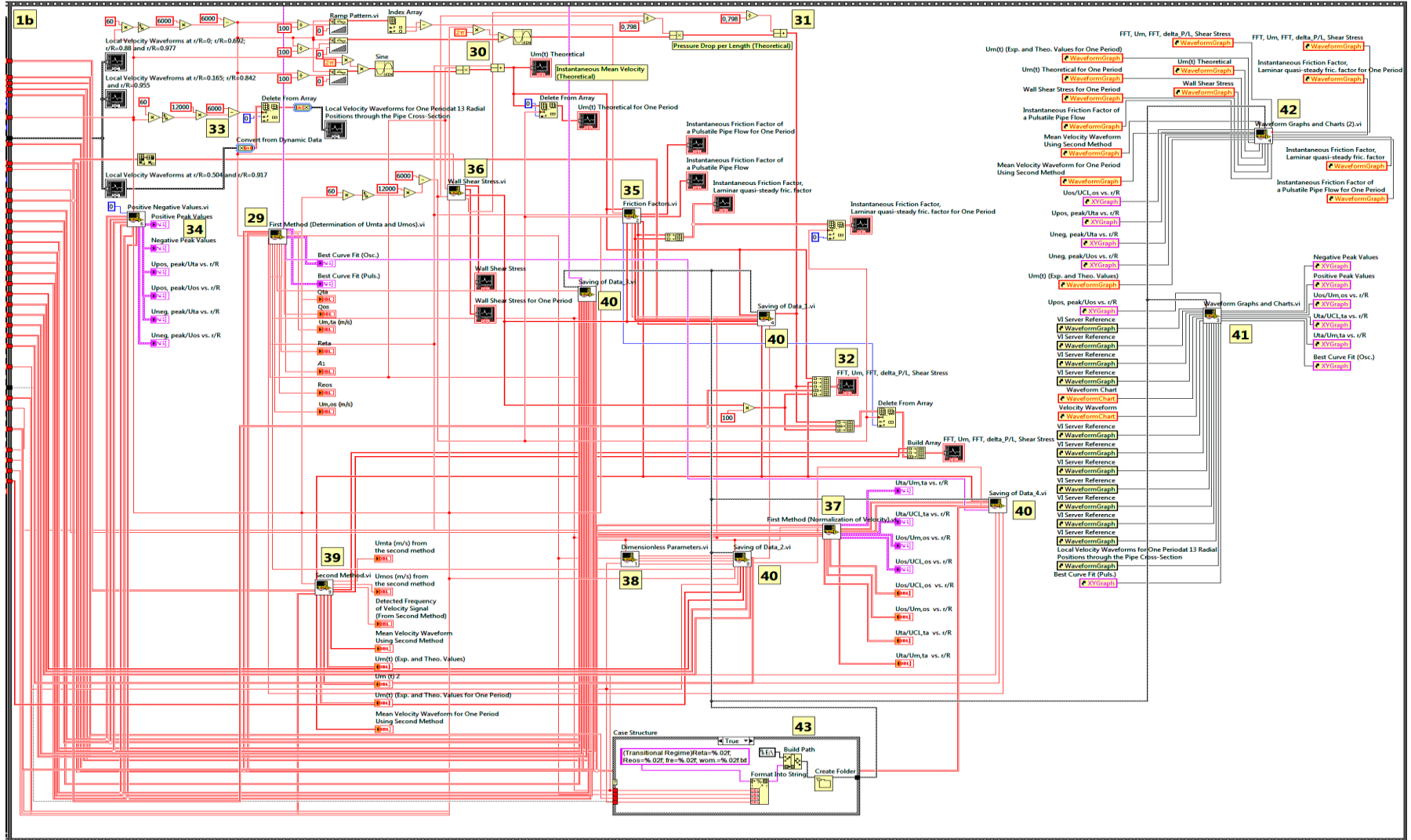


Figure 4.6b. The second part of the block diagram of *TDFC.vi* (The second part of the *Flat Sequence Structure*)

All data of $\lambda_u(t)$, $\lambda_{u,ta}$, $\lambda_{qL}(t)$ and λ_{sL} are evaluated and the results are plotted in the waveform graphs in *Friction Factors.vi* (35). $\lambda_u(t)$ and $\lambda_{qL}(t)$ are plotted together for comparison.

The instantaneous wall shear stress, $\bar{\tau}_w(t)$ is evaluated by substituting the evaluated values of $\Delta\bar{P}(t)/L$ and $d\bar{U}_m(t)/dt$ into the well-known momentum-integral equation and the results are plotted in the waveform graph in *Wall Shear Stress.vi* (36). The evaluated values of \bar{U}_{ta} and $|\bar{U}_{os,1}|$ values by using the *First Method* are normalized with $\bar{U}_{m,ta}$ and $|\bar{U}_{m,os,1}|$, $\bar{U}_{CL,ta}$ and $|\bar{U}_{CL,os,1}|$ and their results are plotted in the graphs (37). The dimensionless parameters of ω' , S , δ_s and Re_{δ_s} are evaluated in *Dimensionless Parameters.vi* (38).

In the *Second Method*, the $\bar{U}(t)$ values of the cycle for each phase at 13 different radial positions of the pipe are firstly saved as a matrix form and the cross sectional mean velocity, $\bar{U}_m(t)$, for each phase of the cycle are then evaluated by numerically integrating the ensemble averaged data over the cross section of the pipe by using the well-known Simpson's rule in the program. Then the evaluated $\bar{U}_m(t)$ is approximated in the program by the finite Fourier series expansion using Eq. (2.19). Using the *Second Method*, $\bar{U}_{m,ta}$ and $|\bar{U}_{m,os,1}|$ and f values are then determined in *Second Method.vi* (39). These values are then compared with those obtained using the first method and a good conformity is found with $\pm 0.2\%$ mean deviation for $\bar{U}_{m,ta}$, $\pm 1.1\%$ mean deviation for $|\bar{U}_{m,os,1}|$ and $\pm 0\%$ mean deviation for f .

While saving data into the file, some structures are used. *Write to Text File* and *Array To Spreadsheet String* structures are used in order to write data into the file. In order to write data into the corresponding file in rows and columns, *Insert Into Array*, *Build Array*, *Replace Array Subset* and *Delete From Array* palettes are used in the block diagram of *TDFC.vi*. In order to give headings for each column in the text file, *Concatenate Strings* palette is used in the block diagram. In order to save the file into the specified part of the PC, *Build Path* palette is used. *Format Into*

String palette is used in the block diagram to name the file with evaluated Re_{ta} and Re_{os} values.

All these evaluated values of $\lambda_u(t)$, $\lambda_{u,ta}$, $\lambda_{qL}(t)$, λ_{sL} , $\bar{\tau}_w(t)$ and also $\bar{U}_{m,ta}$, $|\bar{U}_{m,os,1}|$ and f values evaluated by both *First* and *Second Method* are saved into the corresponding file (40). All waveform graphs and charts plotted in both first and second part of *Flat Sequence Structure* (1a, 1b) are saved into the file using the subvis of *Waveform Graphs and Charts.vi* (41) and *Waveform Graphs and Charts (2).vi* (42). *Export Image* as an *Invoke Node* is used for this purpose. In the prepared program, the transition to turbulence is also detected in *Case Structure* (5). The details of the transition to turbulence detection method used in the *TDFC.vi* are given in the next chapters.

As a last operation, all data, their corresponding charts and graphs are saved into the one file which is named automatically as “(Transitional Regime) $Re_{ta}=\dots$; $Re_{os}=\dots$; $fre=\dots$; $wom=\dots$ ” if the transition to turbulence is detected at any radial positions of the probe. If not, the file name is given as only “ $Re_{ta}=\dots$; $Re_{os}=\dots$; $fre=\dots$; $wom=\dots$ ” (43). So, there will be no confusion and it will be easy to find the results in the PC by looking at the file name.

4.6.3. Graphical representations of sample plots generated by *TDFC.vi*

In this section, the graphical outputs of *TDFC.vi* as a result of the acquiring and processing data in pulsatile pipe flow are given in sample two runs; one corresponding to laminar pulsatile pipe flow regime with $Re_{ta}=2160$, $Re_{os}=832$, $\sqrt{\omega'}=17.22$ and $A_1=0.39$, the other corresponding to transitional pulsatile pipe flow regime with $Re_{ta}=3018$, $Re_{os}=1610$, $\sqrt{\omega'}=2.72$ and $A_1=0.53$.

As first plots, the local velocity waveforms for different r/R at $Re_{ta}=2160$, $Re_{os}=832$, $\sqrt{\omega'}=17.22$ and $A_1=0.39$ are seen in Fig. 4.7.

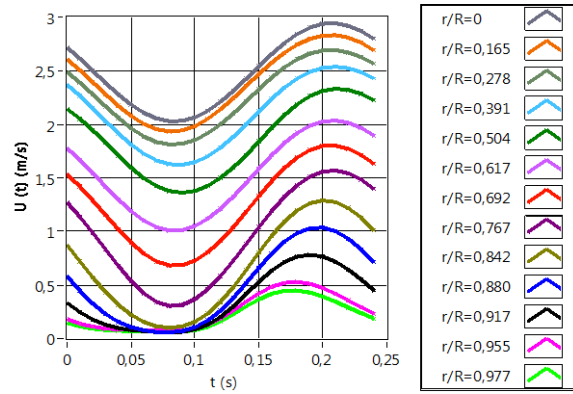


Figure 4.7. Velocity waveforms at different r/R at $Re_{ta}=2160$, $Re_{os}=832$, $\sqrt{\omega'}=17.22$ and $A_1=0.39$

The local velocity waveforms are seen to be quite regular and there is no perturbation on the waveforms, which give an idea of flow regime being laminar. However, when the similar plot at $Re_{ta}=3018$, $Re_{os}=1610$, $\sqrt{\omega'}=2.72$ and $A_1=0.53$ is observed, the disturbances on the velocity waveforms are seen (Fig. 4.8). These disturbances, circled in red on the plots, indicate that laminar to turbulent transition starts. As can be seen from Fig. 4.8, the transition to turbulence starts at the end of the decelerating phase of the waveform and then the relaminarization occurs during the accelerating and at the beginning of the decelerating phases.

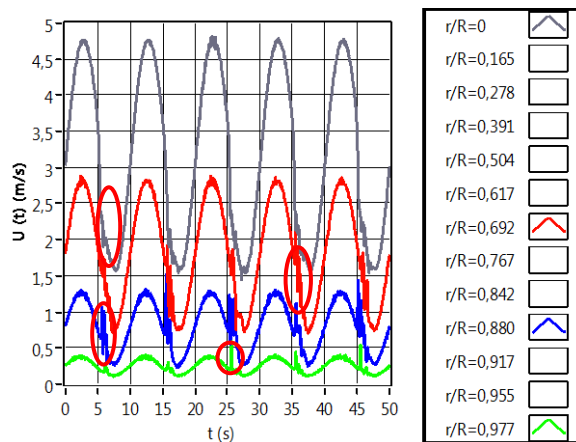


Figure 4.8. Velocity waveforms at different r/R at $Re_{ta}=3018$, $Re_{os}=1610$, $\sqrt{\omega'}=2.72$ and $A_1=0.53$

The velocity waveforms at $r/R=0$ (pipe centerline) and $r/R=0.977$ (near the pipe wall) at $Re_{ta}=2160$, $Re_{os}=832$, $\sqrt{\omega'}=17.22$ and $A_1=0.39$ are recorded at any instant and saved into the file by means of prepared program, *TDFC.vi* as can be seen from Figs. 4.9 and 4.10, respectively.

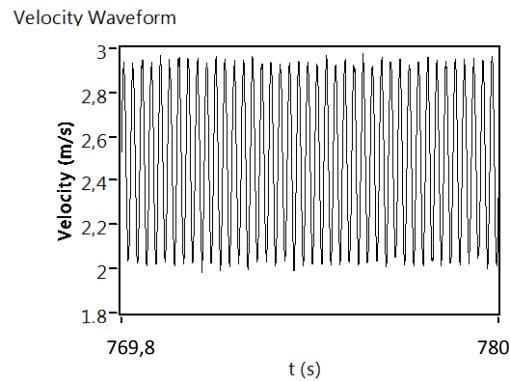


Figure 4.9. Velocity waveforms at $r/R=0$ at $Re_{ta}=2160$, $Re_{os}=832$, $\sqrt{\omega'}=17.22$ and $A_1=0.39$

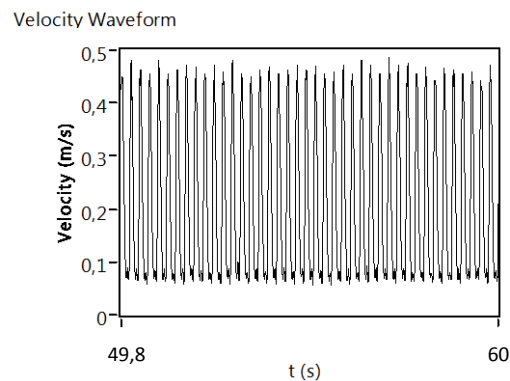


Figure 4.10. Velocity waveforms at $r/R=0.977$ at $Re_{ta}=2160$, $Re_{os}=832$, $\sqrt{\omega'}=17.22$ and $A_1=0.39$

It is observed that the velocity waveforms are very regular and there is no disturbances when compared with those related to $Re_{ta}=3018$, $Re_{os}=1610$, $\sqrt{\omega'}=2.72$ and $A_1=0.53$, which are given in Figs. 4.11 and 4.12.

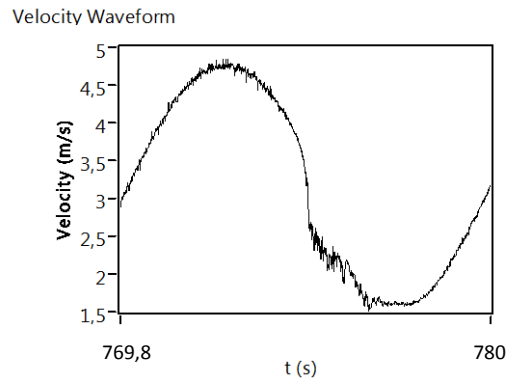


Figure 4.11. Velocity waveforms at $r/R=0$ at $Re_{ta}=3018$, $Re_{os}=1610$, $\sqrt{\omega'}=2.72$ and $A_1=0.53$

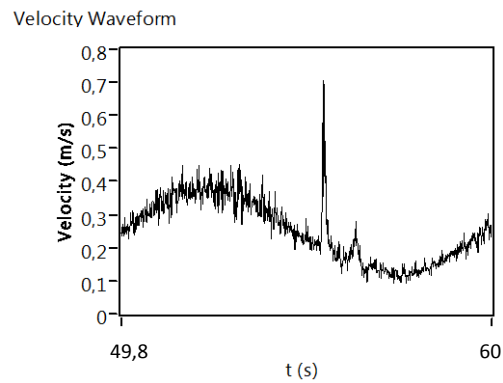


Figure 4.12. Velocity waveforms at $r/R=0.977$ at $Re_{ta}=3018$, $Re_{os}=1610$, $\sqrt{\omega'}=2.72$ and $A_1=0.53$

The transition to turbulence in the decelerating phase is seen clearly in Figs. 4.11 and 4.12. But, there is a difference between these disturbances such that the behavior of the disturbance on the waveform at the pipe centerline is like a collapse; however, the disturbance seems as a sudden peak on the waveform taken at $r/R=0.977$. These behaviors are generally common for all runs. The transitional regime at $Re_{ta}=3018$, $Re_{os}=1610$, $\sqrt{\omega'}=2.72$ and $A_1=0.53$ at $r/R=0.977$ can also be observed in another figure generated by *TDFC.vi*, Fig. 4.13.

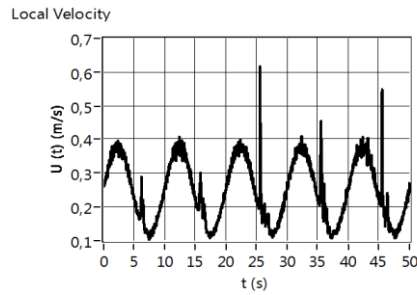


Figure 4.13. Velocity waveforms at $r/R=0.977$ at $Re_{ta}=3018$, $Re_{os}=1610$, $\sqrt{\omega'}=2.72$ and $A_1=0.53$

The laminar to turbulent transition can be seen once more in Fig. 4.14 at the same locations of the decelerating phases. As can be seen from the figure, the behaviors of the transition to turbulence at $r/R=0.977$, 0.955, 0.917, 0.880, 0.842, 0.767, 0.692 and 0.617 look like sudden peaks, however, those seem to be collapses at the positions nearer to the pipe centerline.

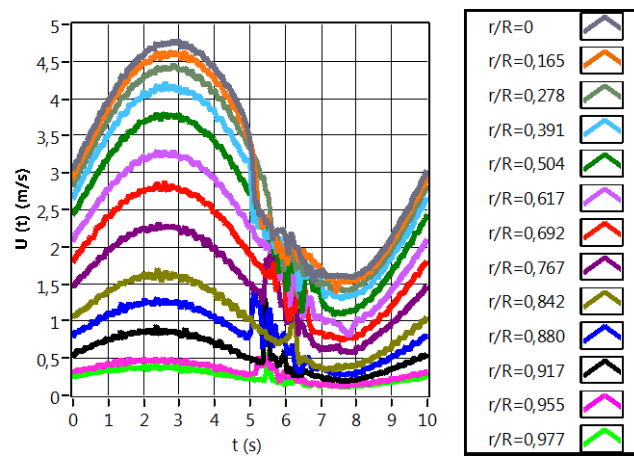


Figure 4.14. Velocity waveforms at all r/R for one period at $Re_{ta}=3018$, $Re_{os}=1610$, $\sqrt{\omega'}=2.72$ and $A_1=0.53$

Besides the velocity waveforms, it is also necessary to investigate the pressure waveforms. In this respect, the *TDFC.vi* analyzes and saves all pressure data and pressure waveform plots. The one-period pressure waveforms for both runs are illustrated in Figs. 4.15. and 4.16. The pressure waveforms in Fig. 4.15 are seen to be

quite regular and their magnitudes tend to decrease at downstream locations. However, the pressure waveforms which belong to the transitional regime in Fig. 4.16 are not seen to be regular. There are some swashes on the waveform due to flow being transitional.

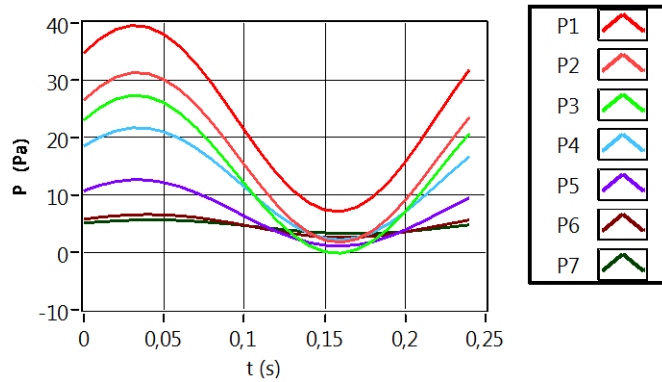


Figure 4.15. Pressure waveforms for 7 pressure transmitters at $Re_{ta}=2160$, $Re_{os}=832$, $\sqrt{\omega'}=17.22$ and $A_1=0.39$

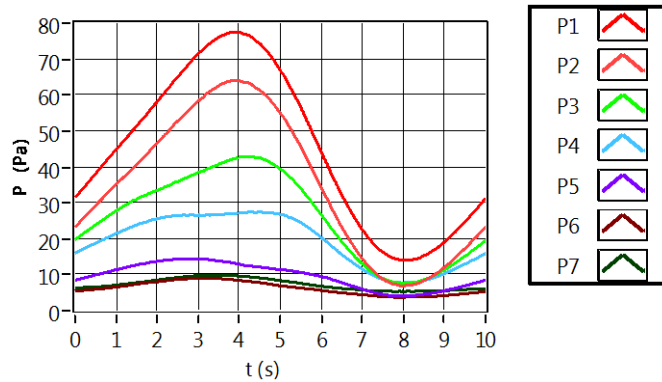


Figure 4.16. Pressure waveforms for 7 pressure transmitters at $Re_{ta}=3018$, $Re_{os}=1610$, $\sqrt{\omega'}=2.72$ and $A_1=0.53$

\bar{U}_{ta} and $|\bar{U}_{os,1}|$ distributions with r , using the *First Method* aforementioned in the previous section, are plotted in Figs. 4.17 and 4.18 for both runs.

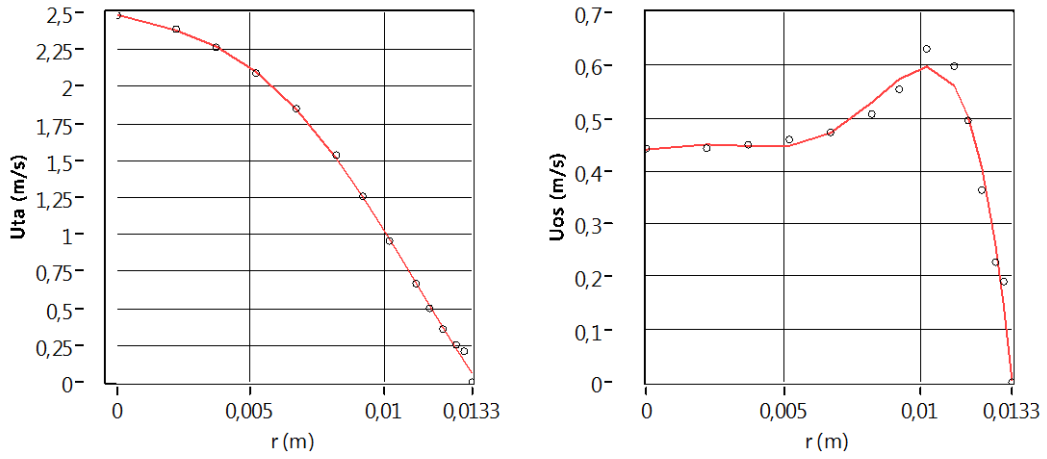


Figure 4.17. \bar{U}_{ta} and $|\bar{U}_{os,1}|$ distributions at $Re_{ta}=2160$, $Re_{os}=832$, $\sqrt{\omega'}=17.22$ and $A_1=0.39$

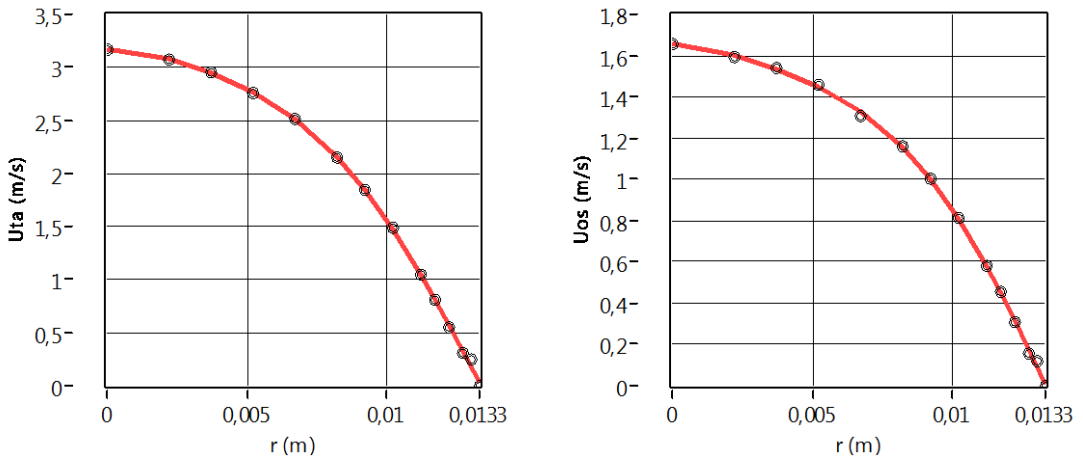


Figure 4.18. \bar{U}_{ta} and $|\bar{U}_{os,1}|$ distributions at $Re_{ta}=3018$, $Re_{os}=1610$, $\sqrt{\omega'}=2.72$ and $A_1=0.53$

The values of the normalized velocities of $\bar{U}_{ta} / \bar{U}_{m,ta}$ and $\bar{U}_{ta} / \bar{U}_{CL,ta}$ are plotted with respect to r/R in Figs. 4.19 and 4.20.

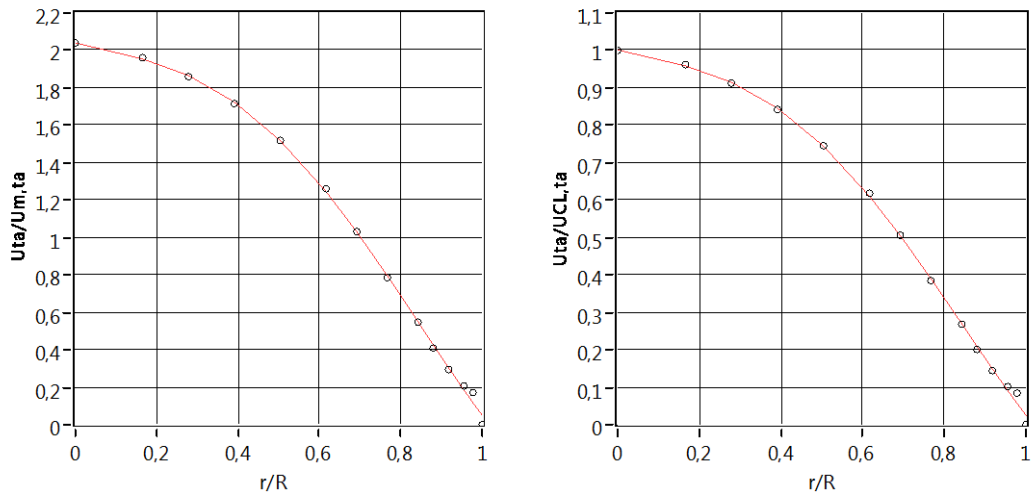


Figure 4.19. $\bar{U}_{ta}/\bar{U}_{m,ta}$ and $\bar{U}_{ta}/\bar{U}_{CL,ta}$ distributions with r/R at $Re_{ta}=2160$,
 $Re_{os}=832$, $\sqrt{\omega'}=17.22$ and $A_1=0.39$

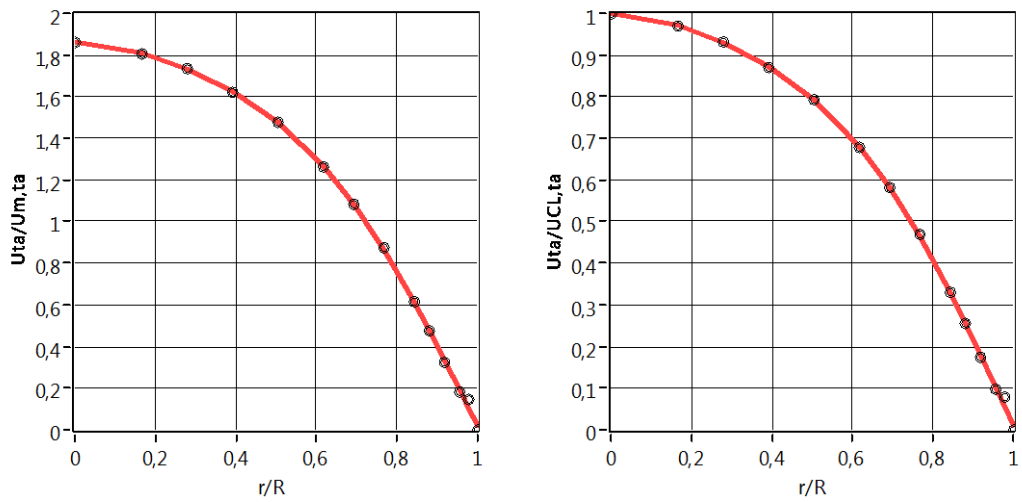


Figure 4.20. $\bar{U}_{ta}/\bar{U}_{m,ta}$ and $\bar{U}_{ta}/\bar{U}_{CL,ta}$ distributions with r/R at $Re_{ta}=3018$,
 $Re_{os}=1610$, $\sqrt{\omega'}=2.72$ and $A_1=0.53$

As seen from Fig. 4.19, $\bar{U}_{ta} / \bar{U}_{m,ta}$ value at the pipe centerline ($r/R=0$) is very close to 2 which denotes that the flow is laminar according to the steady state pipe flow approach. But, for the second run which is transitional regime, $\bar{U}_{ta} / \bar{U}_{m,ta}$ value is near 1.85 at the pipe centerline as seen in Fig. 4.20. For $f \geq 0.6$ Hz, the $|\bar{U}_{os,1}|$ distribution becomes very different than usual in steady flow. The $|\bar{U}_{os,1}|$ distribution is in excellent agreement with the theoretical laminar theory for $|\bar{U}_{os,1}|$ which is also given in the paper of Ohmi et al. (1982) as follows;

$$|\bar{U}_{os,1}| = \frac{1}{\rho_0 \omega} \frac{|\Delta \bar{P}_{os,1}|}{L} \sqrt{1 + \left\{ \frac{M_0(r' \sqrt{\omega'})}{M_0(\sqrt{\omega'})} \right\}^2 - 2 \frac{M_0(r' \sqrt{\omega'})}{M_0(\sqrt{\omega'})} \cos \{ \theta_0(r' \sqrt{\omega'}) - \theta_0(\sqrt{\omega'}) \}} \quad (4.23)$$

where $M_0(\sqrt{\omega'})$ and $\theta_0(\sqrt{\omega'})$ are the modulus and phase of the first kind Bessel function of zeroth order, $J_0(i^{3/2} \sqrt{\omega'})$, respectively.

As seen in Fig. 4.17 which belong to $f=4$ Hz, $|\bar{U}_{os,1}|$ begins to increase towards the pipe centerline until $r=0.0102$ m, and then begins to decrease to some value until $r=0.0052$ m, and then maintain its magnitude constant. This behavior is generally seen in the $|\bar{U}_{os,1}|$ distribution for $f \geq 0.6$ Hz. This behavior are also seen for normalized values of $|\bar{U}_{os,1}| / |\bar{U}_{m,os,1}|$ and $|\bar{U}_{os,1}| / |\bar{U}_{CL,os,1}|$ for $f=4$ Hz ($\sqrt{\omega'} = 17.22$) in Fig. 4.21 although it is not seen for $f=0.1$ Hz ($\sqrt{\omega'} = 2.72$) in Fig. 4.22.

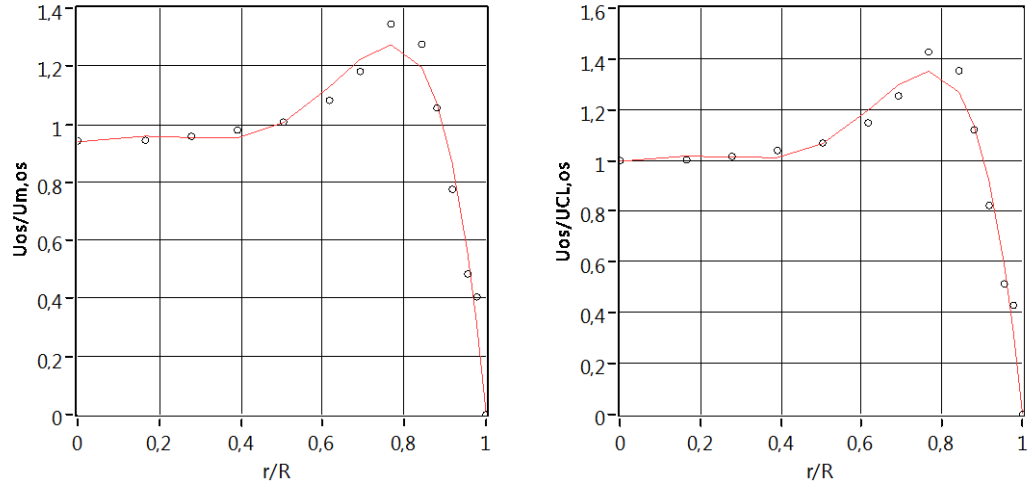


Figure 4.21. $|\bar{U}_{os,1}|/|\bar{U}_{m,os,1}|$ and $|\bar{U}_{os,1}|/|\bar{U}_{CL,os,1}|$ distributions with r/R at $Re_{ta}=2160$, $Re_{os}=832$, $\sqrt{\omega'}=17.22$ and $A_1=0.39$

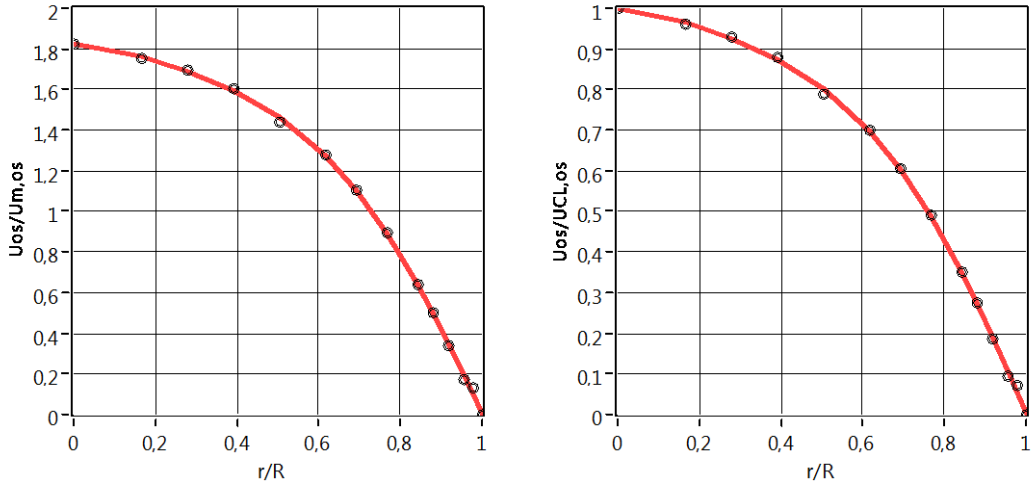


Figure 4.22. $|\bar{U}_{os,1}|/|\bar{U}_{m,os,1}|$ and $|\bar{U}_{os,1}|/|\bar{U}_{CL,os,1}|$ distributions with r/R at $Re_{ta}=3018$, $Re_{os}=1610$, $\sqrt{\omega'}=2.72$ and $A_1=0.53$

The one-period variations of $\bar{U}_m(t)$, $\Delta\bar{P}/L(t)$ with their FFT approximations and $\bar{\tau}_w(t)$ for both runs are given in Figs. 4.23 and 4.24.

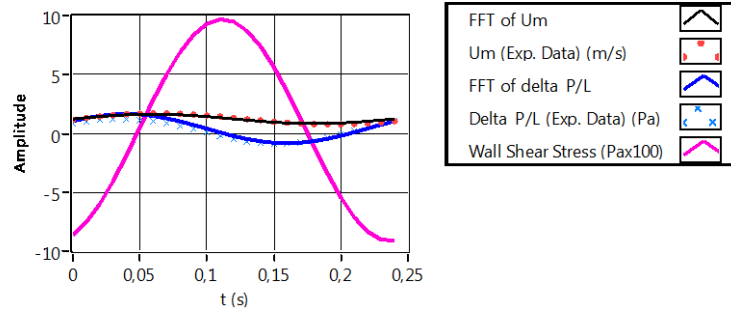


Figure 4.23. Combined graphical representation of $\bar{U}_m(t)$, $\Delta\bar{P}/L(t)$ with their FFT approximations and $\bar{\tau}_w(t)$ at $Re_{ia}=2160$, $Re_{os}=832$, $\sqrt{\omega'}=17.22$ and $A_1=0.39$

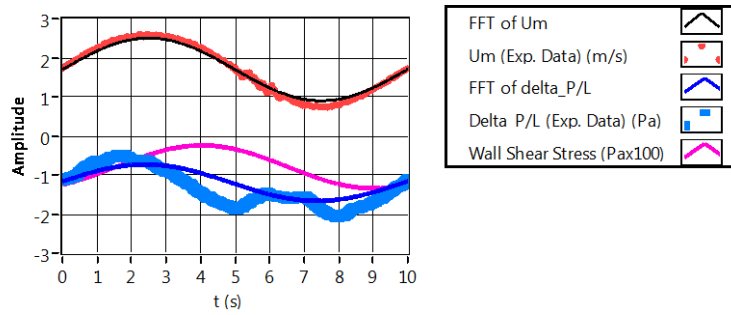


Figure 4.24. Combined graphical representation of $\bar{U}_m(t)$, $\Delta\bar{P}/L(t)$ with their FFT approximations and $\bar{\tau}_w(t)$ at $Re_{ia}=3018$, $Re_{os}=1610$, $\sqrt{\omega'}=2.72$ and $A_1=0.53$

As seen in Fig. 4.23, the experimental data do not deviate from their FFT approximations for both $\bar{U}_m(t)$ and $\Delta\bar{P}/L(t)$ for $Re_{ia}=2160$, $Re_{os}=832$, $\sqrt{\omega'}=17.22$ and $A_1=0.39$ due to the flow being laminar. However, when the laminar to turbulence transition occurs, as can be seen for the run at $Re_{ia}=3018$, $Re_{os}=1610$, $\sqrt{\omega'}=2.72$ and $A_1=0.53$, some deviations between the experimental data and their FFT approximations are observed (Fig. 4.24). The laminar to turbulent transition can also be observed in the decelerating phase of experimental $\bar{U}_m(t)$ data in Fig. 4.24.

The variations of $\lambda_u(t)$ and $\lambda_{qL}(t)$ are seen together for both runs in Figs. 4.25 and 4.26. There are big differences between these two types of friction factors. As a deduction, it can be said that not only $f=4$ Hz but also $f=0.1$ Hz cannot be classified as quasi-steady regime.

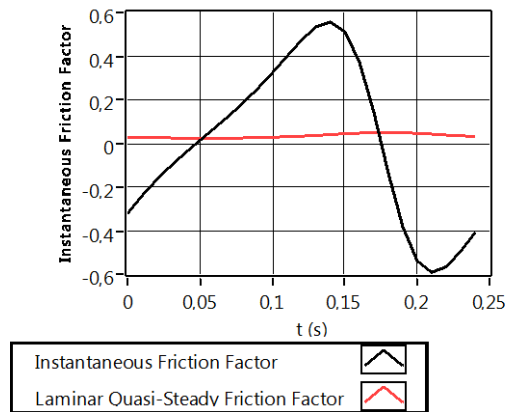


Figure 4.25 Comparison of $\lambda_u(t)$ and $\lambda_{qL}(t)$ at $Re_{ta}=2160$, $Re_{os}=832$, $\sqrt{\omega'}=17.22$ and $A_1=0.39$

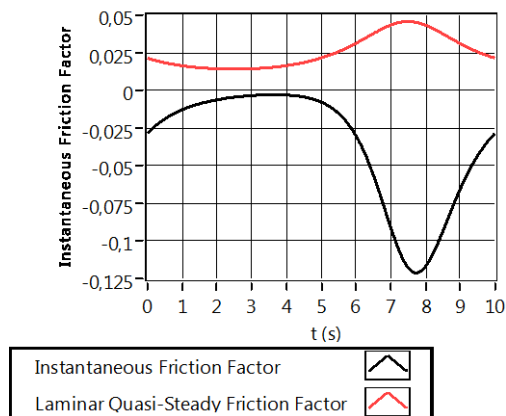


Figure 4.26 Comparison of $\lambda_u(t)$ and $\lambda_{qL}(t)$ at $Re_{ta}=3018$, $Re_{os}=1610$, $\sqrt{\omega'}=2.72$ and $A_1=0.53$

4.7. Conclusions

In this chapter, the data accumulation and processing techniques used in the experimental set-up are presented. The devised program in LabView 2009SP1[®] environment for pulsatile flow measurement and control is presented. The data processing and the experimental processing procedure are given in details verifying the accuracy of the experimental set-up. The sample plots for two runs without a detailed discussion on flow dynamics are given to clarify and verify the applicability of the devised program, *TDFC.vi* for both laminar and transitional regime. These plots are directly as the outputs of the devised program, *TDFC.vi*. To generate these plots, *TDFC.vi* makes lots of analyses and evaluations in itself. All evaluations, analyses, graphs and charts can be obtained immediately when the END ACQUISITION button is clicked on. Hence all difficulties and weary processes to analyze and process the raw data are eliminated with saving time. Besides this, the accurate and precision measurements and analyses are handled by means of the automatically controlled program without any human error. The uncertainties of the set-up can be found in the next chapter.

The designed program, *TDFC.vi* and the used methodology contribute to the literature as a new and original insight. The program has an ability (i) to trigger the MFC unit and control the measurement devices, (ii) to acquire and acquire the data from the measurement devices, (iii) to process, analyze and post-process the data, (iv) to plot the necessary charts and graphs and (v) to save all data and their corresponding results as processed data, charts and graphs into the specified file.

CHAPTER 5

CHARACTERISTICS OF FLOW FIELD IN TERMS OF PRELIMINARY TESTS AND UNCERTAINTY ANALYSIS OF THE MEASUREMENTS

5.1. Introduction

Pulsatile flow in sinusoidal waveform is generated by the MFC unit by means of the devised program, *TDFC.vi*. Before the velocity measurement in the experimental study, it is essential to determine the characteristics of velocity profile at the measurement station for both steady and pulsatile flows. The uncertainty analysis of the whole experimental set-up is also performed before and during the experimental study.

5.2. Character of Steady Velocity Profile

5.2.1. Symmetricity of velocity field

The flow through the pipeline is a two-dimensional flow with angular symmetry along the axis of the pipe. The angular symmetry of the steady flow at $X/D=75$, $X/D=375$, at the measurement station, $X/D=604$ and at $X/D=680$ is controlled. Velocity measurements are performed at 19 different radial positions through the pipe cross-section for 48 different runs without and with flow conditioners. Figures 5.1 and 5.2 illustrate the symmetricity of the radial distributions of the axial velocity for different Reynolds numbers and at different X/D for $Re=2000$, respectively.

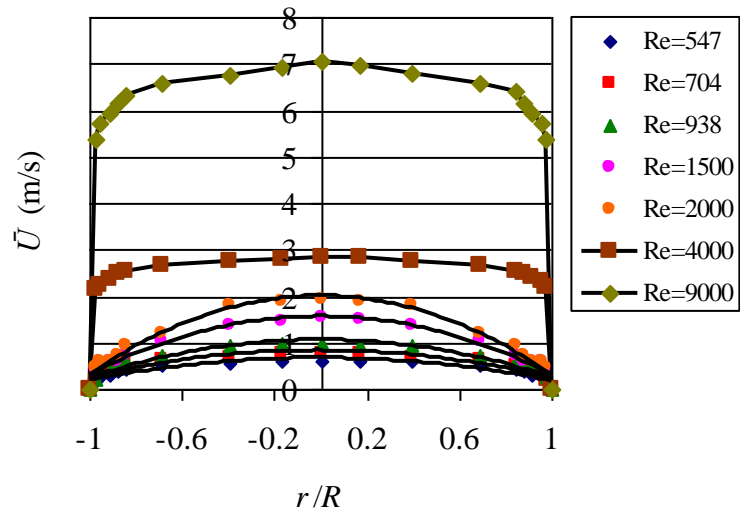


Figure 5.1. Velocity profiles at velocity measurement station ($X/D=604$) for different Reynolds numbers

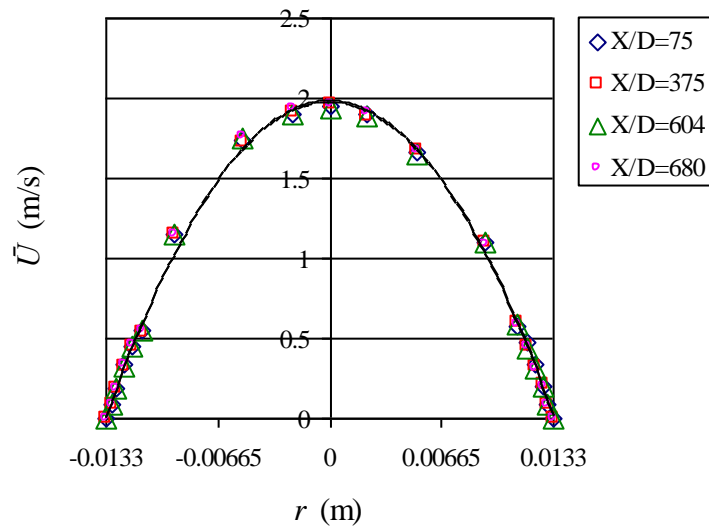


Figure 5.2. Velocity profiles for $Re=2000$ at four different X/D locations along the pipeline

5.2.2. Hydrodynamic development

In pipe flows, the distance between the pipe entrance and the location where the boundary layer reaches the pipe centerline is defined as the pipe entrance length or hydrodynamic entrance length. The region at downstream of the pipe entrance

length is invariant with distance along the pipeline. Hence the flow becomes fully developed behind the pipe entrance length. The measurement station $X/D=604$ is in the fully developed region for both laminar and turbulent pulsatile pipe flow regimes. Hence the velocity measurements are performed for laminar and transitional pulsatile pipe flow in the fully developed region. The development of the velocity field at the measurement station of $X/D=604$ is checked by axial velocity measurements carried out for 10 different Re number and 19 radial positions of the hotwire probe through the pipe cross-section, Figure 5.3.

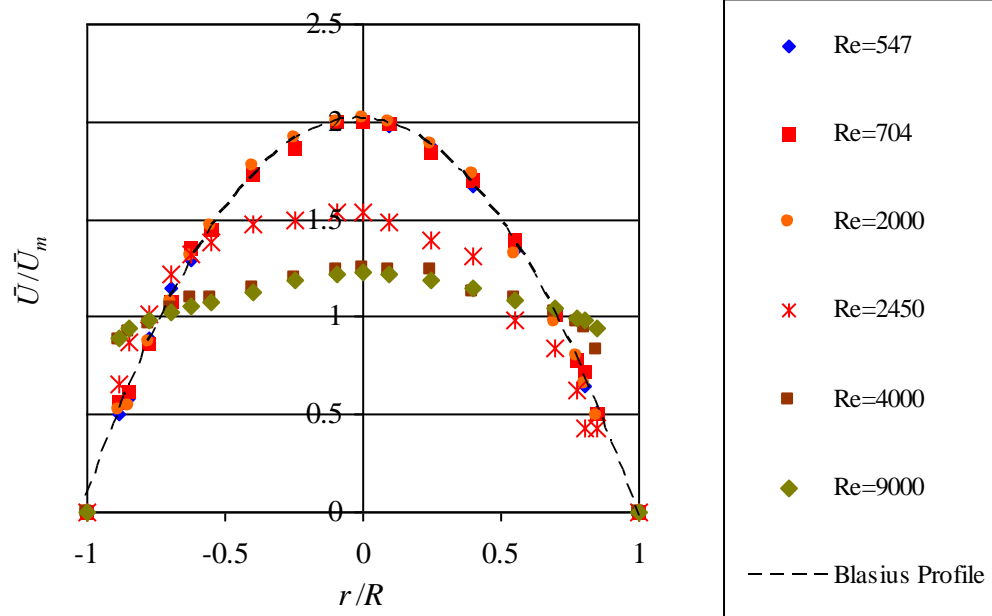


Figure 5.3. Velocity profiles for 10 different Re at velocity measurement station, $X/D=604$

It can be seen from the figure that the velocity profiles for $Re < 2450$ show the same character with the well-known Blasius's parabolic velocity profile $\bar{U}/\bar{U}_m = 2[1 - (r/R)^2]$ with a maximum deviation of $\pm 2\%$. The velocity profiles for $Re \geq 2450$ show a dramatic change from the parabolic velocity profile reaching to the Prandtl's one-seventh power law $\bar{U}/\bar{U}_m = 1.2245[1 - (r/R)]^{1/7}$ with a maximum deviation of $\pm 3\%$. As a result of the preliminary tests, it is deduced that the fully

developed flow regimes for steady state are satisfied at the velocity measurement station. In pulsatile pipe flow measurements, the development length becomes smaller than that for steady flow conditions such as $L_{e_{pulsatile}} / L_{e_{steady}} < 1$ declared in the literature (Durst et al., 2005). Hence the velocity measurement station, $X/D=604$ is also suitable for pulsatile velocity measurements.

5.3. Uncertainty Analysis

In the present study, the uncertainty analysis is also performed to verify the validity of the experimental measurements and the results in the covered ranges. An uncertainty may originate from causes such as the lack of accuracy in measurement equipment, random variation in the measurands and approximations in data reduction relations. An uncertainty is not same as an error. An error in a measurement is difference between true value and recorded value. An uncertainty is a possible value that an error might take on in a given measurement (Coleman and Steele 1989; Wheeler and Ganji 1996).

All uncertainty estimates in the experiment are made to the same confidence level of 95%. For general uncertainty analysis, the well-known equation can be used as follows;

$$w_R = \left[\sum_{i=1}^J \left(w_{x_i} \frac{\partial \bar{R}}{\partial x_i} \right)^2 \right]^{1/2} \quad (5.1)$$

For the detailed uncertainty analysis, the bias and the precision errors in each measured variable are considered. So, the standard deviation, precision limit, standard deviation of the mean and precision limit of the mean are used respectively as follows;

$$S_x = \left[\frac{\sum_{i=1}^J (x_i - \bar{x})^2}{J - 1} \right]^{1/2} \quad (5.2)$$

$$P_{x_i} = tS_{x_i} \quad (5.3)$$

$$S_{\bar{x}} = \frac{S_x}{\sqrt{J}} \quad (5.4)$$

$$P_{\bar{x}} = tS_{\bar{x}} \quad (5.5)$$

According to the ANSI/ASME (1986), the elemental errors are grouped into three categories; calibration errors, data acquisition errors and data reduction errors. In elemental error analysis, the definitions of the bias limits and the precision indices are used respectively as follows;

$$B_x = \left(\sum_{i=1}^k B_i^2 \right)^{1/2} \quad (5.6)$$

$$S_x = \left(\sum_{i=1}^m S_i^2 \right)^{1/2} \quad (5.7)$$

The precision limit for the single measurement variable x is then obtained from;

$$P_x = tS_x \quad (5.8)$$

To determine Student's t value, Welch-Satterthwaite formula (ANSI/ASME 1986) is used as;

$$v_x = \frac{\left(\sum_{i=1}^m S_i^2 \right)^2}{\sum_{i=1}^m (S_i^4 / v_i)} \quad (5.9)$$

where v_i is the degrees of freedom associated with the individual elemental uncertainty (number of data values in the sample minus 1).

Then the uncertainty in the final result is evaluated using the following definition;

$$w_x = \left[B_x^2 + (tS_x)^2 \right]^{1/2} \quad (5.10)$$

In reference to the other method given in (Jorgensen 2002), the uncertainty analysis of the velocity measurement chain can be performed using the following definitions;

The relative standard uncertainty of a calibrator is evaluated by;

$$w_{cal} = \frac{1}{100} STDV(U_{cal}(\%)) \quad (5.11)$$

The calibrator uncertainty is often given as;

$$STDV(U_{cal}) = \pm a_{cal}(\%) + b_{cal}(m/s) \quad (5.12)$$

For pitot-static tube as a calibrator, $a_{cal} \approx \pm 1.5\%$ and $b_{cal} = 0$.

The calibration curve for a hotwire probe has also an uncertainty which is defined as linearization (conversion) uncertainty due to related curve fitting errors in calibration points. The relative standard uncertainty of linearization is calculated as follows;

$$w_{lin} = \frac{1}{100} STDV(\Delta U_{lin}(\%)) \quad (5.13)$$

The other uncertainty in velocity measurement chain is daqboard resolution uncertainty. It is evaluated as follows;

$$w_{res} = \frac{1}{\sqrt{3}} \frac{1}{U} \frac{E_{AD}}{2^{res}} \frac{\partial U}{\partial E} \quad (5.14)$$

The positioning probe uncertainty is related to alignment of a probe in an experimental set-up after calibration. Its uncertainty can be evaluated using the definition as follows

$$w_{positioning} = \frac{1}{\sqrt{3}}(1 - \cos \theta) \quad (5.15)$$

The other important parameter on the uncertainty is effect of temperature variations. The uncertainty of the temperature variation is calculated by;

$$w_{temp} = \frac{1}{\sqrt{3}} \frac{1}{U} \frac{1}{T_w - T_0} \left(\frac{A}{B} U^{-n} + 1 \right)^n \quad (5.16)$$

This estimate is based on the power law calibration function;

$$E^2 = (T_w - T_0) \left(A + B(U_{cal})^n \right) = (T_w - T_0) \left(A + B_1(\rho U)^n \right) \quad (5.17)$$

Since the velocity U_{cal} actually represents the mass flux, ρU , variations in density, ρ , with temperature is added to the uncertainty. This gives the following uncertainty as;

$$w_{density} = \frac{1}{\sqrt{3}} \Delta \rho_T = \frac{1}{\sqrt{3}} \frac{\Delta T}{273} \quad (5.18)$$

Ambient pressure changes also affect density and hence calculated velocity. Its uncertainty is evaluated as follows;

$$w_{pressure} = \frac{1}{\sqrt{3}} \left(\frac{\Delta P}{P_0 + \Delta P} \right) \quad (5.19)$$

Under normal conditions, changes in gas composition are mainly caused by changes in humidity. The influence on heat transfer is small but has an effect ($\partial U / \partial P_{wv} \approx 0.01$ per 1 kPa change in water vapor pressure P_{wv}).

$$w_{humidity} = \frac{1}{\sqrt{3}} \frac{1}{U} \frac{\partial U}{\partial P_{wv}} \Delta P_{wv} \quad (5.20)$$

5.3.1. Uncertainty analysis for velocity measurement chain

The uncertainty of the velocity measurement chain consisted of constant temperature anemometer (CTA), daqboard and calibration procedure is performed using the procedure given in (ANSI/ASME, 1986), (Coleman and Steele, 1989) and (Wheeler and Ganji, 1996). The bias error with 95% confidence level and precision error of the velocity measurement chain are identified in Table 5.1 for 4.5 m/s covering 20 tests.

Table 5.1. Uncertainty analysis of velocity measurement in the experimental study based on the method in (ANSI/ASME, 1986), (Coleman and Steele, 1989) and (Wheeler and Ganji, 1996)

Source of uncertainty	Bias Limit		Precision Index		Degrees of freedom
	%	m/s	%	m/s	#
Calibrator	1.5	0.0675	-	-	20
Linearisation	0.5	0.0225	-	-	
Daqboard Resolution	0.04	0.0018	-	-	
Temperature variations ¹⁾	-	-	0.12	0.0054	
Temperature variations ²⁾	-	-	0.2	0.009	
Ambient pressure	-	-	0.6	0.027	
Humidity	-	-	0.13	0.0059	
Uncertainty of velocity measurement; $w_U = [0.0712^2 + 0.0605^2]^{1/2} = 0.0934$ m/s (2.1%)					

¹⁾ Uncertainty due to change in probe over-temperature alone

²⁾ Uncertainty due to change in air density with temperature alone

The uncertainty of the velocity measurement is also evaluated using the procedure given in (Jorgensen, 2002). Its uncertainty is a combination of the uncertainties of the individually acquired voltages converted into velocity and the uncertainty of the statistical analysis of the velocity series. Herein, the uncertainty of the velocity measurements acquired via the daqboard from DANTEC 56C01 CTA anemometer with a 55P11 probe is introduced. DANTEC 56C01 CTA has low drift, low noise (0.02% turbulence at 10 m/s) and good repeatability so that these factors do not add significantly to the uncertainty analysis in comparison with other error

sources. The frequency noise of the anemometer is not added to the uncertainty analysis due to the frequencies in the flow below approximately 50% of the square wave generator frequency of 1 kHz. The uncertainty of the positioning probe is too small with $\Delta\theta \approx 1^\circ$. The major uncertainty of the velocity measurement belongs to the calibration of the hotwire probe. The calibrator which is a pitot-static tube has a major uncertainty of maximum $\pm 1.5\%$. In the velocity measurements, the curve fitting is found to be compatible with the velocity data with deviation of $\pm 0.5\%$. In Table 5.2, the uncertainty analysis chain from the raw velocity data in voltage to the processed velocity data in m/s is presented for $U_{\max} = 4.5$ m/s. As a result, the relative expanded uncertainty of $\pm 3\%$ is found for velocity measurement.

Table 5.2. Uncertainty analysis of velocity measurement in the experimental study based on the method in (Jorgensen, 2002)

Source of uncertainty	Input variants	Typical value	Relative output variants	Typical value	Cove- rage factor	Relative standard uncertainty
	Δx_i	Δx_i	$\frac{1}{U} \Delta y_i$	$\frac{1}{U} \Delta y_i$	k	$\frac{1}{k} \frac{1}{U} \Delta y_i$
Calibrator	ΔU_{cal}	1.5%	$2STDV(100\Delta U_{cal})$	0.03	2	0.015
Linearisation	ΔU_{lin}	0.5%	$2STDV(100\Delta U_{lin})$	0.01	2	0.005
Daqboard Resolution	$\frac{E_{AD}}{n}$	10 volts 16 bit	$\frac{1}{U} \frac{E_{AD}}{2^{res}} \frac{\partial U}{\partial E}$	0.0007	$\sqrt{3}$	0.0004
Probe positioning	θ	1°	$(1 - \cos \theta)$	0.00015	$\sqrt{3}$	≈ 0
Temperature variations ¹⁾	ΔT	1°C	$\frac{1}{U} \frac{\Delta T}{T_w - T_0} \left(\frac{A}{B} U^{-n} + 1 \right)^n$	0.0021	$\sqrt{3}$	0.0012
Temperature variations ²⁾	ΔT	1°C	$\frac{\Delta T}{273}$	0.004	$\sqrt{3}$	0.002
Ambient pressure	ΔP	1 kPa	$\left(\frac{\Delta P}{P_0 + \Delta P} \right)$	0.01	$\sqrt{3}$	0.006
Humidity	ΔP_{wv}	1 kPa	$\frac{1}{U} \frac{\partial U}{\partial P_{wv}} \Delta P_{wv}$	0.002	$\sqrt{3}$	0.0013
Relative expanded uncertainty of	$w_U = 2 \left[\sum_{i=1}^J \left(\frac{1}{k} \frac{1}{U} \Delta y_i \right)^2 \right]^{1/2} = 0.034$					3.4%

* $T_w - T_0 = 150^\circ\text{C}$, $U \approx 4.5$ m/s, $A = 2.176$, $B = 0.966$, $\partial U / \partial E = 19.83$ m/s/volt

¹⁾ Uncertainty due to change in probe over-temperature alone.

²⁾ Uncertainty due to change in air density with temperature alone.

5.3.2. Uncertainty analysis for pressure measurement chain

In the same manner, the uncertainty of pressure measurement carried out by the WIKA SL-1 pressure transmitter is evaluated using the procedure given in (ANSI/ASME, 1986), (Coleman and Steele, 1989) and (Wheeler and Ganji, 1996). The accuracy, non-linearity, non-repeatability, and one-year stability of the pressure transmitters are given as less than 0.5%, 0.2%, 0.1% and 0.3%, respectively. The bias and precision errors are given in Table 5.3 for 5 V mean reading covering 20 tests. The confidence level is taken as 95%.

Table 5.3. Uncertainty analysis of pressure measurement in the experimental study based on the method in (ANSI/ASME, 1986), (Coleman and Steele, 1989) and Wheeler and Ganji, 1996)

Source of uncertainty	Bias Limit		Precision Index		Degrees of freedom
	%	Volt	%	Volt	#
<i>Data Acquisition</i>					20
Accuracy	0.5	0.025	-	-	
Repeatability	-	-	0.1	0.005	
<i>Data Reduction</i>					
Linearity	0.2	0.01	-	-	
Stability	-	-	0.3	0.015	
Uncertainty of pressure measurement; $w_x = [0.027^2 + 0.033^2]^{1/2} = 0.043$ V (0.8%)					

In order to evaluate the mean velocities, $\bar{U}_{m,ta}$ and $|\bar{U}_{m,os,1}|$, the curve fittings are applied to the cross-sectional \bar{U}_{ta} and $|\bar{U}_{os,1}|$ distributions. The curve fits are found to be compatible with the experimental data with $\pm 1.5\%$ mean deviations. The overall uncertainty of the velocity measurement chain is previously found to be maximum $\pm 3\%$ in reference to (Jorgensen, 2002). By means of the definition of Eq. (5.1), the uncertainties of $\bar{U}_{m,ta}$, $|\bar{U}_{m,os,1}|$, Re_{ta} , Re_{os} , $\Delta\bar{P}(t)/L$, $\bar{\tau}_w(t)$ and $\lambda_u(t)$ are evaluated and the summary of the uncertainties are given in Table 5.4.

Table 5.4. Evaluated uncertainty values of the experimental study ranges

Measured/Evaluated Data in the Experiment	Unit	Overall Uncertainty
$U(r, t)$	m/s	$\pm 3\%$ ¹⁾
	m/s	$\pm 2.1\%$ ²⁾
$P(t)$	V	$\pm 0.8\%$
	Pa	$\pm 1.3\%$
$\bar{U}_{m,ta}, \bar{U}_{m,os,1} $	m/s	$\pm 3.4\%$
Re_{ta}, Re_{os}	-	$\pm 3.4\%$
$\Delta \bar{P}(t) / L$	Pa/m	$\pm 1.6\%$
$\bar{\tau}_w(t)$	Pa	$\pm 1.9\%$
$\lambda_u(t)$	-	$\pm 7.1\%$

¹⁾ Uncertainty evaluated according to the reference (Jorgensen, 2002)

²⁾ Uncertainty evaluated according to the reference (ANSI/ASME, 1986), (Coleman and Steele, 1989) and (Wheeler and Ganji, 1996)

5.4. Conclusions

As a result of the preliminary tests and improvements, it is found that the velocity profile for the covered test cases are symmetrical through the pipe cross-section and the fully developed region is satisfied at the velocity measurement station, $X/D=604$. The symmetricity without any swirl and with reduced turbulence intermittency is provided at the velocity measurement station by means of the usage of the flow conditioners. The details about the flow dynamics behind the flow conditioners, as one of the preliminary tests performed in the experimental set-up, is presented in the next chapter.

In order to verify the accurate and precision measurements and analyses, the uncertainty analyses are performed and the results are introduced in this chapter. The results of the uncertainty analyses for both velocity and pressure measurements are found to be in the acceptable ranges because the velocity and pressure measurements are handled by means of the automatically controlled program, *TDFC.vi* without any human error and with time saving. The uncertainty of the velocity measurement chain is found to be in the acceptable range of $\pm 3\%$ and $\pm 2.1\%$ according to the

references of (Jorgensen, 2002) and (Coleman and Steele, 1989), (Wheeler and Ganji, 1996), respectively. Besides, the uncertainty of the pressure measurement chain is found as $\pm 1.3\%$.

CHAPTER 6

LAMINAR FLOW CONTROL VIA UTILIZATION OF PIPE ENTRANCE INSERTS

6.1. Introduction

As a preliminary test, the laminar steady flow through the pipeline is controlled by means of the utilized pipe entrance inserts; etoile, perforated plate and tube bundle whose details are given in Çarpınlioğlu and Özahi (2011).

Since the study of Zanker (1960), there have been a lot of efforts designing variety of pipe inserts (flow conditioners) to obtain fully-developed flow in a short pipe length. Some experimental and numerical approaches can be referred herein such as Akashi et al. (1978), Laws and Chesnoy (1993), Karnik et al. (1994), Erdal et al. (1994), Laws and Quazzane (1995), Erdal (1997), Morrison et al. (1997), Zanker and Goodson (2000) and Xiong et al. (2003).

Since not only the mean profile is fully developed, it is necessary to examine the effects of turbulent stress and turbulence intensity even in cases where no deviation is observed in the mean velocity. The importance of settling length by a variety of designs inducing similar flow quality and removal of swirl together with the dependence on mean flow Reynolds number, Re are some other primary facts(Ouazzane and Barigou, 1999). It is widely accepted that an efficient flow conditioner should have small pressure losses, reduced axial dimensions and low cost.

It should also be able to minimize the disturbances. In general, while vane and tube bundle flow conditioners are effective for removing swirl, screens and perforated plate flow conditioners are well suited to the cases for which removal of the flow profile distortions are of primary importance.

In the present experimental study, flow conditioners of tube bundle, etoile and perforated plate are tested in Re range of $547 \leq \text{Re} \leq 9000$. The utilization of etoile confirmed the recent numerical study of Frattolillo and Massarotti (2002) who suggested that etoile is more efficient in terms of its minimum settling length. The cross-sectional axial velocity profiles at three downstream X/D locations behind flow conditioners are measured with pressure losses, ΔP . The methodology used for the analysis of the experimental data is presented in terms of settling length, flow uniformity, pressure loss characteristics of flow conditioners and entrance length as follows:

1) The time averaged $\Delta \bar{P}(t)$ and $\bar{U}(r,t)$ are evaluated by the devised program in LabView. The non-dimensional velocity profiles $\bar{U}/\bar{U}_{\max} = \bar{U}/\bar{U}_{\max}(r/R)$ and $\bar{U}/\bar{U}_m = \bar{U}/\bar{U}_m(r/R)$ as a function of X/D and Re are compared with theoretical Blasius velocity profile inside the so-called laminar range of flow. The comparison with Blasius profile is used as an indication of local flow homogeneity and uniformity. Furthermore a discussion on the local profiles of turbulent fluctuation velocity $u' = u'(r)$ expressed in terms of turbulence intensity $I = I(r/R)$ is referred. The root mean square value of axial component of instantaneous turbulent fluctuation and turbulence intensity are evaluated as follows;

$$u'_{rms} = \sqrt{\sum_{i=0}^{999} (u_i - \bar{u})^2 / 1000} \quad (6.1)$$

$$I = u'_{rms} / \bar{u} \quad (6.2)$$

2) The performance of flow conditioners are expressed in terms of the pressure loss coefficient K defined as;

$$K = \frac{\Delta \bar{P}}{1/2 \rho \bar{U}_m^2} \quad (6.3)$$

3) A new correlation is proposed to determine the settling distance behind the pipe entrance inserts and thereby laminar entrance length. In this respect the non-dimensional velocity parameters at two critical locations; as $r/R=0.89$ $r/R=0$ are expressed as a function of Re and X/D in this case study.

6.2. Velocity Flow Fields at Different X/D Locations

6.2.1. Flow nature without an entrance element (Case: WFC) with a comment on entrance length concept of White (1984)

The non-dimensional axial velocity profiles expressed as \bar{U}/\bar{U}_{max} are given in comparison with the well-known Blasius and Prandtl $1/7^{\text{th}}$ power law profile for laminar and turbulent flow at $X/D=680$ (Fig .6.1)

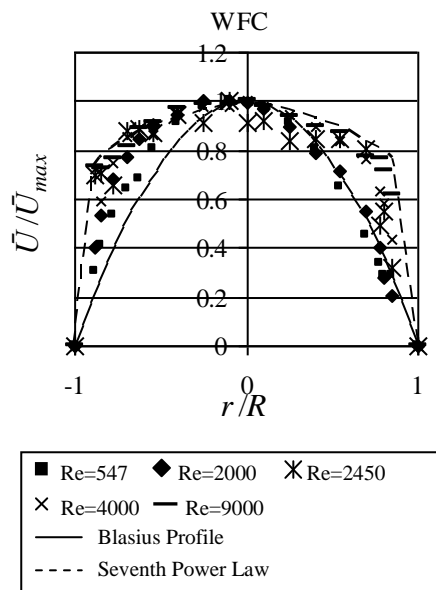


Figure 6.1. Cross-sectional velocity profiles for different Re at $X/D=680$

In the approximate range of $Re < 2450$ flow is laminar while for $Re \geq 2450$ profiles deviating considerably from Blasius profile have a better fit to Prandtl $1/7^{\text{th}}$ power law. Therefore flow is laminar for $Re < 2450$ while turbulent for $Re > 4000$ irrespective

of the measurement station. In reference to the following equation of (White, 1984) laminar entrance length L_e can be determined as:

$$L_e = 0.08D Re + 0.70D \quad (6.4)$$

As can be seen from the sample data for $Re=704$ in Fig. 6.2, the velocity profiles are under the severe influence of X/D with a questionable flow uniformity and a considerable deviation from the Blasius profile in an approximate error margin of $\pm 20\%$. As can be seen from Fig. 6.3 corresponding to the sample data taken at $X/D=75$, profiles of $I=I(r/R)$ are strong functions of cross-sectional position r/R and X/D . However the magnitudes of u'_{rms} at pipe centerline $r/R=0$ are governed by flow nature as expected (Fig. 6.4). Inside laminar flow $u'_{rms_{cl}} < 0.006$ m/s are measured for $Re < 2450$. Meanwhile a radical increase in the magnitudes of $u'_{rms_{cl}}$ is measured inside turbulent flow for $Re \geq 4000$. Therefore necessity of a flow conditioner is apparent to provide fully-developed laminar flow in the covered lengths of X/D .

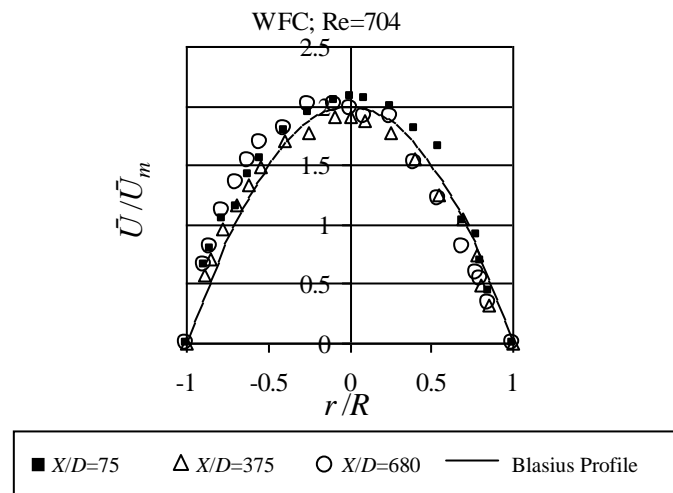


Figure 6.2. Sample non-dimensional axial velocity, \bar{U}/\bar{U}_m profiles as a function of X/D for $Re=704$ for WFC case

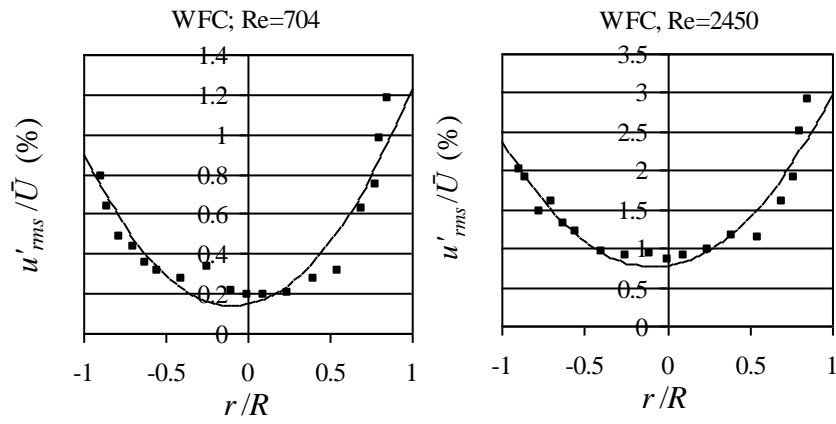


Figure 6.3. Sample turbulence intensity u'_{rms}/\bar{U} profiles for Re=704, Re=2450 at $X/D=75$ for WFC case

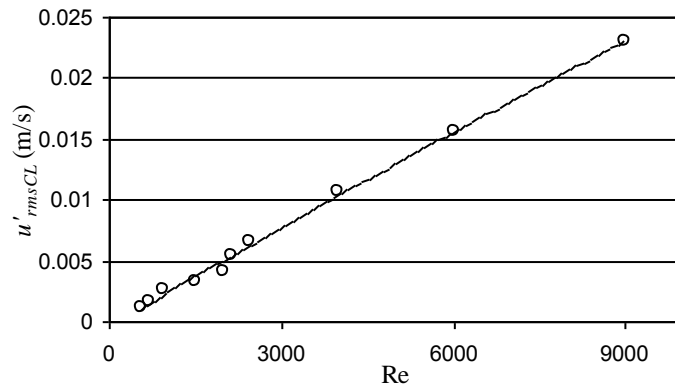


Figure 6.4. Variation of u'_{rmsCL} with Re for WFC case based on data at $X/D=680$

6.2.2. Flow field uniformity behind a variety of flow conditioners (Case: FC) as a function of Reynolds number

The sample velocity profiles in the form of $\bar{U}/\bar{U}_m(r/R)$ for Re=547, Re=704 and Re=938 measured behind utilized flow conditioners are given in Fig. 6.5. As an overall observation the velocity profiles are in a better agreement with the Blasius solution. However downstream flow field is rather sensitive to the type of flow conditioner used. The measured velocity profiles behind etoile are almost independent of X/D . Meanwhile velocity profiles behind perforated plate have a greater deviation from the Blasius profile than those of etoile. The velocity profiles

behind tube bundle have the worst fit to the Blasius profile under a pronounced influence of X/D .

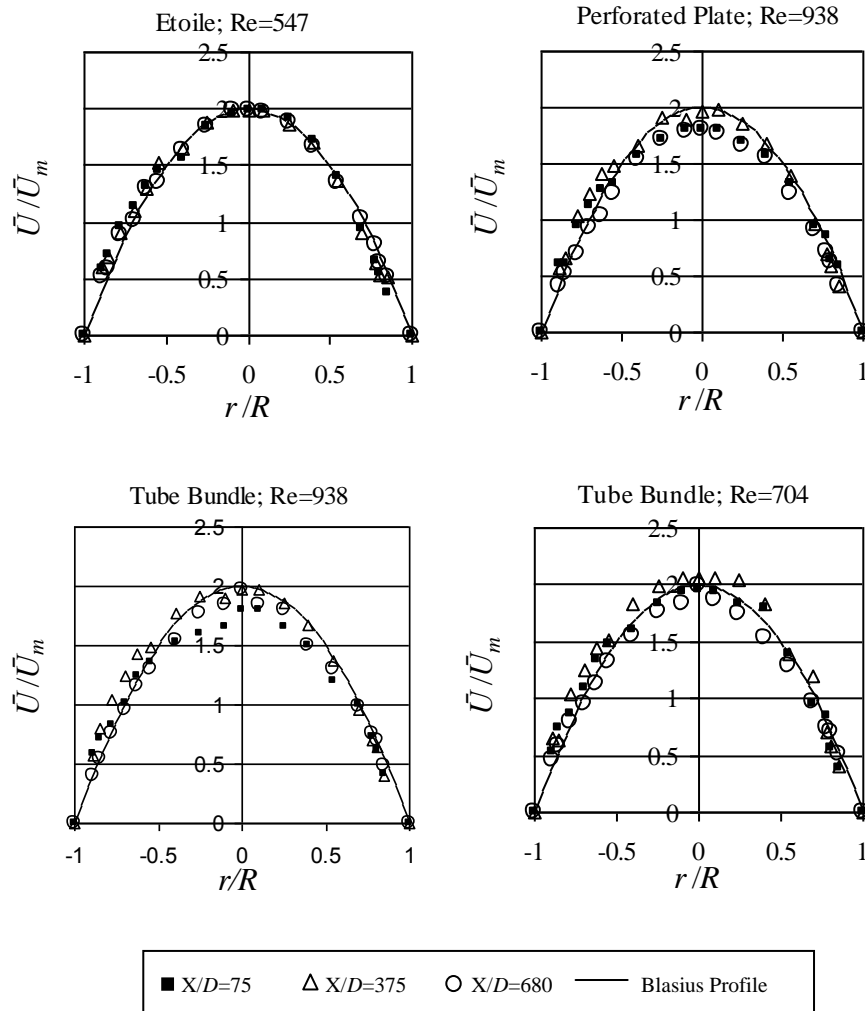


Figure 6.5. Sample non-dimensional axial velocity, \bar{U}/\bar{U}_m profiles behind flow conditioners as a function of X/D

The cross-sectional profiles of turbulence intensity, $I(r/R)$, behind flow conditioners FC and that of WFC are also examined. The sample data taken at $X/D=375$ and at $X/D=680$ are given in Fig. 6.6. Behind the flow conditioners the shape of $I=I(r/R)$ is completely different from the ones of WFC case. For FC cases, $I=I(r/R)$ profiles exhibit almost a constant magnitude of I irrespective of the radial

position. The profiles of $I=I(r/R)$ are independent of X/D , Re and type of flow conditioner. Furthermore the magnitudes of I downstream the flow conditioners are always less than the ones of WFC irrespective of X/D and Re. However the change in flow nature from laminar to turbulent flow results in a significant change in the profiles of $I=I(r/R)$. The cross-sectional position seems to be immaterial for $Re < 2450$ inside laminar range. However inside turbulent range for $Re \geq 2450$ the influence of Re and cross sectional position is significant.

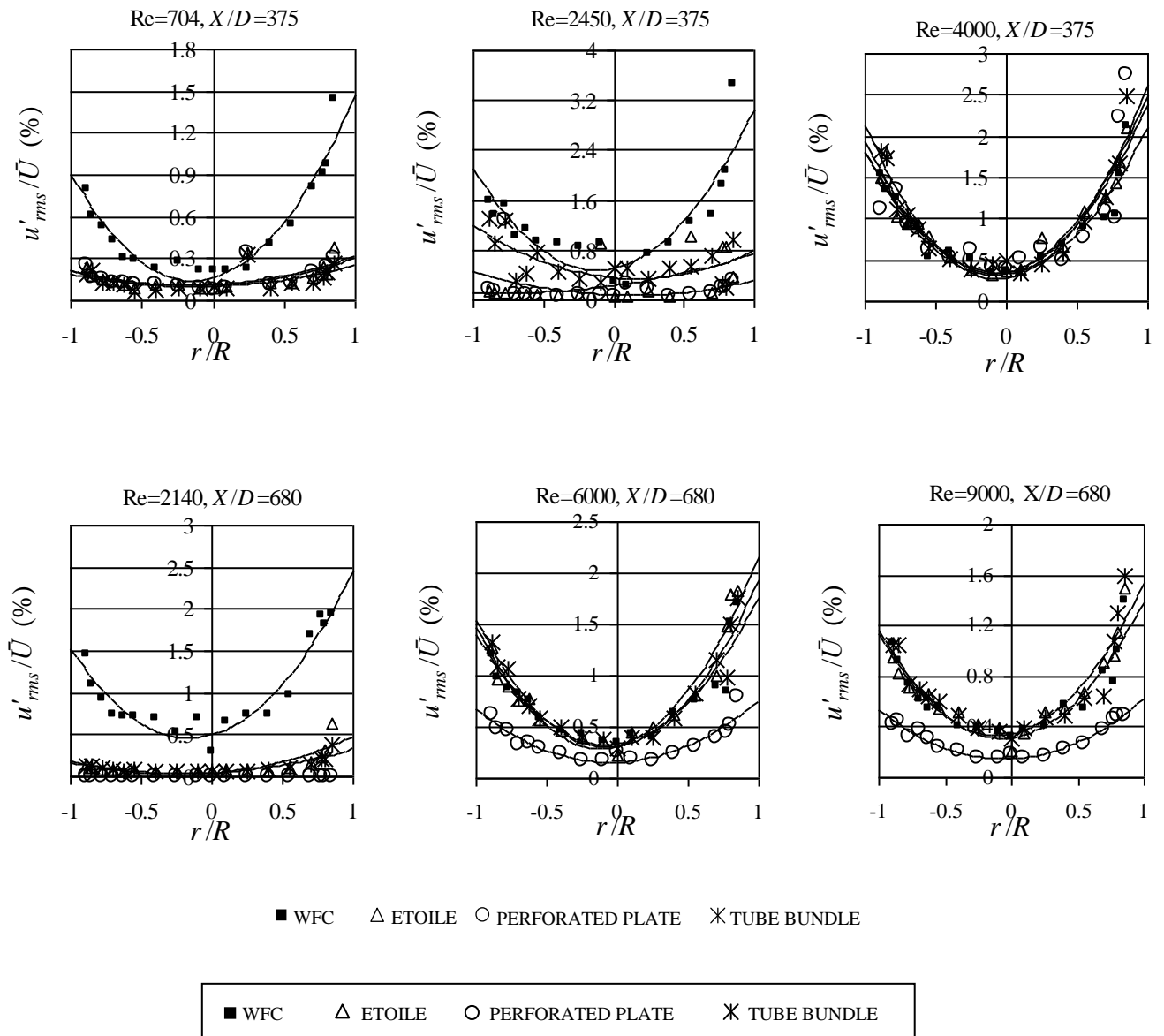


Figure 6.6. Sample turbulence intensity u'_{rms}/\bar{U} profiles behind flow conditioners and WFC at $X/D=375$ and $X/D=680$

The flow is fully-developed laminar with the use of flow conditioners since $I=I(r/R)$ is independent of radial position with almost negligible magnitudes of I in comparison to the values of WFC case. The radical changes in $I=I(r/R)$ at $X/D=375$ and at $X/D=680$ for $Re=2450, 4000, 6000$ and 9000 verify also the laminar range of flow. $I=I(r/R)$ profiles behind perforated plate deviate from those of other inserts for $Re \geq 6000$ at $X/D=680$ without any solid reasoning. Furthermore $I=I(r/R)$ profiles of FC cases are coincident with that of WFC case for $Re=4000$ at $X/D=375$. Therefore it can be assumed that differences in designs are eliminated somehow inside turbulent flow for $Re \geq 2450$.

These observations can lead us to the following simple deductions:

- i) Laminar flow control by the utilization of pipe inserts is essential for $Re < 2450$. However type of insert and its influence on the flow is dominated by the flow nature.
- ii) The differences in the type of inserts seem to be of secondary importance inside the laminar range.
- iii) Almost the negligible amount of turbulence intensity level independent of radial position verifies the satisfaction of fully developed laminar flow at $X/D=75, X/D=375$ and $X/D=680$ with velocity profiles having an acceptable fit to the Blasius profile.

6.3. Performance Characteristics and Settling Distance of Pipe Inserts in Laminar Flow Range with an Approach on Entrance Length

6.3.1. Performance characteristics

In order to determine the performance characteristics of the flow conditioners the calculated values of $\Delta \bar{P}$ are used. As it can be seen from Fig. 6.7, the magnitudes of ensemble averaged pressure loss, $\Delta \bar{P}$ through perforated plate are higher than tube bundle and etoile for $Re \leq 9000$ due to its smallest β value.

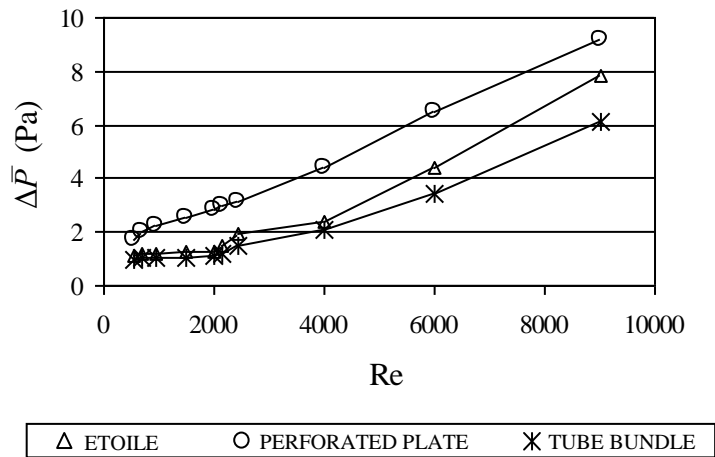


Figure 6.7. Variation of $\Delta\bar{P}$ with Re for the tested flow conditioners

Meanwhile increase in Re is accompanied with an increase in $\Delta\bar{P}$ for all conditioners due to the transition of flow from laminar to turbulent regime. Inside laminar range for $Re < 2450$, the magnitudes of $\Delta\bar{P}$ for the tube bundle and the etoile are almost the same in the order of 1.2 Pa, however the deviation tends to be higher as Re is increased.

The pressure loss through the pipe insert, $\Delta\bar{P}$ is given by means of the pressure loss coefficient, K as a function of Re and β as $K(Re, \beta)$. As it can be seen from Fig. 6.8 a common non-dimensional pressure loss characteristics of the flow conditioners exists irrespective of the flow regime and the differences in designs are apparent.

The experimental data can be represented by the following equation with an approximate error margin of $\pm 18\%$:

$$K = 53634(\text{Re} \beta)^{-1.4} \quad (6.5)$$

Therefore the tested flow conditioners belong to the same family and Eq. (6.5) is of considerable facility for practice providing the calculation of $\Delta\bar{P}$ as a function of Re and β eliminating the need for an experimental measurement.

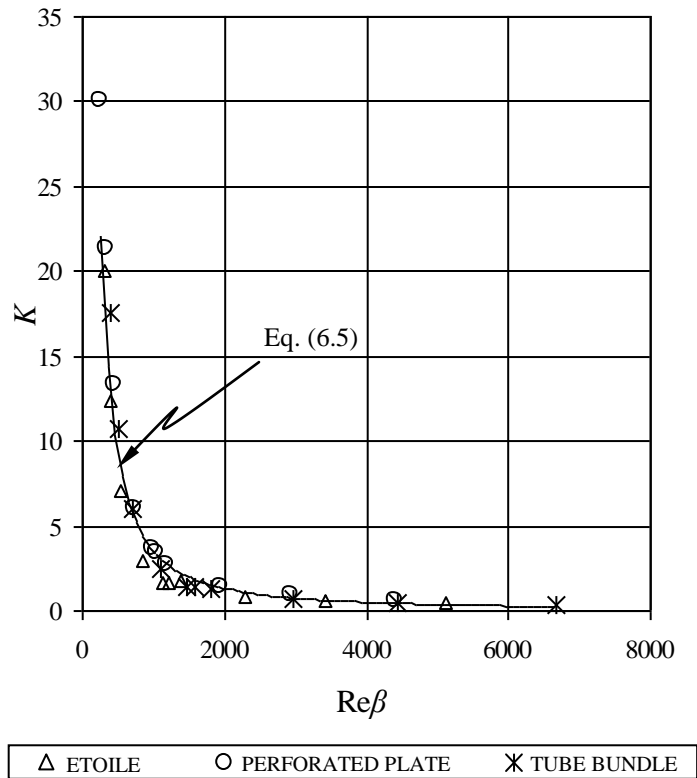


Figure 6.8. Variation of pressure loss coefficient, K with $Re\beta$ for the tested flow conditioners

6.3.2. Settling distance and entrance length in laminar flow range

The experimental data gathered are analyzed in the range of $Re < 2450$ to estimate the settling distance of the tested flow conditioners. In the analysis, the proposed non-dimensional comparison parameters of local velocity data at cross-sectional positions of $r/R=0.89$ and $r/R=0$ are referred as outlined below:

i) *The first comparison parameter: Local turbulence intensity: $I = u'_{rms} / \bar{U}$*

The variation of I at $r/R=0$ and at $r/R=0.89$ behind the flow conditioners is given as a function of Re and X/D in Fig. 6.9 and Fig. 6.10 respectively for $Re < 2450$. In reference to data at $r/R=0$ and disregarding the data deviation belonging to the case of perforated plate at $X/D=75$; irrespective of the type of the flow conditioner for $Re < 2450$, the variation of I with Re , $I=I(Re)$, is independent of X/D . Meanwhile referring to data at $r/R=0.89$ (Fig. 6.10) the same observation with an increased

amount of data scattering due to the influence of wall proximity and design differences of the flow conditioners can be deduced.

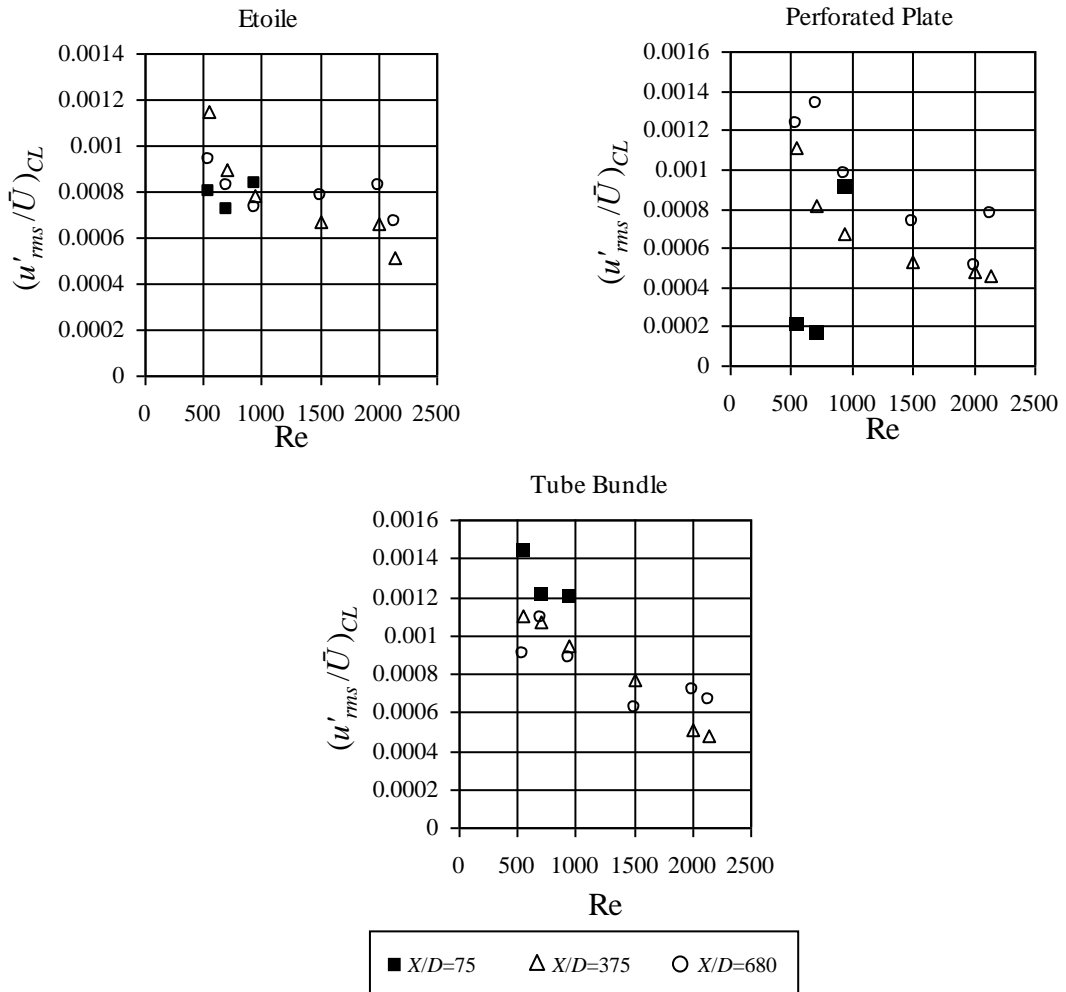
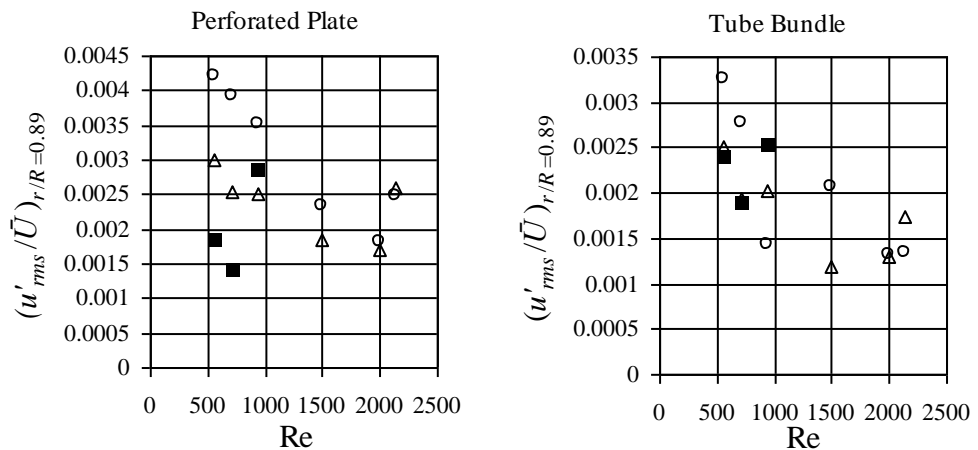


Figure 6.9. Variation of local turbulence intensity $(u'_{rms}/\bar{U})_{CL}$ at $r/R=0$ with Re



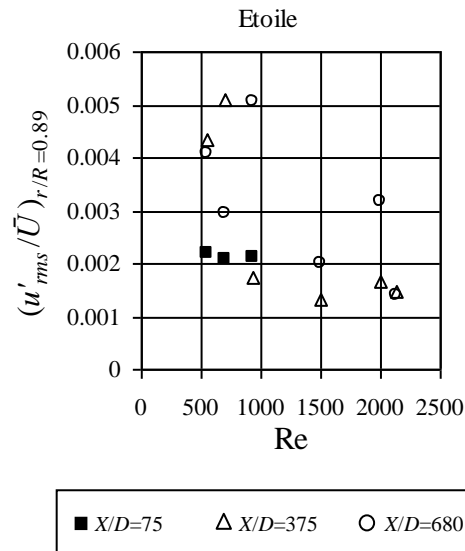
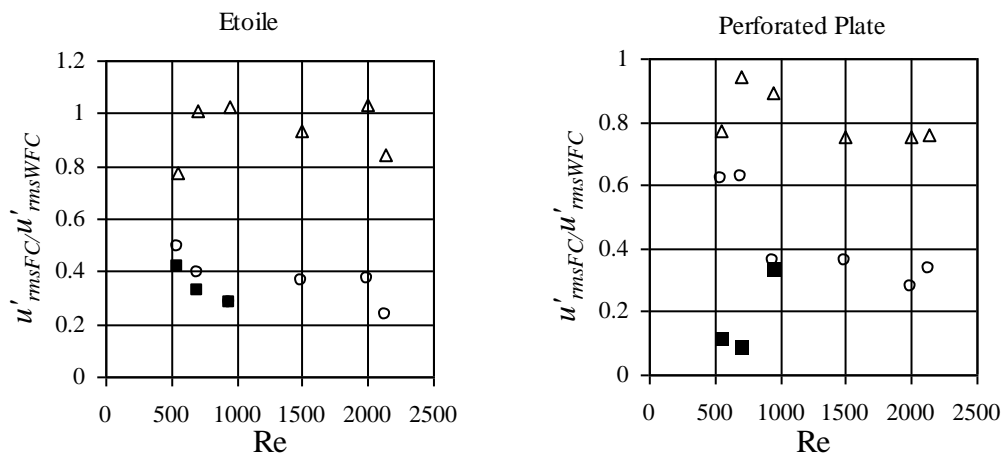


Figure 6.10. Variation of local turbulence intensity $(u'_{rms}/\bar{U})_{r/R=0.89}$ at $r/R=0.89$ with Re

ii) The second comparison parameter: Local respective orders of u'_{rms} measured behind flow conditioners with the corresponding ones without a flow conditioner case: (u'_{rmsFC}/u'_{rmsWFC})

In reference to (u'_{rmsFC}/u'_{rmsWFC}) data shown in Fig. 6.11 and Fig. 6.12 taken at $r/R=0$ and $r/R=0.89$ respectively for $Re < 2450$, it can be said that (u'_{rmsFC}/u'_{rmsWFC}) dependency on Re and X/D is irrespective of the radial position.



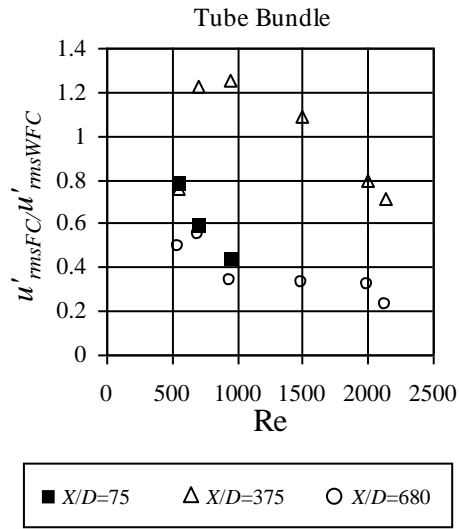


Figure 6.11. Variation of local respective orders $(u'_{rmsFC}/u'_{rmsWFC})_{CL}$ at $r/R=0$ with Re

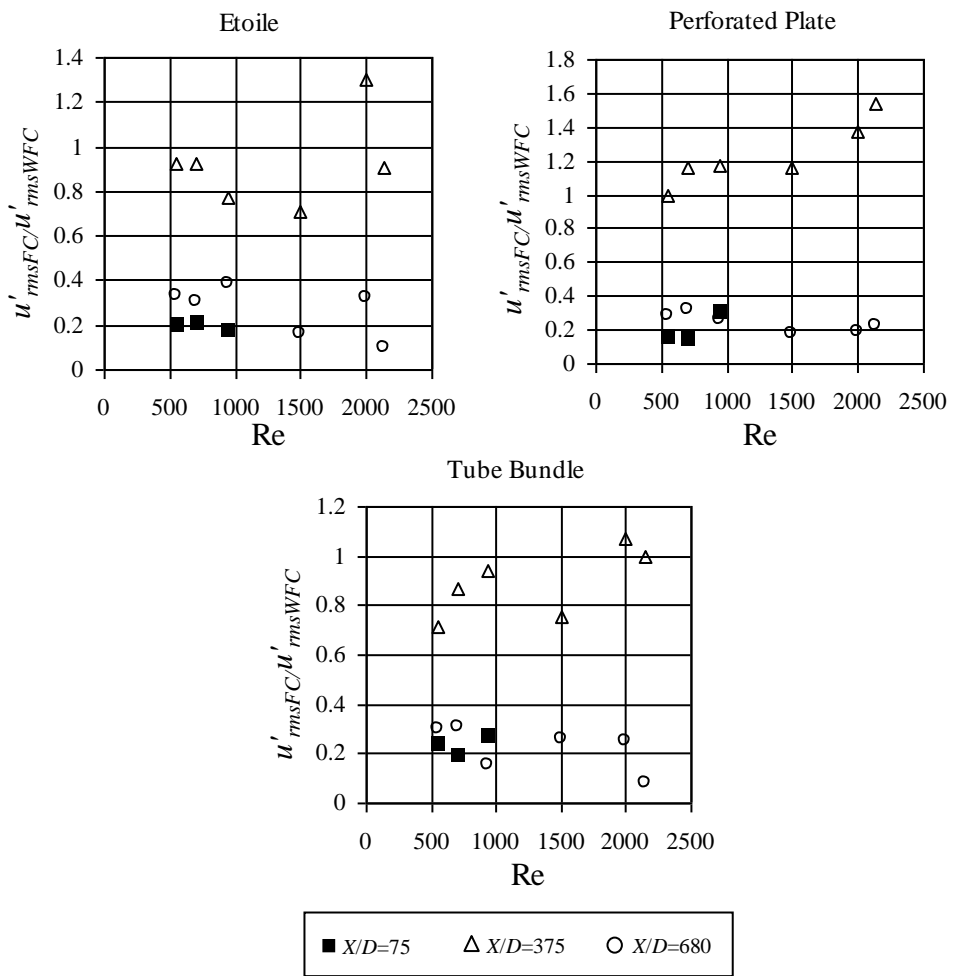


Figure 6.12. Variation of local respective orders $(u'_{rmsFC}/u'_{rmsWFC})_{r/R=0.89}$ at $r/R=0.89$ with Re

Furthermore the variation of $(u'_{rmsFC} / u'_{rmsWFC})$ with Re has similarities at $X/D=75$ and $X/D=680$ having values $(u'_{rmsFC} / u'_{rmsWFC}) < 1$ for all conditioners. However as a surprising fact the variation of $(u'_{rmsFC} / u'_{rmsWFC})$ with Re at $X/D=375$ has approximately in the order of 1 with a considerable deviation from the ones at $X/D=75$ and $X/D=680$ for all flow conditioners. The selected comparison parameter $(u'_{rmsFC} / u'_{rmsWFC})$ which is not dependent on r/R has still under the dominant effect of X/D . However the reasons of similarities observed at $X/D=75$ and $X/D=680$ and the different behavior of data at $X/D=375$ cannot be explained. Therefore in order to explain the influence of X/D , the variation of $(u'_{rmsFC} / u'_{rmsWFC})$ taken at $r/R=0$ defined as $(u'_{rmsFC} / u'_{rmsWFC})_{CL}$ is introduced as a function of $Re_x = (X/D)Re$ which is defined as entrance length Reynolds Number as can be seen from Fig.6.13.

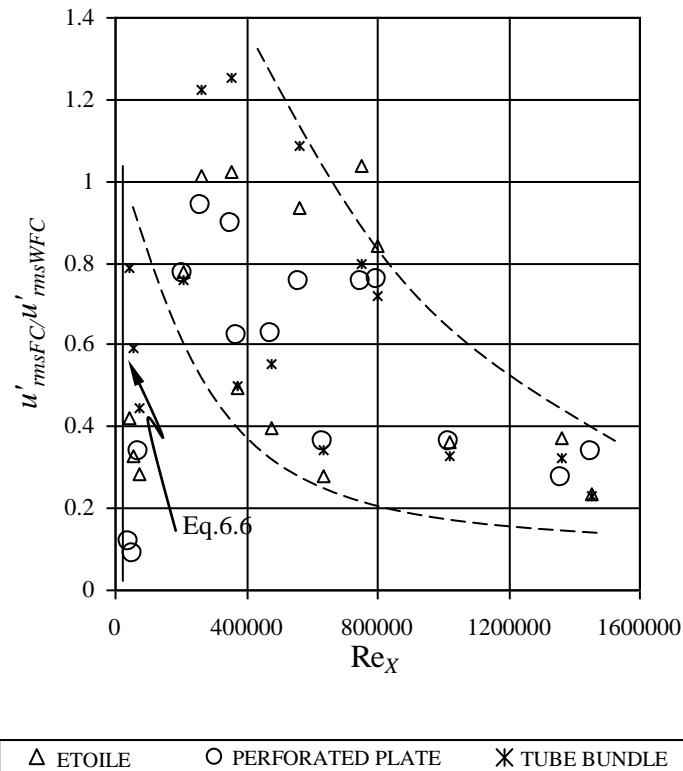


Figure 6.13. Variation of $(u'_{rmsFC} / u'_{rmsWFC})_{CL}$ at $r/R=0$ with $Re_x = (X/D)Re$

The separate behavior of data behind all conditioners corresponding to $X/D=75$ is shown by the solid line indicating an independency of $(u'_{rms_{FC}} / u'_{rms_{WFC}})_{CL}$ to Re_x . The equation of the solid line given below is in conformity with the experimental data in a mean error margin of $\pm 25\%$:

$$Re_x = (X / D) Re = \bar{U}_m X / \nu = 54700 \quad (6.6)$$

However magnitude of $(u'_{rms_{FC}} / u'_{rms_{WFC}})_{CL}$ reduce with Re_x with a considerable data scattering shown by the dashed lines for the data belonging to $X/D=375$ and $X/D=680$. Therefore Eq. (6.6) can be estimated as the relationship for the settling distance of the flow conditioners. In reference to Eq. (6.6) the settling distances of the flow conditioners can be determined as a function of Re as can be seen in Table 6.1.

Table 6.1. Settling distances of the flow conditioners calculated in reference to Eq. (6.6)

Re	X/D
2000	27.35
1000	54.70
500	109.40

Therefore for the flow conditioners in the covered laminar range of Re the minimum settling distance of $X/D=75$ seems to be satisfactory.

iii) The third comparison parameter: Respective order of local-centerline non-dimensional axial velocity with flow conditioner and theoretical Blasius Profile

$$\left[\frac{(\bar{U} / \bar{U}_m)_{FC}}{(\bar{U} / \bar{U}_m)_{Blasius}} \right]_{CL}$$

Under the light of analysis on u' ; to evaluate the deviation from the theoretical Blasius profile, the non-dimensional axial velocity values taken at $r/R=0$,

$\left[\frac{(\bar{U}/\bar{U}_m)_{FC}}{(\bar{U}/\bar{U}_m)_{Blasius}} \right]_{CL}$ can be used. For this purpose; as a result of correlation trials, the variation of $\left[\frac{(\bar{U}/\bar{U}_m)_{FC}}{(\bar{U}/\bar{U}_m)_{Blasius}} \right]_{CL}$ with $Re_x \beta$ shown in Fig. 6.14 is preferred.

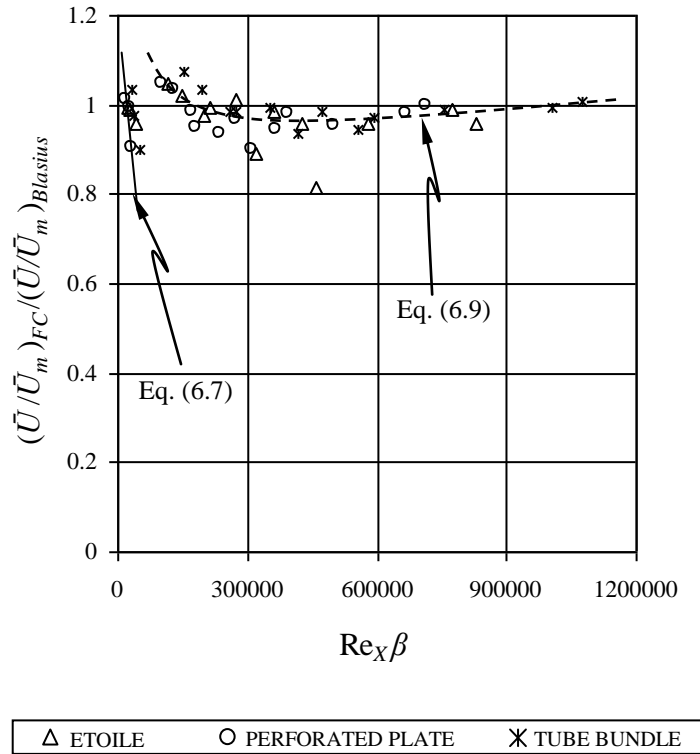


Figure 6.14. Variation of $\left[\frac{(\bar{U}/\bar{U}_m)_{FC}}{(\bar{U}/\bar{U}_m)_{Blasius}} \right]_{CL}$ at $r/R=0$ with $Re_x \beta$

Similar to the data behavior observed in Fig. 6.14, two separate lines are drawn. The following equation of the solid line is in conformity with data in a mean error range of $\pm 4\%$:

$$\left[\frac{(\bar{U}/\bar{U}_m)_{FC}}{(\bar{U}/\bar{U}_m)_{Blasius}} \right]_{CL} = 1,0862 - (3 \times 10^{-6} Re_x \beta) \quad (6.7)$$

In reference to the satisfaction with Blasius profile, $\left[\frac{(\bar{U}/\bar{U}_m)_{FC}}{(\bar{U}/\bar{U}_m)_{Blasius}} \right]_{CL} = 1.0$ can be inserted into Eq. (6.7) resulting:

$$\text{Re}_x \beta = 2.87 \times 10^4 \quad (6.8)$$

Eq. (6.8) is used to determine the nearest position in conformity with theoretical Blasius profile behind the flow conditioners. Furthermore using $\text{Re}_x = 54700$ determined from Eq. (6.6) in Eq. (6.8), $\beta = 0.524$ is obtained. This β value is inside the covered range of experimental data. Therefore Eq. (6.8) can be referred as the equation defining the settling distance of the tested flow conditioners.

Meanwhile, the following equation of the dashed line is in conformity with data in a mean error range of $\pm 6\%$:

$$\left[\frac{(\bar{U}/\bar{U}_m)_{FC}}{(\bar{U}/\bar{U}_m)_{Blasius}} \right]_{CL} = 0,96 + \frac{12000}{\text{Re}_x \beta} \quad (6.9)$$

In a similar manner, inserting $\left[\frac{(\bar{U}/\bar{U}_m)_{FC}}{(\bar{U}/\bar{U}_m)_{Blasius}} \right]_{CL} = 1.0$ into Eq. (6.9) results:

$$\text{Re}_x \beta = 3 \times 10^5 \quad (6.10)$$

In terms of covered range of β , the calculated parameters of Re_x , Re and X/D using Eq. (6.10) are listed in Table 6.2.

Therefore in conformity with the downstream velocity field analysis of the flow conditioners it seems that Eq. (6.10) should be satisfied to have fully developed laminar flow. So, Eq. (6.10) can be used to determine laminar entrance length.

Meanwhile the variation of the same parameter $\left[\frac{(\bar{U}/\bar{U}_m)_{WFC}}{(\bar{U}/\bar{U}_m)_{Blasius}} \right]_{CL}$ with $\text{Re}_x \beta$ obtained for WFC case with $\beta = 1$ is also shown in Fig. 6.15. It is observed that the deviation from the Blasius solution is in the order of $\pm 20\%$ with a strong dependence on X/D indicating the flow is not fully developed. Therefore, the necessity of flow conditioners is verified once more.

Table 6.2 Calculated parameters of Re_x , Re and X/D for the covered range of β in reference to Eq. (6.10)

β	Re_x	Re	X/D
0.50	600,000	2000	300
		1000	600
		500	1200
0.75	400,000	2000	200
		1000	400
		500	800

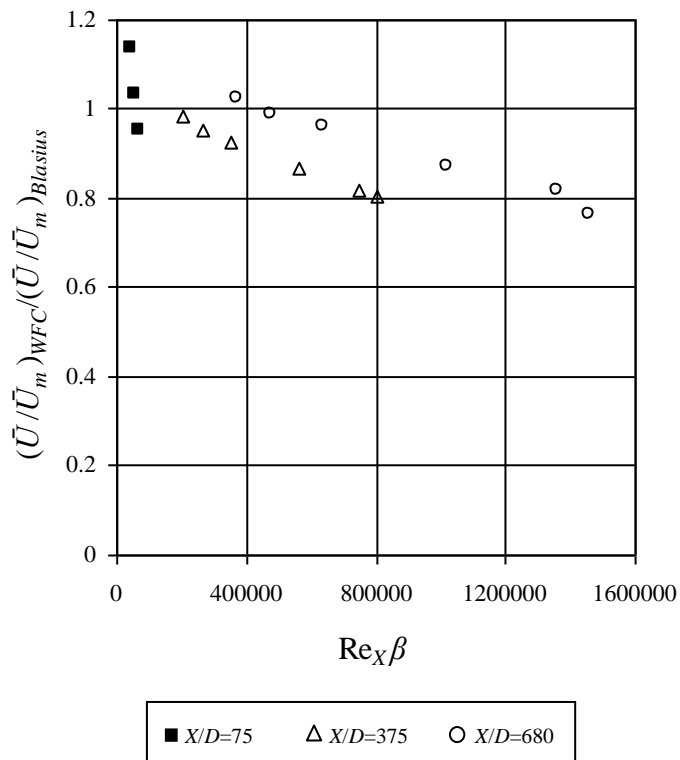


Figure 6.15 Variation of $\left[\frac{(\bar{U}/\bar{U}_m)_{WFC}}{(\bar{U}/\bar{U}_m)_{Blasius}} \right]_{CL}$ at $r/R=0$ with $Re_x \beta$ for WFC
Case of $\beta=1$

6.4. Conclusions

In spite of the well-designed entrance from the compressor out to the pipe line, without a flow conditioner, a fully-developed laminar flow cannot be produced at feasible lengths with a $\pm 20\%$ deviation from Blasius profile. Therefore the accepted laminar entrance length concept (White 1984) is not verified by the cross-sectional axial velocity profiles. Therefore, flow conditioners are essential to produce a fully-developed laminar flow inside the pipe. The utilized flow conditioners having similar characteristics in terms of pressure loss coefficient, $K=K(\text{Re}\beta)$ result in a fully-developed laminar flow with a mean deviation of $\pm 10\%$ from Blasius profile. The flow field measurements downstream of the flow conditioners are also expressed in terms of cross-sectional local non-dimensional velocity parameters through a correlation study with the introduction of Re_x . The settling distance and laminar entrance length are given in terms of equation of " $\text{Re}_x \beta = C$ " where the magnitude of "C" is 2.87×10^4 and 3×10^5 respectively.

CHAPTER 7

DETECTION METHOD AND DEvised PROGRAM FOR ONSET OF TRANSITION TO TURBULENCE IN PULSATILE PIPE FLOW

7.1. Introduction

This chapter introduces the devised program in LabView 2009SP1[®] for the detection of the transition to turbulence in pulsatile pipe flows. The turbulence detection program is embedded in a fully automated *TDFC.vi* which was explained in detail in Chapter 4. The execution of the program and the details of detection of transition to turbulence are the main subjects of this chapter. The methodology used in the detection program is introduced. As a result of comprehensive literature survey, it was recognized that there is no well-defined transition detection program; even a methodology. The flow dynamics in both laminar and transitional regimes are investigated through sample runs to verify the used methodology in the range of the time averaged Reynolds number of $1019 \leq Re_{ta} \leq 4817$, oscillating Reynolds number of $107 \leq Re_{os} \leq 4261$, velocity amplitude ratio of $0.05 \leq A_1 \leq 0.96$ and Womersley number of $2.72 \leq \sqrt{\omega'} \leq 32.21$.

There are two distinct approaches used in the analyses of the experimental results to detect the transition to turbulence in the pulsatile pipe flows. In one of these approaches, the flow is considered as quasisteady (Shemer, 1985). The other approach is based on the unsteady character of the time dependent flow which is subjected to alternating acceleration and deceleration. However, the theoretical studies carried out on the linear stability of the time dependent flows indicate that contrary to steady flows, the inflection points on the velocity profile does not affect

its stability. Moreover, it is shown that superposition of oscillation on the steady flow has a stabilizing effect at intermediate frequencies. (Einav and Sokolov, 1993), (Peacock et al., 1998), (Stettler and Hussain, 1986).

According to the literature, the flow firstly destabilizes and then laminar to turbulent transition begins. In this chapter, we monitor instantaneous character of the laminar to turbulent transition to spot the onset of the transition. Until now, transition to turbulence has been always detected by simply viewing the velocity waveforms. However, it is a quite difficult task to detect the transition by only investigating many waveforms. Also, some illusions can occur during the detection of the transition by visual observations. For this reason, it has been decided to devise a method to detect transition to turbulence. This method is based on taking the derivative of velocity waveform with respect to time. By taking the derivative of the time dependent signal, the time dependency of the signal is removed and if there is any further turbulent burst on the signal, the transition can be easily detected due to presence of peaks on the signal.

7.2. Utilized Methodology

In view of the literature survey, it is seen that the detection of turbulent structures is carried out by means of visual observation on velocity waveforms. However the visual observation is seen to be an elementary and open-ended method. It is not easy, sensitive and objective method giving rise to the possibility of human errors, i.e., illusions. Hence a method is developed and a fully-automated program is devised in LabView 2009SP1 in order to detect the onset of transition in pulsatile pipe flow.

The velocity profile, $U = U(r, t)$ is considered to be used for the detection method. The time-periodicity is eliminated by taking the derivative of velocity profile with respect to time. Hence any perturbation in any frequency can be noticed as a peak in $dU(r, t)/dt$. This parameter is defined as turbulence detection parameter, *TDP* as follows:

$$TDP_1 = dU(r,t)/dt \quad (7.1)$$

The detection method is based on the comparison of a turbulence detection parameter, TDP with a threshold parameter, TP . Any TP should be defined as a comparison tool such that any value of TDP over the value of TP is the signature of the onset of transition. In this respect, a value of TP_1 is defined and compared with $TDP_1 = dU(r,t)/dt$ in the devised program. However, the parameter of $TDP_1 = dU(r,t)/dt$ is found to be nonsense due to both positive and negative values of $dU(r,t)/dt$ appearing in the analysis, which require two different values of TP for both positive and negative values of $dU(r,t)/dt$ for comparison.

For this reason, $TDP_1 = dU(r,t)/dt$ is squared and defined as a new TDP eliminating the negative and magnifying the value as follows:

$$TDP_2 = (dU(r,t)/dt)^2 \quad (7.2)$$

Hence it becomes easier to detect very small perturbations on the velocity waveforms. TDP_2 has been used as a turbulence detector also in the study of Shemer (1985) due to only axial component of the velocity has been measured in his study. However, it is observed that the parameter of $TDP_2 = (dU(r,t)/dt)^2$ with any value of TP does not execute very well for the covered experimental ranges. It is found to be unsatisfactory for the detection of the onset of transition at some instants and radial positions of the hotwire probe, r/R although the turbulent structures are seen on the velocity waveforms.

It is decided to define a new couple of TDP and TP such that the method operates without any error and detects immediately the onset of transition when the turbulent structures occur on the velocity waveforms at any instant and radial position of r/R . It is deduced that TDP should be a function of time-averaged component of local velocity at radial position, \bar{U}_{ta} , pipe radius, R , kinematic viscosity of fluid, ν and oscillation frequency, f as well as $dU(r,t)/dt$. Using the dimensional analysis, the following expression is derived as follows:

$$TDP_3 = R(dU(r,t)/dt)^2 / (\bar{U}_{ta} v \omega^2) \quad (7.3)$$

where ω is the angular frequency and defined as $\omega = 2\pi f$.

TDP_3 is a non-dimensional and dynamic parameter which takes different values with respect to the values of \bar{U}_{ta} , R , v , f and $dU(r,t)/dt$. So, its value changes at any instant and radial position of r/R .

As a comparison tool, a non-dimensional and dynamic TP is derived, whose magnitude is changed with varying of f , as follows:

$$TP_1 = (1/\sqrt{\omega'})^n \quad (7.4)$$

where n is the magnitude of oscillation frequency ($n = |f|$).

As a result of the extended tests, the method based on the comparison of TDP_3 and TP_1 is found to be very accurate and effectiveness for the detection of the onset of transition. The value of TDP_3 at any instant exceeds the value of TP_1 when turbulent structures occur on the velocity waveform at any instant and radial position. The intermittency factor, γ (as a ratio of the time period during the occurrence of turbulence structures to the total time period) at the onset of the transition to turbulence is found to be less than 0.1 in the covered experimental ranges. At that moment, the related devised program detects simultaneously the onset of transition and gives an alert. In the laminar regime, however, the value of TP_1 is always observed to be above the value of TDP_3 . Hence the program does not give any alert at that moment.

However, it is observed that the method does not work well for $f > 1$ Hz. At some instants, the program cannot detect the available turbulent structures on the velocity waveforms for $f > 1$ Hz. For this reason, the program is divided into two

parts for the cases of $f \leq 1$ Hz and $f > 1$ Hz and it becomes essential to define a new couple of TDP and TP for $f > 1$ Hz. TDP and TP are derived for $f > 1$ Hz as follows:

$$TDP_4 = (dU(r,t)/dt)^2 / (\bar{U}_{ia}^2 \omega^2) \quad (7.5)$$

$$TP_2 = (1/\sqrt{\omega'})^4 \quad (7.6)$$

In this form of $TDP_4 = (dU(r,t)/dt)^2 / (\bar{U}_{ia}^2 \omega^2)$, the viscous term, ν is not seen. Moreover, the square of the inertia term, \bar{U}_{ia} is dominant. This verifies that, after $f > 1$ Hz, the flow regime approaches nearer to the inertia dominant regime defined previously by Ohmi and Iguchi (1980) and Ohmi et al. (1982). The new proposed TDP_4 and TP_2 are found to be very effectiveness and successful for the detection of the onset of transition for $f > 1$ Hz.

The viscous term is seen to be disappeared in $TDP_4 = (dU(r,t)/dt)^2 / (\bar{U}_{ia}^2 \omega^2)$. Moreover, the square of the inertia term is dominant for $f > 1$ Hz. This verifies that the flow at $\sqrt{\omega'} > 17.22$ begins to approach the inertia dominant regime defined previously by Ohmi and Iguchi (1980) and Ohmi et al. (1982).

7.3. Utilized Detection Program

The functional properties of $TDFC.vi$ are given previously in Chapter 4. In this chapter, only the detection part of $TDFC.vi$ which is used for the determination of transition to turbulence is introduced. The block diagrams of the detection part are given in Figs. 7.1 and 7.2.

In the *Case Structure* (5), the detection of the onset of transition is performed. On the left hand side of the *Case Structure*, there is a *Comparison Palette* named as *Less Or Equal*. The frequency of oscillation, f , is wired to the comparison palette. The output of the comparison palette is wired to the selector of the *Case Structure*. If

$f \leq 1$ Hz, the *True* case of the structure executes. If $f > 1$ Hz, the *False* case of the structure executes.

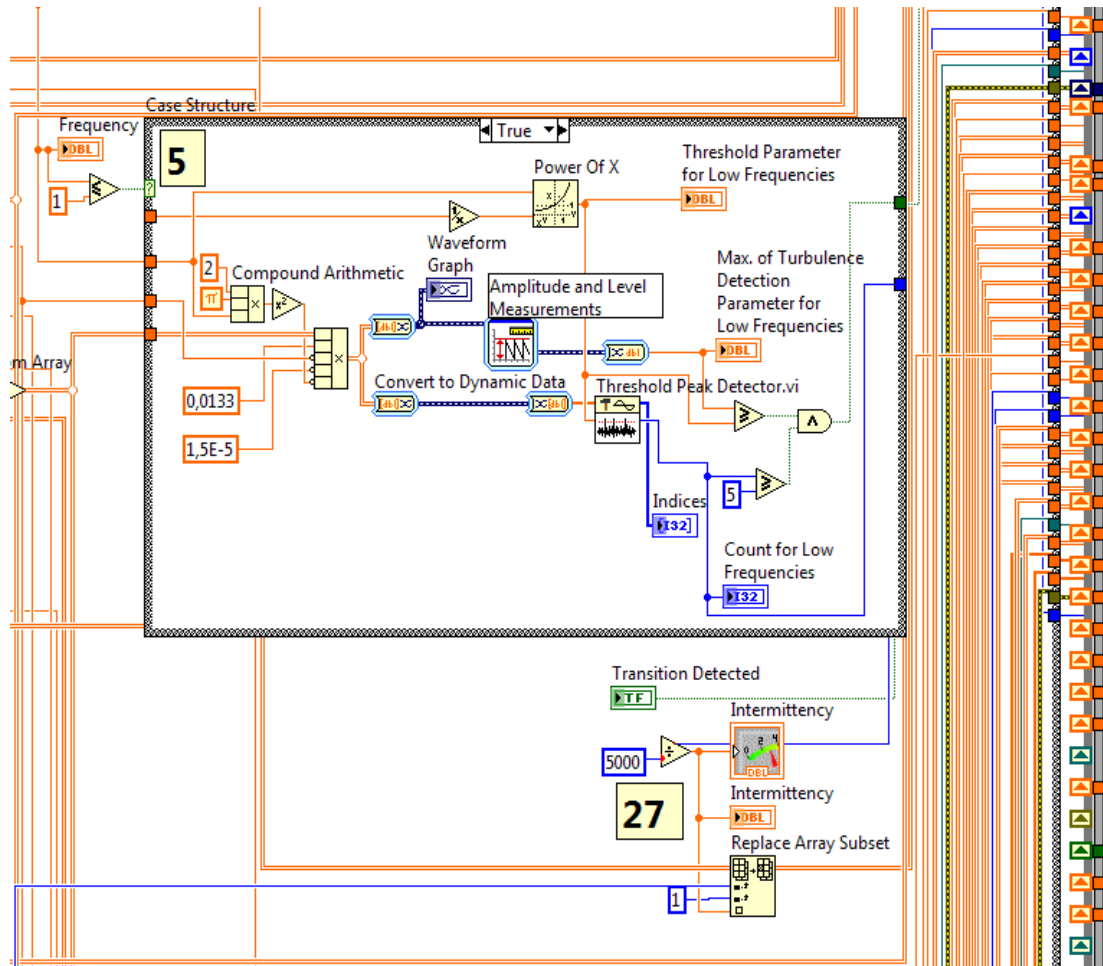


Figure 7.1. A first “True” section of the turbulence detection program for $f \leq 1$ Hz

As can be seen from Fig. 7.1, the mathematical code of the dynamic TDP_3 is constructed in the form of $R(dU(r,t)/dt)^2 / (\overline{U}_{ia} v \omega^2)$ $f \leq 1$ Hz using *Compound Arithmetic* and *Numeric palettes*. The dynamic TDP_3 can also be seen on the front panel using the *Waveform Graph* (Fig. 7.3). The numeric values of $TDP_3 = R(dU(r,t)/dt)^2 / (\overline{U}_{ia} v \omega^2)$ are converted to dynamic values by means of the signal manipulation palette named as *Convert to Dynamic Data*. The dynamic values of TDP_3 is then transferred to *Amplitude and Level Measurements.vi*. In this subvi,

the maximum peak value of the TDP_3 is determined. On the other hand, the dynamic $TP_1 = (1/\sqrt{\omega'})^n$ is constructed in the block diagram by means of *Power Of X* palette.

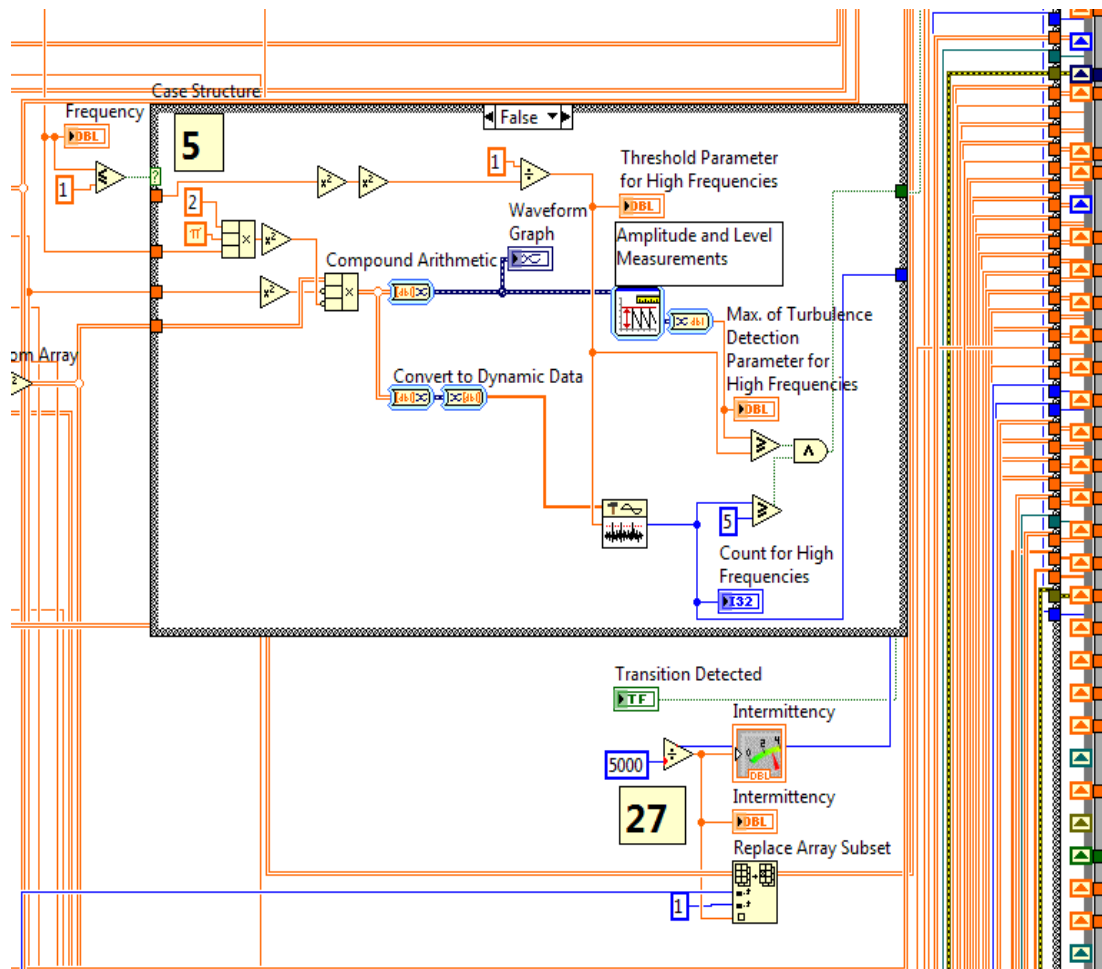


Figure 7.2. A second “False” section of the turbulence detection program for $f > 1$ Hz

Using the *Threshold Peak Detector.vi*, the values of TDP_3 that exceed the value of $TP_1 = (1/\sqrt{\omega'})^n$ are detected. If the number of these values is greater than five and if the maximum peak value of TDP_3 is greater than the dynamic TP_1 , the program gives an alert as “*Transition Detected*”. At the same time, the indicator on the front panel lights (Fig. 7.4).

If $f > 1$ Hz, the *False* case of the structure executes and the same operations are performed for $f > 1$ Hz to detect whether transition to turbulence occurs or not in the structure of *False* case. However, TDP_4 and TP_2 for $f > 1$ Hz become $(dU(r,t)/dt)^2 / (\bar{U}_{ta}^2 \omega^2)$ and $(1/\sqrt{\omega'})^4$, respectively as can be seen in Fig. 7.2. When first turbulent bursts occur on the velocity waveforms, $TDP_4 = (dU(r,t)/dt)^2 / (\bar{U}_{ta}^2 \omega^2)$ exceeds $TP_2 = (1/\sqrt{\omega'})^4$ and the onset of transition to turbulence is detected by *TDFC.vi*.

If the onset of transition to turbulence is detected at any time of the velocity waveform and at any radial positions through the half of the pipe cross-section for $f \leq 1$ Hz and $f > 1$ Hz, the green lamp on the front panel is active and it gives an alert. Then, all data in the corresponding run are saved in the file named automatically as “(Transitional Regime) $Re_{ta} = \dots$; $Re_{os} = \dots$; $fre = \dots$; $wom = \dots$ ”. The intermittency of the velocity waveform, as a ratio of the time period of turbulence detection to the total time period is also evaluated and saved into the file. It is enough to name the file as “(Transitional Regime) $Re_{ta} = \dots$; $Re_{os} = \dots$; $fre = \dots$; $wom = \dots$ ” if any transition to turbulence is detected at any instant of any radial position of the hotwire probe. If no transition to turbulence is detected at any radial position of the hotwire probe, all data are saved in the file only named as “ $Re_{ta} = \dots$; $Re_{os} = \dots$; $fre = \dots$; $wom = \dots$ ”.

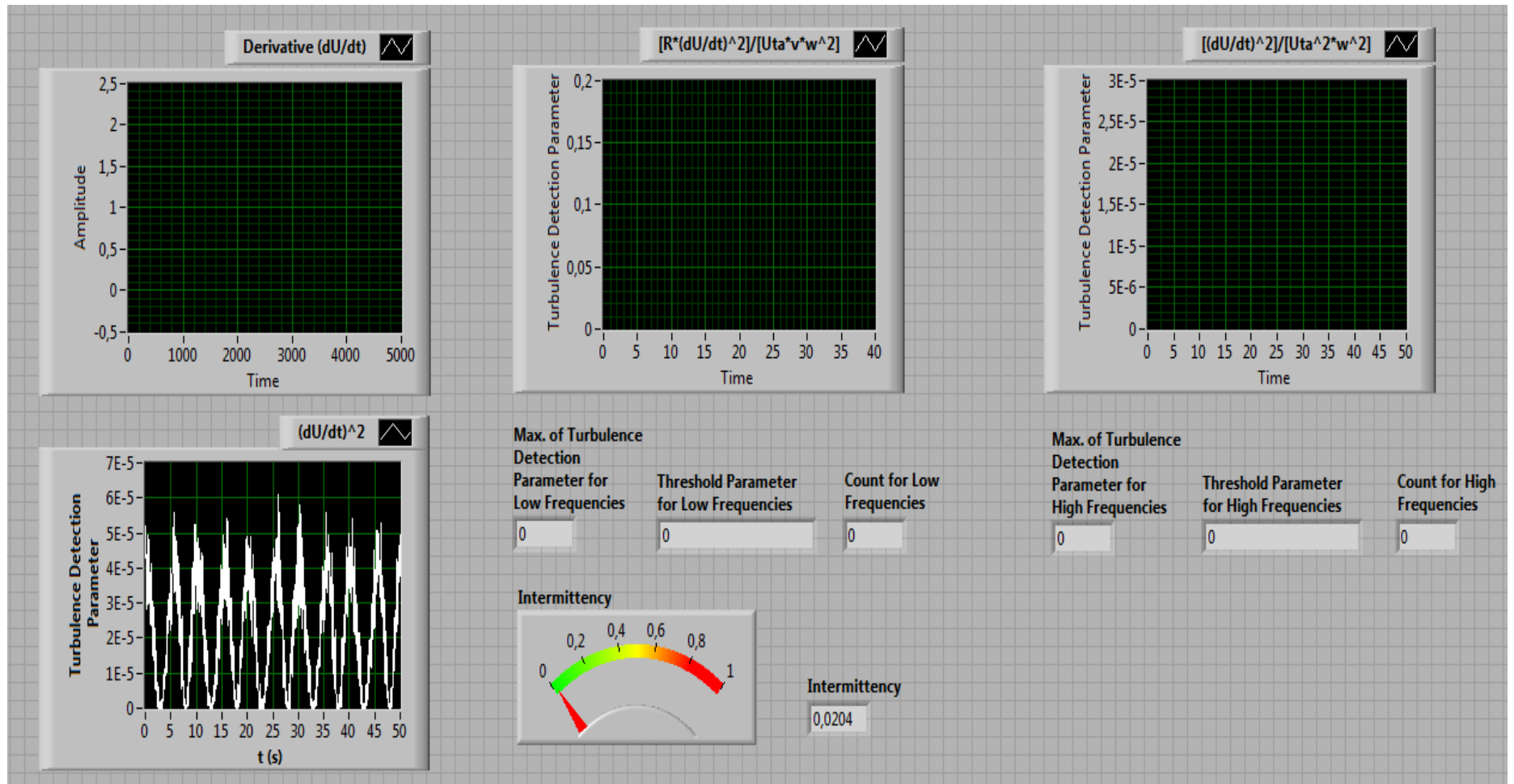


Figure 7.3. Graphical representations of TDP_1 , $TDP_2 = TDP_{Shemer}$, TDP_3 for $f \leq 1$ Hz and TDP_4 for $f > 1$ Hz, and intermittency

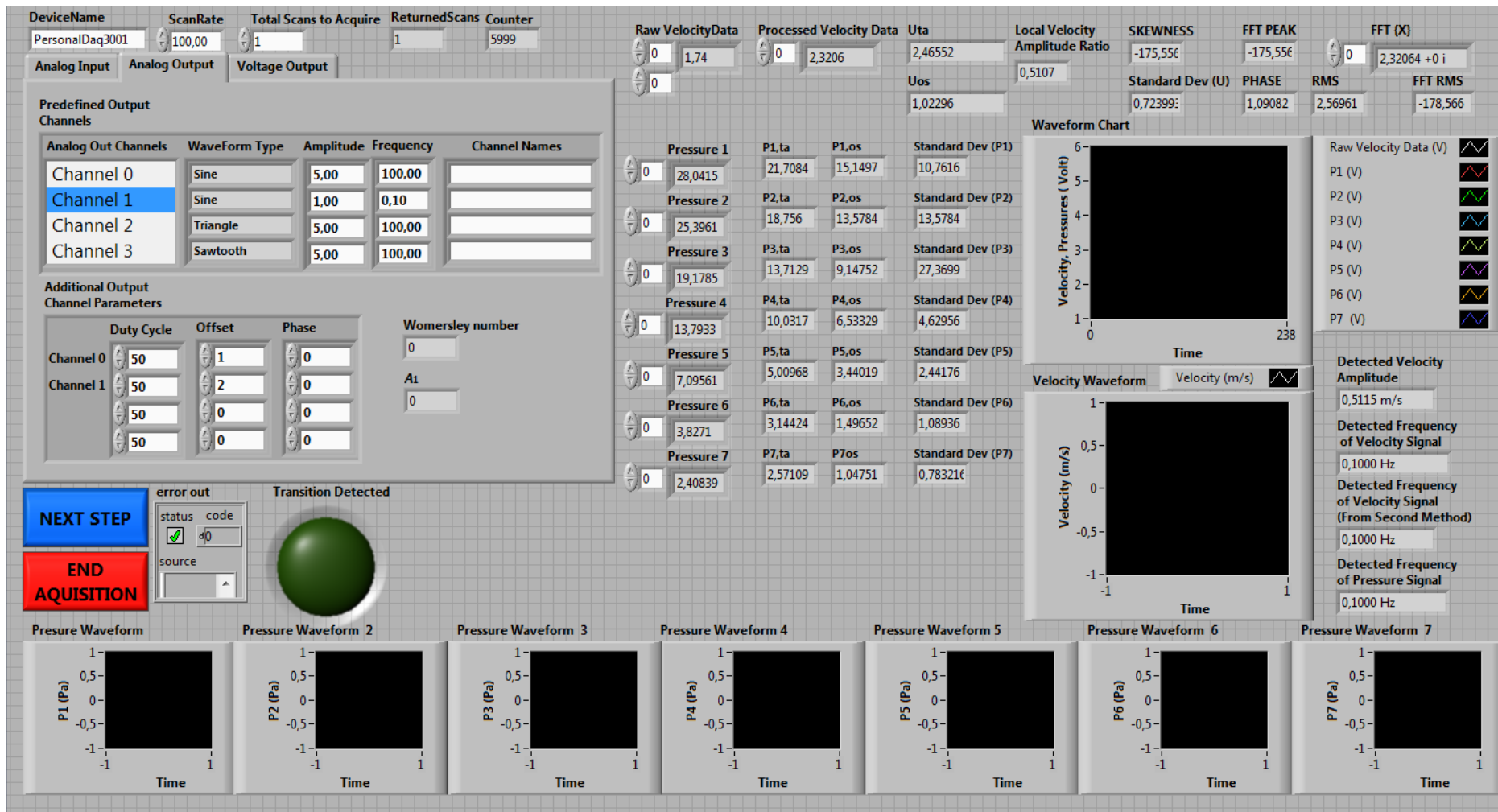


Figure 7.4. Illustration of “Transition Detected” indicator

7.4. Verification of the Transition to Turbulence Detection Program

The devised program and the used methodology for the construction of the program are introduced in Chapter 4. The experimental study is carried out for the detection of transition to turbulence of the pulsatile pipe flow in sinusoidal waveform at any oscillation frequency, f , and velocity amplitude ratio, A_1 in the covered experimental ranges.

The turbulence detection method is tested and its accuracy is verified in the experimental ranges of the time averaged Reynolds number of $1019 \leq Re_{ta} \leq 4817$, oscillating Reynolds number of $107 \leq Re_{os} \leq 4261$, velocity amplitude ratio of $0.05 \leq A_1 \leq 0.96$ and Womersley number of $2.72 \leq \sqrt{\omega'} \leq 32.21$.

The detection program is consisted of two parts for different oscillation frequency ranges of $f \leq 1$ Hz and $f > 1$ Hz. In this manner, two different dimensionless *turbulence detection parameters* and two different dimensionless *threshold parameters* are defined in the study by means of the dimensional analysis. It is deduced that the program in which transition to turbulence detection method is constructed executes accurately for all runs without any human error instead of visual observation on velocity waveforms. It detects accurately whether there is a transition to turbulence at any instant and any radial position or not. In this section, two sample runs are selected to illustrate the functionality of the detection program.

In Fig. 7.5, the velocity waveform at the pipe centerline ($r/R=0$) corresponding to the run at $Re_{ta}=3018$, $Re_{os}=1610$, $\sqrt{\omega'}=2.72$ and $A_1=0.53$ is given as a typical example.

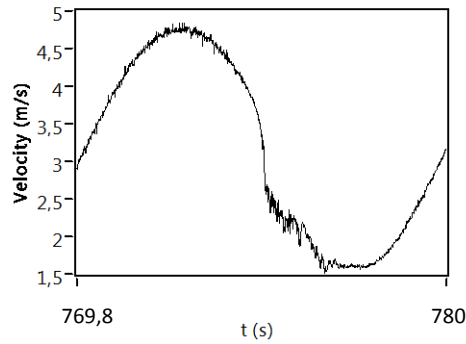


Figure 7.5. Velocity waveforms at $r/R=0$ at $Re_{ta}=3018$, $Re_{os}=1610$, $\sqrt{\omega'}=2.72$ and $A_1=0.53$

The transition to turbulence is seen in the decelerating phase of the waveform. In this run, the transition to turbulence is detected at every radial position as can be observed from Fig. 7.6. These turbulent bursts on the waveforms are detected by the turbulence detection program giving an alert.

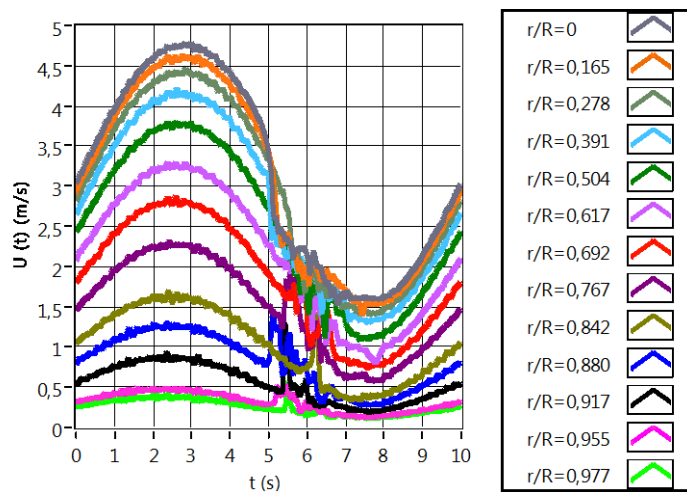


Figure 7.6. Velocity waveforms at all r/R for one period at $Re_{ta}=3018$, $Re_{os}=1610$, $\sqrt{\omega'}=2.72$ and $A_1=0.53$

Figures 7.7 and 7.8 show the transition to turbulence on the velocity waveform near the wall ($r/R=0.977$) for any instant and for the whole period, respectively at the specified run.

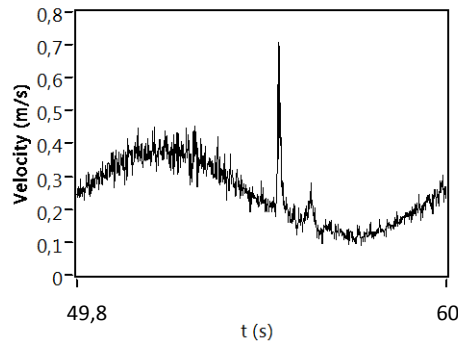


Figure 7.7. One period velocity waveforms at $r/R=0.977$ at $Re_{ta}=3018$, $Re_{os}=1610$, $\sqrt{\omega'}=2.72$ and $A_1=0.53$

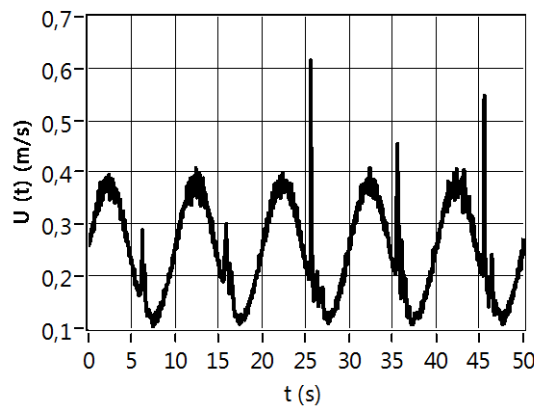


Figure 7.8. Velocity waveforms at $r/R=0.977$ at $Re_{ta}=3018$, $Re_{os}=1610$, $\sqrt{\omega'}=2.72$ and $A_1=0.53$

The transition to turbulence is detected in the decelerating phases of the waveforms as seen from the figures. However, the behavior of the turbulent burst on the waveform at $r/R=0.977$ is different than that observed on the waveform at $r/R=0$. It looks like a sudden peak. This behavior of the turbulent burst is seen on the

waveform up to $r/R=0.617$. After $r/R=0.617$ towards to the pipe centerline, the behavior of the burst seems to be a collapse at each r/R as seen in Fig. 7.5.

Figure 7.9 shows the graphical representation of the detection method for the flow regime at $Re_{ta}=2160$, $Re_{os}=832$, $\sqrt{\omega'}=17.22$ and $A_1=0.39$.

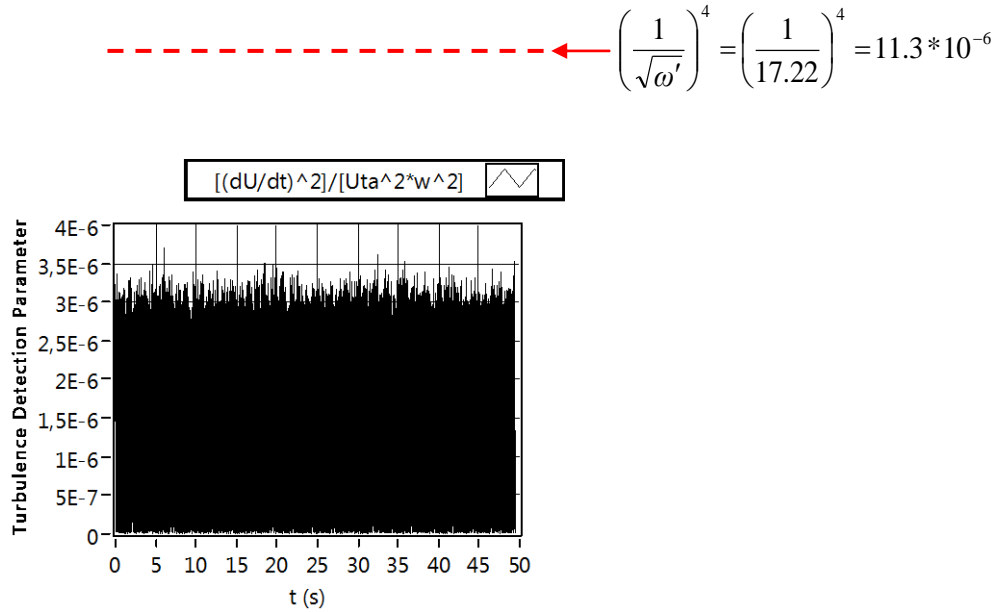


Figure 7.9 Variation of the dynamic TDP_4 at $r/R=0.977$ at $Re_{ta}=2160$, $Re_{os}=832$, $\sqrt{\omega'}=17.22$ and $A_1=0.39$

The oscillation frequency, f is 4 Hz. Therefore, the second part of the detection program which is the *False* case of the structure executes for $f=4$ Hz. As can be seen from Fig. 7.9, the dynamic TDP_4 and TP_2 are shown on the graph as $(dU(r,t)/dt)^2/(\bar{U}_{ta}^2\omega^2)$ and $(1/\sqrt{\omega'})^4$, respectively. For $f=4$ Hz ($\sqrt{\omega'}=17.22$), the value of TP_2 is evaluated as $(1/\sqrt{\omega'})^4 = 1/17.22^4 = 11.3 \cdot 10^{-6}$ specified with the dotted line. However, the values of TDP_4 at any instant at $r/R=0.977$ are rather less than the value of the TP_2 of $11.3 \cdot 10^{-6}$. Hence no transition to turbulence is detected on the velocity waveform at $r/R=0.977$ by the turbulence detection program, which is also shown in Fig. 4.7. As can be seen from Fig. 4.7, transition to turbulence is not

observed at any r/R on the waveform graph, contrary to Fig. 7.6 which is corresponding to the transitional regime at $Re_{ta}=3018$, $Re_{os}=1610$, $\sqrt{\omega'}=2.72$ and $A_1=0.53$. For the same run, the transition to turbulence is also not detected by the devised program for any other radial positions of the hotwire probe.

In this study, it is exactly observed that transition to turbulence is detected firstly near the pipe wall at $r/R=0.977$ for all runs and whether it propagates to the center of the pipe ($r/R=0$) or disappears before reaching the pipe centerline which is denoted as relaminarization. Hence it is deduced that transition to turbulence always generates at the radial position near the pipe wall.

On the other hand, Figure 7.10 illustrates the graphical result of the detection method for the flow regime at $Re_{ta}=3018$, $Re_{os}=1610$, $\sqrt{\omega'}=2.72$ and $A_1=0.53$ at $r/R=0$.

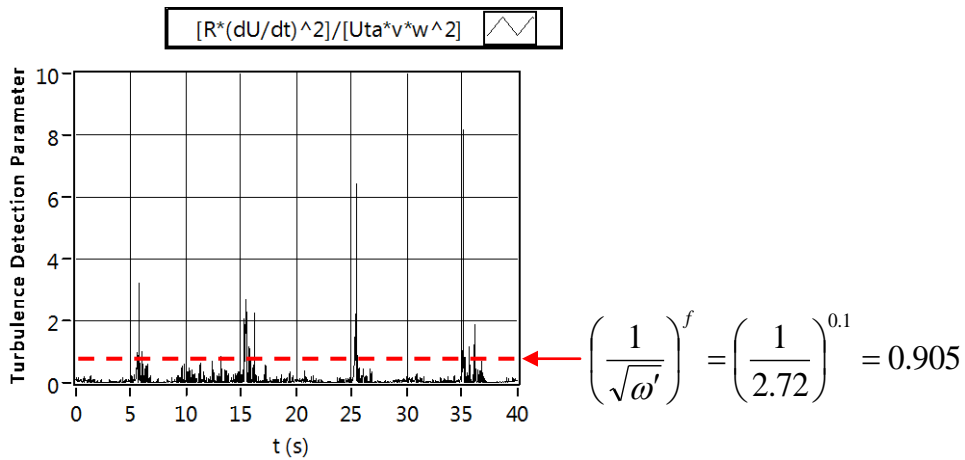


Figure 7.10. Variation of TDP_3 at $r/R=0$ at $Re_{ta}=3018$, $Re_{os}=1610$, $\sqrt{\omega'}=2.72$ and $A_1=0.53$

For this run, the first part of the detection program which is *True* case of the structure for $f \leq 1$ Hz executes due to the oscillation frequency being $f=0.1$ Hz. Therefore TDP_3

and TP_1 become as $R(dU(r,t)/dt)^2/(\bar{U}_{ia}v\omega^2)$ and $(1/\sqrt{\omega'})^n$, respectively. For $f=0.1$ Hz, the value of TP_1 is evaluated by the devised program as $(1/\sqrt{\omega'})^n = (1/2.72)^{0.1} = 0.905$ where $n=|f|=0.1$, which is illustrated with the dotted line on the graph. As can be seen from Fig. 7.10, there are peaks on the graph which represents the transition to turbulence. The values of TDP_3 at these peaks are rather over $TP_1=0.905$. Hence the program detects the transition to turbulence at $r/R=0$. The transition to turbulence corresponding to this run is seen previously in Figs. 7.5 and 7.6 which illustrate the velocity waveform at $r/R=0$ and one-period velocity waveforms for all r/R , respectively. Transition to turbulence is also detected at $r/R=0.977$ and all other r/R positions as seen in Figs. 7.7 and 7.8. Hence the corresponding run at $Re_{ia}=3018$, $Re_{os}=1610$, $\sqrt{\omega'}=2.72$ and $A_1=0.53$ is fully transitional due to the detection of the transition to turbulence at all r/R .

As can be noticed from Fig. 7.10, the occurrence of the transition to turbulence has also time periodicity, due to the propagations of the turbulent plugs to downstream of the pipeline, such that the peaks appear at the definite time and period, i.e. at $t=6$ s, 16 s, 26 s and 36 s with the incremental of 10 s which is the period of $T=10$ s for $f=0.1$ Hz.

TDFC.vi then save automatically all data, the corresponding charts and graphs related to this run to the file named as “(Transitional Regime) $Re_{ia}=3018$; $Re_{os}=1610$; $fre=0.10$; $wom=2.72$ ”.

7.5. Conclusion

Transition to turbulence in pulsatile pipe flow is detected using a new method. The transition detection method is a part of *TDFC.vi* introduced in Chapter 4. This detection method gives the originality to both the devised program and the presented study.

It is difficult to detect the transition to turbulence by observing the turbulent bursts in velocity waveforms. Therefore a detection method is essential to develop for the investigation of transition to turbulence. In this respect, a new method and program are constructed. Two different *turbulence detection parameters* and two different *threshold parameters* are defined for low ($f \leq 1$ Hz) and high ($f > 1$ Hz) frequencies in this program. The dynamic TDP_3 and TDP_4 are found as $R(dU(r,t)/dt)^2 / (\bar{U}_{ia} v \omega^2)$ for $f \leq 1$ Hz and $(dU(r,t)/dt)^2 / (\bar{U}_{ia}^2 \omega^2)$ for $f > 1$ Hz, respectively. The dynamic TP_1 and TP_2 are found as $(1/\sqrt{\omega'})^n$ for $f \leq 1$ Hz and $(1/\sqrt{\omega'})^4$ for $f > 1$ Hz, respectively.

The new transition to turbulence method constructed in *TDFC.vi* is checked and controlled so many times and its verification is satisfied. It is found to be accurate for the detection of the onset of transition to turbulence. Hence this method and the devised program are seen to be very useful for the further studies conducted on the detection of the transition to turbulence in time dependent pipe flows.

CHAPTER 8

PULSATILE FLOW DYNAMICS IN LAMINAR REGIME AND AT THE ONSET OF TRANSITION

8.1. Introduction

Flow dynamics of pulsatile pipe flow in laminar regime and at the onset of the transition to turbulence are experimentally investigated. Pulsatile flow dynamics through 28 runs in laminar regime and 199 runs at the onset of transition to turbulence regime given in Table 8.1 are presented in this chapter.

Table 8.1. Characteristic parameters of the experimental study

Run No	f (Hz)	$\sqrt{\omega'}$	A_1	Re_{ta}	Re_{os}	Re_{δ_s}	Run No	f (Hz)	$\sqrt{\omega'}$	A_1	Re_{ta}	Re_{os}	Re_{δ_s}
1	0.10	2.72	0.10	2702	272	71	27	0.20	3.85	0.10	2720	270	50
2			0.12	2653	321	83	28			0.20	2907	572	105
3			0.18	2416	438	114	29			0.22	2846	615	113
4			0.19	2799	544	141	30			0.29	3272	934	172
5			0.20	2789	572	149	31			0.30	3278	987	181
6			0.22	2922	646	168	32			0.31	3358	1029	189
7			0.25	2994	745	194	33			0.36	3801	1377	253
8			0.30	3100	915	238	34			0.40	4138	1672	307
9			0.34	3062	1030	268	35			0.42	4138	1733	318
10			0.38	3128	1193	310	36			0.43	4087	1732	318
11			0.40	3101	1240	322	37			0.44	4208	1839	338
12			0.43	3133	1338	348	38			0.47	4211	1996	367
13			0.50	2984	1516	394	39			0.5	4292	2165	398
14			0.53	3018	1610	418	40			0.56	4243	2397	440
15			0.59	2983	1766	459	41			0.6	4126	2468	453
16			0.60	2940	1763	459	42			0.61	3696	2264	416
17			0.70	2810	1970	512	43			0.66	4196	2781	511
18			0.71	2805	2001	520	44			0.69	4159	2888	531
19			0.73	2759	2016	524	45			0.70	4155	2922	537
20			0.77	2847	2200	572	46			0.76	3803	2871	527
21			0.8	2778	2209	574	47			0.79	3058	2438	448
22			0.84	2770	2316	602	48			0.80	4436	3533	649
23			0.85	2781	2351	611	49			0.81	4420	3564	655
24			0.87	2884	2517	654	50			0.82	4817	3939	724
25			0.9	2846	2567	667	51			0.88	4767	4211	773
26			0.96	2347	2248	584	52			0.90	4761	4261	783
53	0.40	5.44	0.1	2764	273	36	77	0.60	6.67	0.10	2729	277	29
54			0.2	2924	578	75	78			0.20	2703	541	57
55			0.24	2661	637	83	79			0.22	2707	583	62
56			0.27	3203	868	113	80			0.27	2749	729	77
57			0.28	3192	900	117	81			0.28	2836	803	85
58			0.3	3176	957	124	82			0.30	2884	864	92
59			0.35	2807	987	128	83			0.31	2913	906	96
60			0.37	3601	1347	175	84			0.37	3109	1141	121
61			0.4	3472	1397	181	85			0.40	3271	1293	137
62			0.48	2325	1108	144	86			0.41	2893	1184	126
63			0.49	3707	1833	238	87			0.47	3265	1529	162
64			0.5	3887	1940	252	88			0.50	3229	1616	171
65			0.51	2150	1094	142	89			0.51	3241	1641	174
66			0.55	3684	2009	261	90			0.53	2261	1209	128
67			0.56	3914	2184	284	91			0.60	3181	1907	202
68			0.59	4067	2416	314	92			0.64	1239	795	84
69			0.6	4051	2423	315	93			0.66	3223	2133	226
70			0.69	3513	2418	314	94			0.68	3245	2220	235
71			0.7	3506	2451	318	95			0.70	3238	2257	239
72			0.77	3251	2499	325	96			0.71	3132	2221	236
73			0.78	3463	2707	352	97			0.77	3163	2451	260
74			0.8	3448	2760	358	98			0.80	3247	2587	274
75			0.81	3456	2783	361	99			0.86	3330	2862	304
76			0.9	3433	3040	395	100			0.90	3368	2928	311

Run No	f (Hz)	$\sqrt{\omega'}$	A_1	Re_{ta}	Re_{os}	Re_{δ_s}	Run No	f (Hz)	$\sqrt{\omega'}$	A_1	Re_{ta}	Re_{os}	Re_{δ_s}
101	0.8	7.70	0.10	2669	265	24	122	1	8.61	0.10	2807	274	22
102			0.20	2644	509	47	123			0.19	2759	521	43
103			0.24	2839	682	63	124			0.20	2718	562	46
104			0.29	2822	826	76	125			0.23	2825	671	55
105			0.30	2823	850	78	126			0.30	2889	858	71
106			0.32	2307	732	67	127			0.31	2891	883	73
107			0.38	2980	1132	104	128			0.34	2233	754	62
108			0.40	3188	1291	119	129			0.35	3023	1049	86
109			0.41	3195	1322	121	130			0.40	3058	1206	99
110			0.41	2765	1140	105	131			0.45	3231	1464	120
111			0.45	2992	1348	124	132			0.50	2959	1493	123
112			0.46	2548	1164	107	133			0.55	1473	804	66
113			0.50	3144	1587	146	134			0.60	3051	1831	150
114			0.60	3132	1862	171	135			0.70	3118	2174	179
115			0.70	3200	2234	205	136			0.71	1082	773	64
116			0.71	3219	2281	209	137			0.71	3145	2227	183
117			0.72	3270	2364	217	138			0.73	3198	2338	192
118			0.80	3174	2541	233	139			0.78	3146	2461	202
119			0.83	3200	2646	243	140			0.79	3215	2546	209
120			0.86	3328	2849	262	141			0.80	3208	2571	211
121			0.90	3295	2930	269	142			0.90	3157	2748	226
143	2	12.17	0.10	2592	261	15	163	4	17.22	0.10	2638	277	11
144			0.20	2578	505	29	164			0.15	2662	405	17
145			0.29	2568	741	43	165			0.20	2774	549	23
146			0.30	2541	766	44	166			0.22	2635	569	24
147			0.39	2549	985	57	167			0.30	2654	780	32
148			0.40	2619	1050	61	168			0.39	2160	832	34
149			0.42	2408	1000	58	169			0.40	2677	1087	45
150			0.50	2639	1324	77	170			0.43	1019	443	18
151			0.51	2698	1365	79	171			0.48	2811	1337	54
152			0.53	2831	1500	87	172			0.50	2722	1345	55
153			0.60	2845	1702	99	173			0.51	2695	1378	57
154			0.61	2834	1729	100	174			0.52	1699	888	36
155			0.69	2809	1931	112	175			0.59	2656	1560	64
156			0.70	1390	978	57	176			0.60	2669	1604	66
157			0.70	2815	1960	114	177			0.62	2692	1674	69
158			0.75	2874	2146	125	178			0.66	2891	1914	78
159			0.76	2908	2198	128	179			0.70	2751	1928	79
160			0.80	2852	2302	134	180			0.71	2762	1973	81
161			0.81	2869	2333	136	181			0.76	2803	2135	88
162			0.90	2913	2567	149	182			0.77	2878	2221	91
							183			0.80	2811	2237	92
					184	0.90	2628	2339	96				
185	10	27.22	0.10	2779	284	7	206	14	32.21	0.05	2509	137	3
186			0.12	2762	340	9	207			0.07	1449	107	2
187			0.20	2763	572	15	208			0.10	2582	253	6
188			0.28	1294	366	9	209			0.20	2640	538	12
189			0.30	2873	858	22	210			0.23	2692	607	13
190			0.33	2403	788	20	211			0.27	2674	731	16
191			0.36	2876	1045	27	212			0.29	2712	774	17
192			0.40	2916	1192	31	213			0.30	2728	808	18
193			0.45	2807	1276	33	214			0.35	2643	933	20
194			0.50	2898	1486	39	215			0.40	2688	1147	25
195			0.60	2744	1612	42	216			0.43	2862	1235	27
196			0.62	2868	1764	46	217			0.50	2531	1272	28
197			0.64	2920	1869	49	218			0.55	2662	1453	32
198			0.65	3052	1992	52	219			0.58	2776	1621	36
199			0.70	3036	2084	54	220			0.60	2793	1658	36
200			0.72	2986	2135	55	221			0.62	2739	1702	37
201			0.77	2781	2153	56	222			0.63	2739	1714	38
202			0.80	2795	2209	57	223			0.66	2671	1754	38
203			0.81	2848	2303	60	224			0.68	2650	1803	40
204			0.85	2955	2501	65	225			0.70	2799	1945	43
205			0.90	2935	2709	70	226			0.74	2877	2121	47
					227	0.80	2861	2260	50				

In the experimental study, the transition to turbulence detection method is divided into two parts for $f \leq 1$ Hz and $f > 1$ Hz because the turbulence detection parameter which is valid for $f \leq 1$ Hz is not suitable for $f > 1$ Hz as can be introduced in the previous chapter. The critical Womersley number corresponding to the critical oscillation frequency of $f=1$ Hz is $\sqrt{\omega'} = 8.61$, which is also found as critical value as a result of comprehensive literature survey as can be seen from Figs. 8.1 and 8.2.

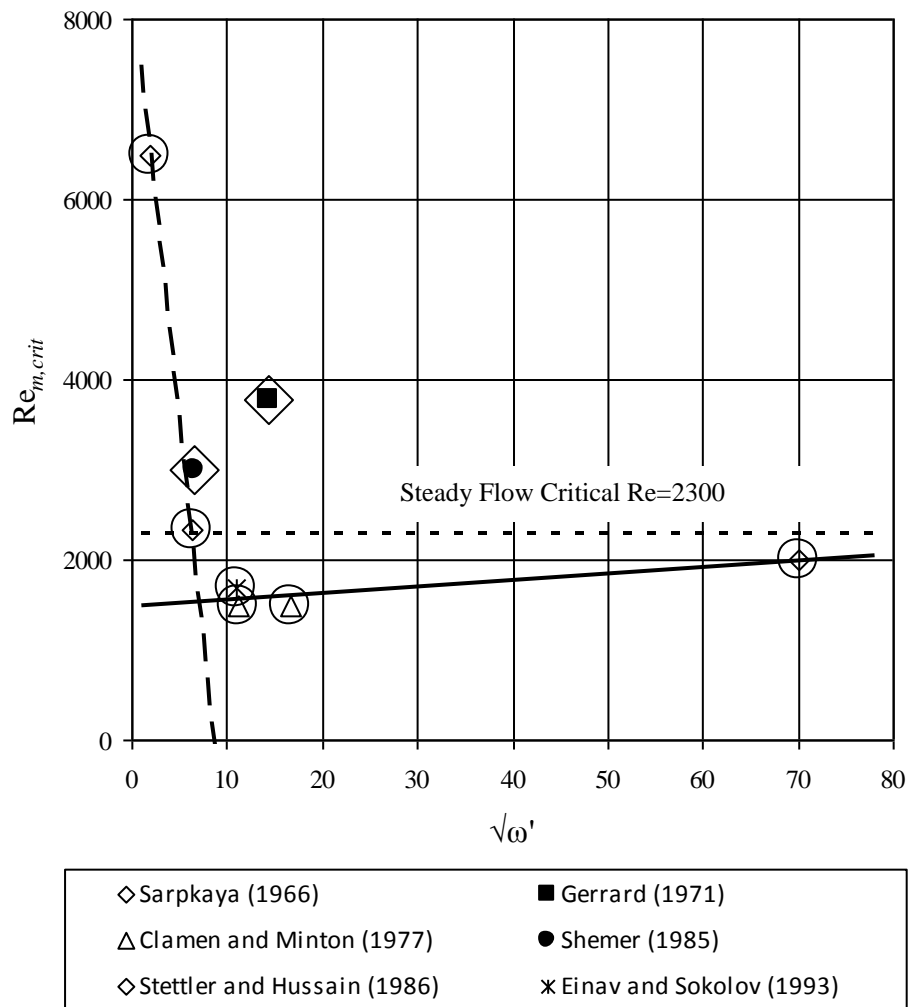


Figure 8.1. Available data for the onset and the end of transition in pulsatile pipe flows in terms of $Re_{m,crit}$

(○) onset of transition; (◇) end of transition)

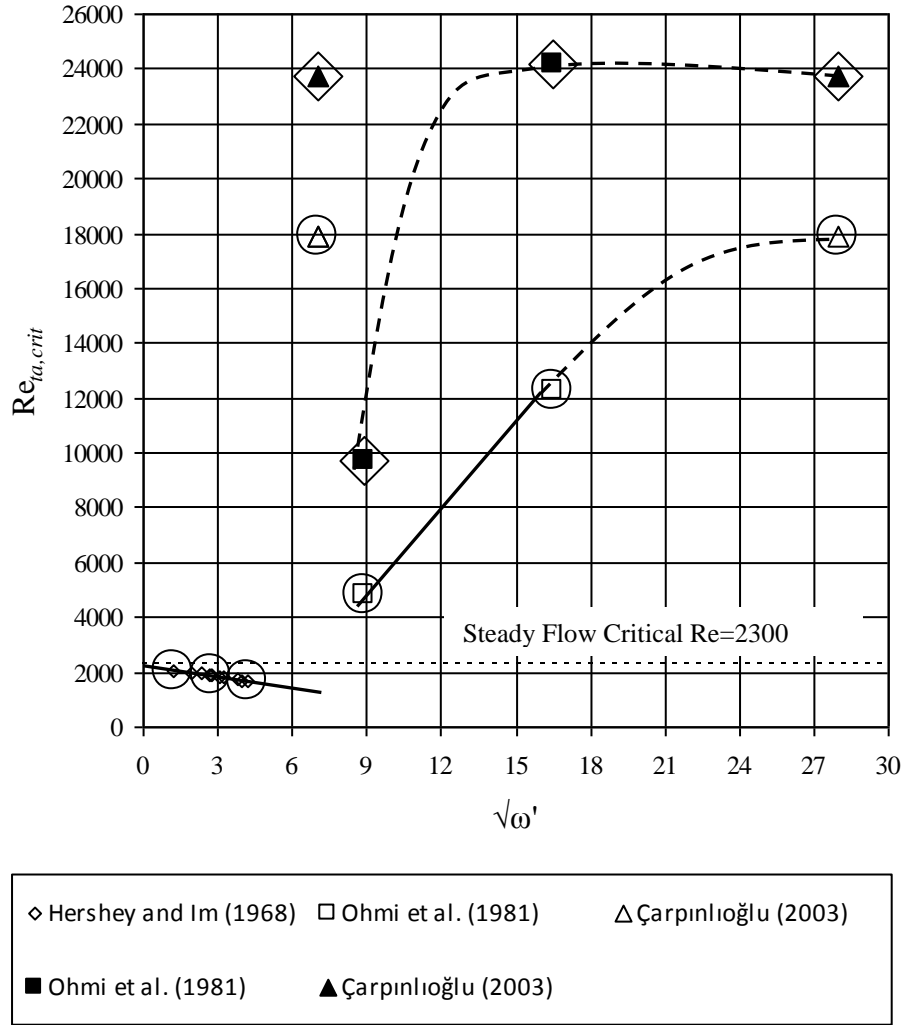


Figure 8.2. Available data for the onset and the end of transition in pulsatile pipe flows in terms of $Re_{ta,crit}$

(○ onset of transition; ◇ end of transition)

Figures 8.1 and 8.2 illustrate the available data on pulsatile flows in terms of $Re_{m,crit} = Re_{m,crit}(\sqrt{\omega'})$ and $Re_{ta,crit} = Re_{ta,crit}(\sqrt{\omega'})$, respectively as a result of literature survey. Although the covered range of $\sqrt{\omega'}$ is $0 < \sqrt{\omega'} < 70$, the available data are confined to the range of $0 < \sqrt{\omega'} < 20$ as can be seen in Fig. 8.1. The steady flow case with $\sqrt{\omega'} = 0$ is also given in the figures by $Re = 2300$. As can be seen from Fig. 8.1, there are two different characteristics of the relations between $Re_{m,crit}$ and

$\sqrt{\omega'}$ described by a dashed line and a solid line drawn in the ranges of $1 < \sqrt{\omega'} < 8$ and $8 < \sqrt{\omega'} < 70$, respectively. For low frequencies, an increase in $\sqrt{\omega'}$ causes a decrease in $Re_{m,crit}$ while, for high frequencies, an increase in $\sqrt{\omega'}$ causes an increase in $Re_{m,crit}$. No analysis can be done in terms of the end of transition due to the insufficient data. The study of Çarpınlioğlu (2003) is based on the investigation of flow dynamics of laminar and turbulent pulsatile pipe flow. Hence the specified points in Fig. 8.2 as the onset and the end of transition are just comment anticipated from the results of the PhD. study of Gündoğdu (2001).

The available data in the literature in terms of $Re_{ta,crit}$ as a function of $\sqrt{\omega'}$ are expressed in Fig. 8.2. The same characteristics for $1 < \sqrt{\omega'} < 8$ and $\sqrt{\omega'} > 8$ are seen in conformity with the above-mentioned expressions. Similarly, for low frequencies in the range of $1 < \sqrt{\omega'} < 8$, an increase in $\sqrt{\omega'}$ causes a decrease in $Re_{ta,crit}$ while, for high frequencies, an increase in $\sqrt{\omega'}$ causes an increase in $Re_{ta,crit}$. In the range of $\sqrt{\omega'} < 8$, the data of Hershey and Im (1968) show that an increase in $\sqrt{\omega'}$ results in a decrease in $Re_{ta,crit}$, whose magnitudes are even less than 2300. However, in the range of $8 < \sqrt{\omega'} < 30$, an increase in $\sqrt{\omega'}$ causes an increase in $Re_{ta,crit}$ for the onset and the end of transition.

In view of these figures, it is expressed that $f=1$ Hz ($\sqrt{\omega'}=8.61$) can be determined as critical state such that this critical number of $f=1$ Hz ($\sqrt{\omega'}=8.61$) is also verified in the following analyses of pulsatile flow dynamics for random selected runs in laminar regime and at the onset of transition to turbulence regime.

8.2. Pulsatile Laminar Regime

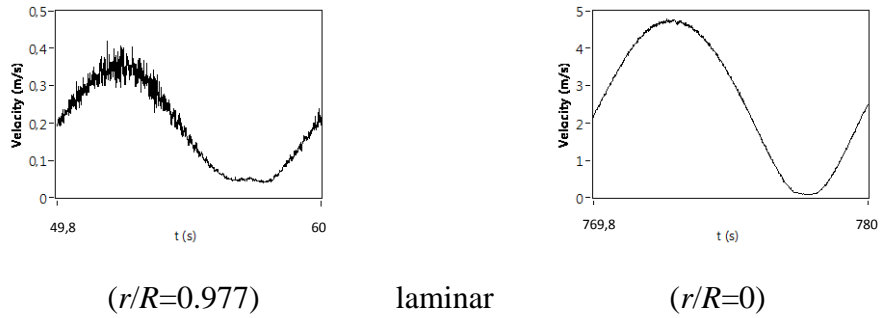
Several runs corresponding to the laminar regime are naturally obtained in the study during the detection of transition to turbulence in pulsatile pipe flow.

8.2.1. Velocity waveforms in pulsatile laminar regime

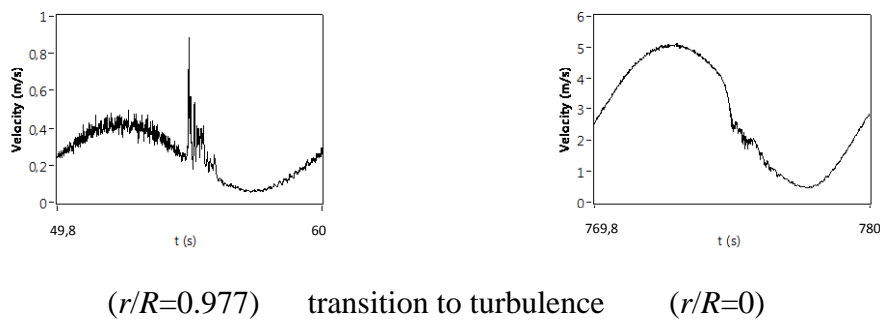
The sample velocity waveforms corresponding to laminar regime are given in this section through Figs. 8.3 and 8.12. The velocity waveforms at the onset of the transition to turbulence are also given to show and verify the differences on velocity waveforms in laminar regime and at the onset of transition. The plots are selected for both $r/R=0.977$ and $r/R=0$ covering all $\sqrt{\omega'}$ in the range of $2.72 \leq \sqrt{\omega'} \leq 32.21$ and for different velocity amplitude ratios of A_1 . In this section, the first two upper plots of velocity waveforms are corresponding to the laminar regime and the last two plots are corresponding to the velocity waveforms at the onset of transition in each figure. The shapes of the velocity profiles are sinusoidal at both $r/R=0.977$ and $r/R=0$ as shown in all figures in this section.

Figure 8.3 shows the velocity waveforms in laminar regime and at the onset of transition for $\sqrt{\omega'}=2.72$ ($f=0.1$ Hz). The small perturbations on the velocity waveform at $r/R=0.977$ in laminar regime (Fig. 8.3a) are due to the wall effect and they do not imply the onset of transition. The transition to turbulence is clearly observed as sensible peaks or collapses on the waveforms at the onset of transition in Fig. 8.3b. These peaks and collapses are defined in the literature (Wynanski and Champagne, 1973), (Wynanski et al., 1975), (Durst and Ünsal, 2006) as puffs in steady transitional flows.

The influence of velocity amplitude ratio, A_1 on flow dynamics is also verified in Fig. 8.3. Although the transition to turbulence is observed at the decelerating phases of waveforms for $A_1=0.84$ in Fig. 8.3b, the flow regime becomes laminar for $A_1=0.96$ as seen in Fig. 8.3a at constant value of $f=0.1$ Hz ($\sqrt{\omega'}=2.72$). Hence it is deduced that the turbulent bursts disappear by keeping the oscillation frequency, f (in other words $\sqrt{\omega'}$) constant and increasing the velocity amplitude ratio, A_1 , which has also been declared in the study of Ertunç et al. (2003).



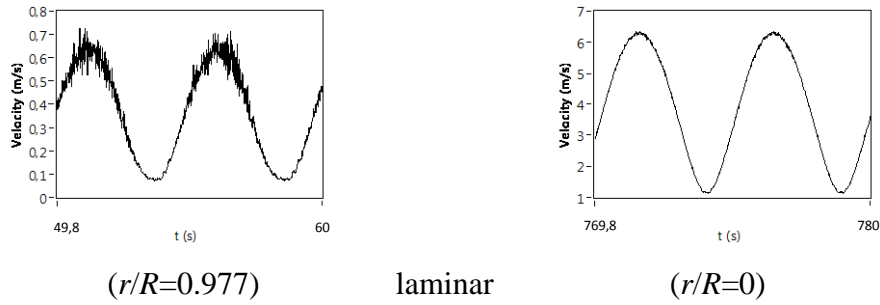
(a) $Re_{ta}=2347$, $Re_{os}=2248$, $\sqrt{\omega'}=2.72$ and $A_1=0.96$



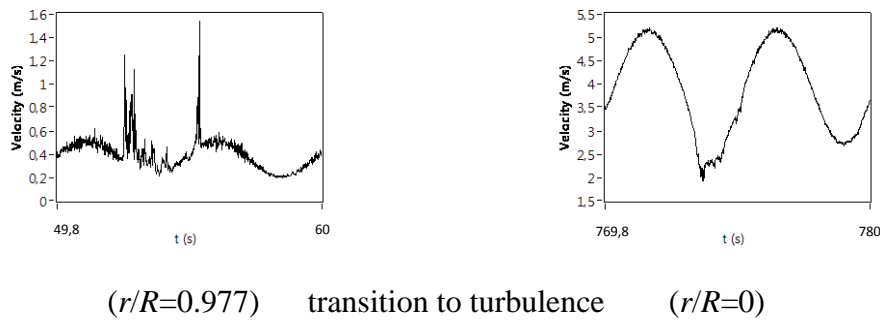
(b) $Re_{ta}=2770$, $Re_{os}=2316$, $\sqrt{\omega'}=2.72$ and $A_1=0.84$

Figure 8.3. Velocity waveforms in laminar and at the onset of transition at $r/R=0.977$ and $r/R=0$ for $\sqrt{\omega'}=2.72$

The velocity waveforms in the laminar regime and at the onset of transition at $\sqrt{\omega'}=3.85$ ($f=0.2$ Hz) are seen in Figs. 8.4a and 8.4b, respectively. The wall effect on the velocity profiles at $r/R=0.977$ is seen in the figures. The effect of A_1 on the flow dynamics is seen once more at $\sqrt{\omega'}=3.85$ ($f=0.2$ Hz). Although the transition to turbulence is seen at $A_1=0.36$, the increase of velocity amplitude ratio to $A_1=0.76$ at $Re_{ta}\approx 3800$ stabilizes the flow and the turbulent bursts at both $r/R=0.977$ and $r/R=0$ disappear resulting in laminar flow.



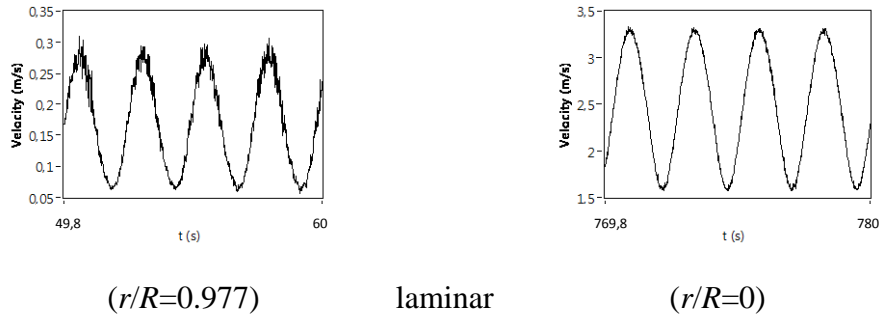
(a) $Re_{ta}=3803$, $Re_{os}=2871$, $\sqrt{\omega'}=3.85$ and $A_1=0.76$



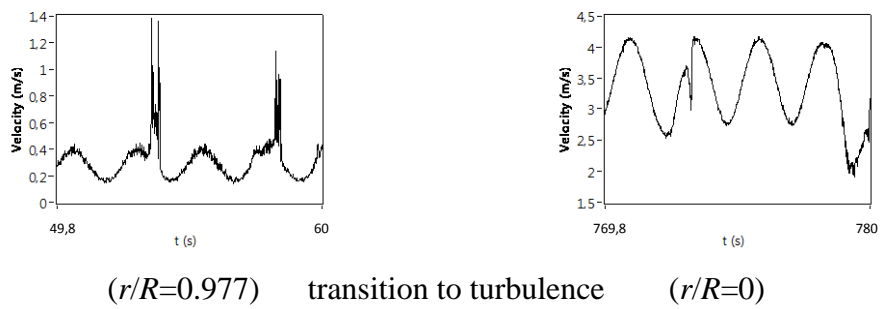
(b) $Re_{ta}=3801$, $Re_{os}=1377$, $\sqrt{\omega'}=3.85$ and $A_1=0.36$

Figure 8.4. Velocity waveforms in laminar and at the onset of transition at $r/R=0.977$ and $r/R=0$ for $\sqrt{\omega'}=3.85$

Figure 8.5 shows the sinusoidal velocity waveforms in laminar and at the onset of transition to turbulence regimes at $\sqrt{\omega'}=5.44$ ($f=0.4$ Hz). The flow is seen to be laminar at $A_1=0.51$ and starts to transition to turbulence at $A_1=0.28$. The turbulent bursts are always seen in the decelerating phase at $r/R=0.977$. The bursts can occur in both decelerating and accelerating phases of waveforms at $r/R=0$ for $\sqrt{\omega'} \geq 5.44$ ($f \geq 0.4$ Hz). However the bursts are always seen in the decelerating phases at $\sqrt{\omega'}=2.72$ ($f=0.1$ Hz) and $\sqrt{\omega'}=3.85$ ($f=0.2$ Hz).



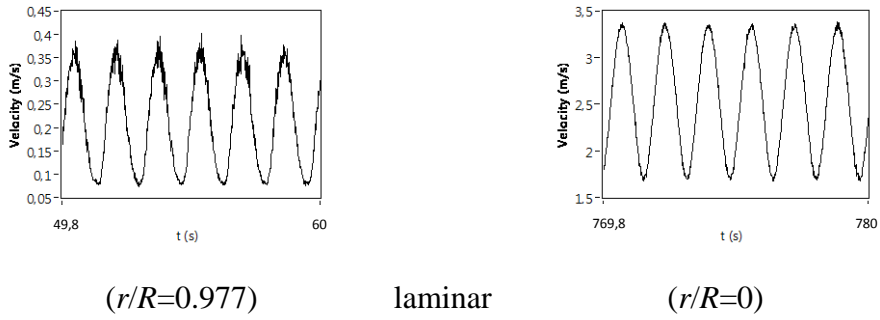
(a) $Re_{ta}=2150$, $Re_{os}=1094$, $\sqrt{\omega'}=5.44$ and $A_1=0.51$



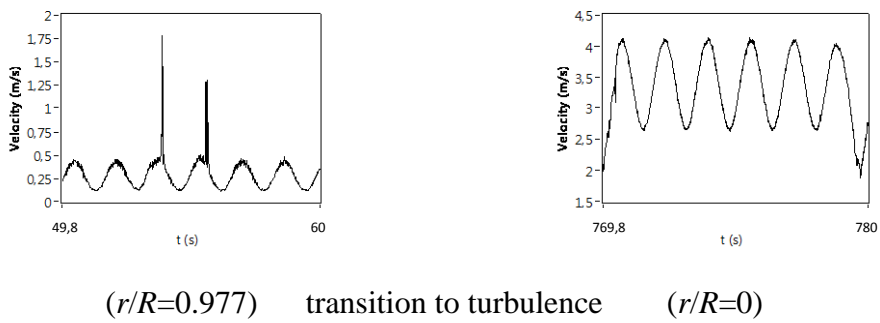
(b) $Re_{ta}=3192$, $Re_{os}=900$, $\sqrt{\omega'}=5.44$ and $A_1=0.28$

Figure 8.5. Velocity waveforms in laminar and at the onset of transition at $r/R=0.977$ and $r/R=0$ for $\sqrt{\omega'}=5.44$

The velocity waveforms at $\sqrt{\omega'}=6.67$ ($f=0.6$ Hz), $\sqrt{\omega'}=7.70$ ($f=0.8$ Hz) and $\sqrt{\omega'}=8.61$ ($f=1$ Hz) in laminar regime and at the onset of transition are given through Figs. 8.6 and 8.8, respectively. In laminar regimes (Figs. 8.6a, 8.7a and 8.8a), no bursts are seen for both $r/R=0.977$ and $r/R=0$. The shapes of the velocity profiles are sinusoidal. The wall effect is observed at $r/R=0.977$ in these figures. The destabilizing effect of A_1 on the velocity waveforms is observed when A_1 is decreased through Figs. 8.6b and 8.8b.

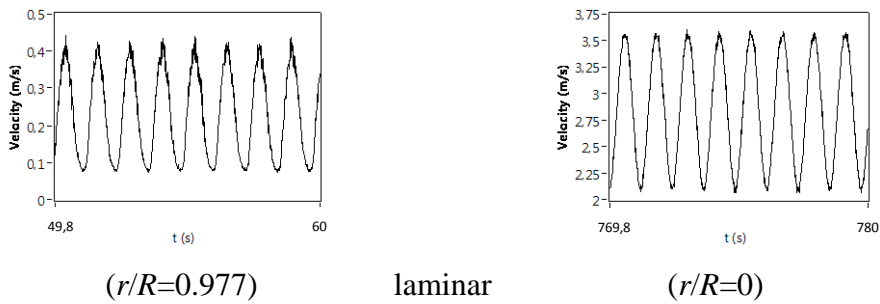


(a) $Re_{ta}=2261$, $Re_{os}=1209$, $\sqrt{\omega'}=6.67$ and $A_1=0.53$

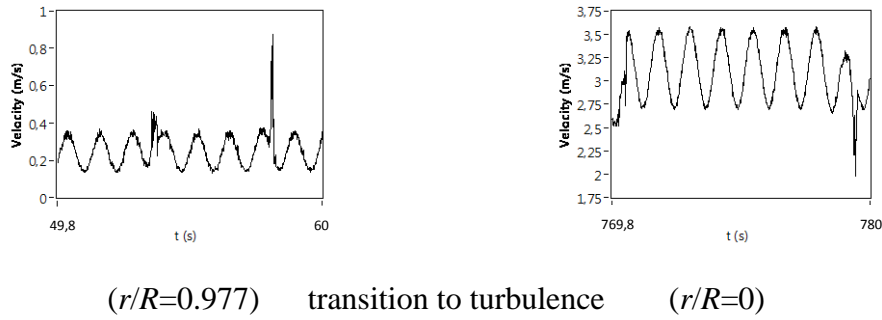


(b) $Re_{ta}=3109$, $Re_{os}=1141$, $\sqrt{\omega'}=6.67$ and $A_1=0.37$

Figure 8.6. Velocity waveforms in laminar and at the onset of transition at $r/R=0.977$ and $r/R=0$ for $\sqrt{\omega'}=6.67$

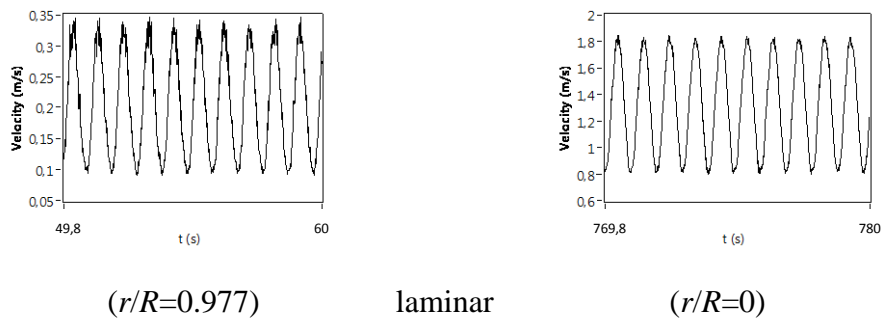


(a) $Re_{ta}=2548$, $Re_{os}=1164$, $\sqrt{\omega'}=7.70$ and $A_1=0.46$

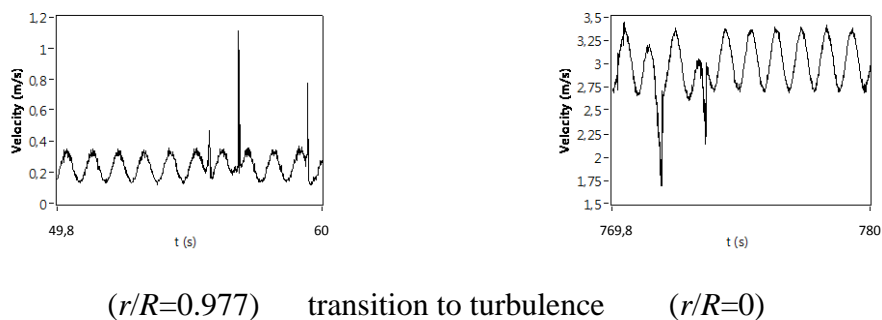


(b) $Re_{ta}=2839$, $Re_{os}=682$, $\sqrt{\omega'}=7.70$ and $A_1=0.24$

Figure 8.7. Velocity waveforms in laminar and at the onset of transition at $r/R=0.977$ and $r/R=0$ for $\sqrt{\omega'}=7.70$



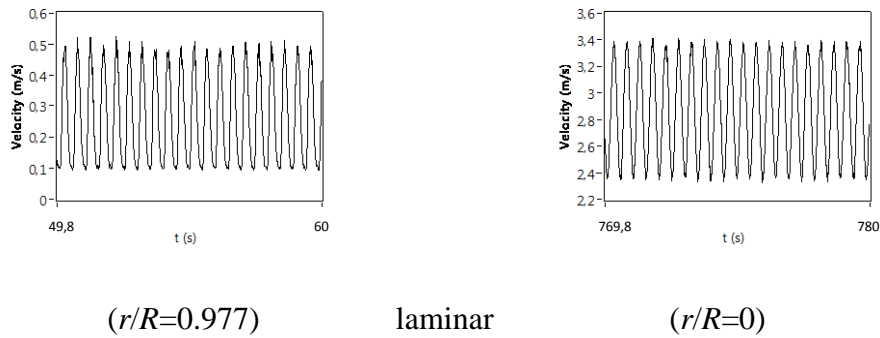
(a) $Re_{ta}=1082$, $Re_{os}=773$, $\sqrt{\omega'}=8.61$ and $A_1=0.71$



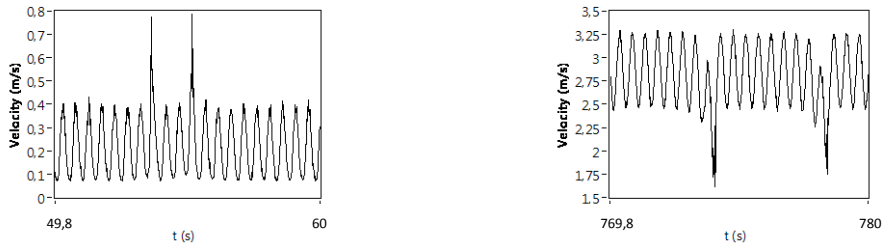
(b) $Re_{ta}=2759$, $Re_{os}=521$, $\sqrt{\omega'}=8.61$ and $A_1=0.19$

Figure 8.8. Velocity waveforms in laminar and at the onset of transition at $r/R=0.977$ and $r/R=0$ for $\sqrt{\omega'}=8.61$

In conformity with the literature survey as expressed in the introduction section of this chapter, the verification of the critical range of oscillation frequency, $f > 1$ Hz, in other words $\sqrt{\omega'} > 8.61$ is satisfied by means of observation of the different behavior of turbulent bursts at $r/R=0$ at the onset of the transition to turbulence. The velocity waveforms in the range of $12.17 \leq \sqrt{\omega'} \leq 32.21$ ($2 \text{ Hz} \leq f \leq 14 \text{ Hz}$) are given through Figs. 8.9 and 8.12. The velocity profiles are in sinusoidal shape and no turbulent bursts are observed in laminar regime through Figs. 8.9a and 8.12a. As can be noticed through Figs. 8.9b and 8.12b, the behaviors of the turbulent bursts at $r/R=0$ are different than collapse. The turbulent bursts are seen to be like sudden and sharp drops at the decelerating phase at the onset of transition, rather than previously observed collapse shape for $f \leq 1$ Hz. As stated before, the increase in A_1 stabilize the flow for $\sqrt{\omega'} < 32.21$ ($f < 14 \text{ Hz}$) and the flow becomes as laminar as seen Figs. 8.9a and 8.11a. However, there is an adverse effect of A_1 for $\sqrt{\omega'} = 32.21$ ($f = 14 \text{ Hz}$) such that an increase in A_1 destabilize the flow.



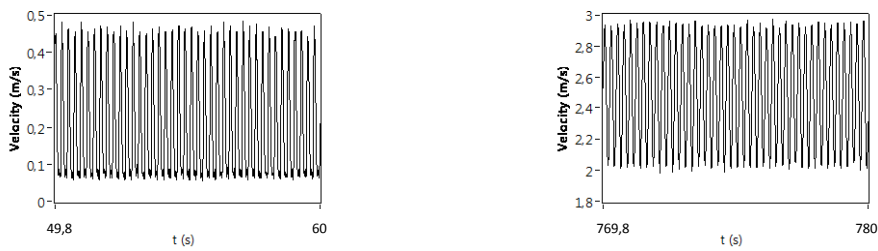
(a) $Re_{ta} = 2549$, $Re_{os} = 958$, $\sqrt{\omega'} = 12.17$ and $A_1 = 0.39$



($r/R=0.977$) transition to turbulence ($r/R=0$)

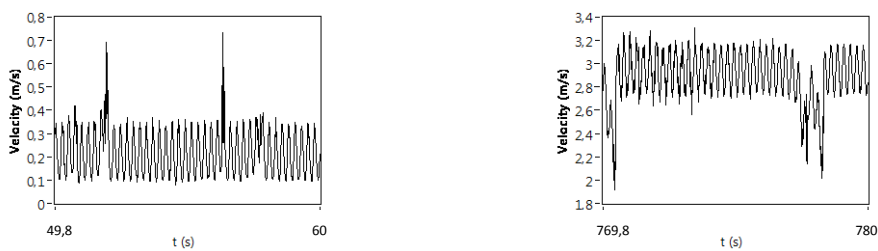
(b) $Re_{ta}=2541$, $Re_{os}=766$, $\sqrt{\omega'}=12.17$ and $A_1=0.30$

Figure 8.9. Velocity waveforms in laminar and at the onset of transition at $r/R=0.977$ and $r/R=0$ for $\sqrt{\omega'}=12.17$



($r/R=0.977$) laminar ($r/R=0$)

(a) $Re_{ta}=2160$, $Re_{os}=832$, $\sqrt{\omega'}=17.22$ and $A_1=0.39$

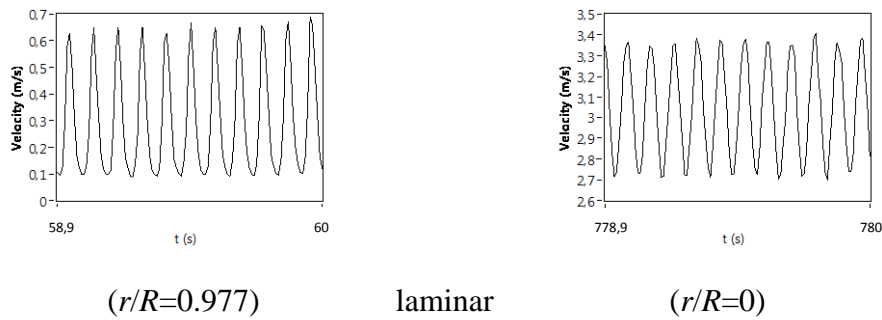


($r/R=0.977$) transition to turbulence ($r/R=0$)

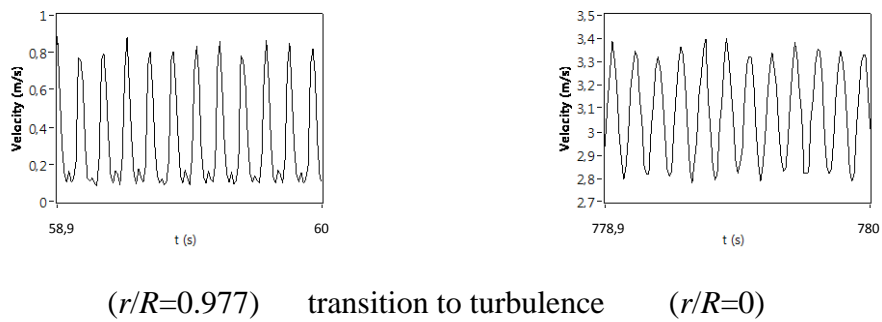
(b) $Re_{ta}=2662$, $Re_{os}=405$, $\sqrt{\omega'}=17.22$ and $A_1=0.15$

Figure 8.10. Velocity waveforms in laminar and at the onset of transition at $r/R=0.977$ and $r/R=0$ for $\sqrt{\omega'}=17.22$

On the other hand, the turbulent bursts at $r/R=0.977$ are rather different than others for $\sqrt{\omega'}=27.22$ and 32.21 as can be seen from Figs. 8.11b and 8.12b. The turbulent bursts at $r/R=0.977$ are like split puff at the end of decelerating phase of the waveform, which is defined in the Ph. D. study of Nishi (2009).

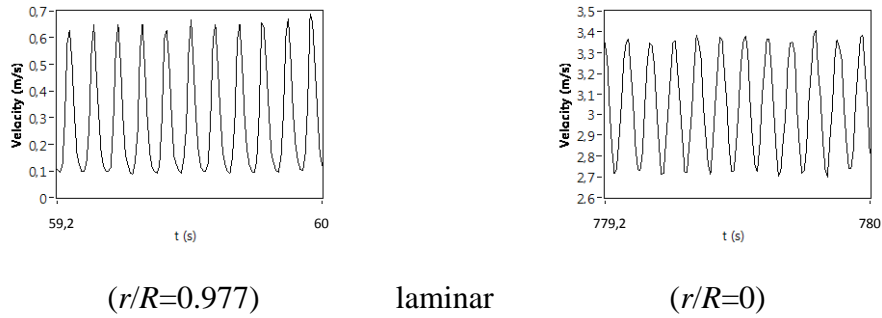


(a) $Re_{ia}=2762$, $Re_{os}=340$, $\sqrt{\omega'}=27.22$ and $A_1=0.12$

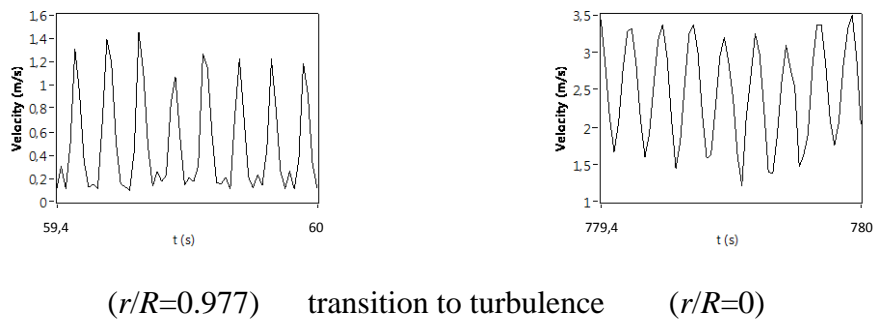


(b) $Re_{ia}=2779$, $Re_{os}=284$, $\sqrt{\omega'}=27.22$ and $A_1=0.10$

Figure 8.11. Velocity waveforms in laminar and at the onset of transition at $r/R=0.977$ and $r/R=0$ for $\sqrt{\omega'}=27.22$



(a) $Re_{ta}=1449$, $Re_{os}=107$, $\sqrt{\omega'}=32.21$ and $A_1=0.07$



(b) $Re_{ta}=2531$, $Re_{os}=1272$, $\sqrt{\omega'}=32.21$ and $A_1=0.50$

Figure 8.12. Velocity waveforms in laminar and at the onset of transition at $r/R=0.977$ and $r/R=0$ for $\sqrt{\omega'}=32.21$

According to the observations on the velocity waveforms, some deductions can be presented as follows:

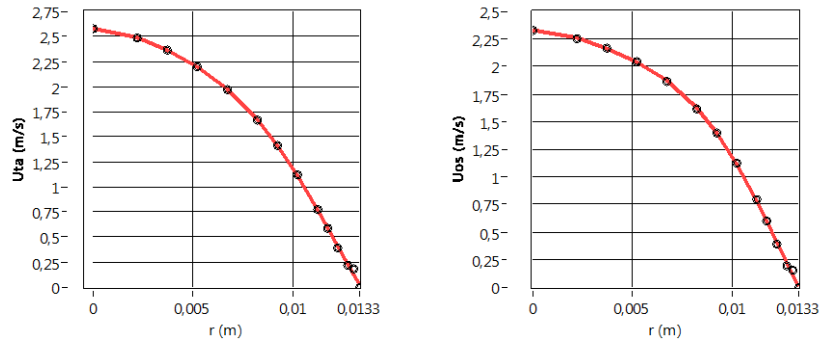
- 1) The observed shapes of the velocity profiles in all runs of the experimental study are sinusoidal.
- 2) The small perturbations on the velocity waveforms at $r/R=0.977$ in laminar regime are due to the wall effect.
- 3) The increase in A_1 causes the shape of the velocity waveforms resembling the laminar one at constant $\sqrt{\omega'}$ for $\sqrt{\omega'} < 32.21$ ($f < 14$ Hz).

4) The condition of $\sqrt{\omega'} \leq 8.61$ ($f \leq 1$ Hz) is verified as the critical state, which is also found as a result of the literature survey. For $\sqrt{\omega'} > 8.61$ ($f > 1$ Hz), the different behavior of turbulent bursts at $r/R=0$ at the onset of the transition to turbulence is observed. The bursts are sudden and sharp drops at the decelerating phase at the onset of transition, rather than previously observed collapse shape for $f \leq 1$ Hz.

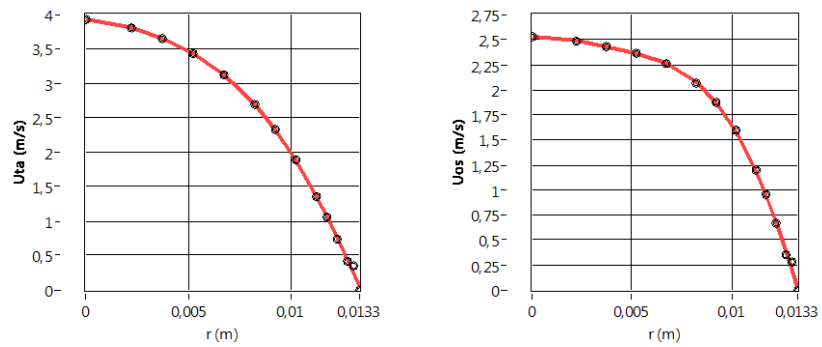
8.2.2. Velocity distributions of time averaged and oscillating components in pulsatile laminar regime

In order to obtain time averaged and oscillating velocity distributions in pulsatile pipe flow, the first method mentioned in previous chapters is used in *TDFC.vi*. In the first method, each time averaged and oscillating component of velocity, \bar{U}_{ta} and $|\bar{U}_{os,1}|$ are evaluated by *TDFC.vi* at each radial position of the hotwire probe. Then evaluated \bar{U}_{ta} and $|\bar{U}_{os,1}|$ data for each radial position through the half of the pipe cross-section are used separately to obtain the cross-sectional \bar{U}_{ta} and $|\bar{U}_{os,1}|$ distributions with respect to radial position, r .

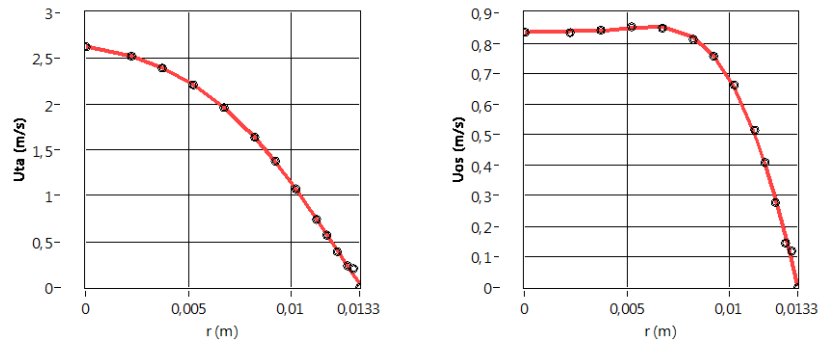
The cross-sectional distributions of \bar{U}_{ta} and $|\bar{U}_{os,1}|$ in laminar regime at $\sqrt{\omega'} = 2.72, 3.85$ and 5.44 for runs 26, 46 and 62 are given in Fig. 8.13. The distributions of \bar{U}_{ta} are parabolic as shown in Fig. 8.14. The distributions of \bar{U}_{ta} is compatible with the steady Blasius profile with a maximum deviation of $\pm 4\%$ for $\sqrt{\omega'} \leq 5.44$. However the distributions of $|\bar{U}_{os,1}|$ are not parabolic and do not obey theoretical steady flow Blasius profile as shown in Fig. 8.15. The cross-sectional distribution of $|\bar{U}_{os,1}|$ begins to collapse near the pipe centerline when $\sqrt{\omega'} \geq 3.85$ as shown in Fig. 8.13.



(a) $Re_{ta}=2347$, $Re_{os}=2248$, $\sqrt{\omega'}=2.72$ and $A_1=0.96$



(b) $Re_{ta}=3803$, $Re_{os}=2871$, $\sqrt{\omega'}=3.85$ and $A_1=0.76$



(c) $Re_{ta}=2325$, $Re_{os}=1108$, $\sqrt{\omega'}=5.44$ and $A_1=0.48$

Figure 8.13. Cross-sectional distributions of \bar{U}_{ta} and $|\bar{U}_{os,1}|$ for runs 26, 46 and 62

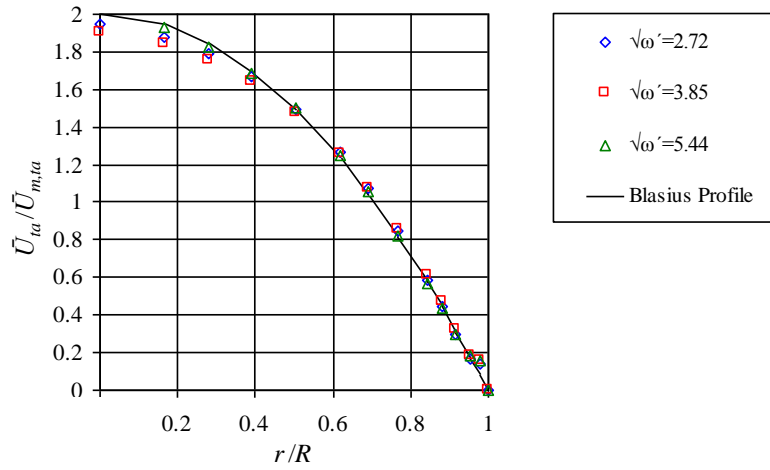


Figure 8.14. Cross-sectional distributions of $\bar{U}_{ta}/\bar{U}_{m,ta}$ with r/R for runs 26, 46 and 62

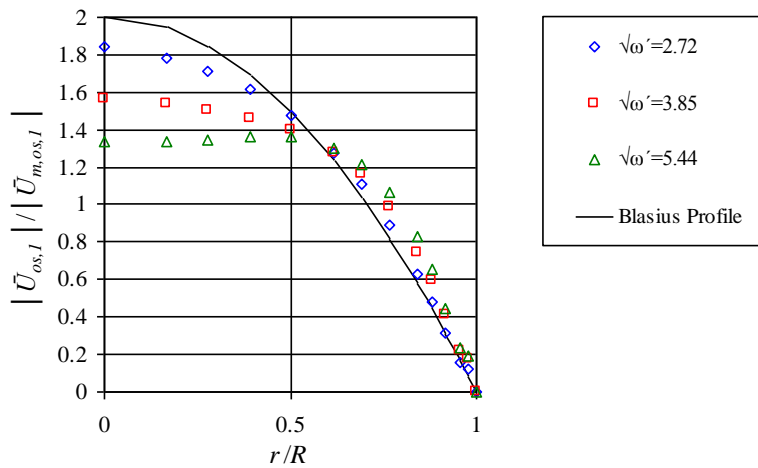
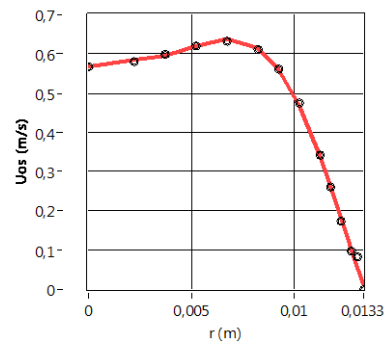
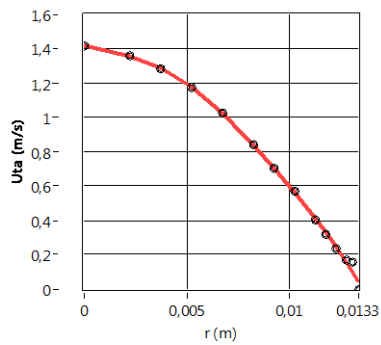


Figure 8.15. Cross-sectional distributions of $|\bar{U}_{os,1}|/|\bar{U}_{m,os,1}|$ with r/R for runs 26, 46,62

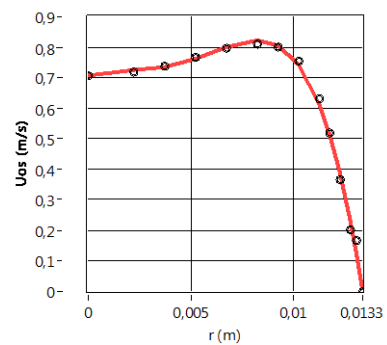
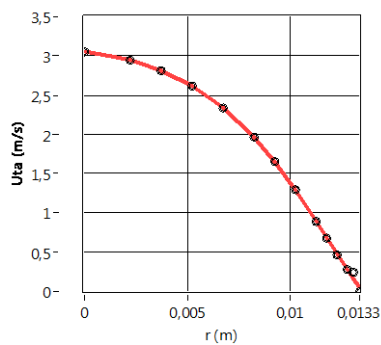
The cross-sectional distributions of \bar{U}_{ta} and $|\bar{U}_{os,1}|$ for $\sqrt{\omega'} \geq 6.67$ ($f \geq 0.6$ Hz) are given in Fig. 8.16. The profiles of $|\bar{U}_{os,1}|$ are rather different than the usual steady laminar profile. As seen from Fig. 8.16, $|\bar{U}_{os,1}|$ distributions firstly begin to increase towards the pipe centerline, then decrease and later maintain its constant magnitude up to pipe centerline. These behaviors of $|\bar{U}_{os,1}|$ distributions are very compatible with

theoretical laminar theory for $|\bar{U}_{os,1}|$, Eq. (4.23), which is given in the paper of Ohmi et al. (1982).

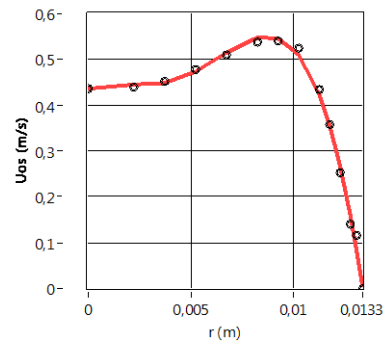
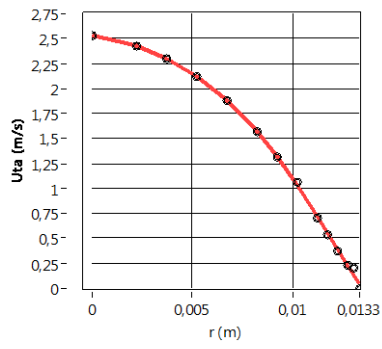
The increase rate of $|\bar{U}_{os,1}|$ distribution is dependent on $\sqrt{\omega'}$. $|\bar{U}_{os,1}|$ increases up to $r=0.0067$ m and then decrease up to pipe centerline at $\sqrt{\omega'}=6.67$. As $\sqrt{\omega'}$ increases, the increase of $|\bar{U}_{os,1}|$ shifts towards the pipe centerline such that $|\bar{U}_{os,1}|$ increases up to $r=0.0082$ m at $\sqrt{\omega'}=7.70$, $r=0.0092$ m at $\sqrt{\omega'}=8.61$ and $r=0.0102$ m at $\sqrt{\omega'} \geq 12.17$.



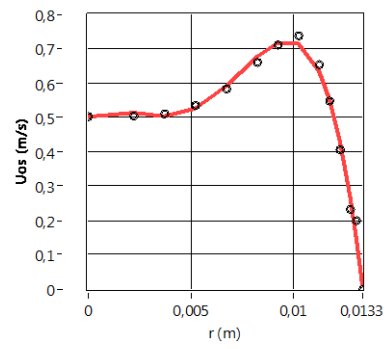
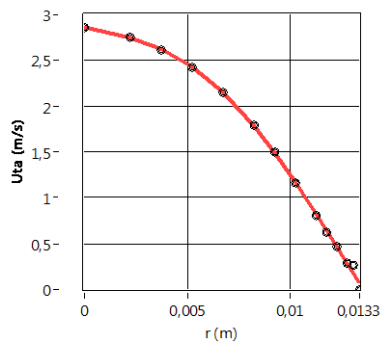
(a) $Re_{ta}=1239$, $Re_{os}=795$, $\sqrt{\omega'}=6.67$ and $A_1=0.64$



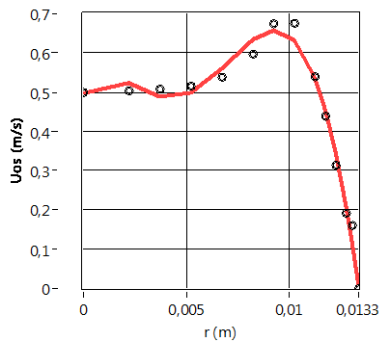
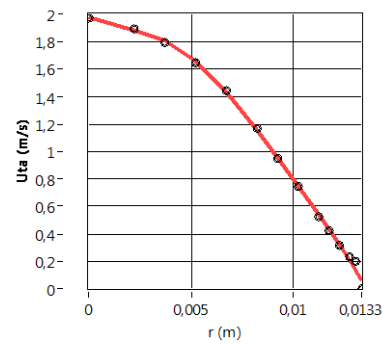
(b) $Re_{ta}=2765$, $Re_{os}=1140$, $\sqrt{\omega'}=7.70$ and $A_1=0.41$



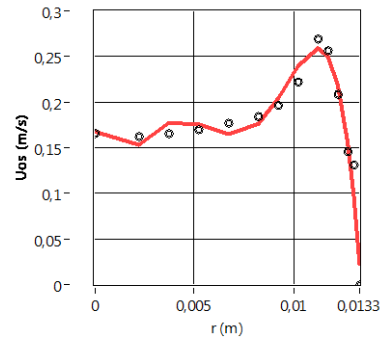
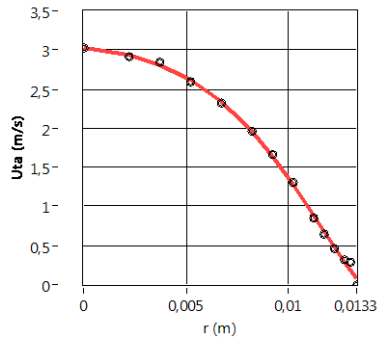
(c) $Re_{ta}=2233$, $Re_{os}=754$, $\sqrt{\omega'}=8.61$ and $A_1=0.34$



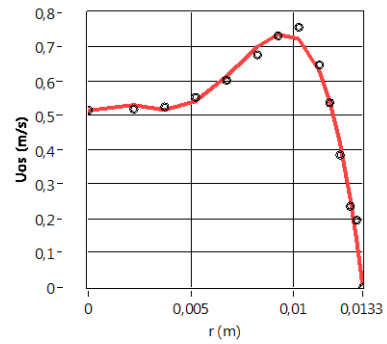
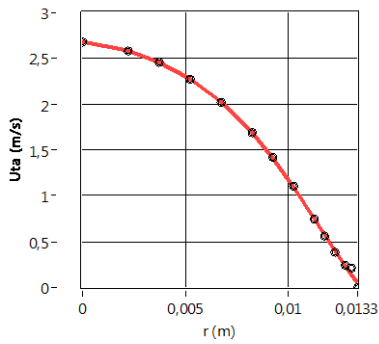
(d) $Re_{ta}=2549$, $Re_{os}=958$, $\sqrt{\omega'}=12.17$ and $A_1=0.39$



(e) $Re_{ta}=1699$, $Re_{os}=888$, $\sqrt{\omega'}=17.22$ and $A_1=0.52$



(f) $Re_{ta}=2762$, $Re_{os}=340$, $\sqrt{\omega'}=27.22$ and $A_1=0.12$



(g) $Re_{ta}=2509$, $Re_{os}=137$, $\sqrt{\omega'}=32.21$ and $A_1=0.05$

Figure 8.16. Cross-sectional distributions of \bar{U}_{ta} and $|\bar{U}_{os,1}|$ for runs 92, 110, 128, 147, 174, 186 and 206

$\bar{U}_{ta}/\bar{U}_{m,ta}$ and $|\bar{U}_{os,1}|/|\bar{U}_{m,os,1}|$ distributions for $\sqrt{\omega'} \geq 6.67$ with the steady flow Blasius profiles are given in Figs. 8.17 and 8.18. As seen from Fig. 8.17, only $\bar{U}_{ta}/\bar{U}_{m,ta}$ profile for run 206 at $\sqrt{\omega'}=32.21$ deviates from the Blasius profile.

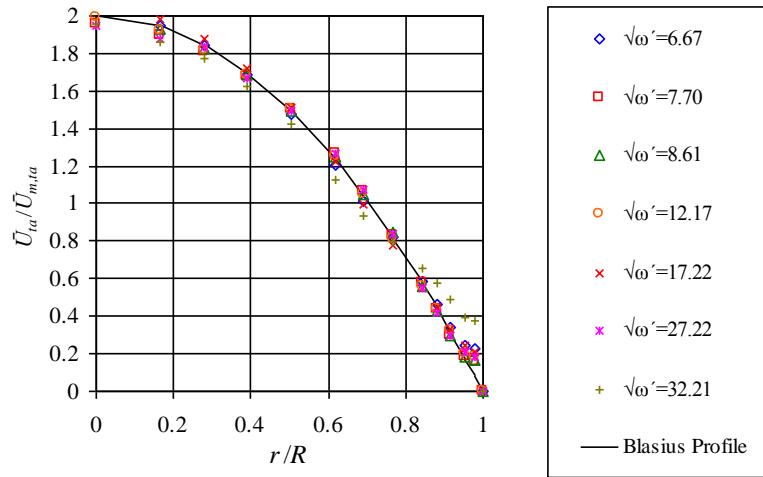


Figure 8.17. Cross-sectional distributions of $\bar{U}_{ta} / \bar{U}_{m,ta}$ with r/R for runs 92, 110, 128, 147, 174, 186 and 206

The distributions of $|\bar{U}_{os,1}| / |\bar{U}_{m,os,1}|$ are rather different than steady flow Blasius profile, obeying the theoretical laminar theory for $|\bar{U}_{os,1}|$ given in Eq. (4.23). However, $|\bar{U}_{os,1}| / |\bar{U}_{m,os,1}|$ distribution at $\sqrt{\omega'}=6.67$ is quite different than the others. The common behavior of $|\bar{U}_{os,1}| / |\bar{U}_{m,os,1}|$ distributions for $\sqrt{\omega'} \geq 6.67$ is given with the dashed line.

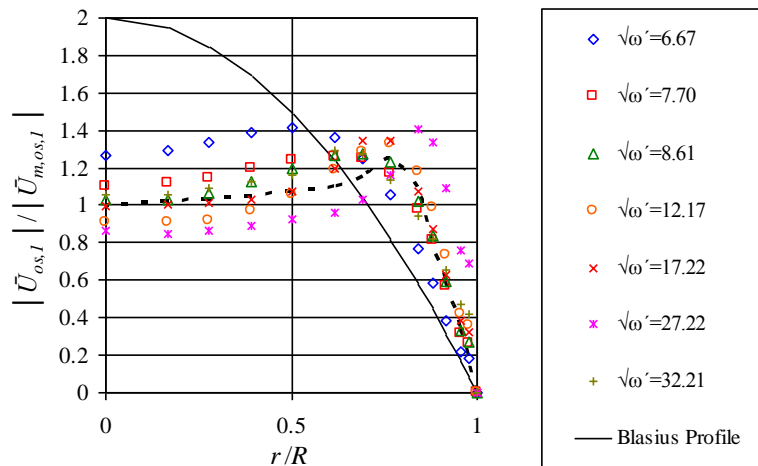


Figure 8.18. Cross-sectional distributions of $|\bar{U}_{os,1}| / |\bar{U}_{m,os,1}|$ with r/R for runs 92, 110, 128, 147, 174, 186 and 206

As a deduction, the observations on \bar{U}_{ta} and $|\bar{U}_{os,1}|$ distributions can be summarized as follows;

1) The cross-sectional distributions of \bar{U}_{ta} at $\sqrt{\omega'} = 2.72, 3.85$ and 5.44 in laminar regime are parabolic with an excellent conformity of theoretical Blasius profile (Fig. 8.14). On the other hand, $|\bar{U}_{os,1}|$ distributions at $\sqrt{\omega'} = 2.72, 3.85$ and 5.44 in laminar regime do not obey theoretical steady flow Blasius profile as shown in Fig. 8.15.

2) The cross-sectional distributions of \bar{U}_{ta} for $\sqrt{\omega'} \geq 6.67$ ($f \geq 0.6$ Hz) are parabolic and there is a good conformity with theoretical steady flow Blasius profile, except that at $\sqrt{\omega'} = 32.21$ ($f = 14$ Hz). As seen from Fig. 8.17, only $\bar{U}_{ta} / \bar{U}_{m,ta}$ distribution at $\sqrt{\omega'} = 32.21$ deviates from the Blasius profile.

3) The distributions of $|\bar{U}_{os,1}|$ for $\sqrt{\omega'} \geq 6.67$ ($f \geq 0.6$ Hz) firstly increase towards the pipe centerline, then decrease and later keep its magnitude constant up to pipe centerline, which are same as Ohmi et al.'s observation on $|\bar{U}_{os,1}|$ distribution (Ohmi et al., 1982).

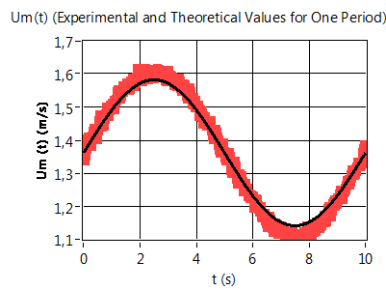
4) The increase rate of $|\bar{U}_{os,1}|$ distribution is dependent on $\sqrt{\omega'}$. When $\sqrt{\omega'}$ increases, the increase of $|\bar{U}_{os,1}|$ shifts towards the pipe centerline from $r=0.0067$ m at $\sqrt{\omega'} = 6.67$ to $r=0.0102$ m at $\sqrt{\omega'} = 32.21$.

8.2.3. Mean velocity profiles in pulsatile laminar regime

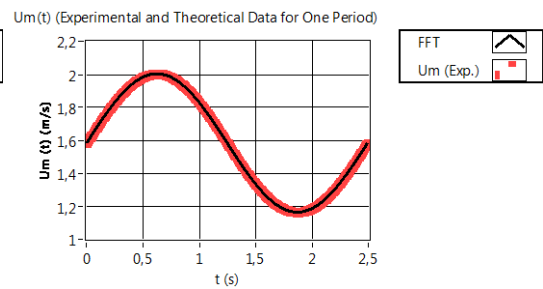
In order to obtain mean velocity profiles through the pipe cross-section in the pulsatile flow, the second method is used in the devised program, *TDFC.vi*. In the second method, the $\bar{U}(t)$ values of the cycle for each phase at 13 different radial positions of the pipe are firstly saved as a matrix form. Next, the cross sectional mean velocity for each phase of the cycle are evaluated by numerically integrating the ensemble averaged data over the cross section of the pipe by using the well-

known Simpson's rule in the program. Then the evaluated $\bar{U}_m(t)$ is approximated in the program by the finite Fourier series expansion using Eq. (2.17).

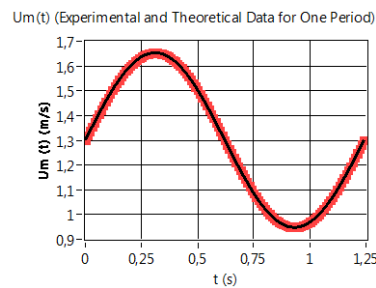
Figure 8.19 shows the mean velocity profiles obtained experimentally and comparisons of them with FFT approximations for runs 3, 59, 106, 149, 170 and 188. As a result of the sampling frequency of 100 Hz, 1000, 250, 125, 50, 25 and 10 data are acquired per a cycle at $\sqrt{\omega'} = 2.72, 5.44, 7.70, 12.17, 17.22$ and 27.22 , respectively as seen from Fig. 8.19. The shapes of the mean velocity profiles obtained experimentally are sinusoidal. Figure 8.19 also shows that there are excellent agreements between the experimental and theoretical mean velocity profiles. This shows the accuracy and sensitivity of the data acquisition and processing processes by means of the used daqboard and the devised program, *TDFC.vi* in LabView environment. Turbulent burst is observed in neither accelerating nor decelerating phases of the mean velocity profiles.



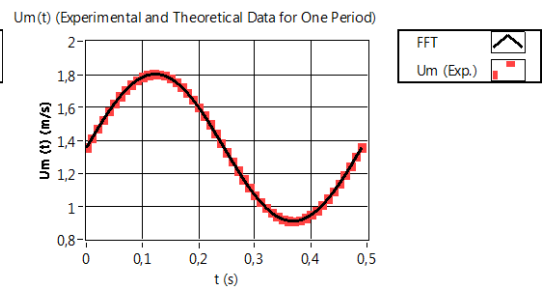
$$Re_{ta} = 2416, Re_{os} = 438, \sqrt{\omega'} = 2.72$$



$$Re_{ta} = 2807, Re_{os} = 987, \sqrt{\omega'} = 5.44$$



$$Re_{ta} = 2307, Re_{os} = 732, \sqrt{\omega'} = 7.70$$



$$Re_{ta} = 2408, Re_{os} = 1000, \sqrt{\omega'} = 12.17$$

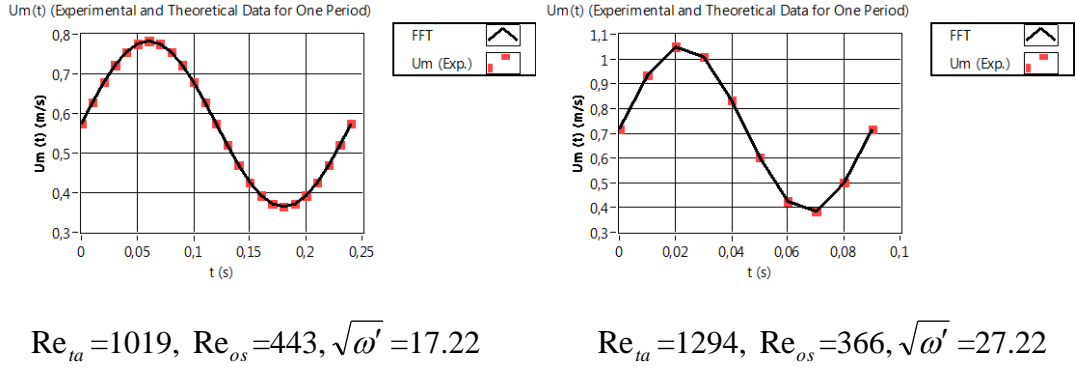


Figure 8.19. Cross-sectional mean velocity profiles obtained experimentally and their FFT approximations for runs 3, 59, 106, 149, 170 and 188

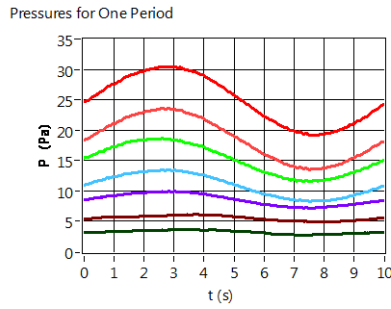
8.2.4. Pressure waveforms in pulsatile laminar regime

Figure 8.20 illustrates the pressure waveforms in laminar regime of pulsatile pipe flow for the sample runs 3, 42, 62, 90, 110, 128, 149, 174, 190 and 207 for all values of $\sqrt{\omega'}$. The shapes of the pressure waveforms are sinusoidal as same as velocity waveforms. Although the time dependency of the pressure waveforms for P_6 and P_7 at the last locations of $X/D=589$ and 619 are not clearly observed, these waveforms are exactly sinusoidal at all values of $\sqrt{\omega'}$, however rather small in magnitude. As noticed from the figure, the magnitude of static pressure at each phase is decreased along the downstream axial locations, X/D at all values of $\sqrt{\omega'}$.

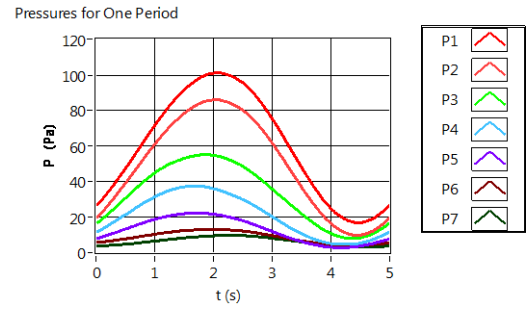
On the other hand, the time averaged and oscillating components of pressure, \bar{P}_{ta} and $|\bar{P}_{os,1}|$ are seen to be increased when Re_{ia} is increased. The maximum \bar{P}_{ta} is found to be $\bar{P}_{ta,1} = 59$ Pa at $\sqrt{\omega'} = 3.85$ ($f = 0.2$ Hz) among the selected plots. Meanwhile, the magnitudes of $|\bar{P}_{os,1}|$ are always seen to be smaller than their corresponding magnitudes of \bar{P}_{ta} ($|\bar{P}_{os,1}|/\bar{P}_{ta} < 1$) at each downstream pressure measurement stations at all values of $\sqrt{\omega'}$, except those at $\sqrt{\omega'} = 8.61$ ($f = 1$ Hz), $\sqrt{\omega'} = 12.17$ ($f = 2$ Hz) and $\sqrt{\omega'} = 17.22$ ($f = 4$ Hz) as being $|\bar{P}_{os,1}|/\bar{P}_{ta} > 1$; i.e. the magnitudes of \bar{P}_{ta} and $|\bar{P}_{os,1}|$ are found as $\bar{P}_{ta_1} = 26$ Pa and $|\bar{P}_{os,1}| = 45$ Pa; $\bar{P}_{ta_2} = 18$ Pa

and $|\bar{P}_{os,1}|_2=44$ Pa; $\bar{P}_{ta_3}=14$ Pa and $|\bar{P}_{os,1}|_3=33$ Pa; $\bar{P}_{ta_4}=10$ Pa and $|\bar{P}_{os,1}|_4=22$ Pa; $\bar{P}_{ta_5}=7$ Pa and $|\bar{P}_{os,1}|_5=12$ Pa; $\bar{P}_{ta_6}=5$ Pa and $|\bar{P}_{os,1}|_6=4.4$ Pa; $\bar{P}_{ta_7}=3$ Pa and $|\bar{P}_{os,1}|_7=2.4$ Pa at $\sqrt{\omega'}=8.61$ ($f=1$ Hz). $\sqrt{\omega'}=8.61$ ($f=1$ Hz) as being the critical limit in this study is verified once more according to $|\bar{P}_{os,1}|/\bar{P}_{ta}<1$. Besides, the amplitudes of the sinusoidal pressure waveforms at $\sqrt{\omega'}\geq 27.22$ ($f\geq 10$ Hz) are seen to be smaller when compared those at $\sqrt{\omega'}<27.22$ ($f<10$ Hz).

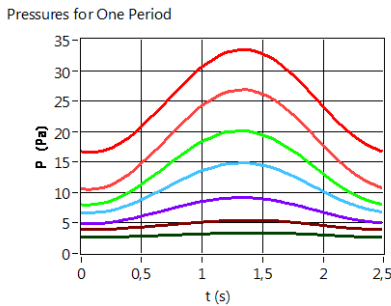
During the accumulation of the velocity data for 13 radial positions, the static pressure data at each pressure measurement station are accumulated 13 times by the devised program, *TDFC.vi*. The pressure data acquired at each station, which are taken for 13 times in one run are found to be same in magnitude with an accuracy of $\pm 0.8\%$. This verifies the accuracy of pressure measurement at each pressure measurement station.



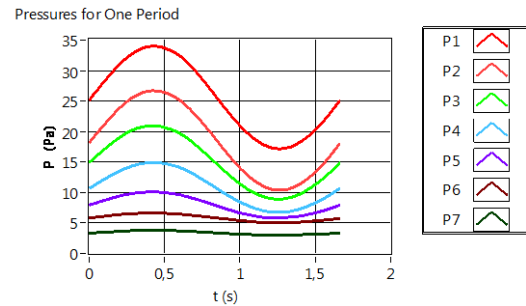
$$Re_{ta}=2416, Re_{os}=438, \sqrt{\omega'}=2.72, \\ A_1=0.18$$



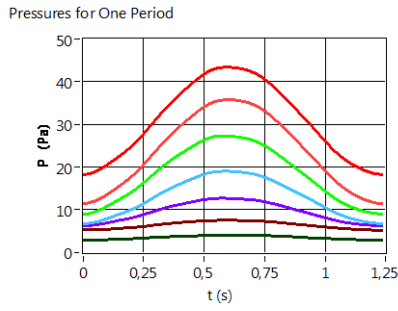
$$Re_{ta}=3696, Re_{os}=2264, \sqrt{\omega'}=3.85, \\ A_1=0.61$$



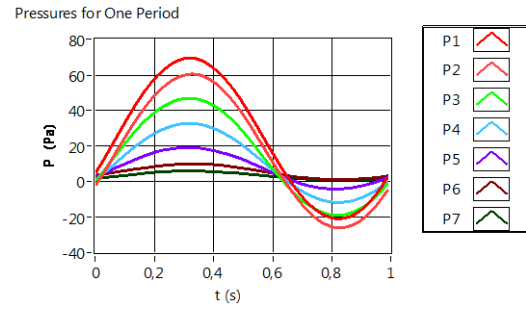
$$Re_{ta}=2325, Re_{os}=1108, \sqrt{\omega'}=5.44, \\ A_1=0.48$$



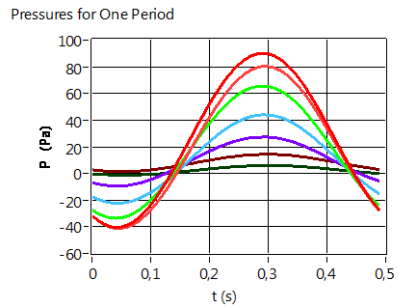
$$Re_{ta}=2261, Re_{os}=1209, \sqrt{\omega'}=6.67, \\ A_1=0.53$$



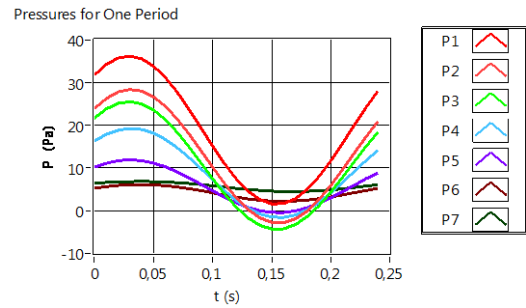
$$Re_{ta}=2765, Re_{os}=1140, \sqrt{\omega'}=7.70, \\ A_1=0.41$$



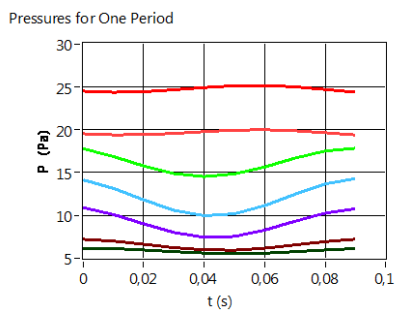
$$Re_{ta}=2233, Re_{os}=754, \sqrt{\omega'}=8.61, \\ A_1=0.34$$



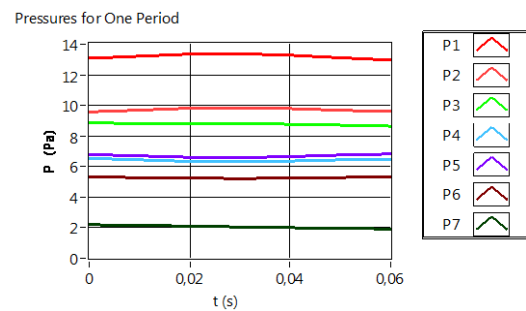
$$Re_{ta}=2408, Re_{os}=1000, \sqrt{\omega'}=12.17, \\ A_1=0.42$$



$$Re_{ta}=1699, Re_{os}=888, \sqrt{\omega'}=17.22, \\ A_1=0.52$$



$$Re_{ta}=2403, Re_{os}=788, \sqrt{\omega'}=27.22, \\ A_1=0.33$$



$$Re_{ta}=1449, Re_{os}=107, \sqrt{\omega'}=32.21, \\ A_1=0.07$$

Figure 8.20. Pressure waveforms acquired from each pressure transmitters for runs 3, 42, 62, 90, 110, 128, 149, 174, 190 and 207

8.2.5. Flow resistance in pulsatile laminar regime

Flow resistance in pulsatile laminar regime is investigated in terms of friction factor, static pressure drop and wall shear stress in this study. The friction factors as instantaneous friction factor, $\lambda_u(t)$, time averaged friction factor, $\lambda_{u,ta}$, and instantaneous laminar quasi-steady friction factor, $\lambda_{qL}(t)$ are evaluated by means of the velocity and pressure measurements.

8.2.5.1. Variations of $\Delta\bar{P}(t)/L$, $\bar{U}_m(t)$ and $\bar{\tau}_w(t)$ in pulsatile laminar regime

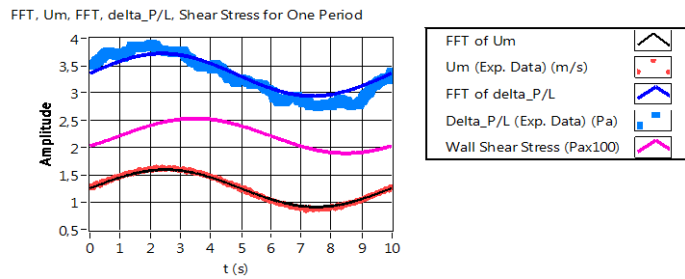
The last two pressure transmitters located at $15D$ downstream and $15D$ upstream of the hotwire probe at the velocity measurement station, $X/D=589$ and 619 , are used to evaluate the instantaneous static pressure drop per unit length, $\Delta P(t)/L$ by means of the devised program, *TDFC.vi*. The experimentally determined $\Delta P(t)/L$ is compared with its FFT approximation for each run. Instantaneous wall shear stress, $\bar{\tau}_w(t)$ is also evaluated using the definition of the well-known momentum integral equation given in Eq. (2.16).

Figure 8.21 shows the combined profiles of the experimentally measured $\bar{U}_m(t)$ and $\Delta P(t)/L$ with their FFT approximations, and the theoretically evaluated $\bar{\tau}_w(t)$ in laminar regime as sample plots. The shapes of the experimentally measured $\bar{U}_m(t)$, $\Delta P(t)/L$ and calculated $\bar{\tau}_w(t)$ are seen to be sinusoidal. The solid lines on the measured $\Delta P(t)/L$ and $\bar{U}_m(t)$ show the first order FFT approximations of $\Delta P(t)/L$ and $\bar{U}_m(t)$.

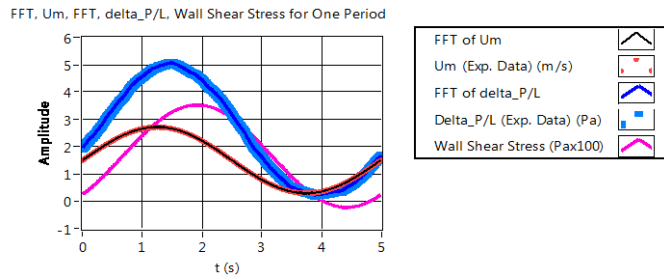
As can be seen from Fig. 8.21, there are excellent agreements between $\Delta P(t)/L$, $\bar{U}_m(t)$ and their FFT approximations with the maximum deviations of $\pm 2\%$. However some deviated data signals are seen on the pressure waveforms at $\sqrt{\omega'} = 2.72$ ($f=0.1$ Hz) with a maximum deviation of $\pm 5\%$. In fact there is a good agreement between $\Delta P(t)/L$ and its FFT approximation at $\sqrt{\omega'} = 2.72$

($f=0.1$ Hz), however it does not look like so due to more pressure data acquired at one period as 1000 data.

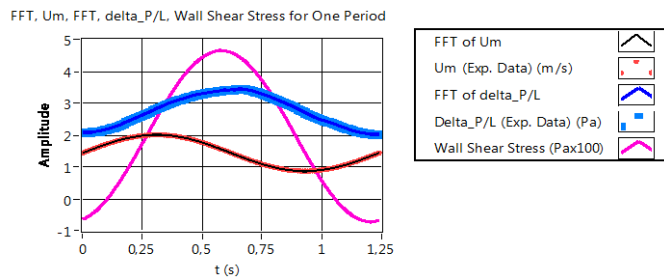
The effect of $\sqrt{\omega'}$ on the behavior of the $\bar{\tau}_w(t)$ profiles can be seen in Fig. 8.21. Although the time averaged and oscillating components of $\bar{\tau}_w(t)$ have always positive values at $\sqrt{\omega'} \leq 3.85$ ($f \leq 0.2$ Hz), $\bar{\tau}_w(t)$ has negative values at some instants at $\sqrt{\omega'} > 3.85$ ($f > 0.2$ Hz). Also, $|\bar{\tau}_{w,os,1}|/\tau_{w,ta} > 1$ is observed at $\sqrt{\omega'} > 3.85$ ($f > 0.2$ Hz).



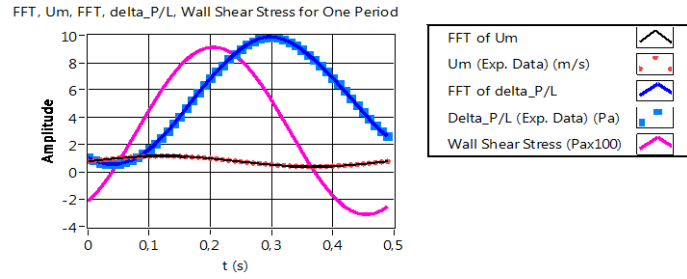
$$Re_{ta} = 2416, Re_{os} = 438, \sqrt{\omega'} = 2.72 \text{ and } A_1 = 0.18$$



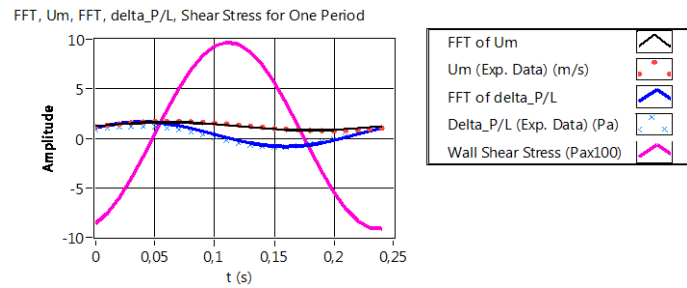
$$Re_{ta} = 3058, Re_{os} = 2438, \sqrt{\omega'} = 3.85 \text{ and } A_1 = 0.79$$



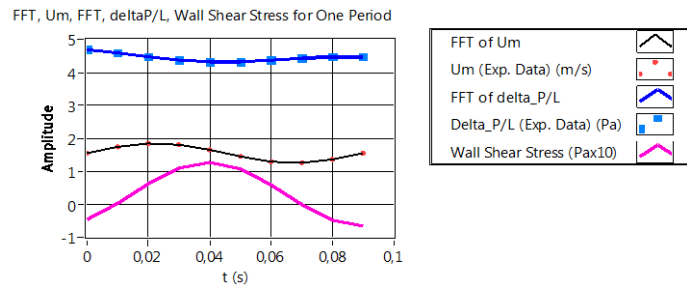
$$Re_{ta} = 2548, Re_{os} = 1164, \sqrt{\omega'} = 7.70 \text{ and } A_1 = 0.46$$



$$Re_{ta} = 1390, Re_{os} = 978, \sqrt{\omega'} = 12.17 \text{ and } A_1 = 0.70$$



$$Re_{ta} = 2160, Re_{os} = 832, \sqrt{\omega'} = 17.22 \text{ and } A_1 = 0.39$$



$$Re_{ta} = 2762, Re_{os} = 340, \sqrt{\omega'} = 27.22 \text{ and } A_1 = 0.12$$

Figure 8.21. Variations of $\Delta\bar{P}(t)/L$, $\bar{U}_m(t)$ with their FFT approximations and $\bar{\tau}_w(t)$ for runs 3, 47, 112, 156, 168, 186

8.2.5.2. The variations of $\lambda_u(t)$ and $\lambda_{qL}(t)$ in pulsatile laminar regime

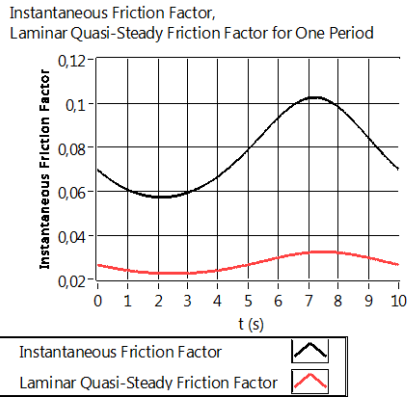
The flow resistance characteristics in terms of instantaneous friction factor, $\lambda_u(t)$, time averaged friction factor, $\lambda_{u,ta}$, and instantaneous laminar quasi-

steady friction factor, $\lambda_{qL}(t)$ are also evaluated by means of the measured data of $\Delta P(t)/L$ and $\bar{U}_m(t)$ in *TDFC.vi*.

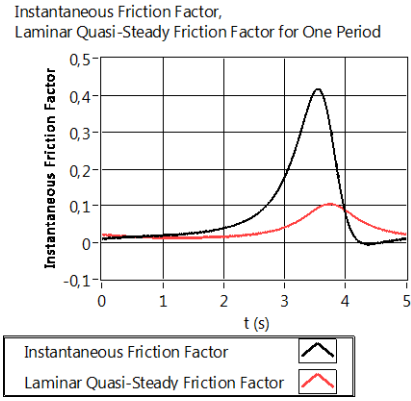
There is a constant value of $\lambda_{u,ta}$ at each run. The variations of $\lambda_u(t)$ and $\lambda_{qL}(t)$ in laminar regime are given together for the sample runs of 3, 47, 133, 156, 168 and 186 in Fig. 8.22. The time dependency of $\lambda_u(t)$ and $\lambda_{qL}(t)$ are seen in the figure although $\lambda_{qL}(t)$ is based on quasi-steady approach. $\lambda_u(t)$ profiles are time dependent but not sinusoidal at all values of $\sqrt{\omega'}$.

As can be seen from the figure, the magnitudes of $\lambda_u(t)$ and $\lambda_{qL}(t)$ are rather different from each other at each run. Hence it is verified that the experimental range is not in quasi-steady regime. As noticed from the figure, the characteristic behaviors of $\lambda_u(t)$ and $\lambda_{qL}(t)$ are completely different at each $\sqrt{\omega'}$. Although $\lambda_{qL}(t)$ has a noticeable time dependency at $\sqrt{\omega'} \leq 8.61$ ($f \leq 1$ Hz), the pulsatile variation disappears at $\sqrt{\omega'} > 8.61$ ($f > 1$ Hz) as seen from the figure.

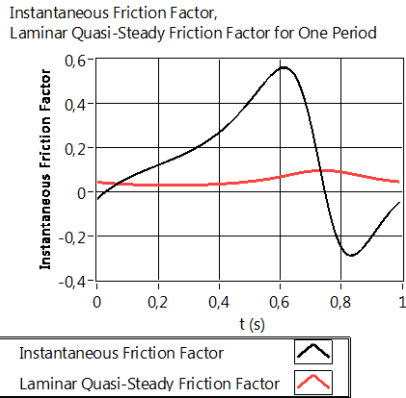
It is also noticed that there is an effect of A_1 on the behavior of $\lambda_u(t)$ profile at each $\sqrt{\omega'}$. When A_1 is increased from $A_1=0.10$ to $A_1=0.90$ at any value of $\sqrt{\omega'}$, the shape of $\lambda_u(t)$ profile is deformed and getting sharp and sharp. The profiles of $\lambda_u(t)$ in Fig. 8.22a and 8.22f are very smooth and almost sinusoidal at $A_1=0.18$ and $A_1=0.12$, respectively. However, $\lambda_u(t)$ profile begins to change in shape as a hill at $A_1 \geq 0.30$ as seen in Fig. 8.22e. Moreover this hill-shape is getting sharp and sharp when A_1 is increased as can be observed in Fig. 8.22b, 8.22c and 8.22d. However, there is no effect of $\sqrt{\omega'}$ on the deformation of the $\lambda_u(t)$ profile.



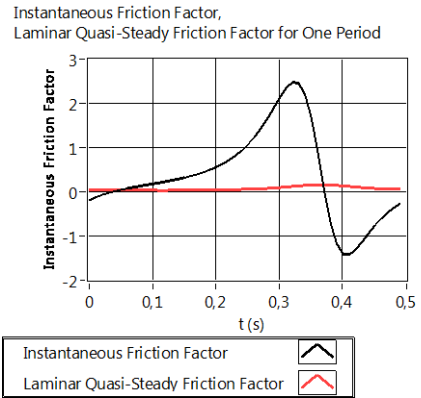
(a) $Re_{ta}=2416$, $Re_{os}=438$, $\sqrt{\omega'}=2.72$,
 $A_1=0.18$



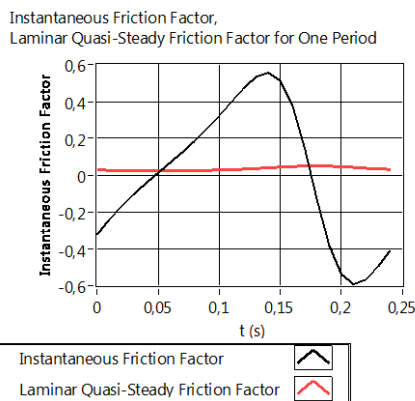
(b) $Re_{ta}=3058$, $Re_{os}=2438$, $\sqrt{\omega'}=3.85$,
 $A_1=0.79$



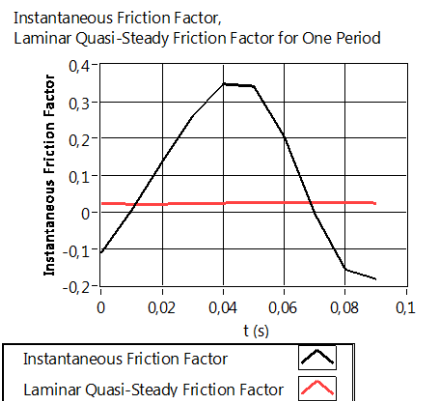
(c) $Re_{ta}=1473$, $Re_{os}=804$, $\sqrt{\omega'}=8.61$,
 $A_1=0.55$



(d) $Re_{ta}=1390$, $Re_{os}=978$, $\sqrt{\omega'}=12.17$,
 $A_1=0.70$



(e) $Re_{ta}=2160$, $Re_{os}=832$, $\sqrt{\omega'}=17.22$,
 $A_1=0.39$



(f) $Re_{ta}=2762$, $Re_{os}=340$, $\sqrt{\omega'}=27.22$,
 $A_1=0.12$

Figure 8.22. Variations of $\lambda_u(t)$ and λ_{qL} for runs 3, 47, 133, 156, 168 and 186

8.3. Pulsatile Flow Regime at the Onset of Transition to Turbulence

8.3.1. Velocity waveforms in pulsatile flow regime at the onset of transition to turbulence

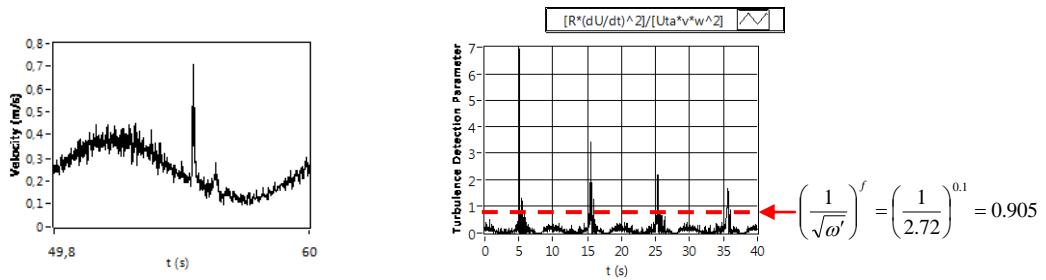
The sample plots of velocity waveforms at the onset of the transition to turbulence are given in this section. Near each velocity waveform, the corresponding graphical representation of the transition detection method is introduced. The plots are selected covering all $\sqrt{\omega'}$ in the range of $2.72 \leq \sqrt{\omega'} \leq 32.21$. The plots are directly outputs of the devised program, *TDFC.vi*. The intermittency factor, γ , at the onset of the transition to turbulence is found to be less than 0.1 in the covered experimental ranges.

Figure 8.23 illustrates the velocity waveforms at the onset of transition and the graphical representation of the used transition detection method at $r/R=0.977$ and $r/R=0$ for $\sqrt{\omega'}=2.72$. The turbulent bursts at $r/R=0.977$ are seen in the decelerating phase of the velocity waveform as peaks in shape (see Fig. 8.23a), however the turbulent bursts at $r/R=0$ are seen in the decelerating phase of the waveform as collapse in shape (see Fig. 8.23b). These typical shapes of the turbulent bursts are seen in the study of Wygnanski and Champagne (1973), Wygnanski et al. (1975), Durst and Ünsal (2006) as puffs in steady transitional flows and in the Ph.D. thesis of Nishi in time dependent pipe flows (Nishi, 2009).

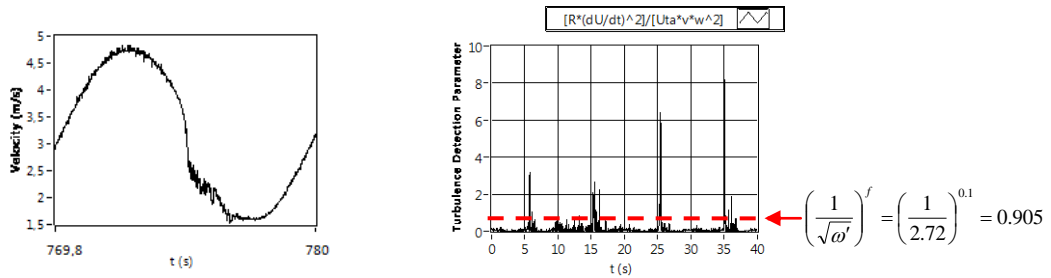
In Fig. 8.23, the graphical representations of the detection method are also introduced for $r/R=0.977$ and $r/R=0$ at $\sqrt{\omega'}=2.72$. The dynamic *turbulence detection parameter*, TDP_3 and the dynamic *threshold parameter*, TP_1 for $f \leq 1$ Hz are introduced in the previous chapter as $R(dU(r,t)/dt)^2/(\bar{U}_{ta}v\omega^2)$ and $(1/\sqrt{\omega'})^n$, respectively. The dynamic TP_1 is denoted with the red dashed line in the detection method.

As is seen from the figure, the instantaneous values of the TDP_3 exceed the $TP_1=0.905$ in magnitude at the instants where the turbulent bursts occur for both $r/R=0.977$ and $r/R=0$ at $\sqrt{\omega'}=2.72$ ($f = 0.1$ Hz). As can be noticed from the figure,

the occurrence of the turbulent bursts (as peaks of turbulence detection parameter on the graphic of the detection method) has also time periodicity, due to the propagations of the turbulent bursts to downstream of the pipeline, such that the peaks appear at the definite time and period, i.e. at $t=5$ s, 15 s, 25 s and 35 s with the incremental of 10 s which is the period of $T=10$ s for $\sqrt{\omega'}=2.72$ ($f=0.1$ Hz). The dynamic TDP_3 is $R(dU(r,t)/dt)^2/(\bar{U}_{ta}v\omega^2)$ for $\sqrt{\omega'} \leq 8.61$ ($f \leq 1$ Hz) as can be seen from the following figures.



(a) $Re_{ta}=3018$, $Re_{os}=1610$, $\sqrt{\omega'}=2.72$ and $A_1=0.53$ ($r/R=0.977$)



(b) $Re_{ta}=3018$, $Re_{os}=1610$, $\sqrt{\omega'}=2.72$ and $A_1=0.53$ ($r/R=0$)

Figure 8.23. Velocity waveforms at the onset of transition and transition to turbulence method at $r/R=0.977$ and $r/R=0$ for run 14

As mentioned in the previous chapter, the TP_1 and TP_2 for both $f \leq 1$ Hz and $f > 1$ Hz, respectively are dynamic and their magnitudes are dependent on $\sqrt{\omega'}$, in other words f . Figure 8.24 shows the variation of the dynamic $TP_1 = (1/\sqrt{\omega'})^f$ for $f \leq 1$ Hz. The value of TP_1 decreases when $\sqrt{\omega'}$ (in other words f) increases.

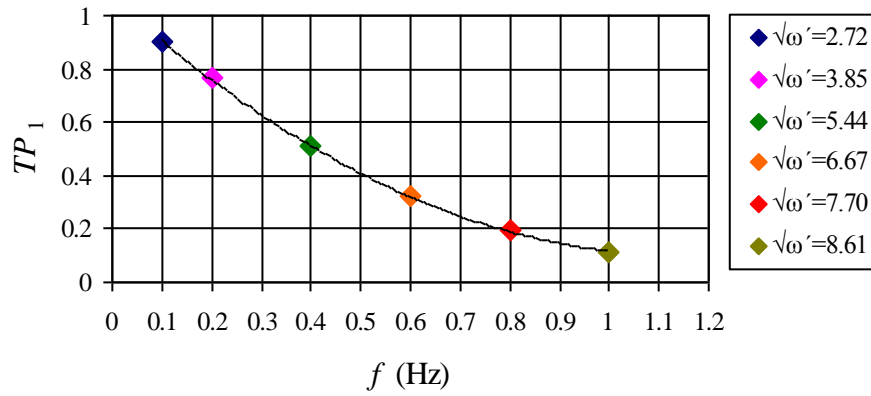
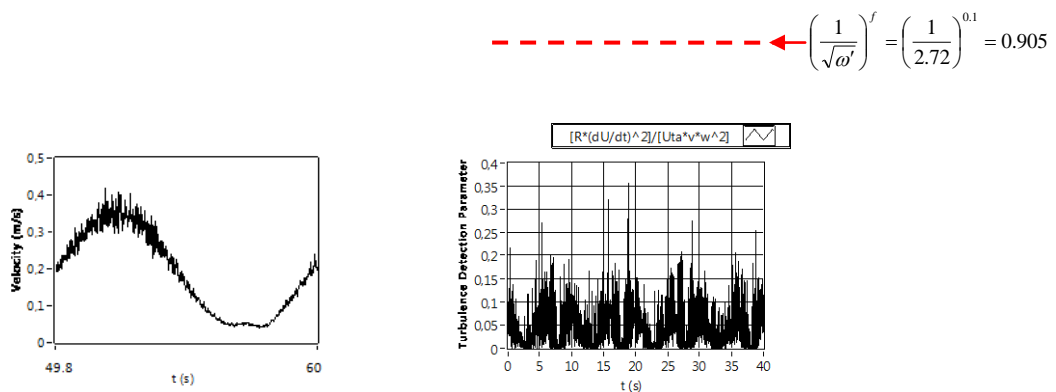


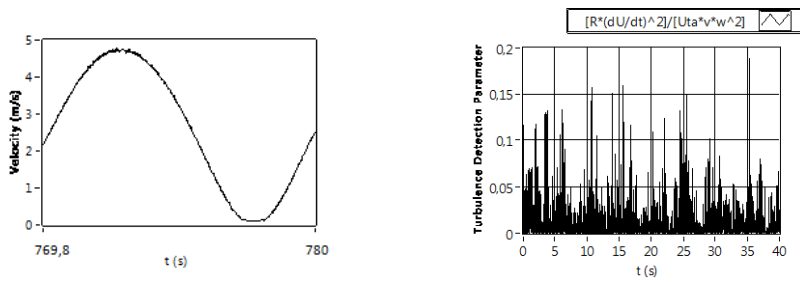
Figure 8.24. Variation of TP_1 with f in the range of $2.72 \leq \sqrt{\omega'} \leq 8.61$

In order to verify the detection method, a sample plot is shown in Fig. 8.25 for laminar regime at $\sqrt{\omega'} = 2.72$. As seen from the figure, the instantaneous values of $TDP_3 = R(dU(r,t)/dt)^2 / (\bar{U}_{ia} v \omega^2)$ at both $r/R=0.977$ and $r/R=0$ do not exceed the dynamic $TP_1 = (1/\sqrt{\omega'})^n$ in the magnitude of 0.905 at any instant for $\sqrt{\omega'} = 2.72$ ($f=0.1$ Hz), due to existing no turbulent burst on the velocity waveforms as shown from the waveform graphs. The small perturbation on the velocity waveform at $r/R=0.977$ (see Fig. 8.25a) is due to the wall effect; however no turbulent burst is detected on the velocity waveform. TP_1 for $\sqrt{\omega'} = 2.72$ are quite above the maximum values of TDP_3 at both radial positions. Hence no transition to turbulence is detected for this run at both $r/R=0.977$ and $r/R=0$ by the devised program, *TDFC.vi*. This verification of the detection method is satisfied for the other runs.



(a) $Re_{ia} = 2347$, $Re_{os} = 2248$, $\sqrt{\omega'} = 2.72$ and $A_1 = 0.96$ ($r/R=0.977$)

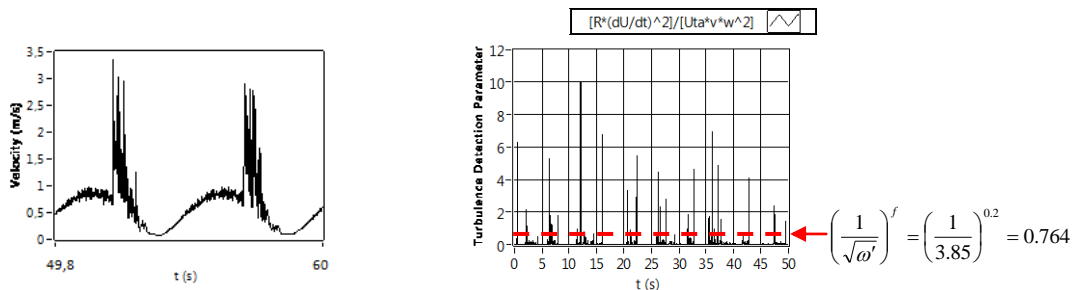
$$-\left(\frac{1}{\sqrt{\omega'}}\right)^f = \left(\frac{1}{2.72}\right)^{0.1} = 0.905$$



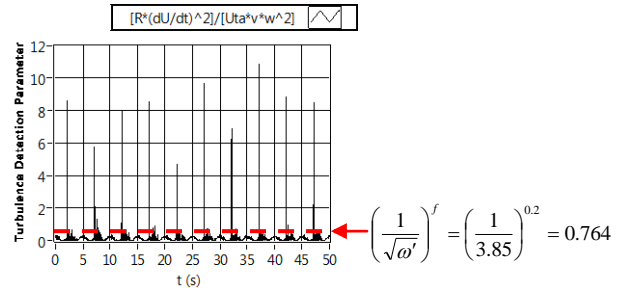
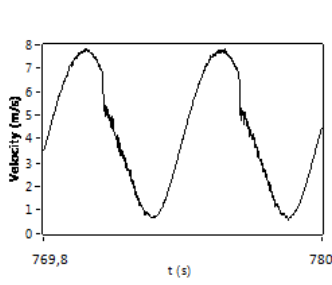
$$(b) Re_{ta} = 2347, Re_{os} = 2248, \sqrt{\omega'} = 2.72 \text{ and } A_1 = 0.96 (r/R=0)$$

Figure 8.25. Laminar velocity waveforms and graphical representations of the detection method at $r/R=0.977$ and $r/R=0$ for run 26

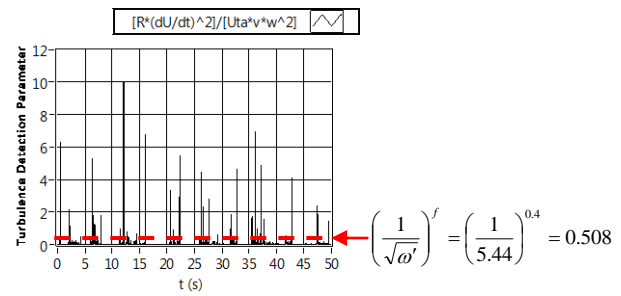
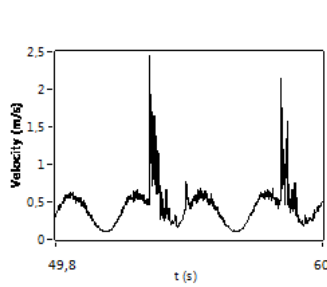
The velocity waveforms at the onset of transition and the graphical representations of the used detection method for both $r/R=0.977$ and $r/R=0$ at $\sqrt{\omega'} = 3.85$, $\sqrt{\omega'} = 5.44$ and $\sqrt{\omega'} = 6.67$ are shown in Fig. 8.26. The turbulent bursts at $r/R=0.977$ are seen as peaks in shape in the decelerating phase of the waveforms. The bursts at $r/R=0$ are seen as collapses in shape in the decelerating phase of the waveforms. As seen from the graphical representations of the detection method, the instantaneous values of TDP_3 for both $r/R=0.977$ and $r/R=0$ at $\sqrt{\omega'} = 3.85$, $\sqrt{\omega'} = 5.44$ and $\sqrt{\omega'} = 6.67$ exceed the dynamic $TP_1 = \left(1/\sqrt{\omega'}\right)^f$ in the magnitudes of 0.764, 0.508 and 0.320, respectively at the instants where the turbulent bursts occur.



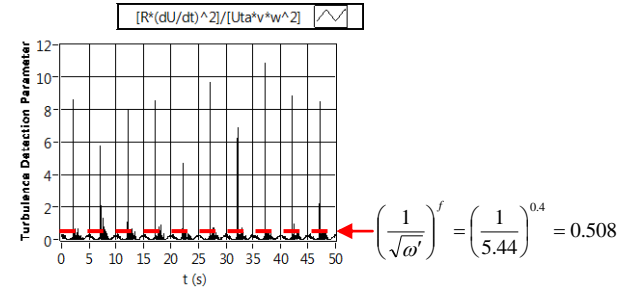
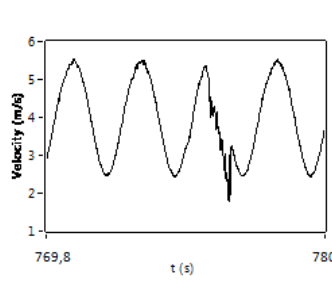
$$(a) Re_{ta} = 4817, Re_{os} = 3939, \sqrt{\omega'} = 3.85 \text{ and } A_1 = 0.82 (r/R=0.977)$$



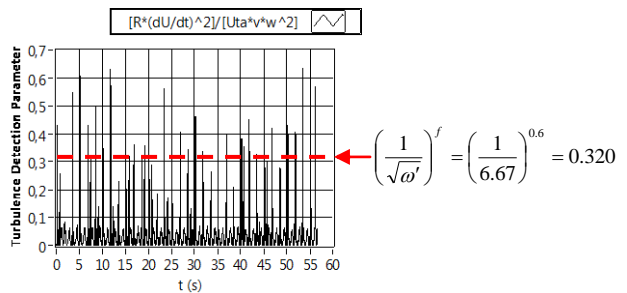
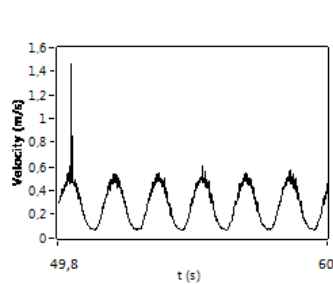
(b) $Re_{ia}=4817$, $Re_{os}=3939$, $\sqrt{\omega'}=3.85$ and $A_1=0.82$ ($r/R=0$)



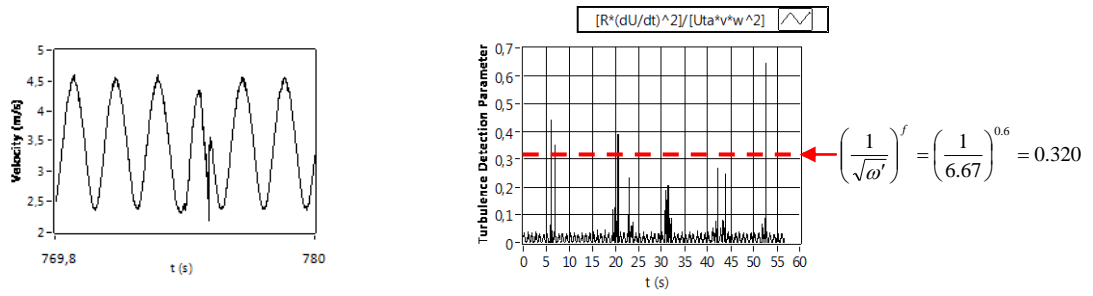
(a) $Re_{ia}=3887$, $Re_{os}=1940$, $\sqrt{\omega'}=5.44$ and $A_1=0.50$ ($r/R=0.977$)



(b) $Re_{ia}=3887$, $Re_{os}=1940$, $\sqrt{\omega'}=5.44$ and $A_1=0.50$ ($r/R=0$)



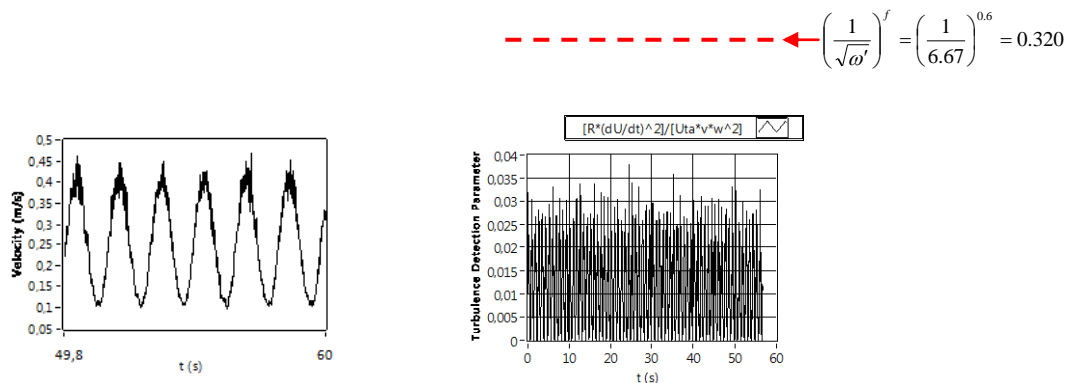
(a) $Re_{ia}=3229$, $Re_{os}=1616$, $\sqrt{\omega'}=6.67$ and $A_1=0.50$ ($r/R=0.977$)



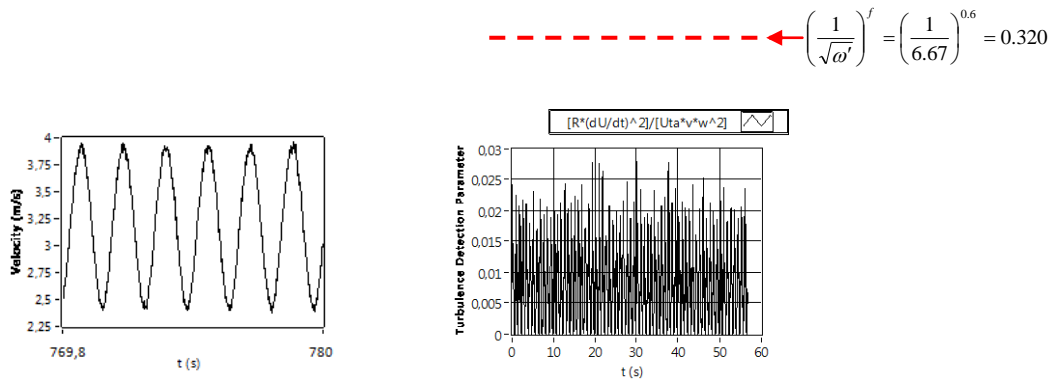
(b) $Re_{ta}=3229$, $Re_{os}=1616$, $\sqrt{\omega'}=6.67$ and $A_1=0.50$ ($r/R=0$)

Figure 8.26. Velocity waveforms at the onset of transition and transition to turbulence method at $r/R=0.977$ and $r/R=0$ for runs 50, 64 and 88

Figure 8.27 shows the velocity waveforms and the graphical representations of the turbulence detection method at $r/R=0.977$ and $r/R=0$ for run 86 in which the flow is laminar at all radial positions of the hotwire probe at $Re_{ta}=2893$ and $\sqrt{\omega'}=6.67$. The small perturbations on the waveform at $r/R=0.977$ is due to the wall effect. As seen from Fig. 8.27, the dynamic TP_1 is quite greater than the maximum value of TDP_3 at both radial positions. Hence $TDFC.vi$ does not detect any turbulent bursts in this run. This illustration is introduced in order to verify the accuracy of the detection method once more.



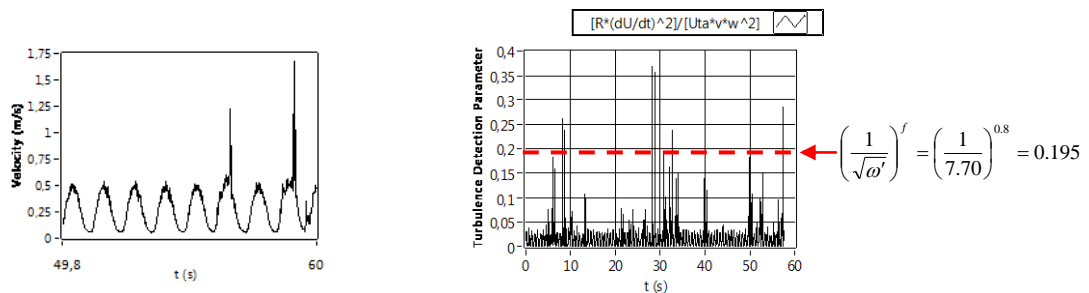
(a) $Re_{ta}=2893$, $Re_{os}=1184$, $\sqrt{\omega'}=6.67$ and $A_1=0.41$ ($r/R=0.977$)



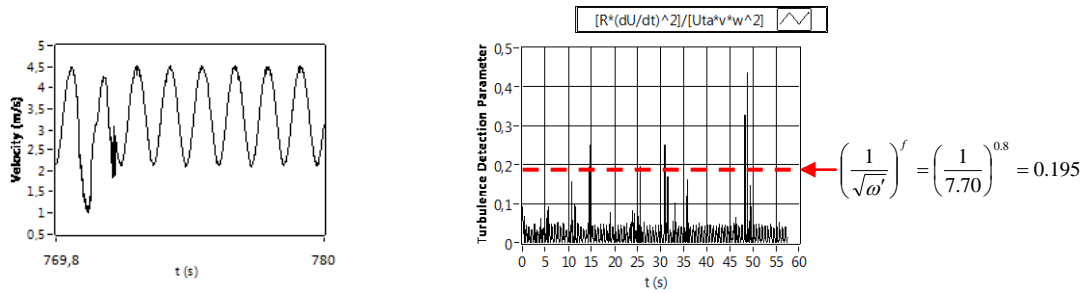
(b) $Re_{ia}=2893$, $Re_{os}=1184$, $\sqrt{\omega'}=6.67$ and $A_1=0.41$ ($r/R=0$)

Figure 8.27. Laminar velocity waveforms and graphical representations of the detection method at $r/R=0.977$ and $r/R=0$ for run 86

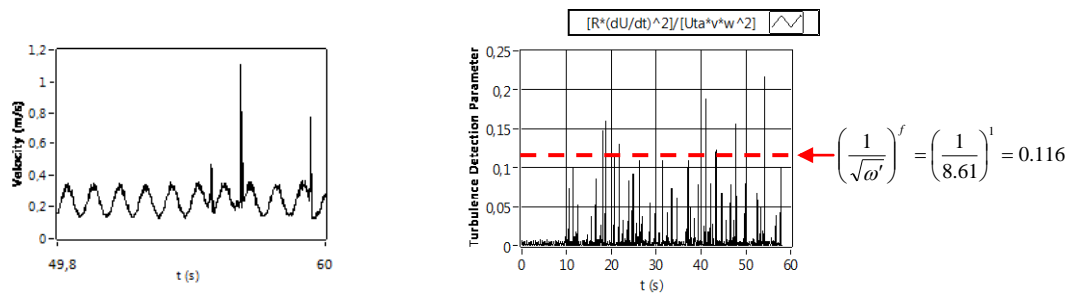
The velocity waveforms at the onset of transition and the detection method at $r/R=0.977$ and $r/R=0$ for $\sqrt{\omega'}=7.70$ and $\sqrt{\omega'}=8.61$ are shown in Fig. 8.28. The turbulent bursts are seen as peaks in shape in the decelerating phase of the waveforms at $r/R=0.977$. They are seen as collapses in shape in the decelerating phase of the waveforms at $r/R=0$. The graphical representations of the transition to turbulence method for both $r/R=0.977$ and $r/R=0$ are also illustrated in the figure. When turbulent bursts occur in the flow, the maximum values of $TDP_3 = R(dU(r,t)/dt)^2 / (\bar{U}_{ia} v \omega^2)$ for $\sqrt{\omega'}=7.70$ and $\sqrt{\omega'}=8.61$ are seen to be above the dynamic $TP_1 = (1/\sqrt{\omega'})^n$ which are 0.195 and 0.116 in magnitude, respectively, as can be observed from the graphical representations of the detection method. Hence, *TDFC.vi* detects the turbulent bursts and gives an alarm.



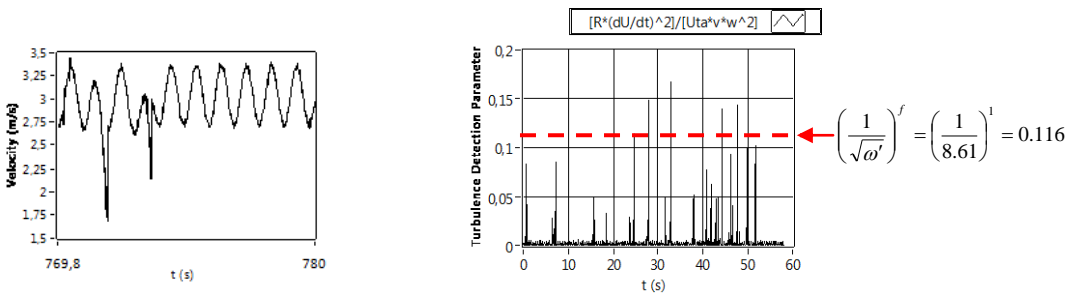
(a) $Re_{ia}=3144$, $Re_{os}=1587$, $\sqrt{\omega'}=7.70$ and $A_1=0.50$ ($r/R=0.977$)



(b) $Re_{ta}=3144$, $Re_{os}=1587$, $\sqrt{\omega'}=7.70$ and $A_1=0.50$ ($r/R=0$)



(a) $Re_{ta}=2759$, $Re_{os}=521$, $\sqrt{\omega'}=8.61$ and $A_1=0.19$ ($r/R=0.977$)



(b) $Re_{ta}=2759$, $Re_{os}=521$, $\sqrt{\omega'}=8.61$ and $A_1=0.19$ ($r/R=0$)

Figure 8.28. Velocity waveforms at the onset of transition and transition to turbulence method at $r/R=0.977$ and $r/R=0$ for runs 113 and 123

As stated in previous chapter, the turbulence detection sub-program embedded into *TDFC.vi* is divided into two parts for the cases of $\sqrt{\omega'} \leq 8.61$ ($f \leq 1$ Hz)

and $\sqrt{\omega'} > 8.61$ ($f > 1$ Hz). The dynamic TDP_4 and the dynamic TP_2 become $(dU(r,t)/dt)^2 / (\bar{U}_{ia}^2 \omega^2)$ and $(1/\sqrt{\omega'})^4$, respectively for $\sqrt{\omega'} > 8.61$ ($f > 1$ Hz), which are used in *TDFC.vi* for detection of the onset of transition when it occurs. Figure 8.29 shows the variation of the dynamic $TP_2 = (1/\sqrt{\omega'})^4$ for $\sqrt{\omega'} > 8.61$ ($f > 1$ Hz). The value of TP_2 decreases when $\sqrt{\omega'}$ (in other words f) increases.

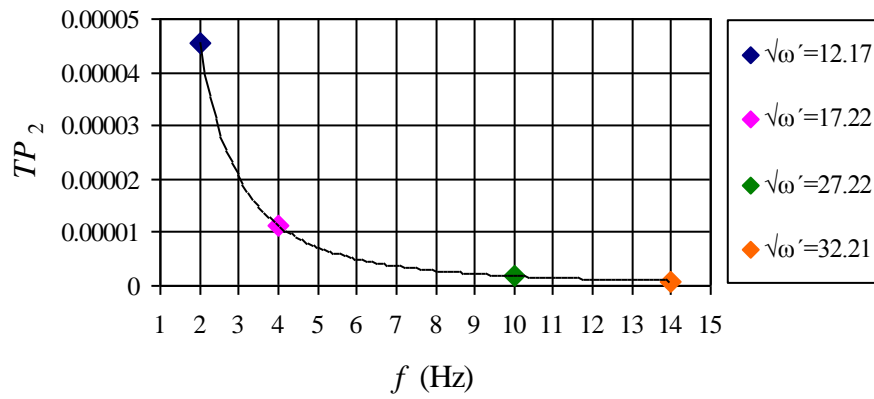
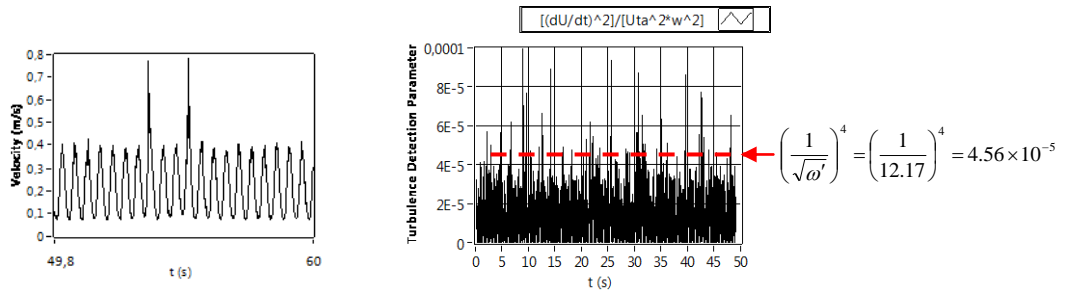
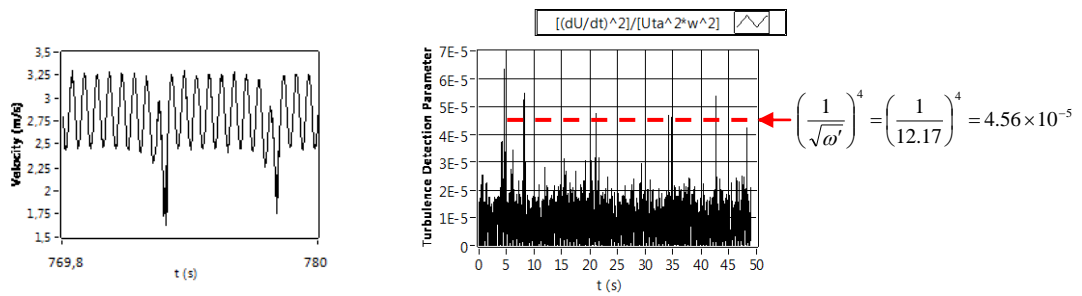


Figure 8.29. Variation of TP_2 with f in the range of $12.17 \leq \sqrt{\omega'} \leq 32.21$

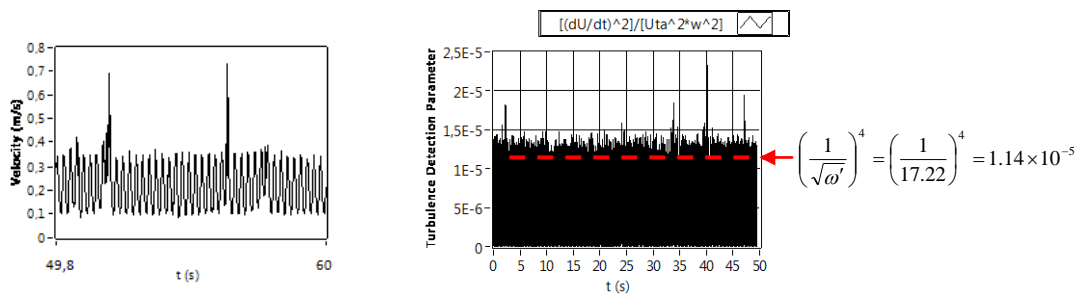
Figure 8.30 shows the velocity waveforms at the onset of transition and the graphics of the detection method at $r/R=0.977$ and $r/R=0$ for $\sqrt{\omega'} > 8.61$ ($f > 1$ Hz) corresponding to $\sqrt{\omega'} = 12.17$, $\sqrt{\omega'} = 17.22$, $\sqrt{\omega'} = 27.22$ and $\sqrt{\omega'} = 32.21$. As can be noticed from Fig. 8.30b, the turbulent bursts are seen to be like sudden and sharp drops in shape in the decelerating phase at $r/R=0$ for $\sqrt{\omega'} > 8.61$, rather than previously observed collapses in shape for $\sqrt{\omega'} \leq 8.61$. As shown in the figure, the instantaneous TDP_4 values are seen to be above TP_2 at the instants where the transition to turbulence starts.



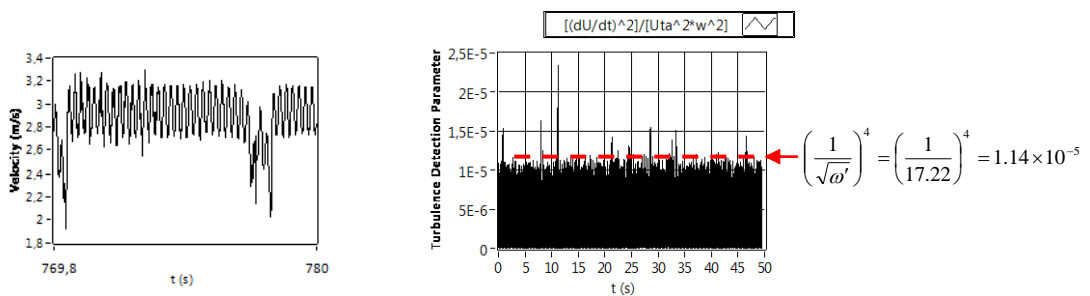
(a) $Re_{ta}=2541$, $Re_{os}=766$, $\sqrt{\omega'}=12.17$ and $A_1=0.30$ ($r/R=0.977$)



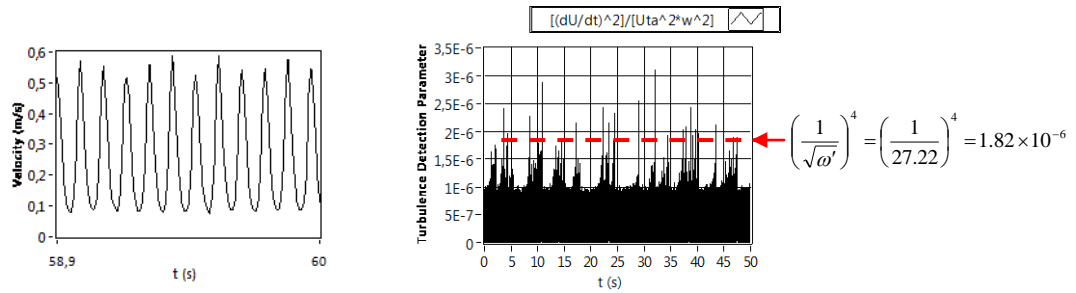
(b) $Re_{ta}=2541$, $Re_{os}=766$, $\sqrt{\omega'}=12.17$ and $A_1=0.30$ ($r/R=0$)



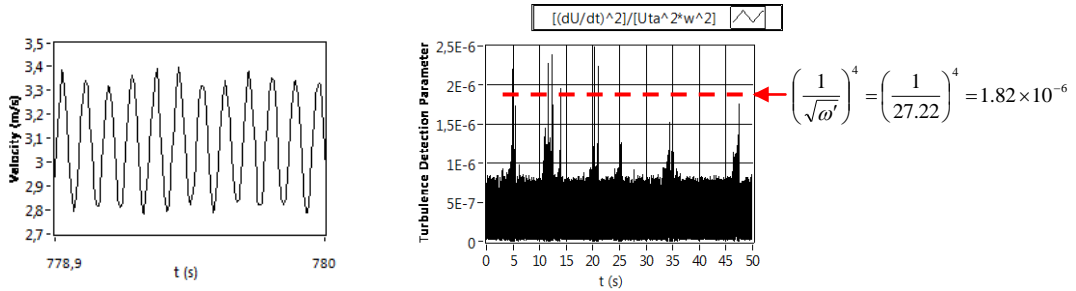
(a) $Re_{ta}=2662$, $Re_{os}=405$, $\sqrt{\omega'}=17.22$ and $A_1=0.15$ ($r/R=0.977$)



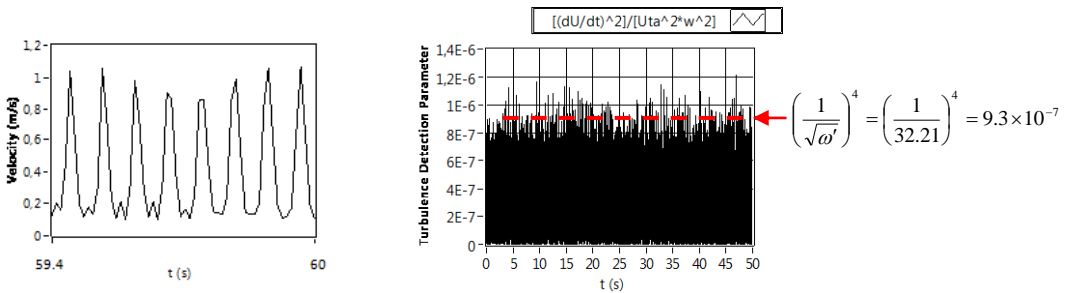
(b) $Re_{ta}=2662$, $Re_{os}=405$, $\sqrt{\omega'}=17.22$ and $A_1=0.15$ ($r/R=0$)



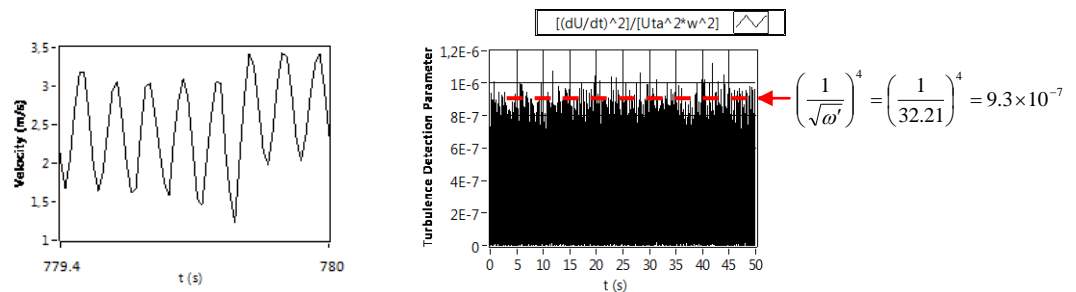
(a) $Re_{ta}=2779$, $Re_{os}=284$, $\sqrt{\omega'}=27.22$ and $A_1=0.10$ ($r/R=0.977$)



(b) $Re_{ta}=2779$, $Re_{os}=284$, $\sqrt{\omega'}=27.22$ and $A_1=0.10$ ($r/R=0$)



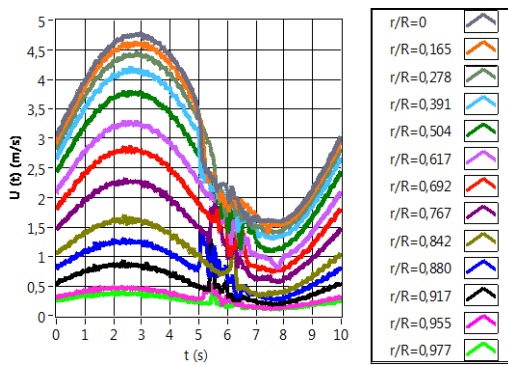
(a) $Re_{ta}=2643$, $Re_{os}=933$, $\sqrt{\omega'}=32.21$ and $A_1=0.35$ ($r/R=0.977$)



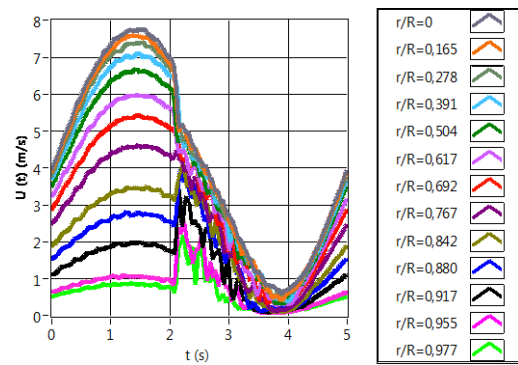
(b) $Re_{ta}=2643$, $Re_{os}=933$, $\sqrt{\omega'}=32.21$ and $A_1=0.35$ ($r/R=0$)

Figure 8.30. Velocity waveforms at the onset of transition and transition to turbulence method for $\sqrt{\omega'} > 8.61$ ($f > 1$ Hz) at $r/R=0.977$ and $r/R=0$ for runs 146, 164, 185, 214

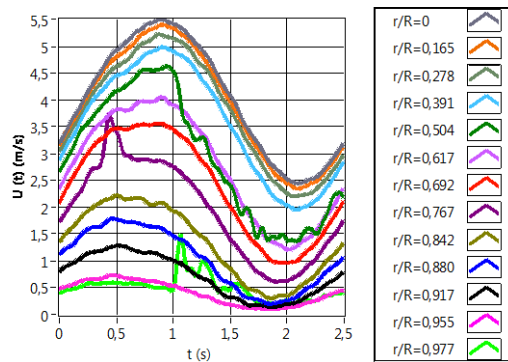
Figure 8.31 shows the velocity waveforms at all r/R at the onset of transition to turbulence for runs 50, 64, 88, 113, 123, 146, 164, 185 and 214. The transition to turbulence in the decelerating phase of the velocity waveforms can be seen clearly at all radial positions for $\sqrt{\omega'} = 2.72$ and $\sqrt{\omega'} = 3.85$ as can be observed from the figure. The turbulent bursts are as peaks in shape from $r/R=0.977$ to $r/R=0.692$. After $r/R=0.692$ towards the pipe centerline, the bursts become as collapses in shape. The same behavior was seen in the Ph.D. thesis of Nishi (Nishi, 2009). However, the turbulent bursts cannot be easily seen on the velocity waveforms for $\sqrt{\omega'} \geq 17.22$ ($f \geq 4$ Hz) by direct visual observation on the velocity waveforms although turbulent bursts occur at $\sqrt{\omega'} \geq 17.22$. Hence the importance of the devised turbulence detection program arises once more.



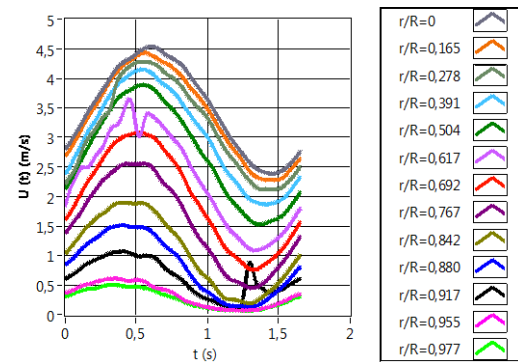
$Re_{\tau a} = 3018, \sqrt{\omega'} = 2.72, A_1 = 0.53$



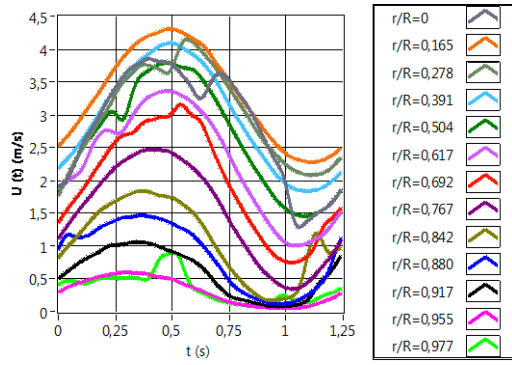
$Re_{\tau a} = 4817, \sqrt{\omega'} = 3.85, A_1 = 0.82$



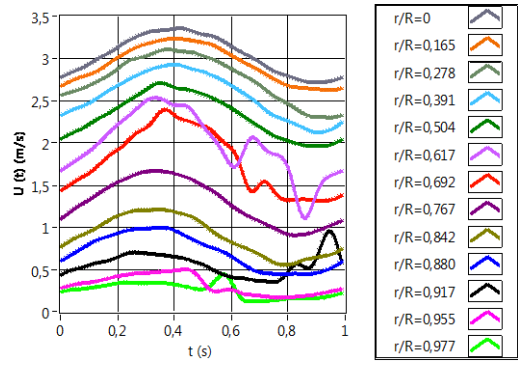
$Re_{\tau a} = 3887, \sqrt{\omega'} = 5.44, A_1 = 0.50$



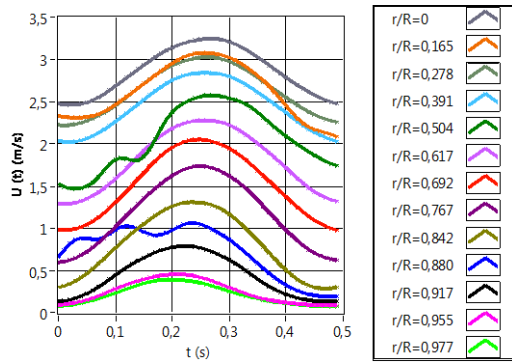
$Re_{\tau a} = 3229, \sqrt{\omega'} = 6.67, A_1 = 0.50$



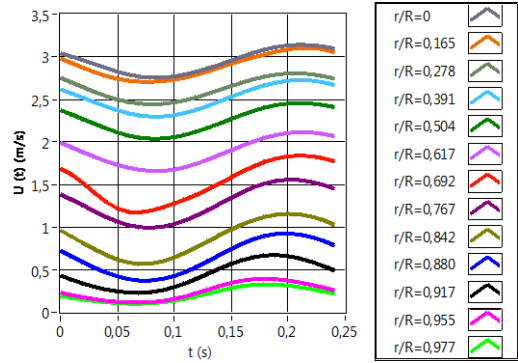
$Re_{\tau a} = 3144, \sqrt{\omega'} = 7.70, A_1 = 0.50$



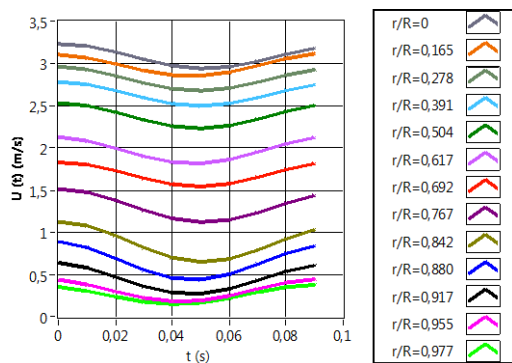
$Re_{\tau a} = 2759, \sqrt{\omega'} = 8.61, A_1 = 0.19$



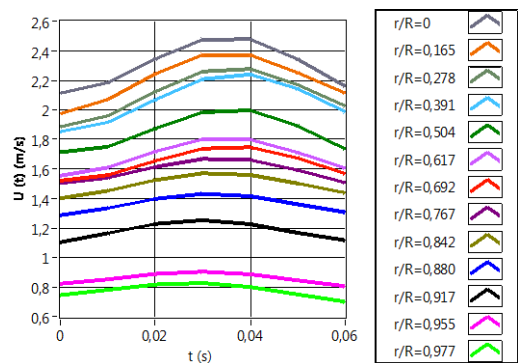
$Re_{\tau a} = 2541, \sqrt{\omega'} = 12.17, A_1 = 0.30$



$Re_{\tau a} = 2662, \sqrt{\omega'} = 17.22, A_1 = 0.15$



$Re_{\tau a} = 2779, \sqrt{\omega'} = 27.22, A_1 = 0.10$



$Re_{\tau a} = 2643, \sqrt{\omega'} = 32.21, A_1 = 0.35$

Figure 8.31. Velocity profiles at all r/R at the onset of transition to turbulence for runs 50, 64, 88, 113, 123, 146, 164, 185 and 214

According to the observations on the velocity waveforms at the onset of transition, the following expressions can be deduced as:

1) The observed shapes of the velocity profiles in all runs of the experimental study are sinusoidal at the onset of transition.

2) The turbulent bursts are seen in the decelerating phase of the velocity waveform as peaks and collapses in shape at $r/R=0.977$ and $r/R=0$, respectively for $\sqrt{\omega'} \leq 8.61$. The turbulent bursts are seen to be like sudden and sharp drops in shape in the decelerating phase at $r/R=0$ for $\sqrt{\omega'} > 8.61$. The critical state of $\sqrt{\omega'} > 8.61$ ($f > 1$ Hz) is verified once more.

3) The dynamic TDP_3 and TP_1 are used $R(dU(r,t)/dt)^2 / (\bar{U}_{ia} v \omega^2)$ and $(1/\sqrt{\omega'})^n$, respectively for $f \leq 1$ Hz. The dynamic TDP_4 and TP_2 become $(dU(r,t)/dt)^2 / (\bar{U}_{ia}^2 \omega^2)$ and $(1/\sqrt{\omega'})^4$, respectively for $\sqrt{\omega'} > 8.61$ ($f > 1$ Hz).

4) The occurrence of the turbulent bursts is found to be time periodicity, due to the propagations of the turbulent bursts to downstream of the pipeline.

5) TP_1 and TP_2 decrease when $\sqrt{\omega'}$ (in other words f) increases for both $f \leq 1$ Hz and $f > 1$ Hz.

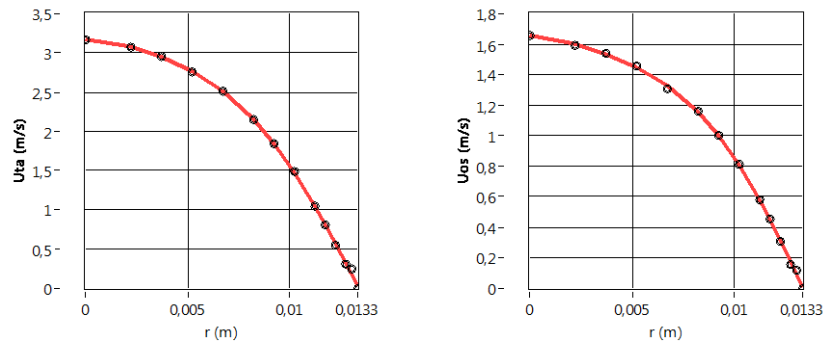
6) It is verified that *TDFC.vi* does not detect any turbulent bursts at any radial position throughout the pipe cross-section and does not give an alarm for runs in laminar regime. This verification of the detection method is satisfied for all runs in laminar regime.

7) The velocity waveforms at all r/R at the onset of transition are also shown in figures for all values of $\sqrt{\omega'}$. The turbulent bursts in the decelerating phase of the velocity waveforms can be seen clearly at all radial positions for $\sqrt{\omega'} < 17.22$. However, the turbulent bursts cannot be detected by means of the visual observation of velocity waveforms for $\sqrt{\omega'} \geq 17.22$ ($f \geq 4$ Hz). Hence the importance of the devised turbulence detection program arises once more.

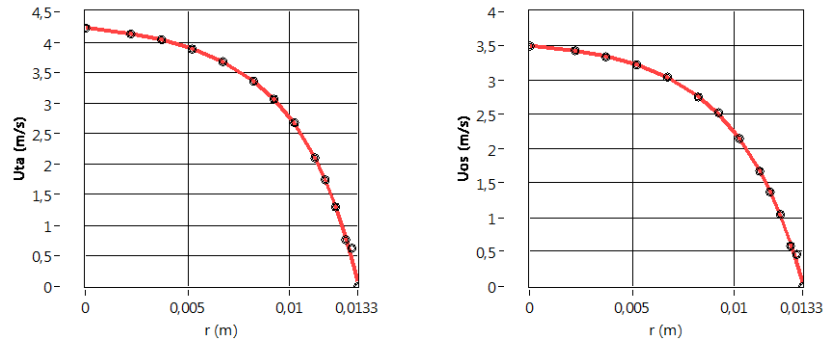
8.3.2. Velocity distributions of time averaged and oscillating components in pulsatile flow regime at the onset of transition to turbulence

To obtain velocity distributions of time averaged and oscillating components, \bar{U}_{ta} and $|\bar{U}_{os,1}|$ in pulsatile pipe flow, the first method is used in *TDFC.vi* as previously mentioned.

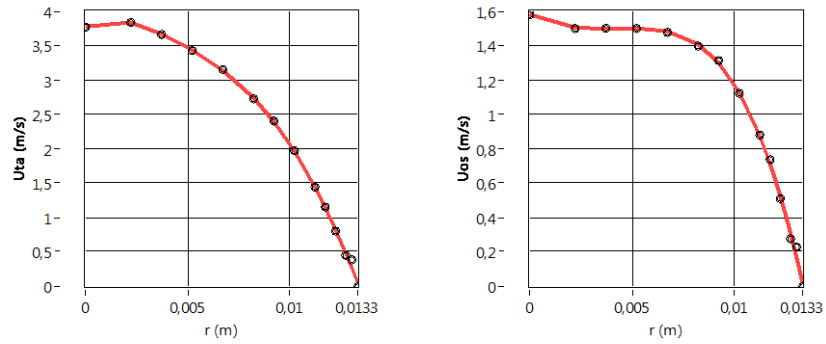
The cross-sectional distributions of \bar{U}_{ta} and $|\bar{U}_{os,1}|$ at the onset of transition at $\sqrt{\omega'} = 2.72, 3.85$ and 5.44 for runs 14, 50 and 64 are given in Fig. 8.32. The distributions of \bar{U}_{ta} are not parabolic in shape, hence do not obey the well-known Blasius profile at the onset of transition as shown in Fig. 8.33. There is a big deviation between the experimental data and the Blasius theory with $\pm 22\%$ near the pipe centerline. The distributions of $|\bar{U}_{os,1}|$ are also not parabolic and do not obey the theoretical steady flow Blasius profile as shown in Fig. 8.34. These deductions certify that these runs are not laminar and they are at the onset of transition. The cross-sectional distribution of $|\bar{U}_{os,1}|$ begins to collapse near the pipe centerline when $\sqrt{\omega'} \geq 3.85$ as shown in Fig. 8.32. This behavior of $|\bar{U}_{os,1}|$ distribution is similar with that in laminar regime.



(a) $Re_{ta} = 3018, Re_{os} = 1610, \sqrt{\omega'} = 2.72$ and $A_1 = 0.53$



(b) $Re_{ta}=4817$, $Re_{os}=3939$, $\sqrt{\omega'}=3.85$ and $A_1=0.82$



(c) $Re_{ta}=3887$, $Re_{os}=1940$, $\sqrt{\omega'}=5.44$ and $A_1=0.50$

Figure 8.32. Cross-sectional distributions of \bar{U}_{ta} and $|\bar{U}_{os,1}|$ for runs 14, 50 and 64

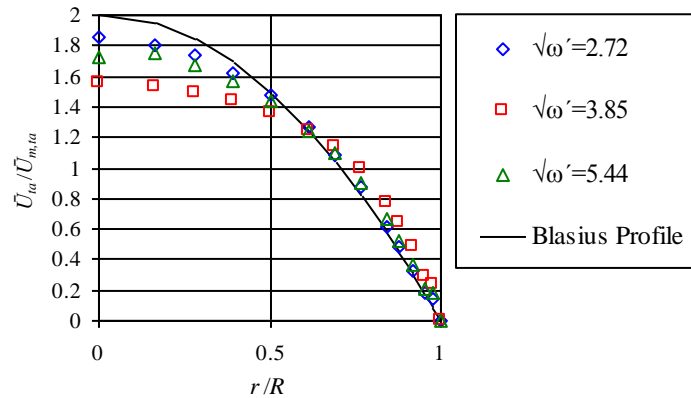


Figure 8.33. Cross-sectional distributions of $\bar{U}_{ta} / \bar{U}_{m,ta}$ with r/R for runs 14, 50 and 64 at the onset of transition

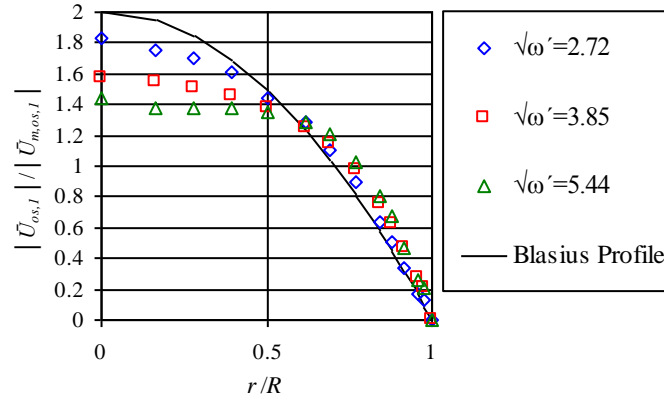
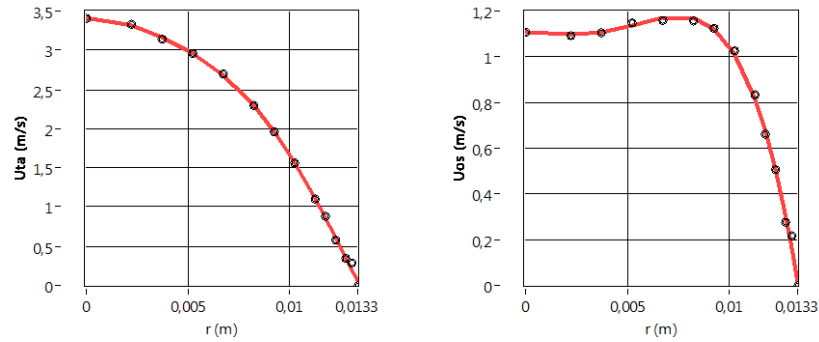


Figure 8.34. Cross-sectional distributions of $|\bar{U}_{os,1}|/|\bar{U}_{m,os,1}|$ with r/R for runs 14, 50 and 64 at the onset of transition

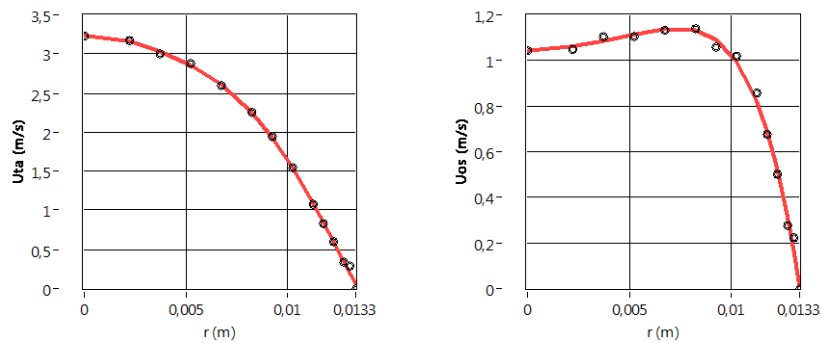
The cross-sectional distributions of \bar{U}_{ta} and $|\bar{U}_{os,1}|$ for $\sqrt{\omega'} \geq 6.67$ ($f \geq 0.6$ Hz) at the onset of transition are given in Fig. 8.35. The profiles of $|\bar{U}_{os,1}|$ are rather different than those $\sqrt{\omega'} < 6.67$ ($f < 0.6$ Hz). As seen from Fig. 8.35, $|\bar{U}_{os,1}|$ distributions firstly begin to increase towards the pipe centerline, then decrease and later maintain its constant magnitude up to pipe centerline, which is similar with those in laminar regime. These behaviors of $|\bar{U}_{os,1}|$ distributions are similar with theoretical laminar theory for $|\bar{U}_{os,1}|$, Eq. (4.23), which is given in the paper of Ohmi et al. (1982), however do not obey exactly due to the onset of transition to turbulence.

The increase rate of $|\bar{U}_{os,1}|$ distribution is dependent on $\sqrt{\omega'}$. $|\bar{U}_{os,1}|$ increases up to $r=0.0067$ m and then decrease up to pipe centerline at $\sqrt{\omega'} = 6.67$. As $\sqrt{\omega'}$ increases, the increase of $|\bar{U}_{os,1}|$ shifts towards the pipe centerline such that $|\bar{U}_{os,1}|$ increases up to $r=0.0082$ m at $\sqrt{\omega'} = 7.70$, $r=0.0092$ m at $\sqrt{\omega'} = 8.61$ and $r=0.0102$ m at $\sqrt{\omega'} \geq 12.17$. This shift of the increase rate is also seen in the $|\bar{U}_{os,1}|$ distribution in laminar regime.

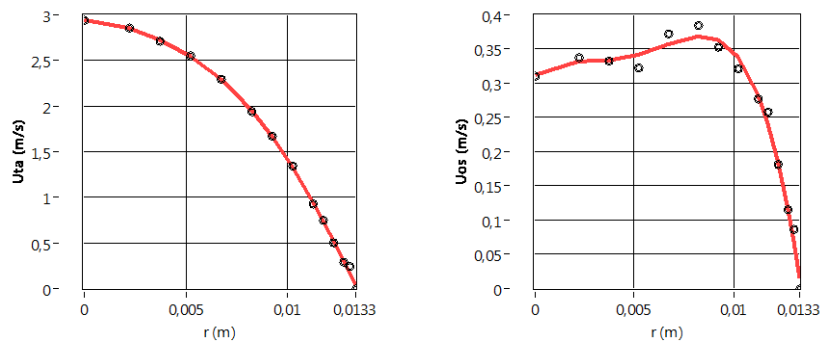
The distribution of $|\overline{U}_{os,1}|$ at $\sqrt{\omega'} = 32.21$ is unexpected in shape at the onset of transition as seen in Fig. 8.35g. The value of $|\overline{U}_{os,1}|$ suddenly increased after $r=0.0052$ m towards pipe centerline. This behavior of $|\overline{U}_{os,1}|$ distribution is seen for only $A_1 \leq 0.35$ at $\sqrt{\omega'} = 32.21$.



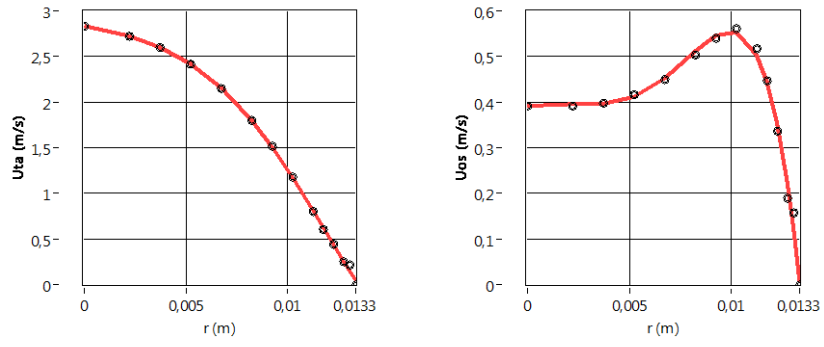
(a) $Re_{ta} = 3229$, $Re_{os} = 1616$, $\sqrt{\omega'} = 6.67$ and $A_1 = 0.50$



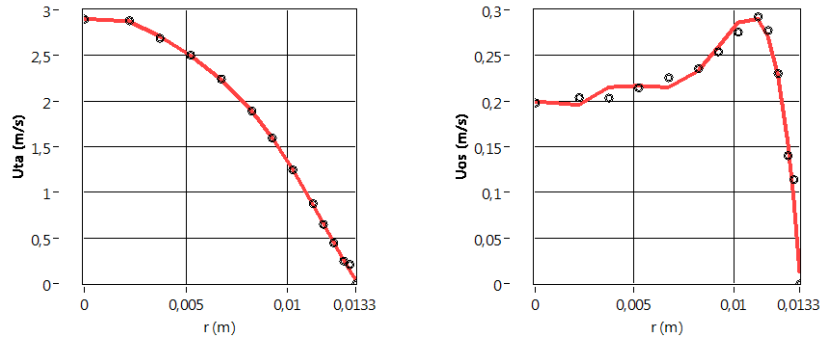
(b) $Re_{ta} = 3144$, $Re_{os} = 1587$, $\sqrt{\omega'} = 7.70$ and $A_1 = 0.50$



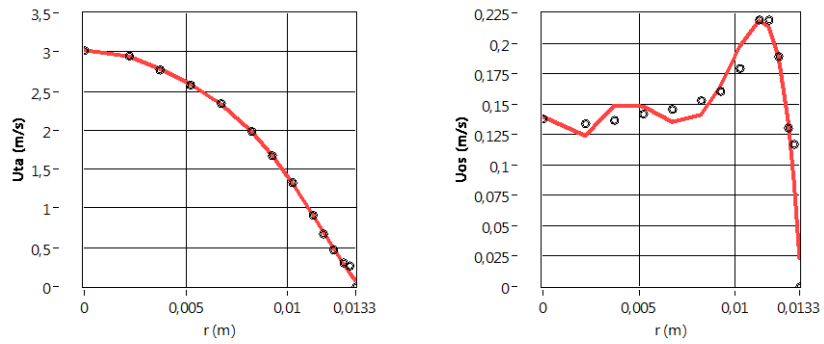
(c) $Re_{ta} = 2759$, $Re_{os} = 521$, $\sqrt{\omega'} = 8.61$ and $A_1 = 0.19$



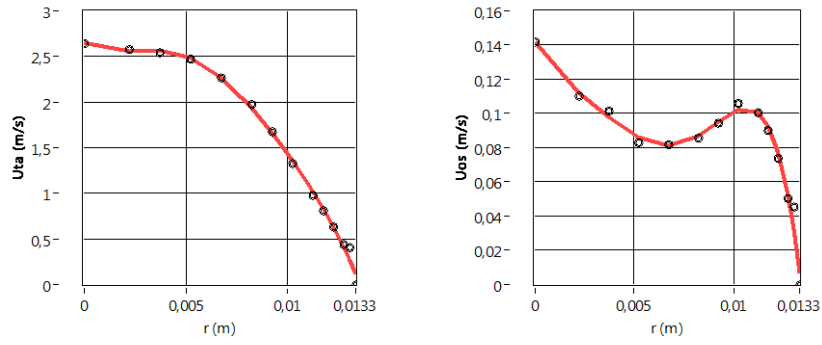
(d) $Re_{ta}=2541$, $Re_{os}=766$, $\sqrt{\omega'}=12.17$ and $A_1=0.30$



(e) $Re_{ta}=2662$, $Re_{os}=405$, $\sqrt{\omega'}=17.22$ and $A_1=0.15$



(f) $Re_{ta}=2779$, $Re_{os}=284$, $\sqrt{\omega'}=27.22$ and $A_1=0.10$



(g) $Re_{ta}=2643$, $Re_{os}=933$, $\sqrt{\omega'}=32.21$ and $A_1=0.35$

Figure 8.35. Cross-sectional distributions of \bar{U}_{ta} and $|\bar{U}_{os,1}|$ for runs 88, 113, 123, 146, 164, 185 and 214

The distributions of \bar{U}_{ta} at $\sqrt{\omega'} \geq 6.67$ ($f \geq 0.6$ Hz) are not parabolic in shape and also do not obey the Blasius profile at the onset of transition as same as those at $\sqrt{\omega'} < 6.67$ ($f < 0.6$ Hz) as shown in Fig. 8.36. The deviation between the experimental data and the Blasius theory is $\pm 20\%$ near the pipe centerline. The distributions of $|\bar{U}_{os,1}|$ are also not parabolic and do not obey the theoretical steady flow Blasius profile as shown in Fig. 8.37. The common behavior of $|\bar{U}_{os,1}|/|\bar{U}_{m,os,1}|$ distributions for $\sqrt{\omega'} \geq 6.67$ is given with the dashed line.

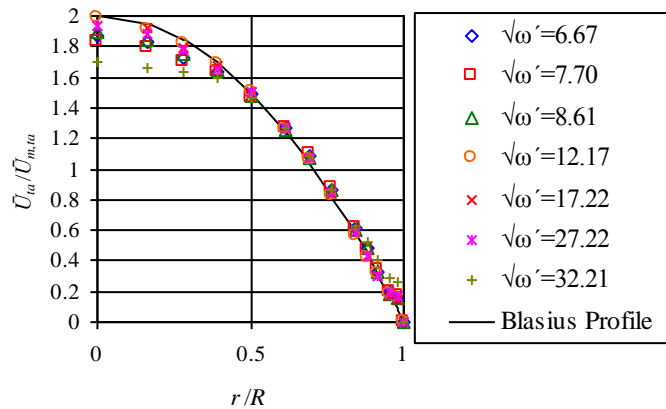


Figure 8.36. Cross-sectional distributions of $\bar{U}_{ta} / \bar{U}_{m,ta}$ with r/R for runs 88, 113, 123, 146, 164, 185 and 214 at the onset of transition

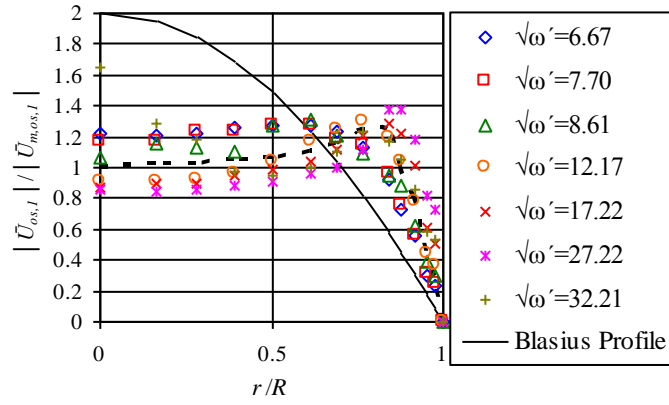


Figure 8.37. Cross-sectional distributions of $|\bar{U}_{os,1}|/|\bar{U}_{m,os,1}|$ with r/R for runs 88, 113, 123, 146, 164, 185 and 214 at the onset of transition

As a result, the following deductions on the cross-sectional distributions of \bar{U}_{ta} and $|\bar{U}_{os,1}|$ at the onset of transition can be given as follows;

- 1) The distributions of \bar{U}_{ta} are not parabolic in shape and do not obey the Blasius profile at the onset of transition for $\sqrt{\omega'} \leq 5.44$ with a big deviation between the experimental data and the Blasius theory of $\pm 22\%$ near the pipe centerline. The distributions of \bar{U}_{ta} at $\sqrt{\omega'} \geq 6.67$ ($f \geq 0.6$ Hz) are not parabolic in shape and are not compatible with the Blasius profile at the onset of transition with a maximum deviation of $\pm 20\%$ near the pipe centerline.
- 2) The distributions of $|\bar{U}_{os,1}|$ are also not parabolic and do not obey the theoretical steady flow Blasius profile.
- 3) The cross-sectional distribution of $|\bar{U}_{os,1}|$ begins to collapse near the pipe centerline when $\sqrt{\omega'} \geq 3.85$.
- 4) The cross-sectional distributions of $|\bar{U}_{os,1}|$ for $\sqrt{\omega'} \geq 6.67$ ($f \geq 0.6$ Hz) at the onset of transition are rather different than those $\sqrt{\omega'} < 6.67$ ($f < 0.6$ Hz).
- 5) The increase rate of $|\bar{U}_{os,1}|$ distribution is dependent on $\sqrt{\omega'}$. As $\sqrt{\omega'}$ increases,

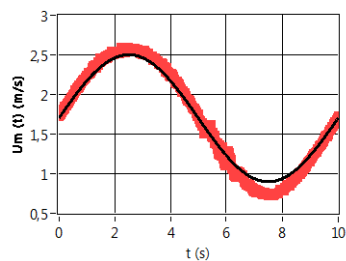
the increase of $|\overline{U}_{os,1}|$ shifts towards the pipe centerline such that $|\overline{U}_{os,1}|$ increases up to $r=0.0082$ m at $\sqrt{\omega'}=7.70$, $r=0.0092$ m at $\sqrt{\omega'}=8.61$ and $r=0.0102$ m at $\sqrt{\omega'}\geq 12.17$.

6) The distribution of $|\overline{U}_{os,1}|$ at $\sqrt{\omega'}=32.21$ for only $A_1\leq 0.35$ is different in shape than others at the onset of transition. The value of $|\overline{U}_{os,1}|$ suddenly increased after $r=0.0052$ m towards pipe centerline. This behavior of $|\overline{U}_{os,1}|$ distribution is seen at only $\sqrt{\omega'}=32.21$.

8.3.3. Mean velocity profiles in pulsatile flow regime at the onset of transition to turbulence

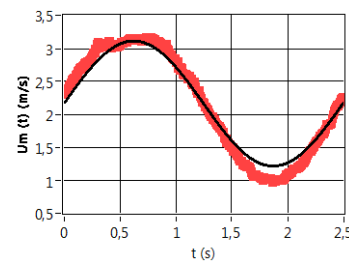
The mean velocity profiles obtained experimentally with their FFT approximations as direct output plots of *TDFC.vi* are shown in Fig. 8.38 for runs 14, 64, 113, 146, 164 and 185. The shapes of the mean velocity profiles obtained experimentally are sinusoidal. The influence of the turbulent bursts can be seen on the mean velocity profiles. Due to the transition to turbulence, there are some deviations between the experimental and theoretical mean velocity profiles. The mean deviations between the experimental and theoretical mean velocity are $\pm 8\%$ for all runs.

Um(t) (Experimental and Theoretical Values for One Period)



$$Re_{ta}=3018, \sqrt{\omega'}=2.72, A_1=0.53$$

Um(t) (Experimental and Theoretical Values for One Period)



$$Re_{ta}=3887, \sqrt{\omega'}=5.44, A_1=0.50$$

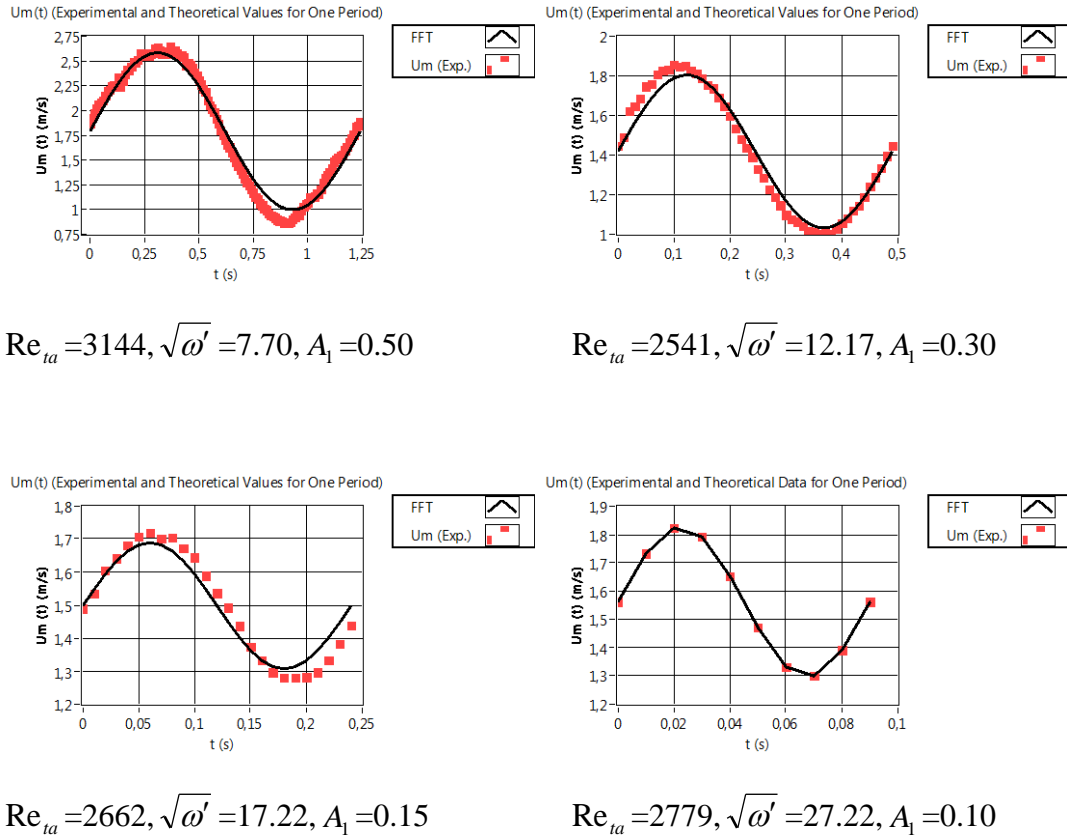


Figure 8.38. Cross-sectional mean velocity profiles obtained experimentally and theoretically for runs 14, 64, 113, 146, 164 and 185

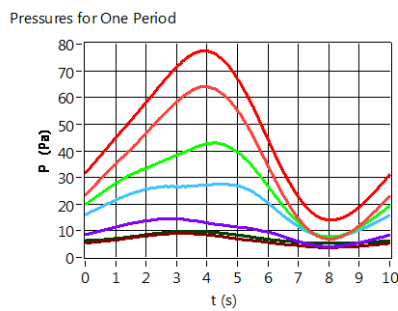
8.3.4. Pressure waveforms in pulsatile flow regime at the onset of transition to turbulence

The pressure waveforms at the onset of transition are seen in Fig. 8.39 for runs 14, 50, 64, 88, 113, 123, 146, 164, 185 and 214. The shapes of the pressure waveforms at the onset of transition are sinusoidal at each downstream location as same as velocity waveforms. Although the time dependency of the pressure waveforms for P_6 and P_7 at last two axial locations of $X/D=589$ and 619 are not clearly observed, these waveforms are exactly sinusoidal at all values of $\sqrt{\omega'}$, however rather small in magnitude, as observed those in laminar regime.

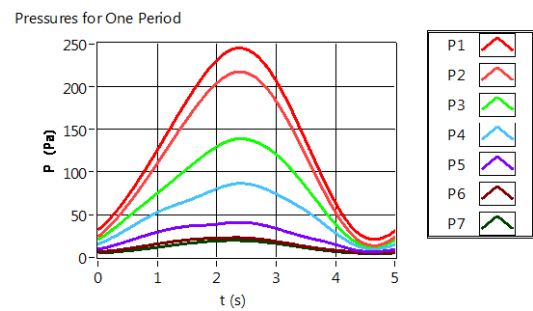
As noticed from the figure, the magnitude of static pressures at each phase is decreased at downstream locations. The oscillation amplitudes of the sinusoidal pulsation become very small at $\sqrt{\omega'} = 27.22$ and $\sqrt{\omega'} = 32.21$ as can be seen from the

last two plots. Meanwhile, the magnitudes of $|\overline{P}_{os,1}|$ are always seen to be smaller than their corresponding magnitudes of \overline{P}_{ta} ($|\overline{P}_{os,1}|/\overline{P}_{ta} < 1$) at each downstream pressure measurement stations at all values of $\sqrt{\omega'}$, except those at $\sqrt{\omega'} = 8.61$ ($f=1$ Hz) and $\sqrt{\omega'} = 12.17$ ($f=2$ Hz), as being $|\overline{P}_{os,1}|/\overline{P}_{ta} > 1$ at the onset of transition as same as the pressure waveforms in the laminar regime. At $\sqrt{\omega'} = 27.22$ and $\sqrt{\omega'} = 32.21$, the magnitudes of the oscillation amplitude at each axial location of the pressure transmitter are found to be smaller when compared with those at $\sqrt{\omega'} < 27.22$.

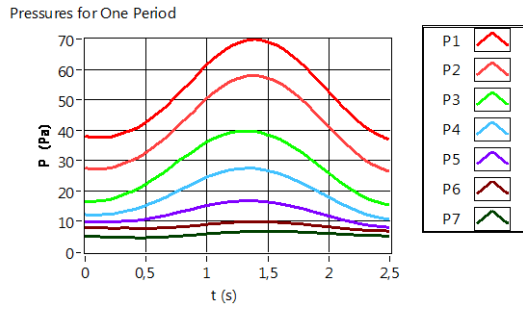
It is not meaningful to say that the time averaged and oscillating components of pressure, \overline{P}_{ta} and $|\overline{P}_{os,1}|$ are seen to increase when an increase of Re_{ta} . On contrary to laminar regime, the higher values of \overline{P}_{ta} and $|\overline{P}_{os,1}|$ can be seen for lower Re_{ta} . The maximum \overline{P}_{ta} is found to be 130 Pa at the axial location of the first pressure transmitter at maximum $Re_{ta}=4817$. Meanwhile, the accelerating phases of the pressure waveforms for $\sqrt{\omega'} = 2.72$ and $\sqrt{\omega'} = 3.85$ are inclined rightwards which are seen only at the onset of transition as seen from the figure. This behavior is not observed for other values of $\sqrt{\omega'}$.



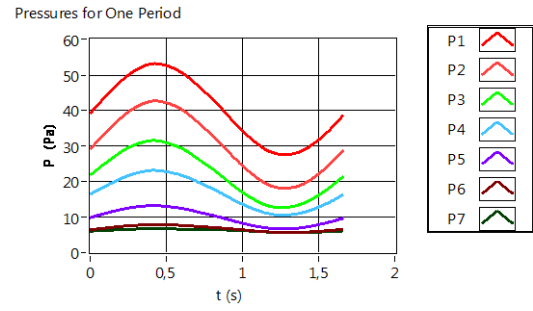
$$Re_{ta} = 3018, \sqrt{\omega'} = 2.72, A_1 = 0.53$$



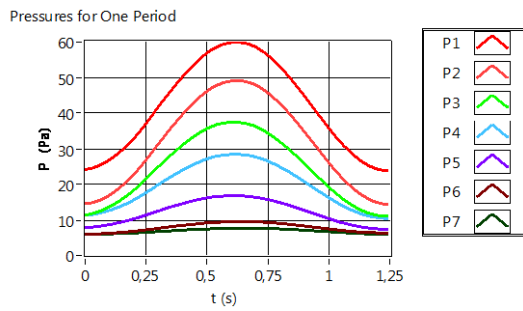
$$Re_{ta} = 4817, \sqrt{\omega'} = 3.85, A_1 = 0.82$$



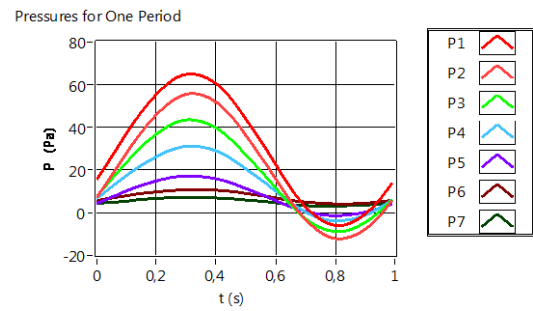
$$Re_{ta} = 3887, \sqrt{\omega'} = 5.44, A_1 = 0.50$$



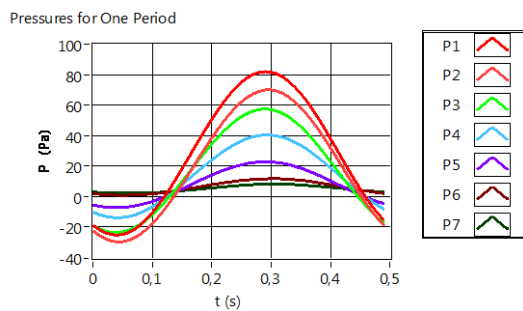
$$Re_{ta} = 3229, \sqrt{\omega'} = 6.67, A_1 = 0.50$$



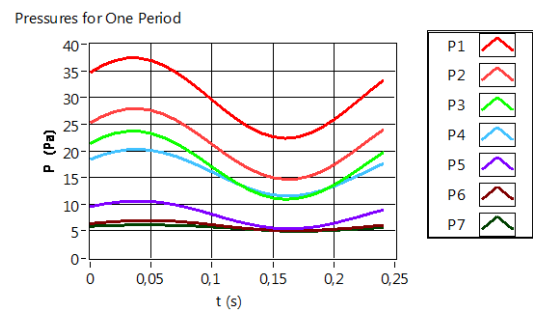
$$Re_{ta} = 3144, \sqrt{\omega'} = 7.70, A_1 = 0.50$$



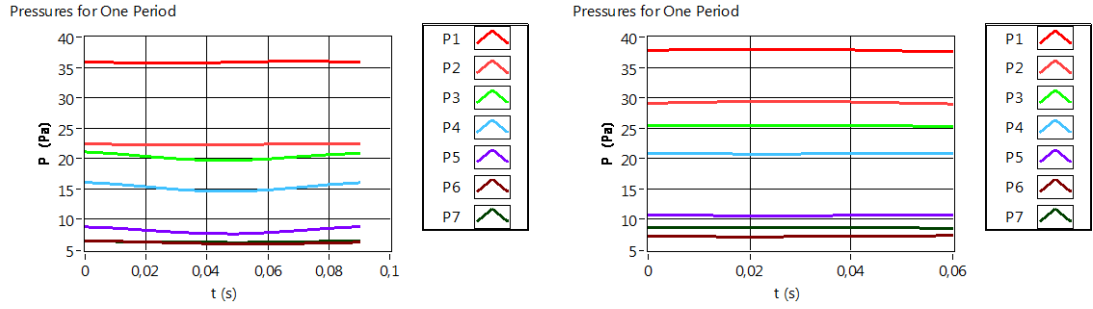
$$Re_{ta} = 2759, \sqrt{\omega'} = 8.61, A_1 = 0.19$$



$$Re_{ta} = 2541, \sqrt{\omega'} = 12.17, A_1 = 0.30$$



$$Re_{ta} = 2662, \sqrt{\omega'} = 17.22, A_1 = 0.15$$



$$Re_{ta} = 2779, \sqrt{\omega'} = 27.22, A_1 = 0.10$$

$$Re_{ta} = 2643, \sqrt{\omega'} = 32.21, A_1 = 0.35$$

Figure 8.39. Pressure waveforms acquired from each pressure transmitters for runs 14, 50, 64, 88, 113, 123, 146, 164, 185 and 214

8.3.5. Flow resistance in pulsatile flow regime at the onset of transition to turbulence

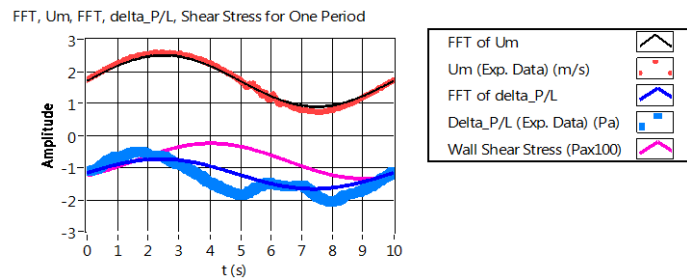
Frictional loss characteristics at the onset of the transition to turbulence are also investigated in the experimental study. The frictional factors as instantaneous friction factor, $\lambda_u(t)$, time averaged friction factor, $\lambda_{u,ta}$, and instantaneous laminar quasi-steady friction factor, λ_{qL} are evaluated by means of the velocity and pressure measurements.

8.3.5.1. Variations of $\Delta\bar{P}(t)/L$, $\bar{U}_m(t)$ and $\bar{\tau}_w(t)$ in pulsatile flow regime at the onset of transition to turbulence

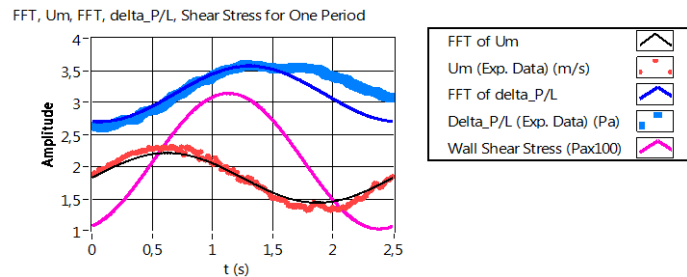
The last two pressure transmitters at $X/D=589$ and 619 are used to evaluate the pressure drop through the test section. In the devised program, *TDFC.vi*, the instantaneous pressure drop per unit length, $\Delta P(t)/L$ is evaluated at the onset of transition to turbulence. The experimentally determined values of $\Delta P(t)/L$ are compared with FFT approximations for each run. Instantaneous wall shear stress, $\bar{\tau}_w(t)$ is also evaluated using the definition of momentum integral equation given in Eq. (2.16). In Fig. 8.40, the solid lines on the measured $\Delta P(t)/L$ and $\bar{U}_m(t)$ show the first order FFT approximations of $\Delta P(t)/L$ and $\bar{U}_m(t)$ for runs 14,

57, 113, 146, 164, 185. The shapes of the experimentally measured $\bar{U}_m(t)$, $\Delta P(t)/L$ and theoretically evaluated $\bar{\tau}_w(t)$ are seen to be sinusoidal.

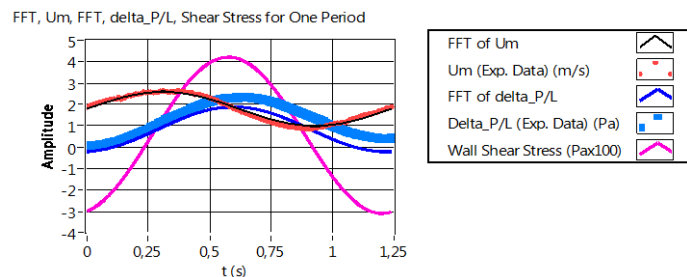
The mean deviation between $\Delta P(t)/L$ and its FFT approximation is found to be $\pm 10\%$ due to flow being at the onset of transition. The deviation of $\Delta P(t)/L$ and its FFT approximation becomes closer to each other for $\sqrt{\omega'} > 7.70$ at the onset of transition. The turbulent bursts on the pressure and velocity waveforms are seen at the same instants.



$$Re_{ta} = 3018, Re_{os} = 1610, \sqrt{\omega'} = 2.72 \text{ and } A_1 = 0.53$$



$$Re_{ta} = 3192, Re_{os} = 900, \sqrt{\omega'} = 5.44 \text{ and } A_1 = 0.28$$



$$Re_{ta} = 3144, Re_{os} = 1587, \sqrt{\omega'} = 7.70 \text{ and } A_1 = 0.50$$

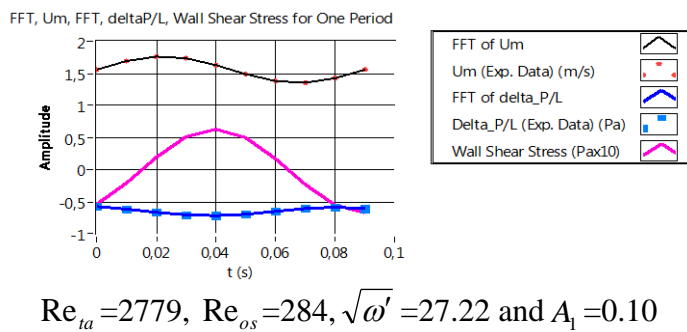
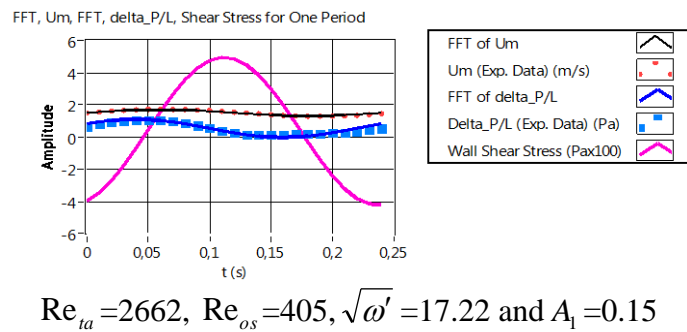
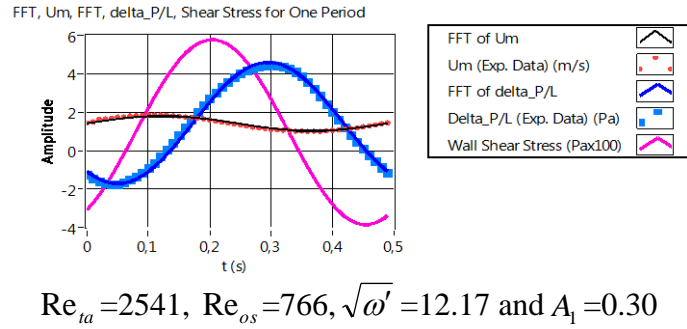


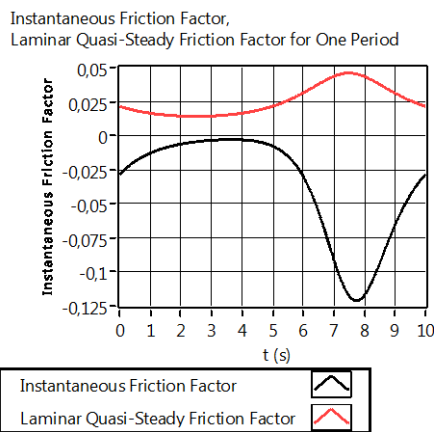
Figure 8.40. Variations of $\Delta\bar{P}(t)/L$, $\bar{U}_m(t)$ with their FFT approximations and $\bar{\tau}_w(t)$ for runs 14, 57, 113, 146, 164, 185

8.3.5.2. The variations of $\lambda_u(t)$ and $\lambda_{qL}(t)$ in pulsatile flow regime at the onset of transition to turbulence

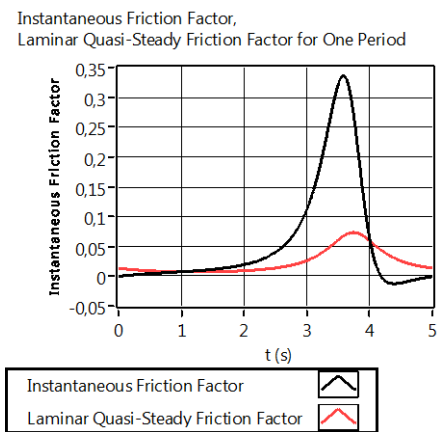
The variations of $\lambda_u(t)$ and λ_{qL} for runs 14, 50, 113, 146, 164, 185 are given in Fig. 8.41. The time dependency of $\lambda_u(t)$ and $\lambda_{qL}(t)$ are seen in the figure although $\lambda_{qL}(t)$ is based on quasi-steady approach. $\lambda_u(t)$ and $\lambda_{qL}(t)$ profiles are time

dependent but not sinusoidal at all values of $\sqrt{\omega'}$. As can be seen from the figure, the magnitudes of $\lambda_u(t)$ and $\lambda_{qL}(t)$ are rather different from each other at each run as same as those in laminar regime. Hence it is verified that the experimental range is not in quasi-steady regime. Although $\lambda_{qL}(t)$ has a time dependency at $\sqrt{\omega'} \leq 8.61$ ($f \leq 1$ Hz), the pulsatile variation disappears at $\sqrt{\omega'} > 8.61$ ($f > 1$ Hz).

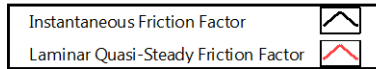
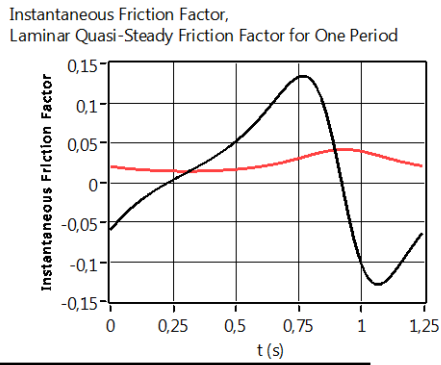
It is also noticed that there is an effect of A_1 on the behavior of $\lambda_u(t)$ profile at each $\sqrt{\omega'}$ as observed in laminar regime. When A_1 is increased from $A_1=0.10$ to $A_1=0.90$ at any value of $\sqrt{\omega'}$, the shape of $\lambda_u(t)$ profile is deformed and getting sharp and sharp. $\lambda_u(t)$ profile begins to change in shape as a hill at $A_1 \geq 0.30$ as seen in Fig. 8.41. The same deduction is expressed for $\lambda_u(t)$ profile in laminar regime. Moreover this hill-shape is getting sharp and sharp when A_1 is increased. However, there seems to be no effect of $\sqrt{\omega'}$ on the shape formation of the $\lambda_u(t)$ profile.



$$\text{Re}_{\tau a} = 3018, \text{Re}_{os} = 2.72, \sqrt{\omega'} = 2.72, \\ A_1 = 0.53$$

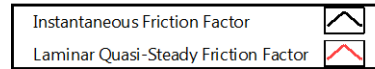
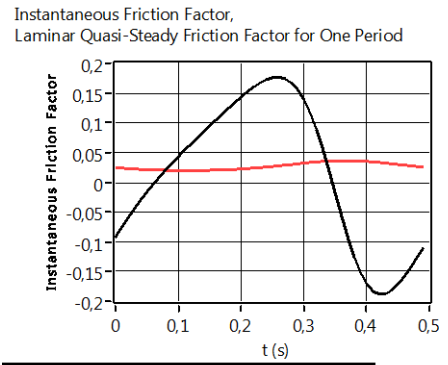


$$\text{Re}_{\tau a} = 4817, \text{Re}_{os} = 3939, \sqrt{\omega'} = 3.85, \\ A_1 = 0.82$$



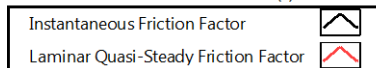
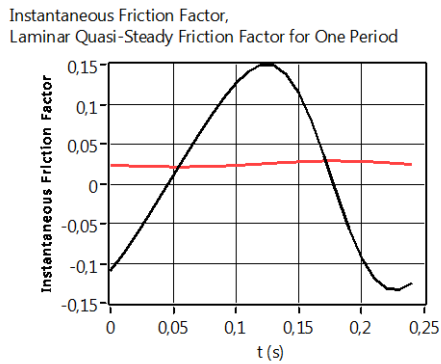
$$Re_{ta}=3144, Re_{os}=1587, \sqrt{\omega'}=7.70$$

$$A_1=0.50$$



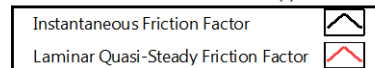
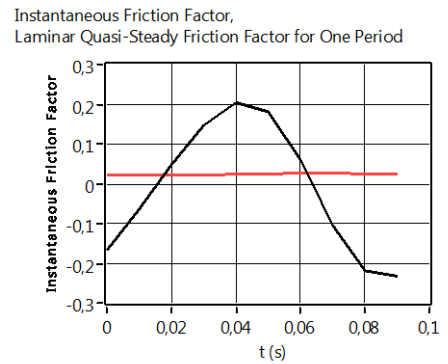
$$Re_{ta}=2541, Re_{os}=766, \sqrt{\omega'}=12.17$$

$$A_1=0.30$$



$$Re_{ta}=2662, Re_{os}=405, \sqrt{\omega'}=17.22$$

$$A_1=0.15$$



$$Re_{ta}=2779, Re_{os}=284, \sqrt{\omega'}=27.22$$

$$A_1=0.10$$

Figure 8.41. Variations of $\lambda_u(t)$ and λ_{qL} for runs 14, 50, 113, 146, 164, 185

8.6. Conclusions

Flow dynamics of pulsatile flow in laminar regime and at the onset of transition can be expressed as follows;

- 1) The observed shapes of the velocity profiles both in laminar regime and at the onset of transition are sinusoidal.

2) The increase in A_1 at constant $\sqrt{\omega'}$ causes the flow to keep in laminar regime for $\sqrt{\omega'} < 32.21$ ($f < 14$ Hz).

3) $\sqrt{\omega'} > 8.61$ ($f > 1$ Hz) is found to be the critical state both in the laminar regime and at the onset of transition. This critical state has also been expressed previously by means of the data available in the literature. For $\sqrt{\omega'} > 8.61$ ($f > 1$ Hz), the turbulent bursts are seen as sudden and sharp drops in shape in the decelerating phase at $r/R=0$ at the onset of the transition to turbulence although they are as collapses in shape for $f \leq 1$ Hz.

4) The occurrence of the turbulent bursts is found to be time periodicity as a result of the propagations of the turbulent bursts along the pipeline.

5) The cross-sectional distributions of \bar{U}_{ta} in laminar regime obey the theoretical Blasius profile with a maximum deviation of $\pm 4\%$ for all values of $\sqrt{\omega'}$, except for $\sqrt{\omega'} = 31.22$ ($f = 14$ Hz). However, the distributions of \bar{U}_{ta} at the onset of transition are not parabolic in shape and do not obey the Blasius profile with a mean deviation $\pm 22\%$ near the pipe centerline.

6) The cross-sectional distributions of $|\bar{U}_{os,1}|$ both in laminar regime and at the onset of transition do not obey the theoretical steady flow Blasius profile. The distributions of $|\bar{U}_{os,1}|$ for $\sqrt{\omega'} \geq 6.67$ ($f \geq 0.6$ Hz) firstly tends to increase towards the pipe centerline, then decrease and later keep its magnitude constant up to pipe centerline both in laminar regime and at the onset of transition. The increase rate of $|\bar{U}_{os,1}|$ distribution is dependent on $\sqrt{\omega'}$. When $\sqrt{\omega'}$ increases, the increase of $|\bar{U}_{os,1}|$ shifts towards the pipe centerline from $r=0.0067$ m at $\sqrt{\omega'} = 6.67$ to $r=0.0102$ m at $\sqrt{\omega'} = 32.21$.

7) At the onset of transition, the distribution of $|\bar{U}_{os,1}|$ at $\sqrt{\omega'} = 32.21$ is different in shape than others for $A_1 \leq 0.35$. The value of $|\bar{U}_{os,1}|$ suddenly increased after $r=0.0052$ m towards pipe centerline.

8) The shapes of the mean velocity profiles obtained experimentally in laminar regime and at the onset of transition are sinusoidal. There are excellent agreements between the experimental and theoretical mean velocity profiles in laminar regime. However, the influence of the turbulent bursts can be seen on the mean velocity profiles at the onset of transition. The mean deviations between the experimental and theoretical mean velocities are found as $\pm 8\%$ for all runs due to the onset of transition.

9) The static pressure data at each pressure measurement station are accumulated 13 times by the devised program, *TDFC.vi* due to the velocity measurements throughout 13 radial positions. The pressure data acquired at each station, which are taken for 13 times in one run are found to be same in magnitude with an accuracy of $\pm 0.8\%$.

10) The shapes of the pressure waveforms are sinusoidal as same as velocity waveforms in laminar regime and at the onset of transition. The magnitudes of $|\bar{P}_{os,1}|$ are found to be greater than \bar{P}_{ta} ($|\bar{P}_{os,1}|/\bar{P}_{ta} > 1$) at $\sqrt{\omega'} = 8.61$ ($f=1$ Hz), $\sqrt{\omega'} = 12.17$ ($f=2$ Hz) and $\sqrt{\omega'} = 17.22$ ($f=4$ Hz) in laminar regime. On the other hand, the magnitudes of $|\bar{P}_{os,1}|$ are found to be greater than \bar{P}_{ta} ($|\bar{P}_{os,1}|/\bar{P}_{ta} > 1$) at $\sqrt{\omega'} = 8.61$ ($f=1$ Hz) and $\sqrt{\omega'} = 12.17$ ($f=2$ Hz) at the onset of transition.

11) The conformity between $\Delta P(t)/L$, $\bar{U}_m(t)$ and their FFT approximations are found to be excellent with the maximum deviations of $\pm 2\%$ in laminar regime. However, the mean deviation between $\Delta P(t)/L$ and its FFT approximation is found to be $\pm 10\%$ due to flow being at the onset of transition. The deviation of $\Delta P(t)/L$ and its FFT approximation becomes closer to each other for $\sqrt{\omega'} > 7.70$ at the onset of transition.

12) There is an effect of A_1 on the behavior of $\lambda_u(t)$ profile at each $\sqrt{\omega'}$. $\lambda_u(t)$ profile begins to deform and becomes as a hill in shape for $A_1 \geq 0.30$ both in laminar regime and at the onset of transition. Moreover this hill-shape is getting sharp and sharp when A_1 is increased. However, no influence of $\sqrt{\omega'}$ on the deformation of the $\lambda_u(t)$ profile is found.

CHAPTER 9

INTERACTIVE INFLUENCES OF OSCILLATION FREQUENCY AND AMPLITUDE ON THE CRITICAL REYNOLDS NUMBERS AND FRICTION FACTORS AT THE ONSET OF TRANSITION

9.1. Introduction

In this study, the time averaged Reynolds number, Re_{ta} , the oscillating Reynolds number, Re_{os} and the Reynolds number based on the Stokes layer thickness, Re_{δ_s} are defined at the onset of the transition to turbulence as the corresponding critical values of $Re_{ta,crit}$, $Re_{os,crit}$ and $Re_{\delta_s,crit}$, respectively. These critical values of $Re_{ta,crit}$, $Re_{os,crit}$ and $Re_{\delta_s,crit}$ are determined by *TDFC.vi* when the first turbulent bursts are seen on the velocity waveforms.

In this chapter, the effects of pulsatile flow parameters; Womersley number, $\sqrt{\omega'}$ and velocity amplitude ratio, A_1 on $Re_{ta,crit}$, $Re_{os,crit}$ and $Re_{\delta_s,crit}$ are investigated. In view of the study of Ohmi and Iguchi (1981), the variation between the parameter of $\sqrt{\omega'}/\sqrt{Re_{ta}^{3/4}}$ calculated from the combination of $\sqrt{\omega'}$ and Re_{ta} and the parameter of $\lambda_{sL}/\lambda_{u,ta}$ is discussed in the laminar regime and at the onset of transition.

As a result of the comprehensive study on the effects of the pulsatile flow parameters, some correlation studies are carried out in view of the literature. These correlations are also introduced in this chapter.

9.2. Effect of A_1 on $Re_{ta,crit}$ at Constant Value of $\sqrt{\omega'}$

Figure 9.1 shows the effect of A_1 on $Re_{ta,crit}$ in the range of $2.72 \leq \sqrt{\omega'} \leq 32.21$. As shown in the figure, the maximum $Re_{ta,crit}$ at which the transition to turbulence starts in the flow is satisfied at $\sqrt{\omega'} = 3.85$ ($f = 0.2$ Hz). The pulsatile flow can be kept as laminar up to $Re_{ta,crit} = 4817$ at $\sqrt{\omega'} = 3.85$. Generally, it can be said that $Re_{ta,crit}$ is increased at each $\sqrt{\omega'}$ when A_1 increases. However, the variations of $Re_{ta,crit}$ with A_1 are investigated separately at each $\sqrt{\omega'}$ in order to clarify the effect of A_1 on $Re_{ta,crit}$ in details.

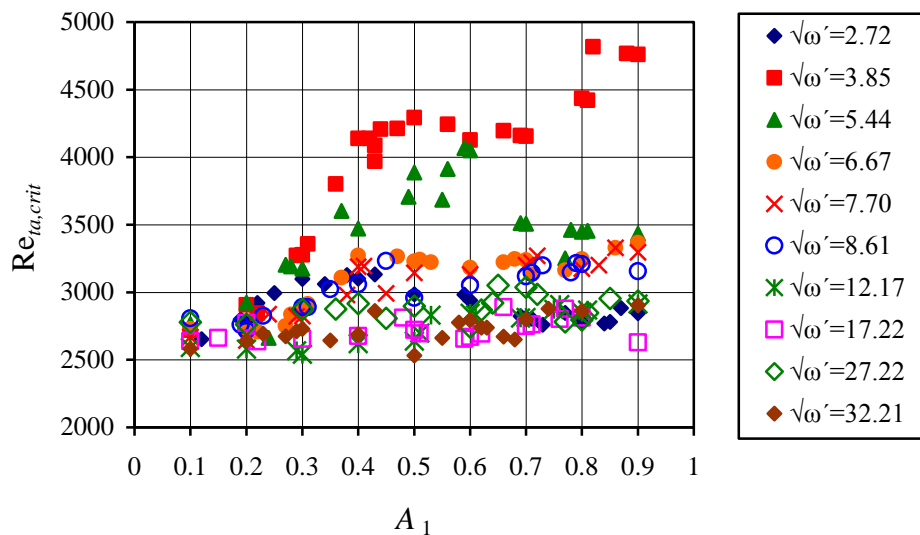


Figure 9.1. Effect of A_1 on $Re_{ta,crit}$ in the range of $2.72 \leq \sqrt{\omega'} \leq 32.21$

The effect of A_1 on $Re_{ta,crit}$ at $\sqrt{\omega'} = 2.72$ at the onset of transition to turbulence is given in the range of $0.10 \leq A_1 \leq 0.90$ in Fig. 9.2. The variation of $Re_{ta,crit}$ with A_1 is seen to be sinusoidal. The value of $Re_{ta,crit} = 2702$ at $A_1 = 0.10$ increases up to $Re_{ta,crit} = 3133$ at $A_1 = 0.43$, then begins to decrease to $Re_{ta,crit} = 2759$ at $A_1 = 0.73$, and later increases again to $Re_{ta,crit} = 2884$ at $A_1 = 0.87$, which varies in the sinusoidal form in the range of $0.10 \leq A_1 \leq 0.90$. However there is no upward or

downward inclination of the sinusoidal behavior. The mean value of $Re_{ta,crit}$ in the range of $0.10 \leq A_1 \leq 0.90$ is $Re_{ta,crit} = 2891$ with a maximum deviation of $\pm 8\%$ as denoted with the red dashed line. As a result, the pulsatile flow through the pipeline can be kept as laminar up to maximum value of $Re_{ta,crit} = 3133$ at $\sqrt{\omega'} = 2.72$ if the velocity amplitude ratio is adjusted to $A_1 = 0.43$.

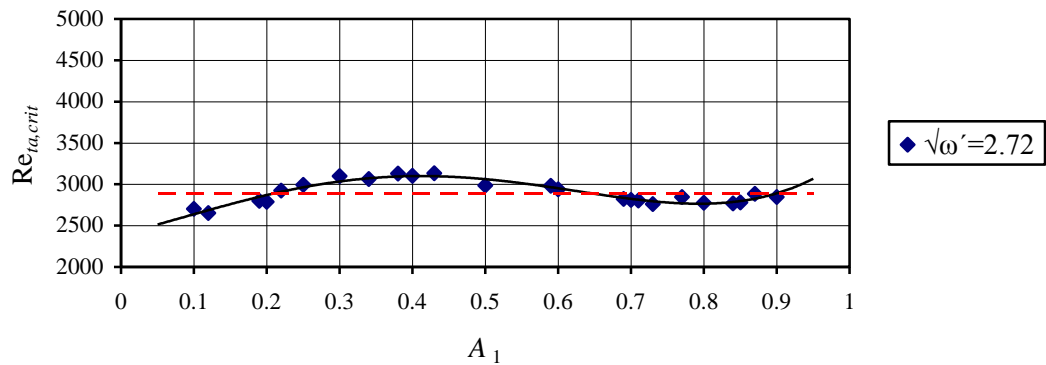


Figure 9.2. Effect of A_1 on $Re_{ta,crit}$ at $\sqrt{\omega'} = 2.72$

The variation of $Re_{ta,crit}$ with A_1 at $\sqrt{\omega'} = 3.85$ in the range of $0.10 \leq A_1 \leq 0.90$ is given in Fig. 9.3. The different behavior of $Re_{ta,crit}$ variation with A_1 is seen at $\sqrt{\omega'} = 3.85$ when compared with that at $\sqrt{\omega'} = 2.72$. There is an upward inclination in the relationship, in which this variation tends to increase up to $A_1 = 0.90$. In the experimental study, the maximum value of $Re_{ta,crit}$ is found as $Re_{ta,crit} = 4817$ at $A_1 = 0.87$ and $\sqrt{\omega'} = 3.85$ as seen from the figure. This means that the flow through the pipeline can be kept as laminar up to $Re_{ta} = 4817$ in the experiment by adjusting the oscillation frequency of the pulsation to $f = 0.2$ Hz ($\sqrt{\omega'} = 3.85$).

Figure 9.4 illustrates the relationship between $Re_{ta,crit}$ and A_1 at $\sqrt{\omega'} = 5.44$ at the onset of transition to turbulence. The similar behavior like that at $\sqrt{\omega'} = 2.72$ is seen at $\sqrt{\omega'} = 5.44$ but the values of $Re_{ta,crit}$ are higher than those at $\sqrt{\omega'} = 2.72$.

$Re_{ta,crit}=2764$ is found at $A_1=0.10$. Its value is increased up to $Re_{ta,crit}=4067$ at $A_1=0.59$ and then decreases to 3422 at $A_1=0.90$.

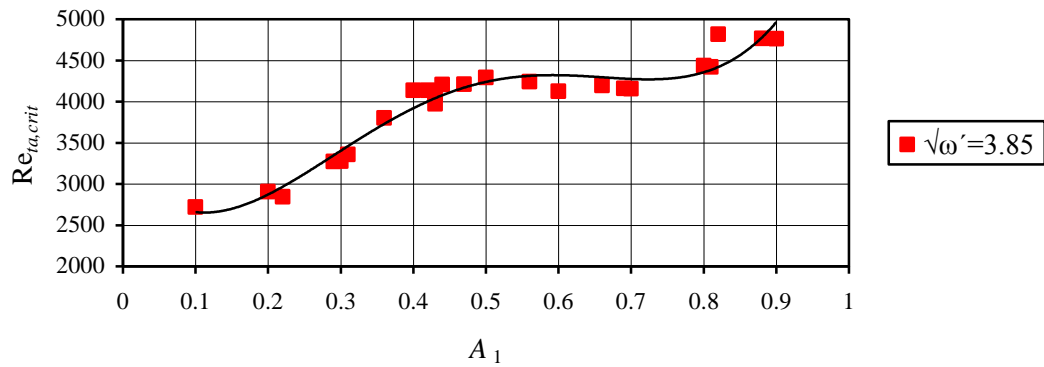


Figure 9.3. Effect of A_1 on $Re_{ta,crit}$ at $\sqrt{\omega'}=3.85$

All these values are found to be higher when compared with those at $\sqrt{\omega'}=2.72$, but lower when compared with those at $\sqrt{\omega'}=3.85$. However, the same sinusoidal behavior of the variation with upward trend is seen at $\sqrt{\omega'}=5.44$.

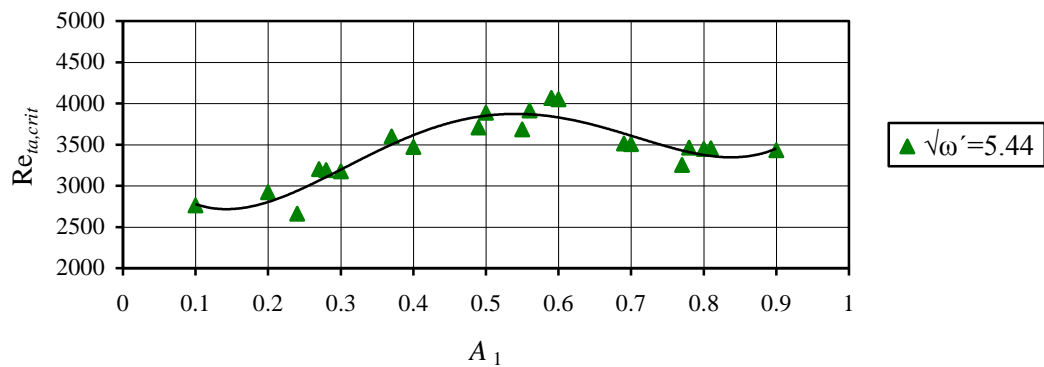


Figure 9.4. Effect of A_1 on $Re_{ta,crit}$ at $\sqrt{\omega'}=5.44$

As seen from Fig. 9.5, the sinusoidal variation of $Re_{ta,crit}$ at $\sqrt{\omega'}=6.67$ tends to raise upwards when A_1 increases similarly to the upward trend of the

$Re_{ta,crit}$ variation with A_1 at $\sqrt{\omega'} = 3.85$ and $\sqrt{\omega'} = 5.44$. The value of $Re_{ta,crit}$ is found to be $Re_{ta,crit} = 2729$ at $A_1 = 0.10$, and increases up to the maximum value of $Re_{ta,crit} = 3368$ at $A_1 = 0.90$.

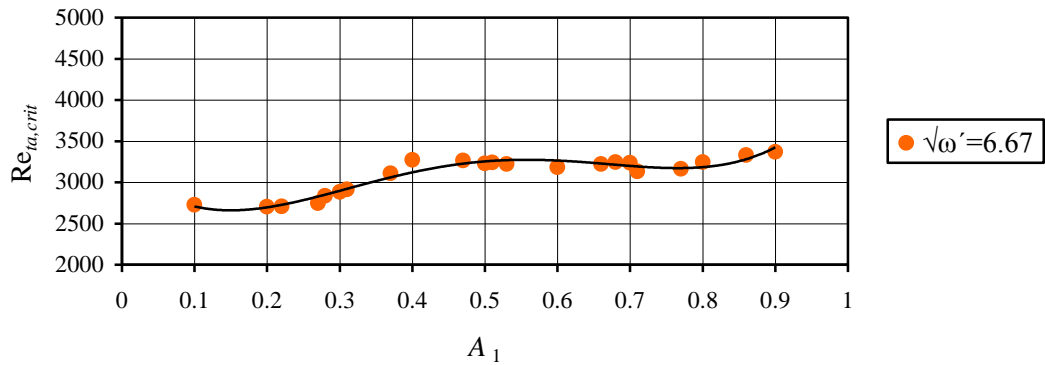


Figure 9.5. Effect of A_1 on $Re_{ta,crit}$ at $\sqrt{\omega'} = 6.67$

As seen in Figs. 9.6 and 9.7, the variations of $Re_{ta,crit}$ with A_1 are seen to become slightly sinusoidal at $\sqrt{\omega'} = 7.70$ and $\sqrt{\omega'} = 8.61$ when compared with those at $\sqrt{\omega'} \leq 6.67$. The value of $Re_{ta,crit}$ is found as $Re_{ta,crit} = 2669$ at $A_1 = 0.10$ and increase up to $Re_{ta,crit} = 3295$ at $A_1 = 0.90$ at $\sqrt{\omega'} = 7.70$ in Fig. 9.6. $Re_{ta,crit} = 2807$ is found at $\sqrt{\omega'} = 8.61$ and $A_1 = 0.10$ and increases to the maximum value of $Re_{ta,crit} = 3157$ at $A_1 = 0.90$ as seen in Fig. 9.7.

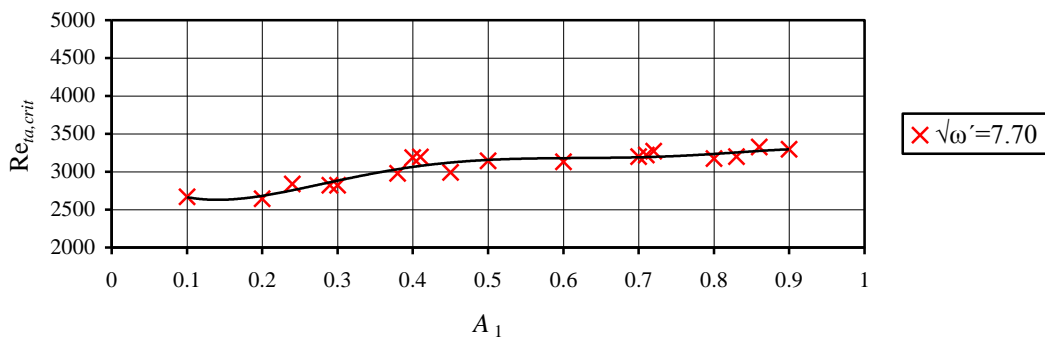


Figure 9.6. Effect of A_1 on $Re_{ta,crit}$ at $\sqrt{\omega'} = 7.70$

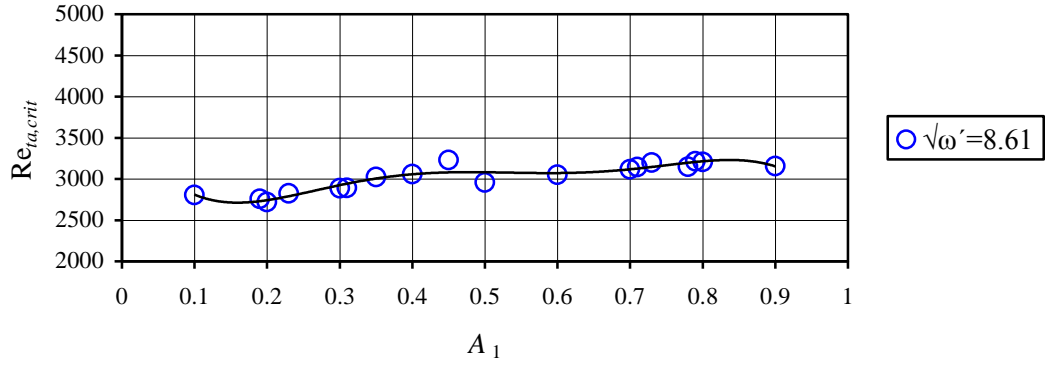


Figure 9.7. Effect of A_1 on $Re_{ta,crit}$ at $\sqrt{\omega'} = 8.61$

The sinusoidal variations of $Re_{ta,crit}$ with A_1 disappear when $\sqrt{\omega'} \geq 12.17$, as illustrated in Figs. 9.8-9.11. Figure 9.8 shows the relation between $Re_{ta,crit}$ and A_1 at $\sqrt{\omega'} = 12.17$. The effect of A_1 on $Re_{ta,crit}$ begins to disappear at $\sqrt{\omega'} = 12.17$. The values of $Re_{ta,crit}$ are found to be $Re_{ta,crit} = 2592$ at $A_1 = 0.10$ and $Re_{ta,crit} = 2913$ at $A_1 = 0.90$. The mean value of $Re_{ta,crit}$ in the range of $0.10 \leq A_1 \leq 0.90$ is $Re_{ta,crit} = 2752$ with a maximum deviation of $\pm 7\%$ as denoted with the red dashed line.

The sinusoidal behavior of the variation between $Re_{ta,crit}$ and A_1 is not seen at $\sqrt{\omega'} = 17.22$ in Fig. 9.9. There is almost no effect of A_1 on $Re_{ta,crit}$ such that the mean value of is $Re_{ta,crit} = 2727$ in the range of $0.10 \leq A_1 \leq 0.90$ with a maximum deviation of $\pm 4\%$ as denoted with the red dashed line. The $Re_{ta,crit}$ values are found as $Re_{ta,crit} = 2638$ at $A_1 = 0.10$ and $Re_{ta,crit} = 2811$ at $A_1 = 0.90$ for $\sqrt{\omega'} = 17.22$. The values of $Re_{ta,crit}$ at each A_1 are seen to be very close to each other for $\sqrt{\omega'} \geq 12.17$ ($f \geq 2$ Hz). This verifies the critical state of $\sqrt{\omega'} = 8.61$ once more such that everything on flow dynamics become different at $\sqrt{\omega'} > 8.61$.

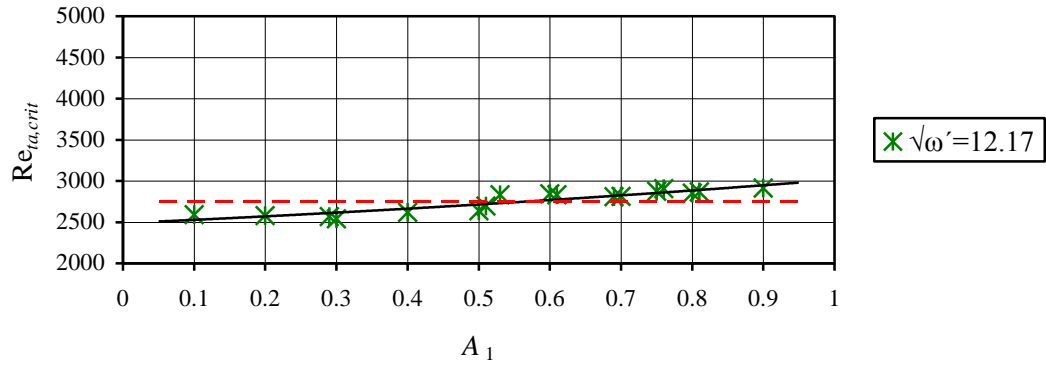


Figure 9.8. Effect of A_1 on $Re_{ta,crit}$ at $\sqrt{\omega'} = 12.17$

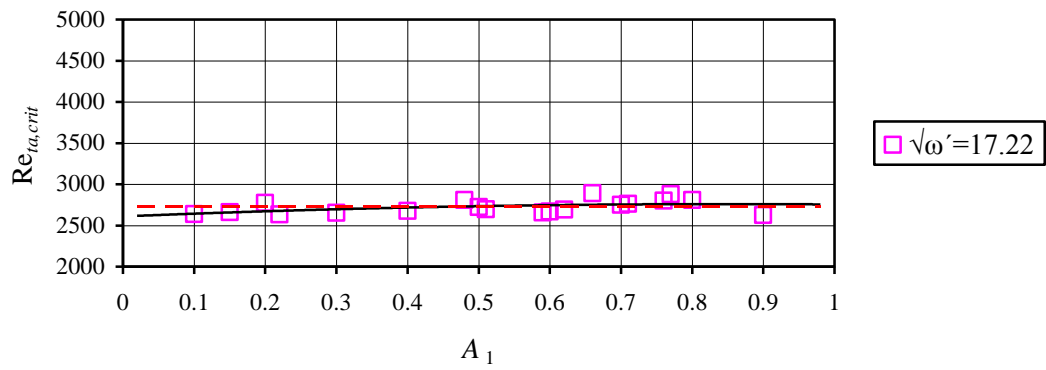


Figure 9.9. Effect of A_1 on $Re_{ta,crit}$ at $\sqrt{\omega'} = 17.22$

The values of $Re_{ta,crit}$ become absolutely independent from A_1 at $\sqrt{\omega'} = 27.22$ and $\sqrt{\omega'} = 32.21$ as seen in Figs. 9.10 and 9.11. The values of $Re_{ta,crit}$ are found to be nearly constant value as $Re_{ta,crit} = 2880$ and $Re_{ta,crit} = 2725$ with maximum deviations of $\pm 5\%$ and $\pm 6\%$ at $\sqrt{\omega'} = 27.22$ and $\sqrt{\omega'} = 32.21$, respectively.

As a deduction, the effect of A_1 on $Re_{ta,crit}$ begins to disappear when $\sqrt{\omega'} \geq 12.17$, and there is almost no effect of A_1 on $Re_{ta,crit}$ at $\sqrt{\omega'} \geq 17.22$.

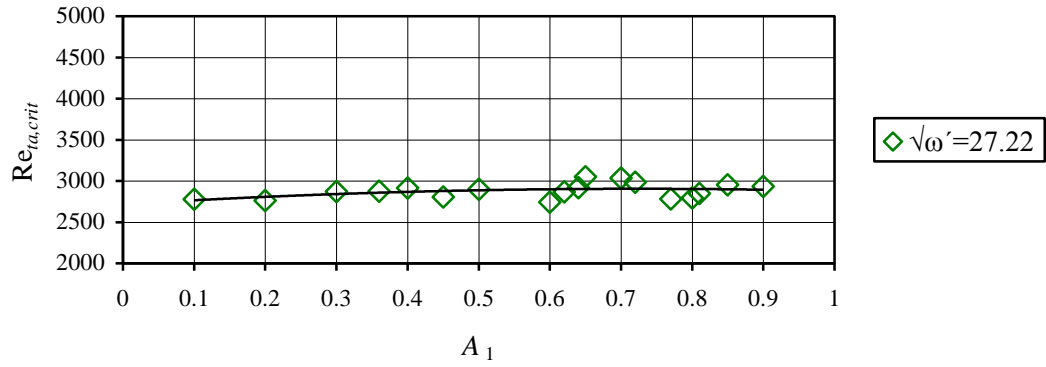


Figure 9.10. Effect of A_1 on $Re_{ta,crit}$ at $\sqrt{\omega'} = 27.22$

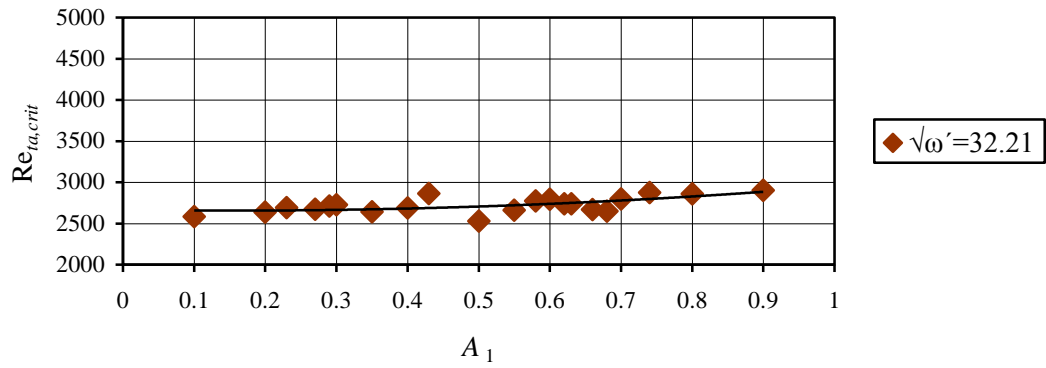


Figure 9.11. Effect of A_1 on $Re_{ta,crit}$ at $\sqrt{\omega'} = 32.21$

9.3. Effect of A_1 on $Re_{os,crit}$ at Constant Value of $\sqrt{\omega'}$

Figure 9.12 shows the effect of A_1 on $Re_{os,crit}$ in the range of $2.72 \leq \sqrt{\omega'} \leq 32.21$. $Re_{os,crit}$ is definitely dependent on A_1 and there is a linear relationship between $Re_{os,crit}$ and A_1 at all values of $\sqrt{\omega'}$.

The effect of A_1 on $Re_{os,crit}$ at $\sqrt{\omega'} = 2.72$ at the onset of transition is given in the range of $0.10 \leq A_1 \leq 0.90$ in Fig. 9.13. The variation of $Re_{os,crit}$ with A_1 is linear,

and $Re_{os,crit}$ increases when A_1 increases. The value of $Re_{os,crit}=272$ at $A_1=0.10$ increases up to $Re_{os,crit}=2567$ at $A_1=0.90$.

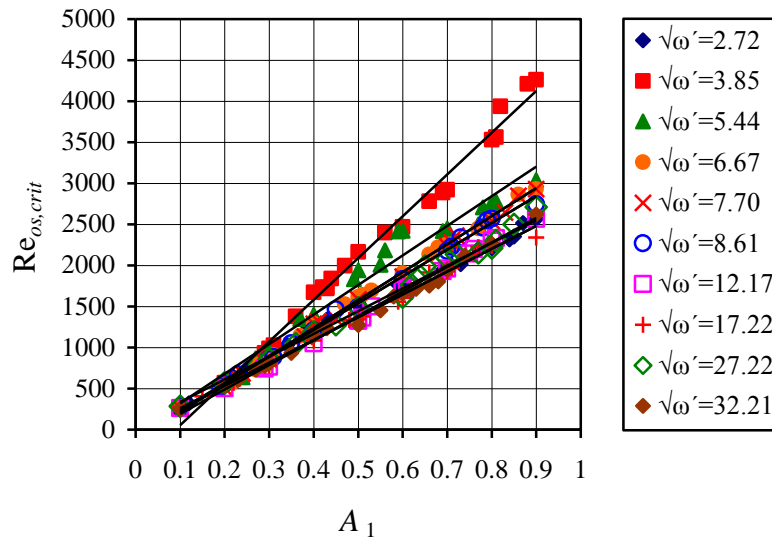


Figure 9.12. Effect of A_1 on $Re_{os,crit}$ in the range of $2.72 \leq \sqrt{\omega'} \leq 32.21$

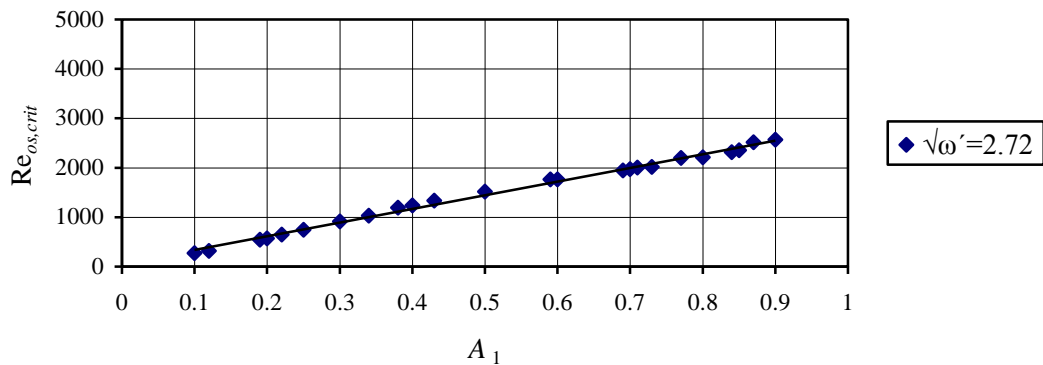


Figure 9.13. Effect of A_1 on $Re_{os,crit}$ at $\sqrt{\omega'}=2.72$

The maximum values of $Re_{os,crit}$ at the onset of transition are seen at $\sqrt{\omega'}=3.85$ ($f=0.2$ Hz) as seen in Fig. 9.14. The maximum value of $Re_{os,crit}$ is found as $Re_{os,crit}=4261$ at $A_1=0.90$.

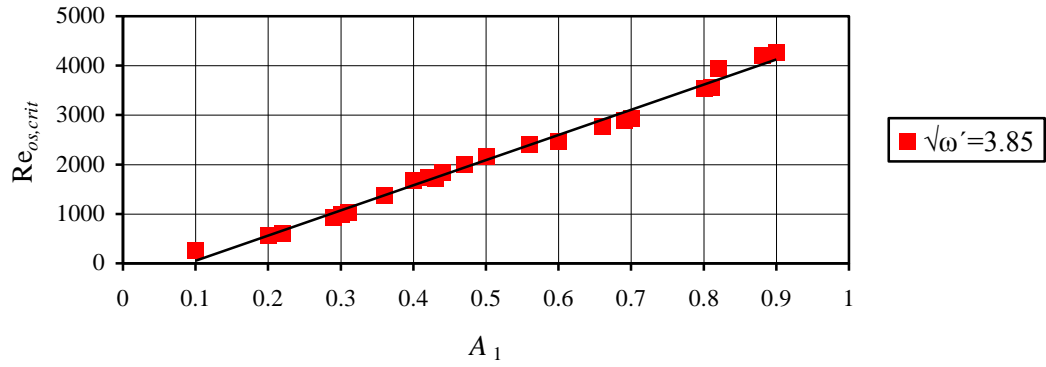


Figure 9.14. Effect of A_1 on $Re_{os,crit}$ at $\sqrt{\omega'} = 3.85$

The relations between $Re_{os,crit}$ and A_1 at $\sqrt{\omega'} = 5.44$, $\sqrt{\omega'} = 6.67$ and $\sqrt{\omega'} = 7.70$ are given in Figs. 9.15-9.17, respectively. The linear relationships between $Re_{os,crit}$ and A_1 are observed again. The minimum and maximum values of $Re_{os,crit}$ at $A_1 = 0.10$ and $A_1 = 0.90$ are seen to be almost same such as $Re_{os,crit} = 272$ at $A_1 = 0.10$ and $Re_{os,crit} = 2966$ at $A_1 = 0.90$ with maximum deviations of $\pm 2\%$ at $\sqrt{\omega'} = 5.44$, $\sqrt{\omega'} = 6.67$ and $\sqrt{\omega'} = 7.70$.

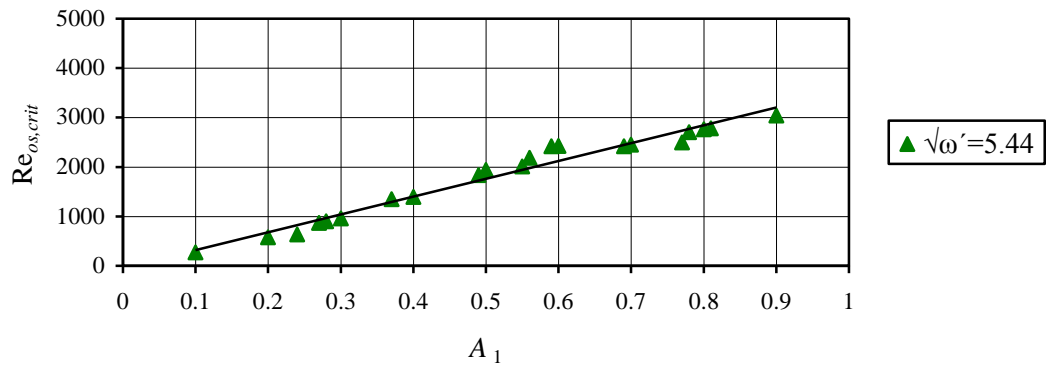


Figure 9.15. Effect of A_1 on $Re_{os,crit}$ at $\sqrt{\omega'} = 5.44$

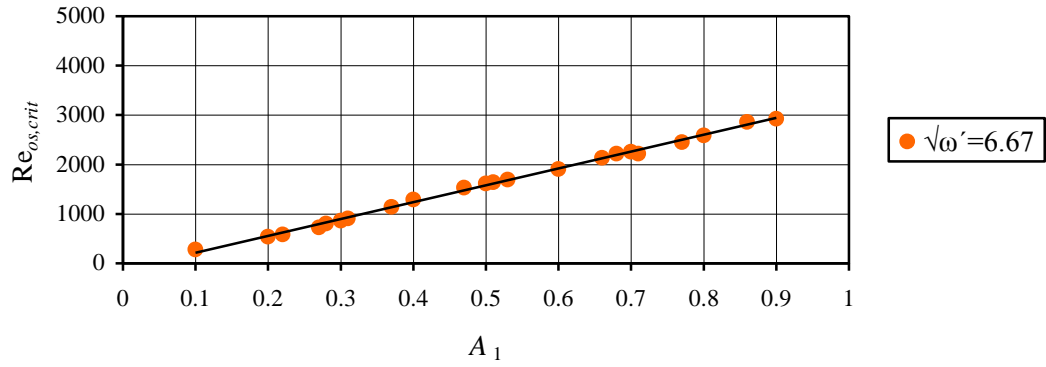


Figure 9.16. Effect of A_1 on $Re_{os,crit}$ at $\sqrt{\omega'} = 6.67$

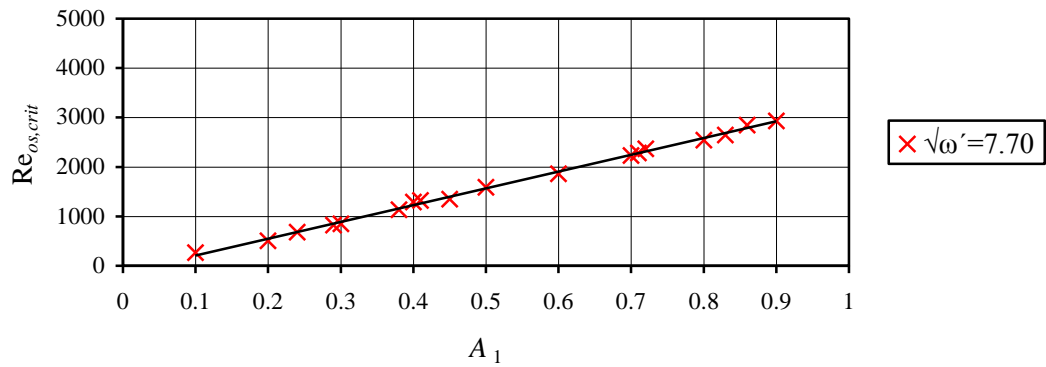


Figure 9.17. Effect of A_1 on $Re_{os,crit}$ at $\sqrt{\omega'} = 7.70$

There is a linear relation between $Re_{os,crit}$ and A_1 at $\sqrt{\omega'} \geq 8.61$ as seen in Figs. 9.18-9.22. $Re_{os,crit}$ increases when A_1 increases. However, the maximum values of $Re_{os,crit}$ at $A_1 = 0.90$ are found to be lower at $\sqrt{\omega'} \geq 8.61$ when compared with those at $\sqrt{\omega'} < 8.61$ as $Re_{os,crit} = 2597$ with maximum deviation of $\pm 8\%$ in the range of $8.61 \leq \sqrt{\omega'} \leq 32.21$.

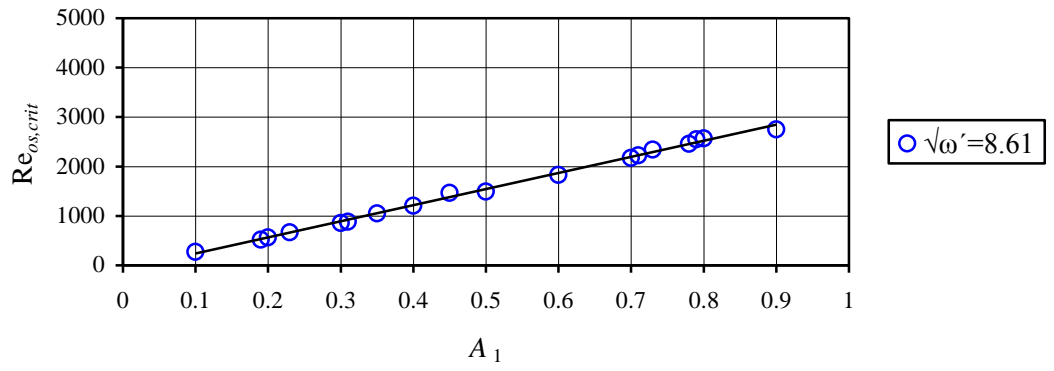


Figure 9.18. Effect of A_1 on $Re_{os,crit}$ at $\sqrt{\omega'} = 8.61$

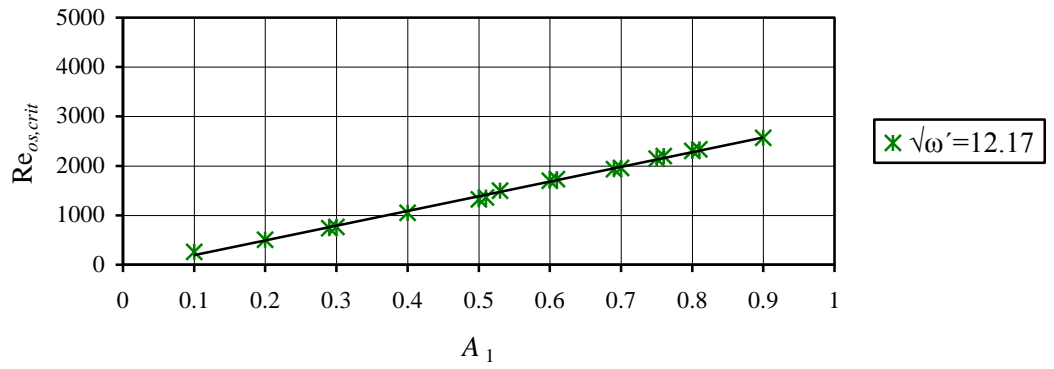


Figure 9.19. Effect of A_1 on $Re_{os,crit}$ at $\sqrt{\omega'} = 12.17$

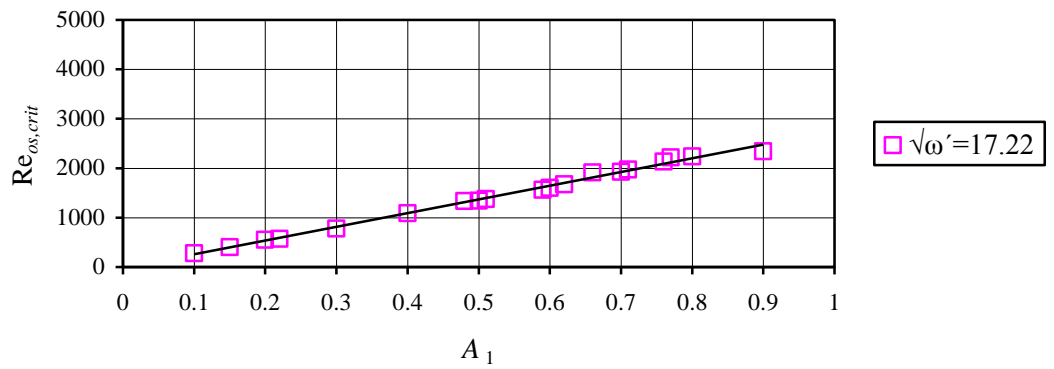


Figure 9.20. Effect of A_1 on $Re_{os,crit}$ at $\sqrt{\omega'} = 17.22$

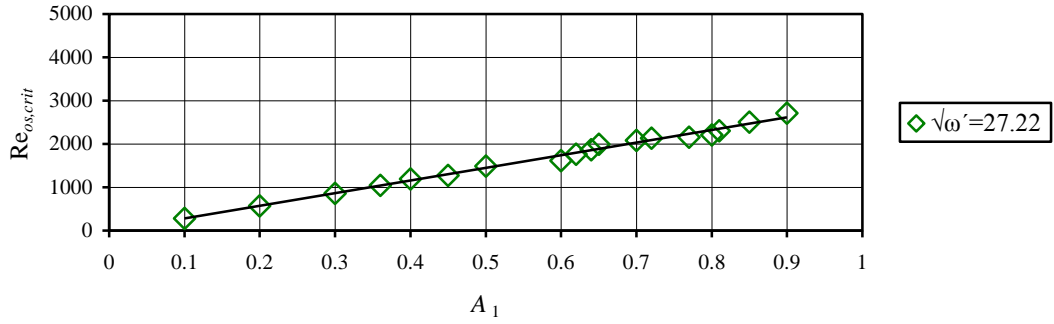


Figure 9.21. Effect of A_1 on $Re_{os,crit}$ at $\sqrt{\omega'} = 27.22$

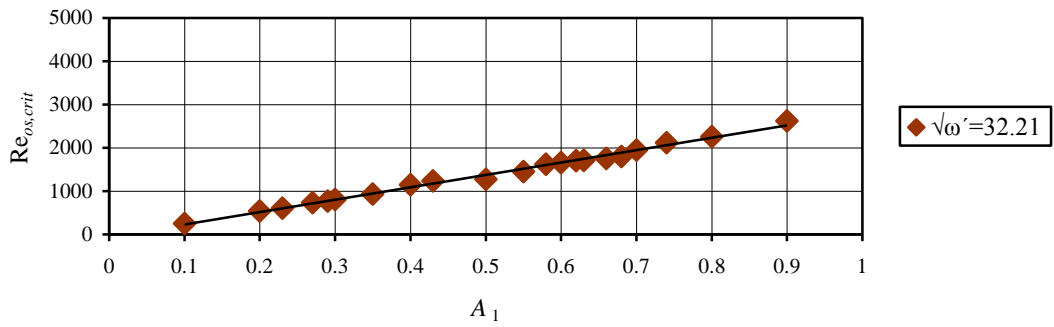


Figure 9.22. Effect of A_1 on $Re_{os,crit}$ at $\sqrt{\omega'} = 32.21$

The linear relations between $Re_{os,crit}$ and A_1 in the range of $2.72 \leq \sqrt{\omega'} \leq 32.21$ are found to be in the form of $Re_{os,crit} = c_1 A_1 + c_2$ which are given in Table 9.1.

Table 9.1. Linear relations between $Re_{os,crit}$ and A_1 in the range of $2.72 \leq \sqrt{\omega'} \leq 32.21$

$\sqrt{\omega'}$	c_1	c_2	Mean Deviation (%)
2.72	2766	59.6	± 0.5
3.85	5088	-455.4	± 1
5.44	3604	-41.2	± 3
6.67	3411	-128.1	± 0.5
7.70	3394	-130.5	
8.61	3256	-86.7	
12.17	2981	-105.2	
17.22	2777	-19.8	± 1
27.22	2914	-9.6	
32.21	2859	-54.7	

9.4. Effect of A_1 on $Re_{\delta_s,crit}$ at Constant Value of $\sqrt{\omega'}$

Figure 9.23 shows the relationships between $Re_{\delta_s,crit}$ and A_1 at the onset of transition in the range of $2.72 \leq \sqrt{\omega'} \leq 32.21$. $Re_{\delta_s,crit}$ is dependent on A_1 for all values of $\sqrt{\omega'}$. The relationships between $Re_{\delta_s,crit}$ and A_1 are found to be linear such as $Re_{\delta_s,crit}$ increases when A_1 increases. However, the inclination of the relationship between $Re_{\delta_s,crit}$ and A_1 tends to decrease when $\sqrt{\omega'}$ increases as can be noticed from the figure, expect the inclination of the relationship between $Re_{\delta_s,crit}$ and A_1 at $\sqrt{\omega'} = 3.85$. The maximum value of $Re_{\delta_s,crit}$ is seen again at $\sqrt{\omega'} = 3.85$.

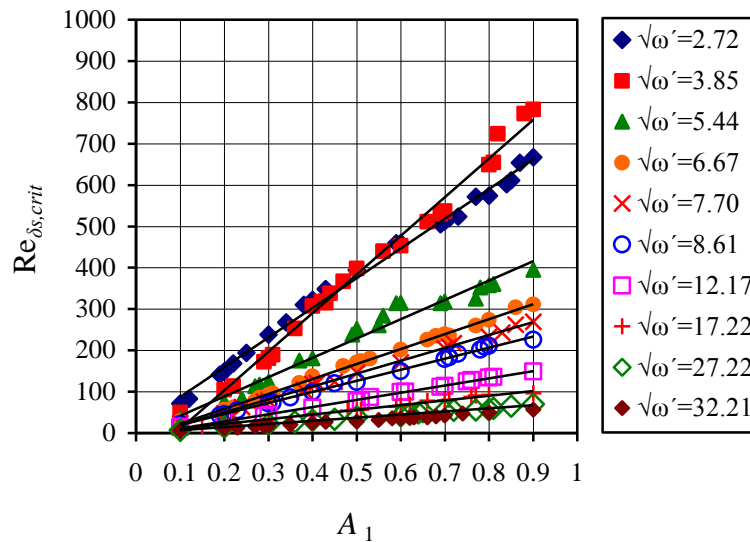


Figure 9.23. Effect of A_1 on $Re_{\delta_s,crit}$ in the range of $2.72 \leq \sqrt{\omega'} \leq 32.21$

The linear relations between $Re_{\delta_s,crit}$ and A_1 in the range of $2.72 \leq \sqrt{\omega'} \leq 32.21$ are in the form of $Re_{\delta_s,crit} = c_1 A_1 + c_2$ and they are given in Table 9.2.

Table 9.2. Linear relations between $Re_{\delta_s, crit}$ and A_1 in the range of $2.72 \leq \sqrt{\omega'} \leq 32.21$

$\sqrt{\omega'}$	c_1	c_2	Mean Deviation (%)
2.72	719	15.6	±0.5
3.85	935	-83.7	
5.44	468	-5.2	±3
6.67	362	-13.8	±0.5
7.70	311	-11.9	
8.61	268	-7.2	
12.17	174	-6.5	
17.22	114	-0.6	
27.22	76	-0.3	
32.21	63	-1.2	

9.5. Effect of $\sqrt{\omega'}$ on $Re_{ta, crit}$ at Constant Value of A_1

The other important pulsatile flow parameter which affects the value of $Re_{ta, crit}$ is $\sqrt{\omega'}$. In this section, the effect of $\sqrt{\omega'}$ on $Re_{ta, crit}$ is discussed in the range of $0.10 \leq A_1 \leq 0.90$.

Figure 9.24 shows the variation of $Re_{ta, crit}$ with $\sqrt{\omega'}$ in the ranges of $0.10 \leq A_1 \leq 0.90$ and $2.72 \leq \sqrt{\omega'} \leq 32.21$. The variation between $Re_{ta, crit}$ and $\sqrt{\omega'}$ can roughly be described such that the value of $Re_{ta, crit}$ increases from $\sqrt{\omega'} = 2.72$ to $\sqrt{\omega'} = 3.85$, later decreases up to $\sqrt{\omega'} = 12.17$, and maintains almost at constant value between $\sqrt{\omega'} = 12.17$ and $\sqrt{\omega'} = 17.22$. Then, it begins to increase up to $\sqrt{\omega'} = 27.22$ and decreases again up to $\sqrt{\omega'} = 32.21$ as seen from Fig. 9.24. Hence the behavior of the relationship between $Re_{ta, crit}$ and $\sqrt{\omega'}$ is found to change with respect to the value of $\sqrt{\omega'}$ at each A_1 . The maximum values of $Re_{ta, crit}$ are seen at $\sqrt{\omega'} = 3.85$ ($f = 0.2$ Hz). The relationship between $Re_{ta, crit}$ with $\sqrt{\omega'}$ is also discussed separately at each A_1 in details.

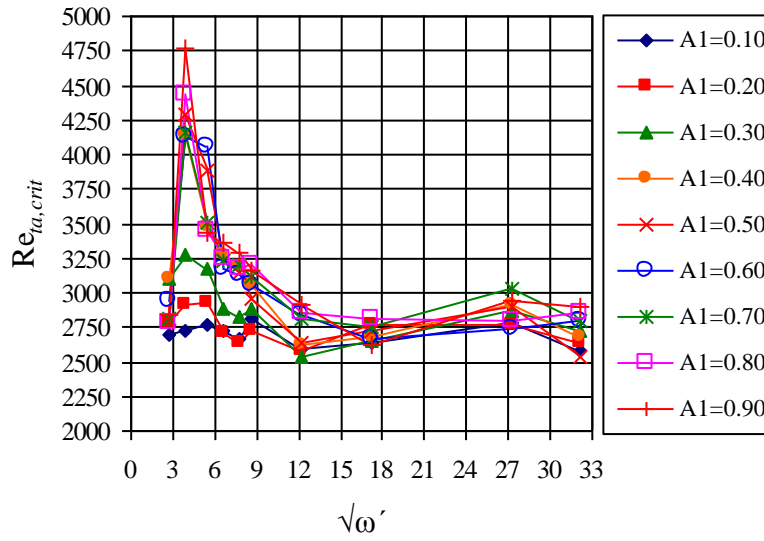


Figure 9.24. Effect of $\sqrt{\omega'}$ on $Re_{ta,crit}$ in the range of $0.10 \leq A_1 \leq 0.90$

As seen from Fig. 9.25, the value of $Re_{ta,crit}$ is almost independent on $\sqrt{\omega'}$ at $A_1 = 0.10$ resulting the mean values of $Re_{ta,crit} = 2698$ with maximum deviation of $\pm 4\%$, which is denoted with red dashed line.

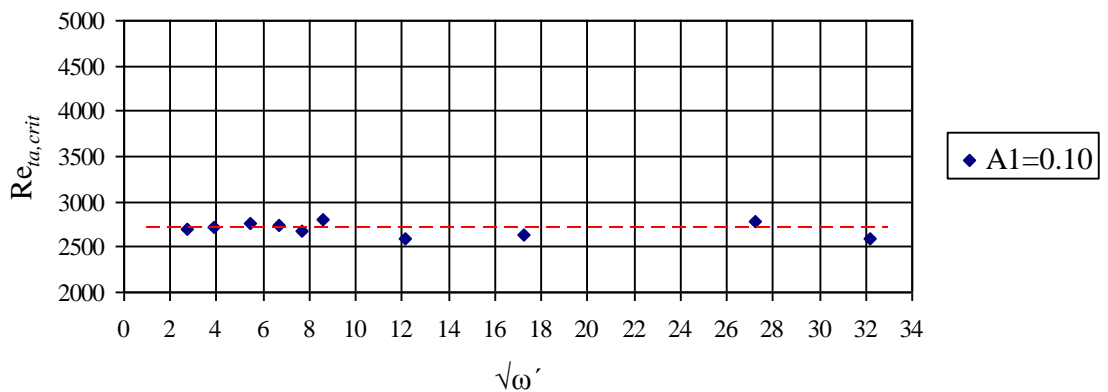


Figure 9.25. Effect of $\sqrt{\omega'}$ on $Re_{ta,crit}$ at $A_1 = 0.10$

Figure 9.26 shows the variation of $Re_{ta,crit}$ with $\sqrt{\omega'}$ at $A_1=0.20$. The mean value of $Re_{ta,crit}$ is denoted with the red dashed line as $Re_{ta,crit}=2764$. However, there are maximum deviations at $\sqrt{\omega'}=3.85$ and $\sqrt{\omega'}=5.44$ with $\pm 8\%$ between the value of $Re_{ta,crit}$ and its mean value denoted with red dashed line. If these deviations at $\sqrt{\omega'}=3.85$ and $\sqrt{\omega'}=5.44$ are not taken into consideration, it can be said that the value of $Re_{ta,crit}$ is independent from $\sqrt{\omega'}$ at $A_1=0.20$ as same as observed at $A_1=0.10$.

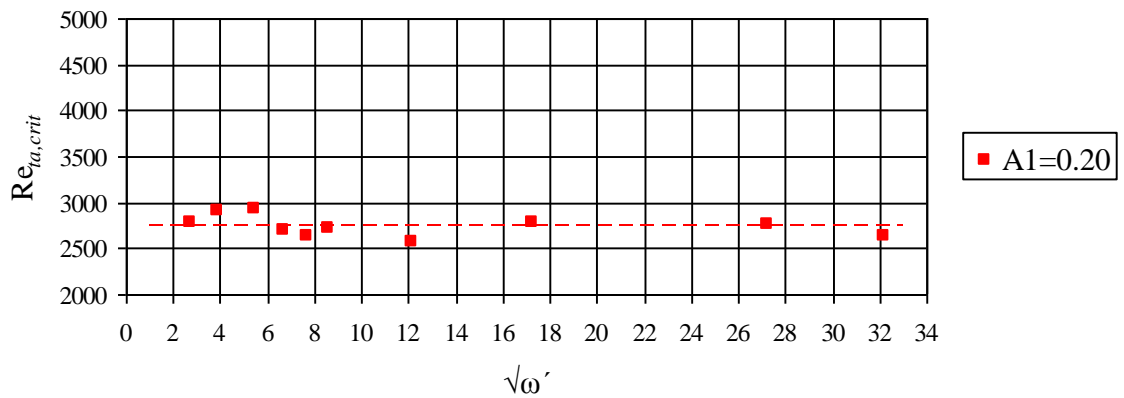


Figure 9.26. Effect of $\sqrt{\omega'}$ on $Re_{ta,crit}$ at $A_1=0.20$

Figure 9.27 shows the variation between $Re_{ta,crit}$ and $\sqrt{\omega'}$ at $A_1=0.30$. The sinusoidal variation between $Re_{ta,crit}$ and $\sqrt{\omega'}$ at $A_1=0.30$ is clearly seen from the figure. The maximum value of $Re_{ta,crit}=3278$ is seen at $\sqrt{\omega'}=3.85$ ($f=0.2$ Hz) and $A_1=0.30$. After $\sqrt{\omega'}=3.85$, $Re_{ta,crit}$ decreases up to $\sqrt{\omega'}=12.17$, later it increases up to $\sqrt{\omega'}=27.22$ and then decreases again at $\sqrt{\omega'}=32.21$.

The variations between $Re_{ta,crit}$ and $\sqrt{\omega'}$ at $A_1>0.30$ are found to be completely different in shape when compared with those at $A_1\leq 0.30$ as shown in Figs. 9.28-9.33.

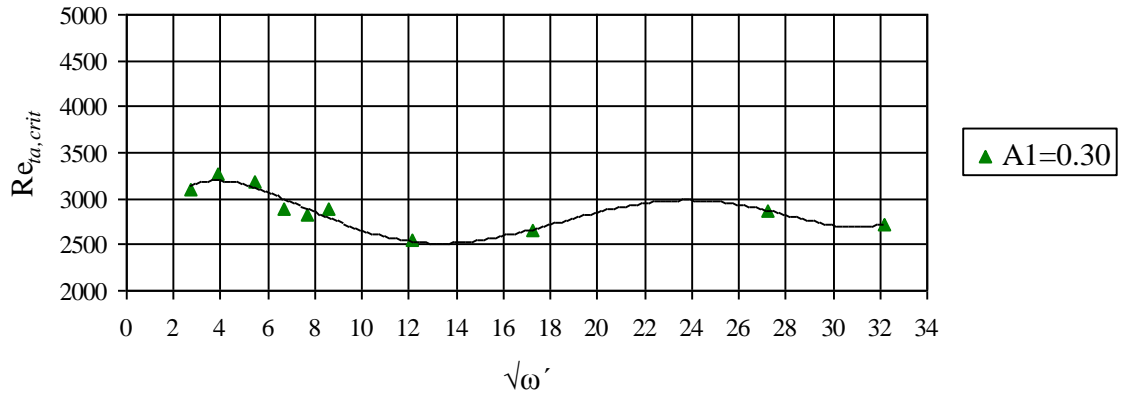


Figure 9.27. Effect of $\sqrt{\omega'}$ on $Re_{ta,crit}$ at $A_1=0.30$

The value of $Re_{ta,crit}$ increases suddenly up to $\sqrt{\omega'}=3.85$ forming a sharp jump and then begins to decrease $\sqrt{\omega'}>3.85$ at $A_1>0.30$. There are also two different behaviors of the relationship between $Re_{ta,crit}$ and $\sqrt{\omega'}$ for $3.85\leq\sqrt{\omega'}\leq 8.61$ and $\sqrt{\omega'}>8.61$ at $A_1>0.30$. The value of $Re_{ta,crit}$ decreases sharply for $3.85\leq\sqrt{\omega'}\leq 8.61$, however its value is nearly maintained constant for $\sqrt{\omega'}>8.61$ at $A_1>0.30$. This difference observed in the behaviors of the relationship between $Re_{ta,crit}$ and $\sqrt{\omega'}$ for $3.85\leq\sqrt{\omega'}\leq 8.61$ and $\sqrt{\omega'}>8.61$ verifies $\sqrt{\omega'}=8.61$ being as the critical state once more.

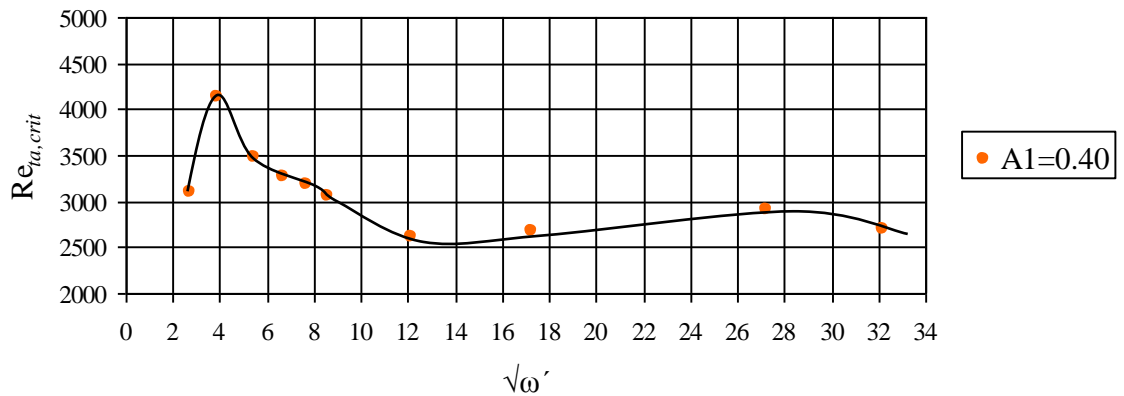


Figure 9.28. Effect of $\sqrt{\omega'}$ on $Re_{ta,crit}$ at $A_1=0.40$

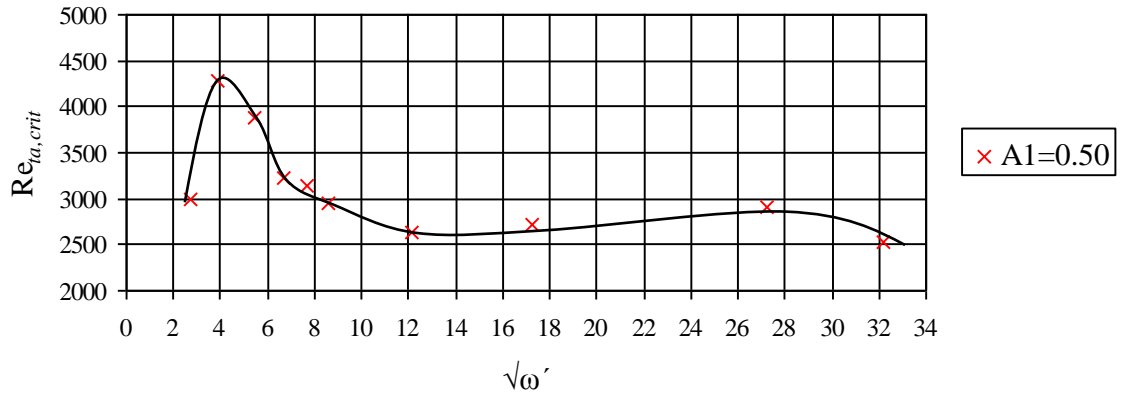


Figure 9.29. Effect of $\sqrt{\omega'}$ on $Re_{ta,crit}$ at $A_1=0.50$

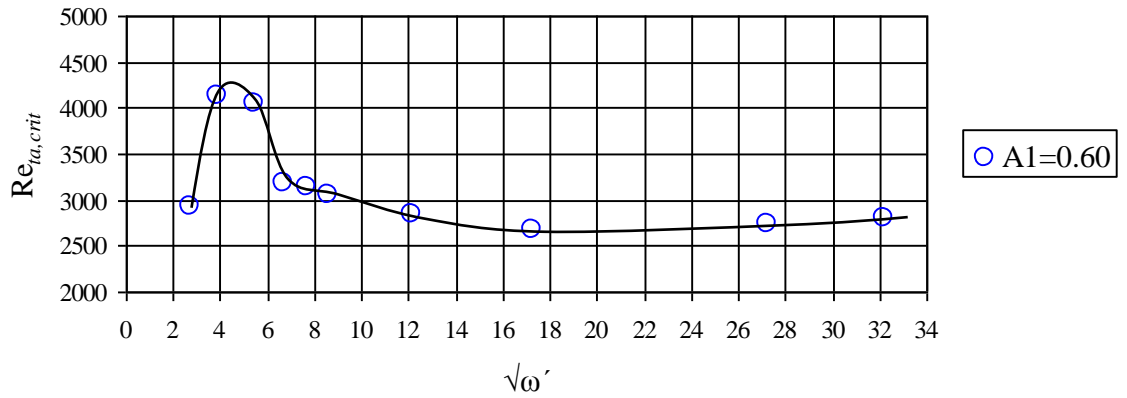


Figure 9.30. Effect of $\sqrt{\omega'}$ on $Re_{ta,crit}$ at $A_1=0.60$

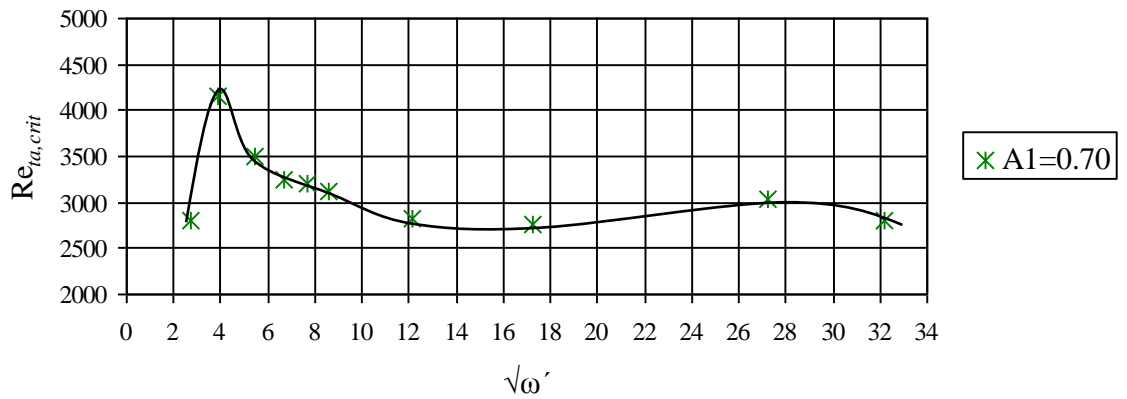


Figure 9.31. Effect of $\sqrt{\omega'}$ on $Re_{ta,crit}$ at $A_1=0.70$

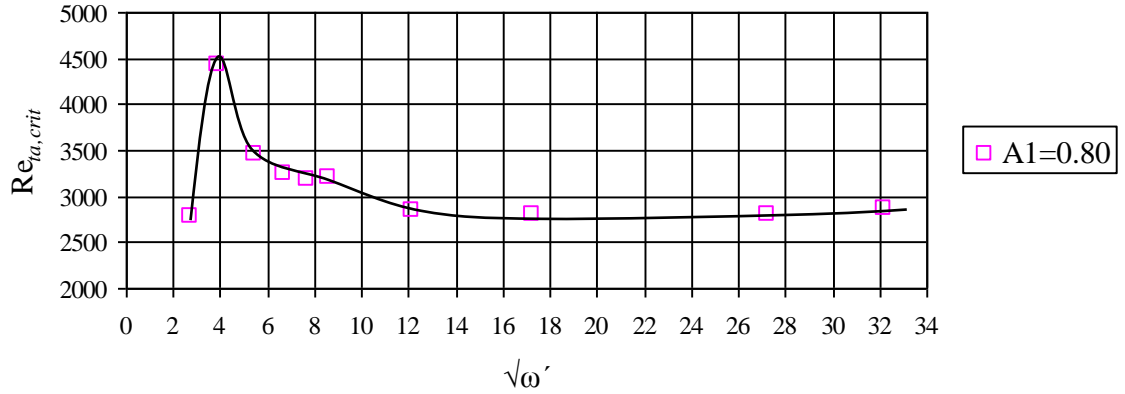


Figure 9.32. Effect of $\sqrt{\omega'}$ on $Re_{ta,crit}$ at $A_1=0.80$

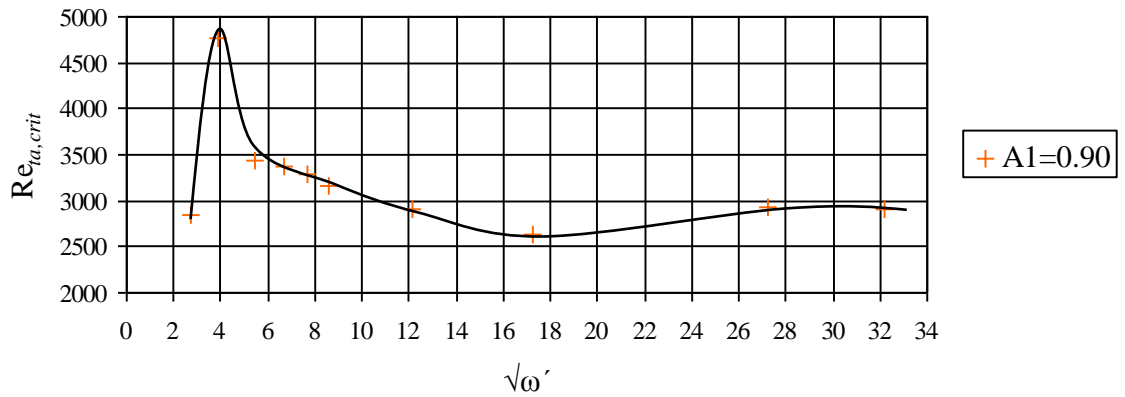


Figure 9.33. Effect of $\sqrt{\omega'}$ on $Re_{ta,crit}$ at $A_1=0.90$

The available data of $Re_{ta,crit}$ in the literature, which are scarce in amount, at the onset and at the end of transition in the pulsatile pipe flows are presented in Fig. 9.34. The experimental data obtained at the onset of transition in the present study are also inserted into Fig. 9.34 in order to compare them with those in the literature in the covered range of $\sqrt{\omega'}$.

The critical range of $\sqrt{\omega'}=8.61$, as mentioned in the previous sections, is also seen in Fig. 9.34. The average value of $Re_{ta,crit}$ is taken at each $\sqrt{\omega'}$ in the range of

$0.10 \leq A_1 \leq 0.90$. The behavior of the averaged $Re_{ta,crit}$ value is denoted by the red dashed line in Fig. 9.34. As seen from the figure, the averaged value of $Re_{ta,crit}$ decreases when $\sqrt{\omega'}$ increases at $3.85 \leq \sqrt{\omega'} \leq 8.61$, however the averaged value of $Re_{ta,crit}$ is nearly maintained constant at $\sqrt{\omega'} > 8.61$.

Moreover, only the data of Hershey-Im (1968) at $\sqrt{\omega'} < 8$ and the data of Ohmi et al. (1982) at $\sqrt{\omega'} > 8$ in terms of $Re_{ta,crit}$ are available at the onset of transition in the literature. Hence the experimental data in the range of $2.72 \leq \sqrt{\omega'} \leq 32.21$ provide a contribution to the literature filling the gap in $\sqrt{\omega'}$ range. However, there is a difference in terms of $Re_{ta,crit}$ value between the present data and the data of Ohmi et al. (1981) at $\sqrt{\omega'} > 8$. Ohmi et al. (1982) studied on transition to turbulence in pulsatile flow at two different $\sqrt{\omega'}$ values of $\sqrt{\omega'} = 8.93$ and $\sqrt{\omega'} = 16.48$ for 15 runs and found $Re_{ta,crit} = 4830$ at $\sqrt{\omega'} = 8.93$ and $Re_{ta,crit} = 12300$ at $\sqrt{\omega'} = 16.48$ due to the appearance of the first turbulent bursts in the later stage of decelerating phase of the velocity waveform. The differences between the present and Ohmi et al.'s data in terms of $Re_{ta,crit}$ at $\sqrt{\omega'} > 8$ may be due to the difference between the transition detection methods or the investigation in the limited range of $\sqrt{\omega'}$ at which only two values of $\sqrt{\omega'}$ used for 15 experimental runs in the study of Ohmi et al. (1982). The detection method of Ohmi et al. (1982) is based on the visual observation of the turbulent bursts on the velocity waveforms. However the fully-automated computerized detection method is used in the present study in order to detect the turbulent structures as peaks near the wall region and as collapses at the pipe centerline. The differences between the present and Ohmi et al.'s data in terms of $Re_{ta,crit}$ at $\sqrt{\omega'} > 8$ may be due to the differences in these proposed detection methods and/or the differences in the criteria used at the definition of the onset of transition.

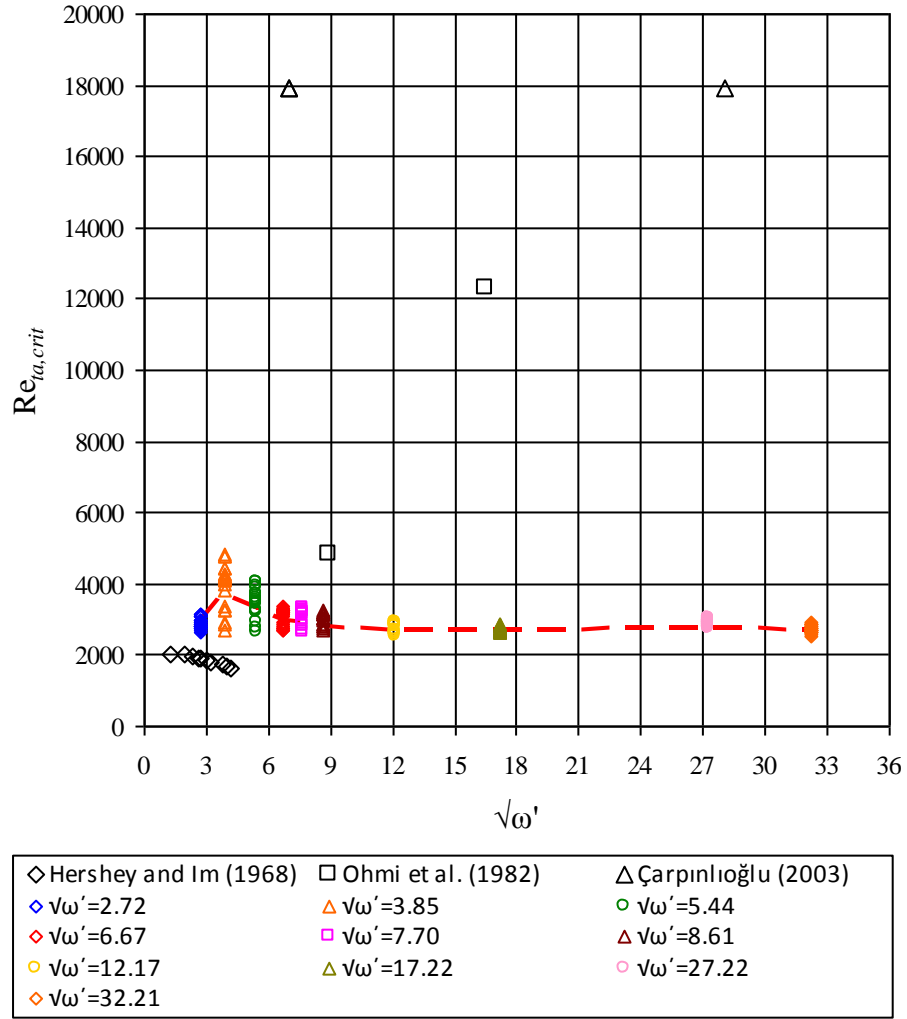


Figure 9.34. Comparison of the experimental data with the data available in the literature in terms $Re_{ta,crit}$ with $\sqrt{\omega'}$ in pulsatile pipe flows at the onset of transition

9.6. Effect of $\sqrt{\omega'}$ on $Re_{os,crit}$ at Constant Value of A_1

The effect of $\sqrt{\omega'}$ on $Re_{os,crit}$ is also investigated at constant value of A_1 in the range of $0.10 \leq A_1 \leq 0.90$ at the onset of the transition to turbulence as can be seen from Fig. 9.35. In order to investigate the effect of $\sqrt{\omega'}$ on $Re_{os,crit}$ in details, the variations between them are presented separately at each A_1 through Figs. 9.36-9.44.

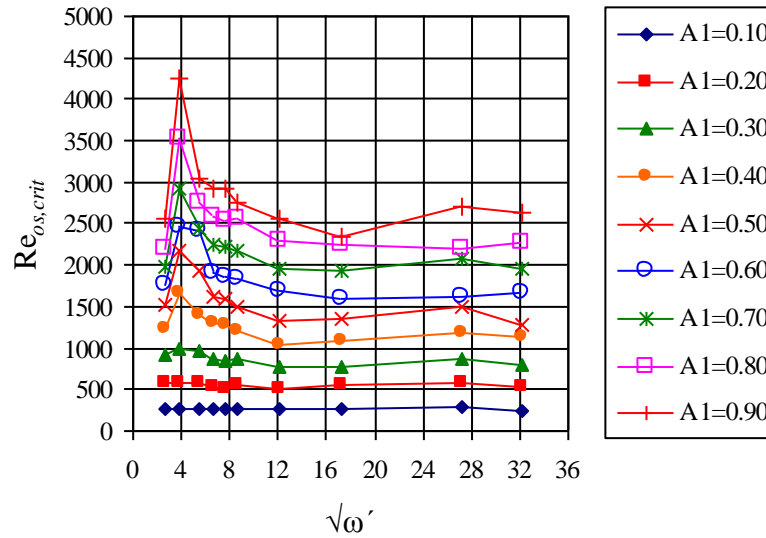


Figure 9.35. Effect of $\sqrt{\omega'}$ on $Re_{os,crit}$ in the range of $0.10 \leq A_1 \leq 0.90$

The similar behaviors which are observed in the relationships of $Re_{ta,crit}$ and $\sqrt{\omega'}$ at $A_1=0.10$ and $A_1=0.20$ are observed in Figs. 9.36 and 9.37 such that the value of $Re_{os,crit}$ is independent on $\sqrt{\omega'}$ at $A_1=0.10$ and $A_1=0.20$ resulting the mean values of $Re_{os,crit}=271$ and $Re_{os,crit}=550$ with maximum deviations of $\pm 5\%$ and $\pm 8\%$, respectively.

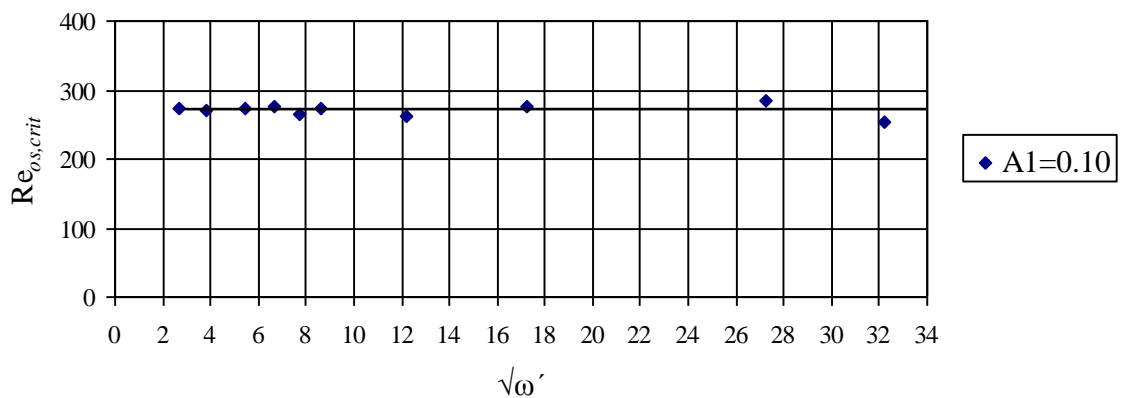


Figure 9.36. Effect of $\sqrt{\omega'}$ on $Re_{os,crit}$ at $A_1=0.10$

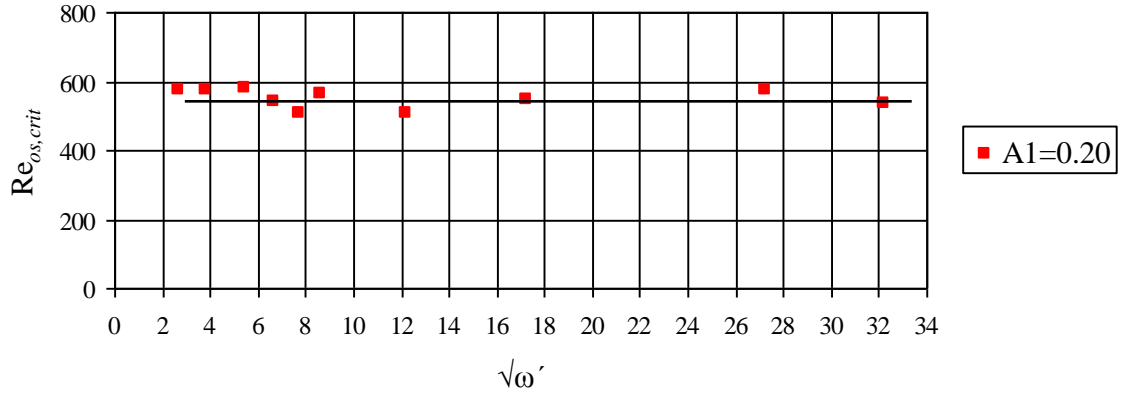


Figure 9.37. Effect of $\sqrt{\omega'}$ on $\text{Re}_{\omega_{crit}}$ at $A_1=0.20$

The influence of $\sqrt{\omega'}$ on $\text{Re}_{\omega_{crit}}$ is seen after $A_1 \geq 0.30$, which is as same as the influence of $\sqrt{\omega'}$ on $\text{Re}_{\omega_{ta,crit}}$ after $A_1 \geq 0.30$. The same characteristic behavior like at $\text{Re}_{\omega_{ta,crit}}$ is seen with drawn line for $\sqrt{\omega'} > 2.72$ on the figures. The maximum value of $\text{Re}_{\omega_{crit}}$ is always seen at $\sqrt{\omega'} = 3.85$ ($f = 0.2$ Hz) as deduced previously after $A_1 \geq 0.30$. The same behaviors of the relationships like those between $\text{Re}_{\omega_{ta,crit}}$ and $\sqrt{\omega'}$ are also seen for the relationships between $\text{Re}_{\omega_{crit}}$ and $\sqrt{\omega'}$ for $A_1 \geq 0.30$.

The maximum value of $\text{Re}_{\omega_{crit}}$ at $A_1 = 0.30$ is found to be $\text{Re}_{\omega_{crit}} = 987$ at $\sqrt{\omega'} = 3.85$ as seen in Fig. 9.38. After $\sqrt{\omega'} = 3.85$, the value of $\text{Re}_{\omega_{crit}}$ decreases up to $\sqrt{\omega'} = 12.17$ as $\text{Re}_{\omega_{crit}} = 766$, and then becomes nearly constant as $\text{Re}_{\omega_{crit}} = 803$ with a maximum deviation of $\pm 6\%$.

The similar relationship is seen at $A_1 = 0.40$ in Fig. 9.39. The maximum value of $\text{Re}_{\omega_{crit}}$ at $A_1 = 0.40$ is found to be $\text{Re}_{\omega_{crit}} = 1672$ at $\sqrt{\omega'} = 3.85$. After $\sqrt{\omega'} = 3.85$, the value of $\text{Re}_{\omega_{crit}}$ decreases up to $\sqrt{\omega'} = 12.17$ as $\text{Re}_{\omega_{crit}} = 1050$, and then its value becomes nearly constant as $\text{Re}_{\omega_{crit}} = 1119$ with a maximum deviation of $\pm 6\%$.

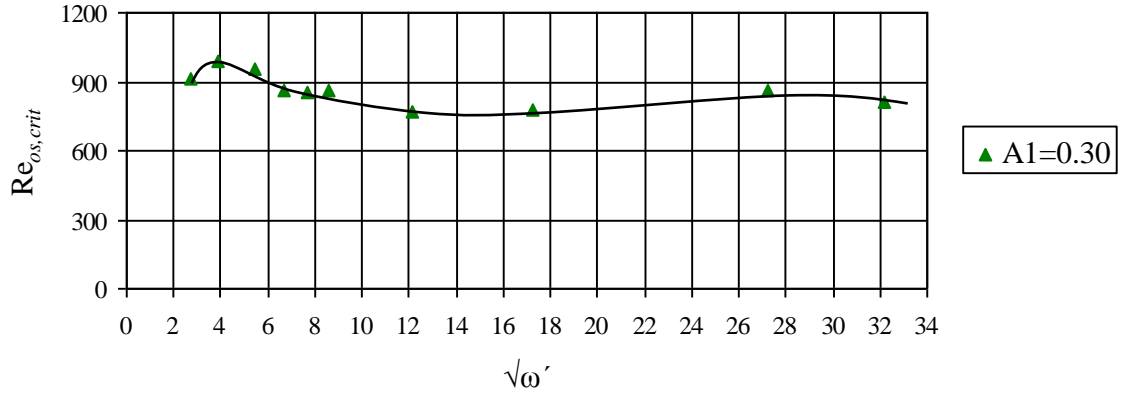


Figure 9.38. Effect of $\sqrt{\omega'}$ on $Re_{os,crit}$ at $A_1=0.30$

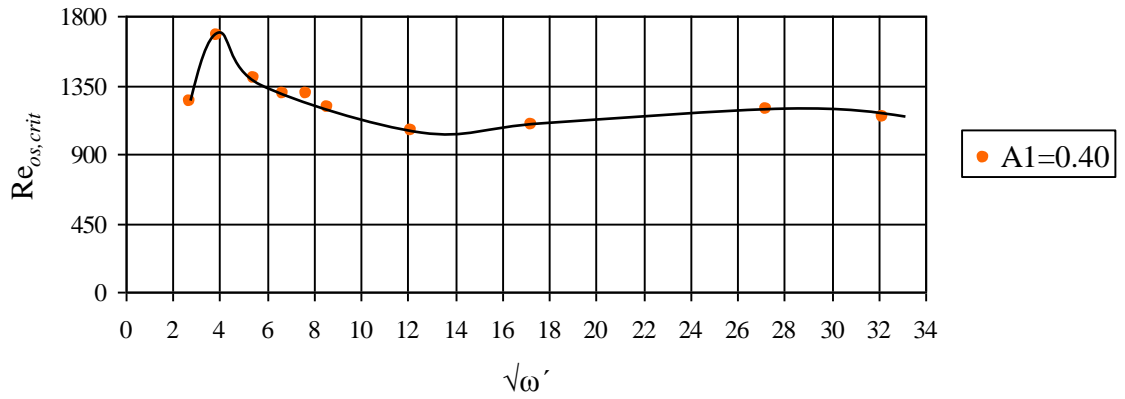


Figure 9.39. Effect of $\sqrt{\omega'}$ on $Re_{os,crit}$ at $A_1=0.40$

The relationship between $Re_{os,crit}$ and $\sqrt{\omega'}$ at $A_1=0.50$ is seen in Fig. 9.40. The maximum value of $Re_{os,crit}$ at $A_1=0.50$ is found to be $Re_{os,crit}=2165$ at $\sqrt{\omega'}=3.85$. After $\sqrt{\omega'}=3.85$, the value of $Re_{os,crit}$ begins to decrease to $Re_{os,crit}=1324$ at $\sqrt{\omega'}=12.17$, and becomes constant as $Re_{os,crit}=1357$ with a maximum deviation of $\pm 9\%$. The maximum deviation of $\pm 9\%$ is seen at $\sqrt{\omega'}=27.22$.

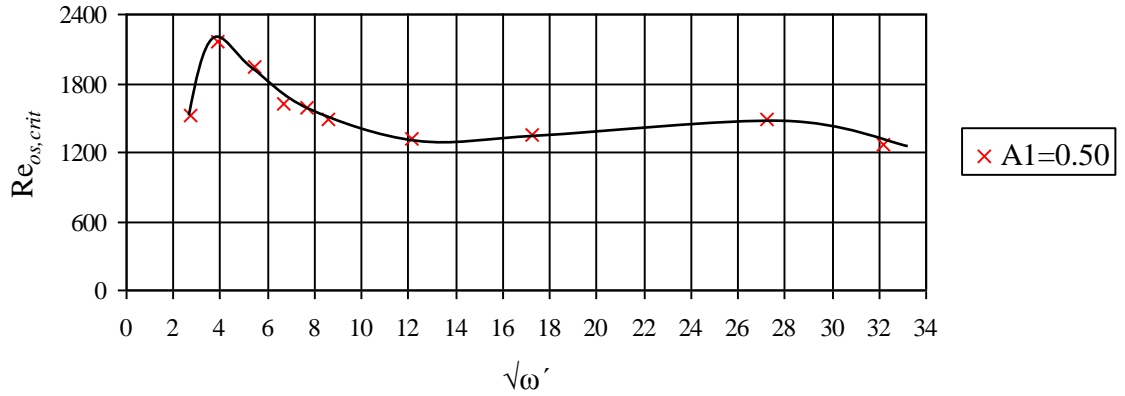


Figure 9.40. Effect of $\sqrt{\omega'}$ on $Re_{os,crit}$ at $A_1=0.50$

The relationships between $Re_{os,crit}$ and $\sqrt{\omega'}$ at $A_1=0.60, 0.70, 0.80$ and 0.90 are given in Figs. 9.41-9.44. The maximum values of $Re_{os,crit}$ are found to be $Re_{os,crit}=2468, 2922, 3533$ and 4261 , respectively at $\sqrt{\omega'}=3.85$. After $\sqrt{\omega'}=3.85$, the values of $Re_{os,crit}$ decrease to $Re_{os,crit}=1702, 1960, 2302$ and 2567 at $\sqrt{\omega'}=12.17$, and become constant as $Re_{os,crit}=1644, 1979, 2252$ and 2560 with maximum deviations of $\pm 3\%, \pm 5\%, \pm 2\%$ and $\pm 8\%$, respectively.

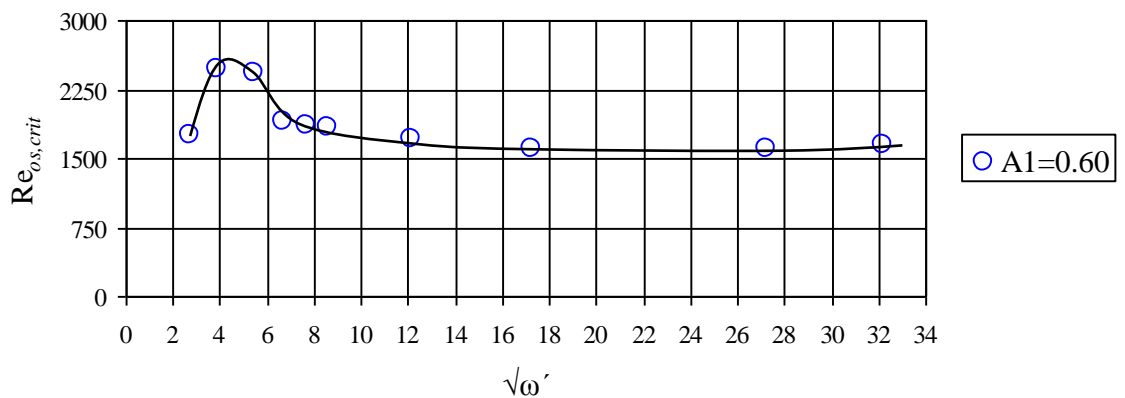


Figure 9.41. Effect of $\sqrt{\omega'}$ on $Re_{os,crit}$ at $A_1=0.60$

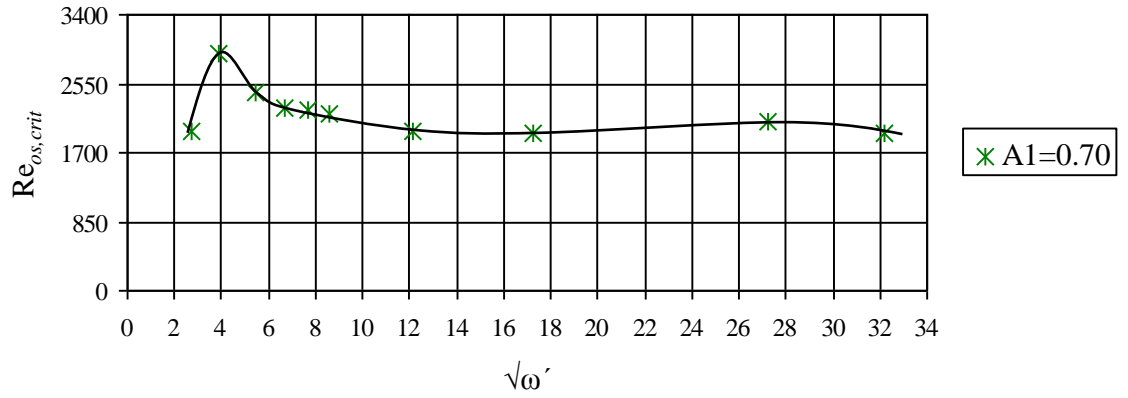


Figure 9.42. Effect of $\sqrt{\omega'}$ on $Re_{os,crit}$ at $A_1=0.70$

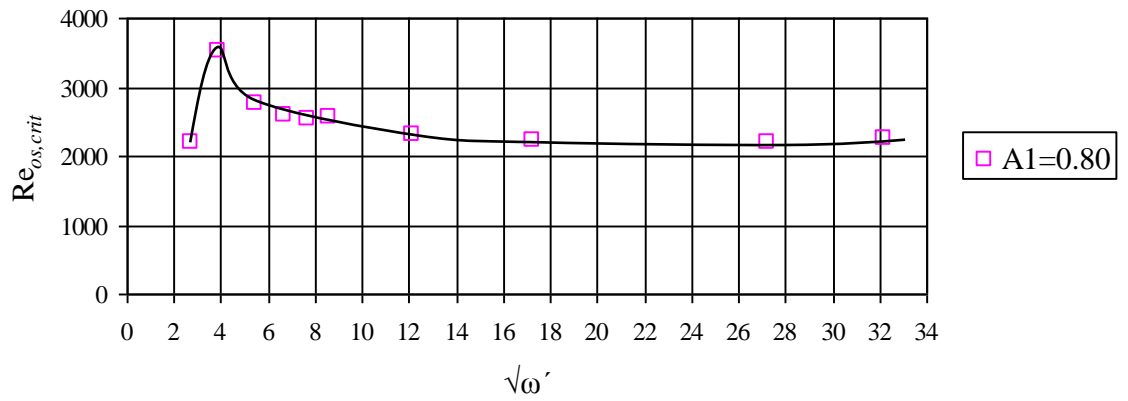


Figure 9.43. Effect of $\sqrt{\omega'}$ on $Re_{os,crit}$ at $A_1=0.80$

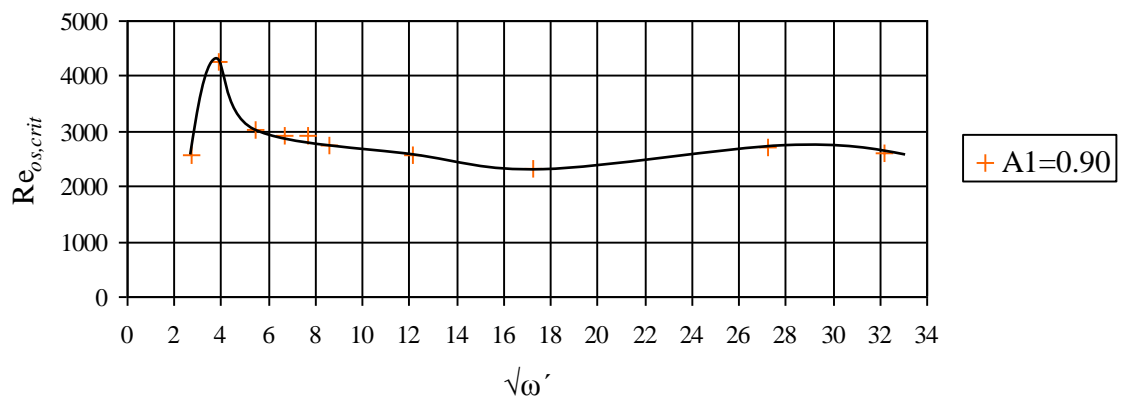


Figure 9.44. Effect of $\sqrt{\omega'}$ on $Re_{os,crit}$ at $A_1=0.90$

9.7. Effect of $\sqrt{\omega'}$ on $Re_{\delta_s, crit}$ at Constant Value of A_1

The effect of $\sqrt{\omega'}$ on $Re_{\delta_s, crit}$ is also investigated at constant value of A_1 in the range of $0.10 \leq A_1 \leq 0.90$ at the onset of the transition to turbulence in the experimental study. When the value of $\sqrt{\omega'}$ increases, $Re_{\delta_s, crit}$ decreases at each value of A_1 as can be seen in Fig. 9.45. The value of $Re_{\delta_s, crit}$ decreases dramatically until $\sqrt{\omega'} = 12.17$. After $\sqrt{\omega'} = 12.17$, the value of $Re_{\delta_s, crit}$ still decreases, however not dramatically. On the other hand, the maximum values of $Re_{\delta_s, crit}$ are always seen at $A_1 = 0.90$ for each $\sqrt{\omega'}$.

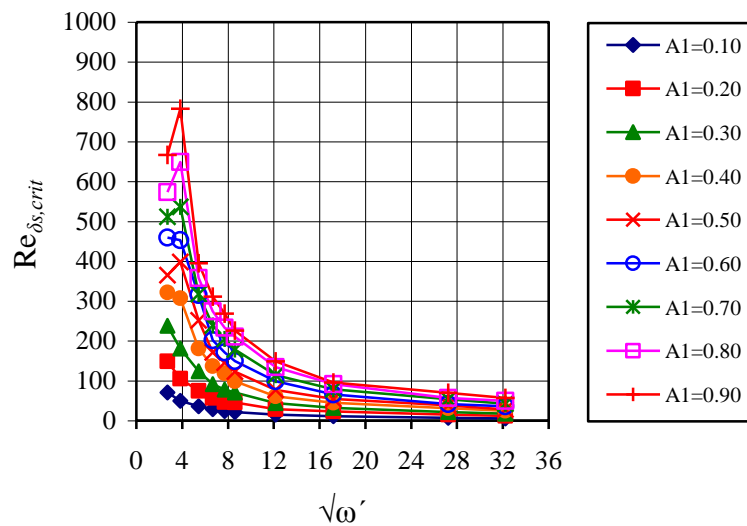


Figure 9.45. Effect of $\sqrt{\omega'}$ on $Re_{\delta_s, crit}$ in the range of $0.10 \leq A_1 \leq 0.90$

The relationships between $Re_{\delta_s, crit}$ and $\sqrt{\omega'}$ in the range of $0.10 \leq A_1 \leq 0.90$ are given in the form of $Re_{\delta_s, crit} = c_1 \sqrt{\omega'}^{-m}$ in Table 9.3.

Table 9.3. Relations between $Re_{\delta_s, crit}$ and $\sqrt{\omega'}$ in the range of $0.10 \leq A_1 \leq 0.90$

A_1	c_1	m	Mean Deviation (%)
0.10	193	1.0063	±1
0.20	399	1.0104	
0.30	715	1.0723	
0.40	1112	1.1041	±2
0.50	1433	1.1222	±3
0.60	1750	1.1284	±2
0.70	1860	1.0853	
0.80	2186	1.0963	
0.90	2511	1.1020	±3

9.8. Correlations on Critical Reynolds Numbers

As a result of the detailed investigations on the flow dynamics in the previous sections, it is essential to perform a correlation study on $Re_{ta, crit}$, $Re_{os, crit}$ and $Re_{\delta_s, crit}$ in terms of $\sqrt{\omega'}$ and A_1 . Figure 9.46 shows the flow map of $Re_{ta, crit}$ and $Re_{os, crit}$, classifying the laminar regime and the onset of transition to turbulence in the range of $2.72 \leq \sqrt{\omega'} \leq 32.21$. As is seen from the figure, the transition to turbulence starts when $Re_{ta, crit}$ is above roughly 2700. Below this value, the flow is roughly seen to be laminar. Hence this figure gives an overall idea about the border of the critical states. The flow can be kept as laminar at higher Re_{ta} in the order of nearly 3500 at $\sqrt{\omega'} = 3.85$ ($f=0.2$ Hz). Hence these data of $Re_{ta} = 3696$, $Re_{ta} = 3803$ and $Re_{ta} = 3058$ in which the flow is still laminar at $\sqrt{\omega'} = 3.85$ ($f=0.2$ Hz) are above the border of critical state of $Re_{ta, crit} \approx 2700$, circled in the figure. In the figure, (L) and (OT) represent the data in the laminar regime and at the onset of transition to turbulence, respectively.

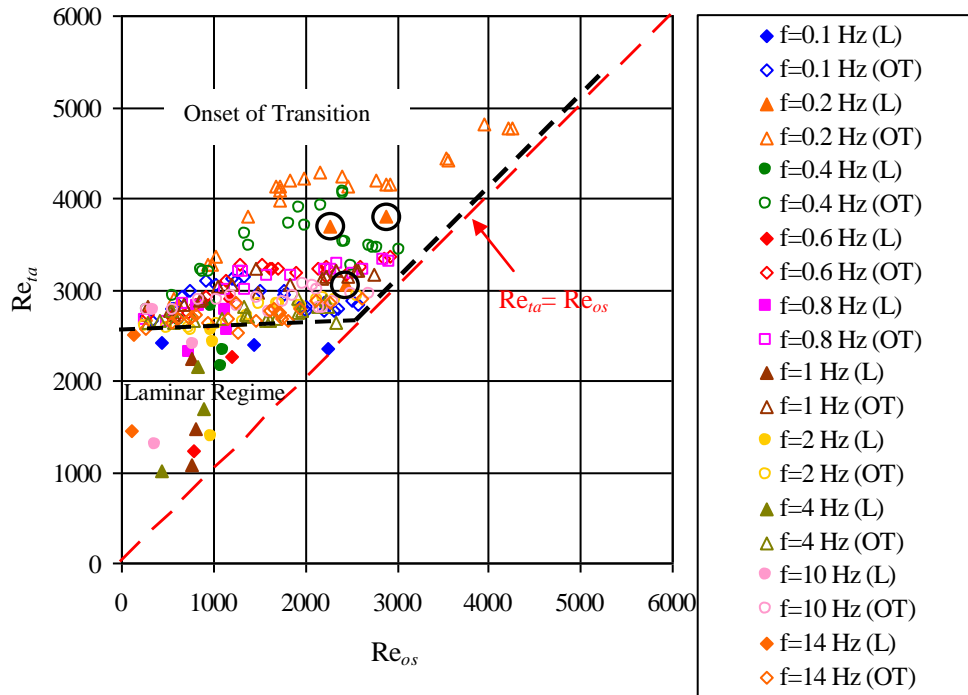


Figure 9.46. Flow map showing laminar regime and onset of transition in terms of Re_{ta} and Re_{os}

Figure 9.47 shows the critical limit between the laminar regime (L) and the onset of transition (OT) to turbulence in the range of $2.72 \leq \sqrt{\omega'} \leq 32.21$. The overall characteristic of the relationship between $Re_{ta,crit}$ and $\sqrt{\omega'}$ is given with the dashed line. It can be deduced that the behavior of $Re_{ta,crit}$ varies differently with respect to $\sqrt{\omega'}$ in the intermediate region. The value of $Re_{ta,crit}$ increases with increasing of $\sqrt{\omega'}$ up to $\sqrt{\omega'} = 3.85$. After $\sqrt{\omega'} = 3.85$, $Re_{ta,crit}$ decreases sharply with increasing of $\sqrt{\omega'}$ in the range of $3.85 \leq \sqrt{\omega'} \leq 8.61$, however $Re_{ta,crit}$ increases in the range of $8.61 < \sqrt{\omega'} < 27.22$ and then begins to decrease at $\sqrt{\omega'} \geq 27.22$. Hence the intermediate region may be divided into sub-regions in view of the different characteristics of $Re_{ta,crit}$ variations with $\sqrt{\omega'}$, which are observed at all values of A_1 .

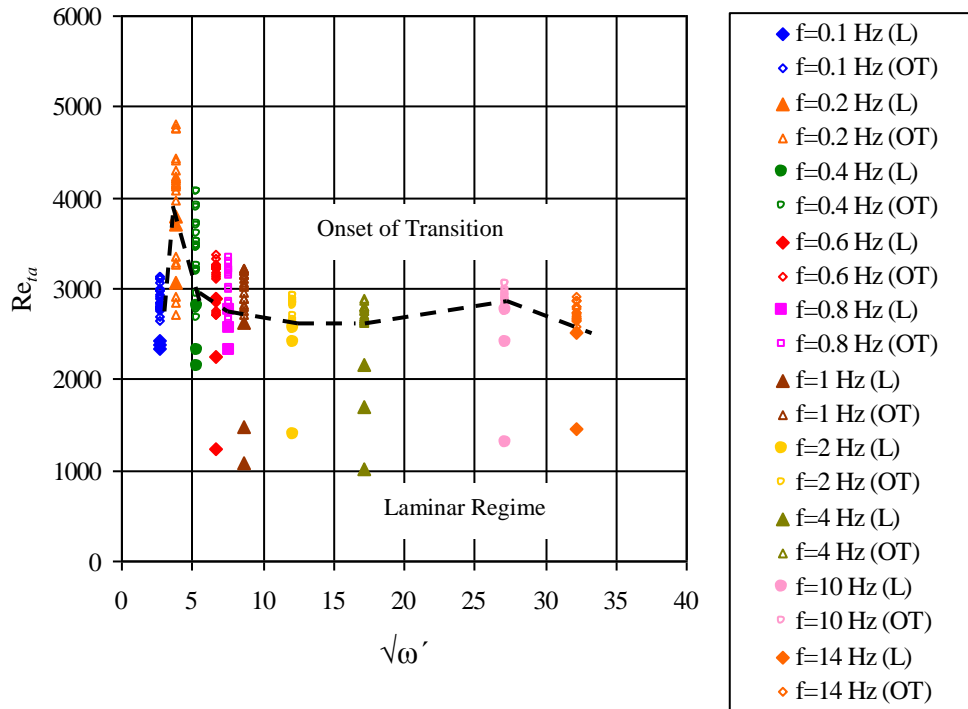


Figure 9.47. Flow map showing laminar regime and onset of transition in terms of $Re_{\tau_a,crit}$ with respect to $\sqrt{\omega'}$

As a correlation study, the relationship between $Re_{\tau_a,crit}$ and $A_1\sqrt{\omega'}$ at the onset of transition is presented in Fig. 9.48. Although $Re_{\tau_a,crit}$ is dependent on the combination effect of A_1 and $\sqrt{\omega'}$ for $\sqrt{\omega'} \leq 8.61$ ($f \leq 1$ Hz), given with dashed lines, the influence of $A_1\sqrt{\omega'}$ on $Re_{\tau_a,crit}$ disappears for $\sqrt{\omega'} > 8.61$, denoted with solid line in Fig. 9.48. This figure shows the validity of the critical state at $\sqrt{\omega'} = 8.61$ once more.

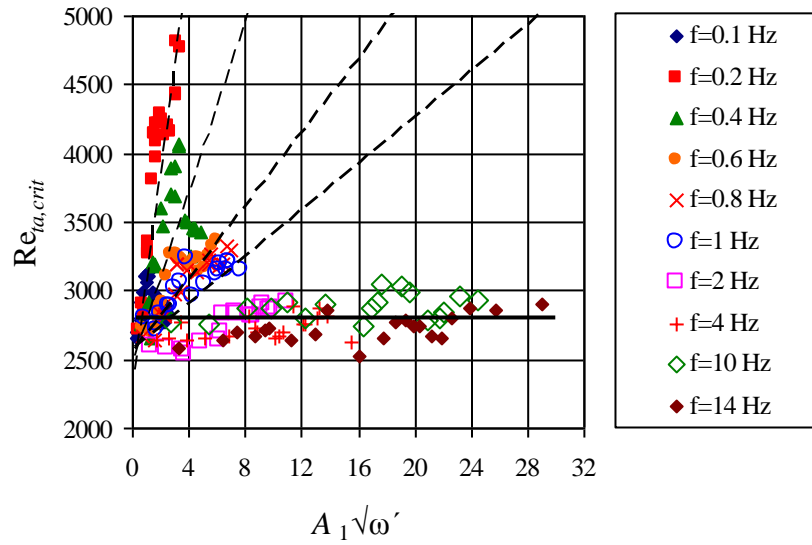


Figure 9.48. Relationship between $Re_{ta,crit}$ and $A_1 \sqrt{\omega'}$ at the onset of transition

The variations of $Re_{os,crit}$ with $\sqrt{\omega'}$ in the covered ranges of $2.72 \leq \sqrt{\omega'} \leq 32.21$ and $0.10 \leq A_1 \leq 0.90$ are given in Fig. 9.49. The maximum value of $Re_{os,crit}$ is seen as $Re_{os,crit} = 4261$ at $\sqrt{\omega'} = 3.85$ ($f = 0.2$ Hz) and $A_1 = 0.90$. The value of $Re_{os,crit}$ at each $\sqrt{\omega'}$ varies with A_1 as shown in Fig. 9.49.

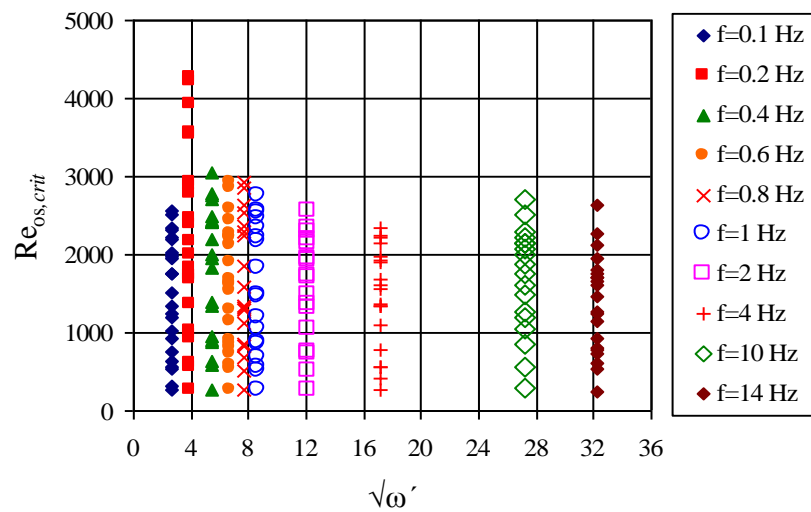


Figure 9.49. Relationship between $Re_{os,crit}$ and $\sqrt{\omega'}$ at the onset of transition

In order to investigate the influences of $\sqrt{\omega'}$ and A_1 together on $Re_{os,crit}$, some trials are performed and a relation between $Re_{os,crit}$ and $A_1\sqrt{\omega'}$ is found at each f as can be seen in Fig. 9.50. The inclination angle of the relationship between $Re_{os,crit}$ and $A_1\sqrt{\omega'}$ tends to decrease with increasing of f . The relationship between $Re_{os,crit}$ and $A_1\sqrt{\omega'}$ at each f is given in the form of $Re_{os,crit} = c_1 A_1 \sqrt{\omega'} - c_2$ in Table 9.4.

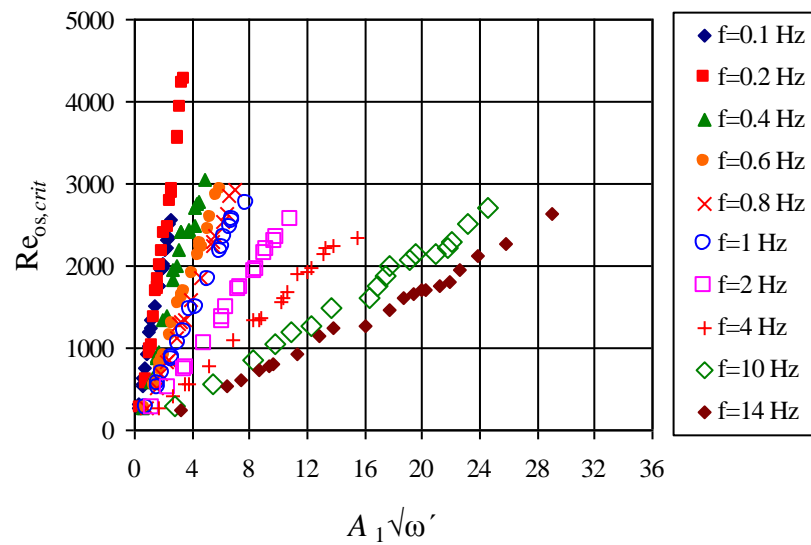


Figure 9.50. Relationship between $Re_{os,crit}$ and $A_1\sqrt{\omega'}$ at the onset of transition

Table 9.4. Relations between $Re_{os,crit}$ and $A_1\sqrt{\omega'}$ in the range of $0.1 \text{ Hz} \leq f \leq 14 \text{ Hz}$

f	c_1	c_2	Mean Deviation (%)
0.1	1017	-60	± 0.5
0.2	1322	455	± 1
0.4	663	41	± 3
0.6	511	128	± 0.5
0.8	441	130	
1	378	87	
2	245	105	
4	161	20	
10	107	9.6	
14	89	55	

9.9. Correlations on Friction Factors

In reference to the study of Ohmi and Iguchi (1981), the variation between the parameter of $\sqrt{\omega'}/\sqrt{\text{Re}_{ta}^{3/4}}$ calculated from the combination of $\sqrt{\omega'}$ and Re_{ta} and the parameter of $\lambda_{sL}/\lambda_{u,ta}$ is discussed in the laminar regime and at the onset of transition. The relations between $\lambda_{sL}/\lambda_{u,ta}$ and $\sqrt{\omega'}/\sqrt{\text{Re}_{ta}^{3/4}}$ in laminar regime and at the onset of transition are given in Figs. 9.51 and 9.52. The relations in the laminar regime and at the onset of transition are also given with deviations of $\pm 7\%$ and $\pm 19\%$, respectively as follows:

$$\lambda_{sL}/\lambda_{u,ta} = 0.0011 \left(\sqrt{\omega'}/\sqrt{\text{Re}_{ta}^{3/4}} \right)^{-2.3125} \quad (9.1)$$

$$\lambda_{sL}/\lambda_{u,ta} = 0.0018 \left(\sqrt{\omega'}/\sqrt{\text{Re}_{ta}^{3/4}} \right)^{-2.0375} \quad (9.2)$$

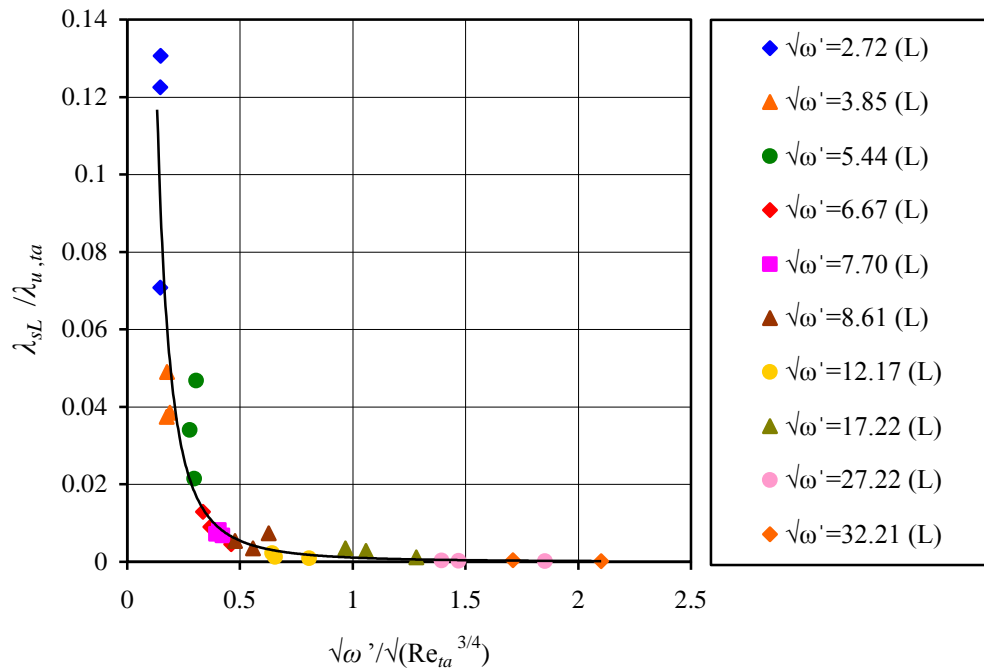


Figure 9.51. Relationship between $\sqrt{\omega'}/\sqrt{\text{Re}_{ta}^{3/4}}$ and $\lambda_{sL}/\lambda_{u,ta}$ in the laminar regime

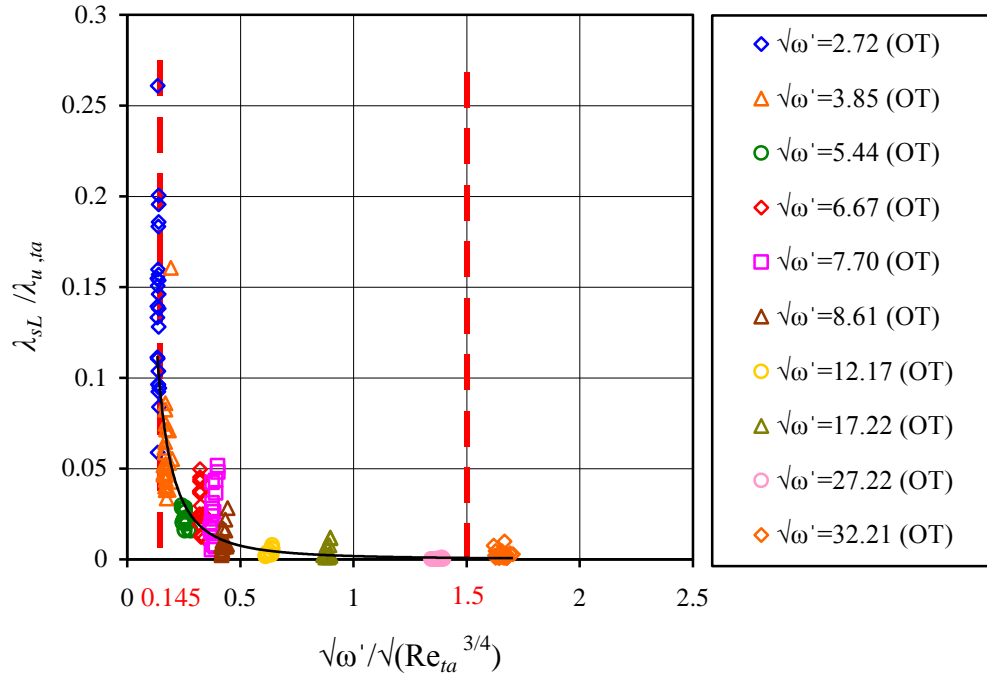


Figure 9.52. Relationship between $\sqrt{\omega'}/\sqrt{\text{Re}_{ta}^{3/4}}$ and $\lambda_{sL}/\lambda_{u,ta}$ at the onset of transition

The variations between $\sqrt{\omega'}/\sqrt{\text{Re}_{ta}^{3/4}}$ and $\lambda_{sL}/\lambda_{u,ta}$ in laminar regime and at the onset of transition are presented together in Fig. 9.53. As can be seen from the figure, there is a link between data in laminar regime and at the onset of transition. The relation between $\sqrt{\omega'}/\sqrt{\text{Re}_{ta}^{3/4}}$ and $\lambda_{sL}/\lambda_{u,ta}$ which is valid for both data in laminar regime and at onset of transition is given with a deviation of $\pm 18\%$ as follows:

$$\lambda_{sL}/\lambda_{u,ta} = 0.0017 \left(\sqrt{\omega'}/\sqrt{\text{Re}_{ta}^{3/4}} \right)^{-2.0789} \quad (9.3)$$

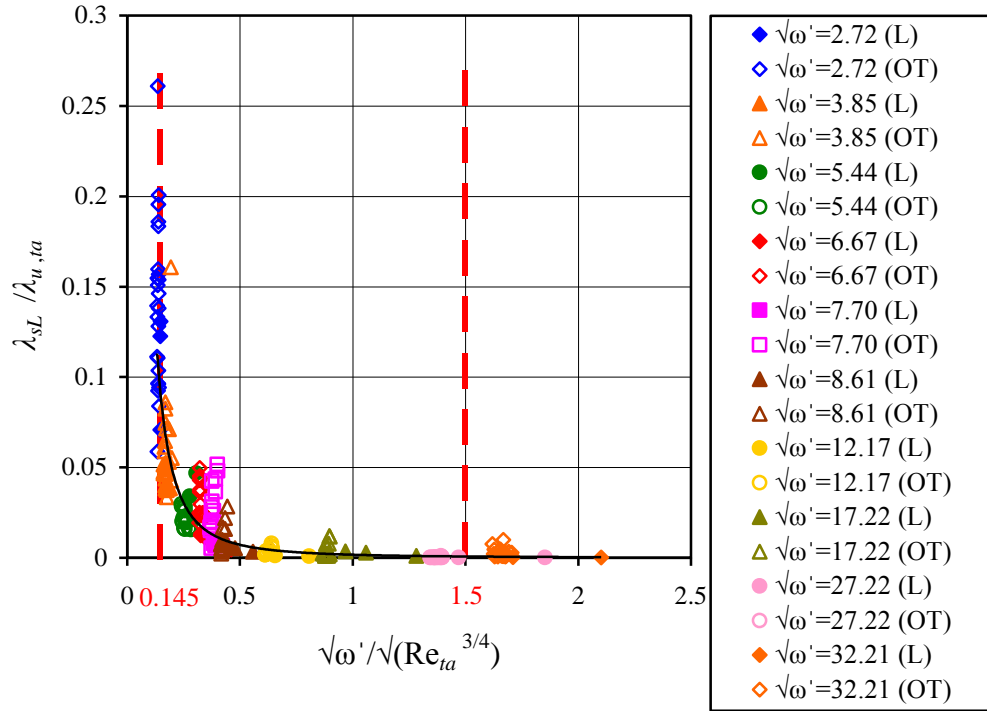


Figure 9.53. Relationship between $\sqrt{\omega'}/\sqrt{\text{Re}_{ta}^{3/4}}$ and $\lambda_{sL}/\lambda_{u,ta}$ in the laminar regime and at the onset of transition

In the study of Ohmi and Iguchi (1981), the limit between quasi-steady and intermediate regions as well as the limit between intermediate and inertia dominant ones are defined by $\sqrt{\omega'}/\sqrt{\text{Re}_{ta}^{3/4}}=0.145$ and 1.50, respectively which are also identified in Figs. 9.52 and 9.53 with red dashed lines. As can be noticed from the figures, the verification is also satisfied with the present study in which the regions at $\sqrt{\omega'} < 5.44$ and $\sqrt{\omega'} > 27.22$ are considered to be quasi-steady and inertia dominant, respectively.

9.10. Conclusions

In this section, the effects of $\sqrt{\omega'}$ and A_1 on $\text{Re}_{ta,crit}$, $\text{Re}_{os,crit}$ and $\text{Re}_{\delta_s,crit}$ are presented. Some correlation studies are carried out similar to the literature. The following deductions are expressed in view of the detailed investigations;

i) Effect of A_1 on $Re_{ta,crit}$ at constant value of $\sqrt{\omega'}$

1) The maximum $Re_{ta,crit}=4817$ at the onset of transition is obtained at $\sqrt{\omega'}=3.85$ ($f=0.2$ Hz).

2) The variation of $Re_{ta,crit}$ with A_1 at $\sqrt{\omega'}=2.72$ at the onset of transition to turbulence is seen to be sinusoidal.

3) Although the behavior of $Re_{ta,crit}$ variation with A_1 at $\sqrt{\omega'}=3.85$ is seen to be sinusoidal, there is also an upward inclination in the sinusoidal form, in which this variation tends to increase up to $A_1=0.90$.

4) The sinusoidal behavior of $Re_{ta,crit}$ variation with A_1 at $\sqrt{\omega'}=5.44$ is found as similar as that at $\sqrt{\omega'}=2.72$, however the values of $Re_{ta,crit}$ are higher than those at $\sqrt{\omega'}=2.72$.

5) The sinusoidal variation of $Re_{ta,crit}$ at $\sqrt{\omega'}=6.67$ tends to raise upwards when A_1 increases similarly to the upward trend of the $Re_{ta,crit}$ variation with A_1 at $\sqrt{\omega'}=3.85$.

6) The variations of $Re_{ta,crit}$ with A_1 are seen to become slightly sinusoidal at $\sqrt{\omega'}=7.70$ and $\sqrt{\omega'}=8.61$ when compared with those at $\sqrt{\omega'} \leq 6.67$.

7) The effect of A_1 on $Re_{ta,crit}$ begins to disappear at $\sqrt{\omega'}=12.17$. The values of $Re_{ta,crit}$ at each A_1 are seen to be very close to each other for $\sqrt{\omega'} \geq 12.17$ ($f \geq 2$ Hz). This verifies the critical state of $\sqrt{\omega'}=8.61$. The values of $Re_{ta,crit}$ become absolutely independent from A_1 at $\sqrt{\omega'}=27.22$ and $\sqrt{\omega'}=32.21$.

ii) Effect of A_1 on $Re_{os,crit}$ at constant value of $\sqrt{\omega'}$

1) The variation of $Re_{os,crit}$ with A_1 at each $\sqrt{\omega'}$ is linear in the form of $Re_{os,crit} = c_1 A_1 + c_2$. When A_1 increases, $Re_{os,crit}$ increases.

2) The maximum value of $Re_{os,crit}$ is found at $\sqrt{\omega'} = 3.85$ ($f=0.2$ Hz) as $Re_{os,crit} = 4261$ at $A_1 = 0.90$.

iii) *Effect of A_1 on $Re_{\delta_s,crit}$ at constant value of $\sqrt{\omega'}$*

1) The relationships between $Re_{\delta_s,crit}$ and A_1 at each $\sqrt{\omega'}$ are found to be linear in the form of $Re_{\delta_s,crit} = c_1 A_1 + c_2$ such as $Re_{\delta_s,crit}$ increases when A_1 increases. However, the inclination of the relationship between $Re_{os,crit}$ and A_1 tends to decrease when $\sqrt{\omega'}$ increases.

2) The maximum value of $Re_{\delta_s,crit}$ is seen again at $\sqrt{\omega'} = 3.85$ ($f=0.2$ Hz).

iv) *Effect of $\sqrt{\omega'}$ on $Re_{ta,crit}$ at constant value of A_1*

1) The value of $Re_{ta,crit}$ increases in the range of $2.72 \leq \sqrt{\omega'} \leq 3.85$. Later it decreases up to $\sqrt{\omega'} = 12.17$, and maintains almost at constant value between $\sqrt{\omega'} = 12.17$ and $\sqrt{\omega'} = 17.22$. Then, it begins to increase up to $\sqrt{\omega'} = 27.22$ and again decreases up to $\sqrt{\omega'} = 32.21$.

2) The value of $Re_{ta,crit}$ is almost independent on $\sqrt{\omega'}$ at $A_1 = 0.10$ resulting the mean values of $Re_{ta,crit} = 2698$ with maximum deviation of $\pm 4\%$.

3) The value of $Re_{ta,crit}$ is almost independent from $\sqrt{\omega'}$ at $A_1 = 0.20$ as same as observed at $A_1 = 0.10$ if the deviations at $\sqrt{\omega'} = 3.85$ and $\sqrt{\omega'} = 5.44$ are not taken into consideration.

4) There is a sinusoidal variation between $Re_{ta,crit}$ and $\sqrt{\omega'}$ at $A_1 = 0.30$.

5) The variations between $Re_{ta,crit}$ and $\sqrt{\omega'}$ at $A_1 > 0.30$ are found to be completely different in shape when compared with those at $A_1 \leq 0.30$. The value of $Re_{ta,crit}$ increases suddenly up to $\sqrt{\omega'} = 3.85$ and then begins to decrease $\sqrt{\omega'} > 3.85$ at $A_1 > 0.30$. The value of $Re_{ta,crit}$ decreases sharply for $3.85 \leq \sqrt{\omega'} \leq 8.61$, however its value is nearly maintained constant for $\sqrt{\omega'} > 8.61$ at $A_1 > 0.30$. It verifies once more that $\sqrt{\omega'} = 8.61$ is the critical state.

6) The critical range of $\sqrt{\omega'} = 8.61$ is also seen in view of the data in the literature although only $Re_{ta,crit}$ data of Hershey-Im (1968) at $\sqrt{\omega'} < 8$ and $Re_{ta,crit}$ data of Ohmi et al. (1981) at $\sqrt{\omega'} > 8$ are available at the onset of transition in the literature.

7) The experimental data in the range of $2.72 \leq \sqrt{\omega'} \leq 32.21$ provide a contribution to the literature filling the gap in $\sqrt{\omega'}$ range.

8) However, there is a difference in terms of $Re_{ta,crit}$ value between the present data and the data of Ohmi et al. (1982) at $\sqrt{\omega'} > 8$. The differences between the present and Ohmi et al.'s data in terms of $Re_{ta,crit}$ at $\sqrt{\omega'} > 8$ may be due to the differences in the experimental conditions, transition detection methods and the pipe diameters or the investigation in the limited range of $\sqrt{\omega'}$ at which only two values of $\sqrt{\omega'}$ used for 15 experimental runs in the study of Ohmi et al. (1982).

v) *Effect of $\sqrt{\omega'}$ on $Re_{os,crit}$ at constant value of A_1*

1) The value of $Re_{os,crit}$ is independent on $\sqrt{\omega'}$ at $A_1 = 0.10$ and $A_1 = 0.20$ resulting the mean values of $Re_{os,crit} = 271$ and $Re_{os,crit} = 550$ with maximum deviations of $\pm 5\%$ and $\pm 8\%$, respectively.

2) The influence of $\sqrt{\omega'}$ on $Re_{os,crit}$ is seen after $A_1 \geq 0.30$, which is as same as the influence of $\sqrt{\omega'}$ on $Re_{ta,crit}$ after $A_1 \geq 0.30$.

3) The maximum value of $Re_{os,crit}$ at $A_1=0.30$ is found to be $Re_{os,crit}=987$ at $\sqrt{\omega'}=3.85$.

vi) *Effect of $\sqrt{\omega'}$ on $Re_{\delta_s,crit}$ at constant value of A_1*

1) The value of $Re_{\delta_s,crit}$ decreases when $\sqrt{\omega'}$ increases at each value of A_1 . $Re_{\delta_s,crit}$ decreases dramatically until $\sqrt{\omega'}=12.17$. After $\sqrt{\omega'}=12.17$, the value of $Re_{\delta_s,crit}$ still decreases, however not dramatically.

2) The maximum values of $Re_{\delta_s,crit}$ are always seen at $A_1=0.90$ for each $\sqrt{\omega'}$.

3) The relationships between $Re_{\delta_s,crit}$ and $\sqrt{\omega'}$ in the range of $0.10 \leq A_1 \leq 0.90$ are given in the form of $Re_{\delta_s,crit} = c_1 \sqrt{\omega'}^{-m}$.

vii) *Correlation studies*

1) The behavior of $Re_{ta,crit}$ varies differently with respect to $\sqrt{\omega'}$ in the intermediate region. The value of $Re_{ta,crit}$ increases with increasing of $\sqrt{\omega'}$ up to $\sqrt{\omega'}=3.85$. After $\sqrt{\omega'}=3.85$, $Re_{ta,crit}$ decreases sharply with increasing of $\sqrt{\omega'}$ in the range of $3.85 \leq \sqrt{\omega'} \leq 8.61$, however $Re_{ta,crit}$ increases in the range of $8.61 < \sqrt{\omega'} < 27.22$ and then begins to decrease at $\sqrt{\omega'} \geq 27.22$. Hence the intermediate region may be divided into sub-regions in view of the different characteristics of $Re_{ta,crit}$ variations with $\sqrt{\omega'}$, which are observed at all values of A_1 .

2) $Re_{ta,crit}$ is dependent on the dimensionless parameter of $A_1 \sqrt{\omega'}$ for $\sqrt{\omega'} \leq 8.61$ ($f \leq 1$ Hz), however the influence of $A_1 \sqrt{\omega'}$ disappears on $Re_{ta,crit}$ for $\sqrt{\omega'} > 8.61$. This behavior of $Re_{ta,crit}$ with $A_1 \sqrt{\omega'}$ shows the validity of the critical state at $\sqrt{\omega'}=8.61$ once more.

3) The inclination angle of the relationship between $\text{Re}_{os,crit}$ and $A_1\sqrt{\omega'}$ tends to decrease with increasing of f . The relationship between $\text{Re}_{os,crit}$ and $A_1\sqrt{\omega'}$ at each f is given in the form of $\text{Re}_{os,crit} = c_1 A_1 \sqrt{\omega'} - c_2$.

4) In reference to the study of Ohmi and Iguchi (1981), the relationships between $\lambda_{sL}/\lambda_{u,ta}$ and $\sqrt{\omega'}/\sqrt{\text{Re}_{ta}^{3/4}}$ in the laminar regime and at the onset of transition are found with deviations of $\pm 7\%$ and $\pm 19\%$, respectively as $\lambda_{sL}/\lambda_{u,ta} = 0.0011\left(\sqrt{\omega'}/\sqrt{\text{Re}_{ta}^{3/4}}\right)^{-2.3125}$ and $\lambda_{sL}/\lambda_{u,ta} = 0.0018\left(\sqrt{\omega'}/\sqrt{\text{Re}_{ta}^{3/4}}\right)^{-2.0375}$.

5) The relation between $\sqrt{\omega'}/\sqrt{\text{Re}_{ta}^{3/4}}$ and $\lambda_{sL}/\lambda_{u,ta}$ which is valid for both data in laminar regime and at onset of transition is found with a deviation of $\pm 18\%$ as $\lambda_{sL}/\lambda_{u,ta} = 0.0017\left(\sqrt{\omega'}/\sqrt{\text{Re}_{ta}^{3/4}}\right)^{-2.0789}$.

CHAPTER 10

RECOMMENDATIONS FOR FURTHER STUDIES

The results and the conclusions of the present study are given in details at the end of each chapter of the thesis. Hence some suggestions for further studies are presented in this chapter.

1. Until now, the investigations on the time-dependent pipe flow dynamics at the onset of transition to turbulence are quite rare, which have been generally carried out by means of the observation of velocity waveforms to detect turbulent structures in transitional regime. Moreover, there are opposite results in terms of the effect of oscillation frequency on flow stability and transition. In the present study, the flow dynamics and the detection of the onset of transition to turbulence are investigated in pulsatile pipe flows in details by means of the well-controlled program devised in LabView 2009 environment.

It is deduced that the oscillation frequency, f is also an important parameter alone despite of existing in Womersley number, $\sqrt{\omega'}$. In the present study, the maximum values of $Re_{ta,crit}$ and $Re_{os,crit}$ are observed at $f = 0.2$ Hz at the onset of the transition to turbulence in 26.6 mm-diameter pipe. Hence the flow dynamics at the onset of transition should be investigated for different pipe diameters.

2. As a result of the detailed investigation on the flow dynamics of pulsatile pipe flow, it is found that there is a difference in terms of $Re_{ta,crit}$ value between the present data and the data of Ohmi et al. (1982) at $\sqrt{\omega'} > 8$ at the onset of transition to

turbulence. The differences between the present data and Ohmi et al.'s data in terms of $Re_{ta,crit}$ at $\sqrt{\omega'} > 8$ may be due to the differences in the experimental conditions, transition detection methods and the pipe diameters and/or the investigation in the limited range of $\sqrt{\omega'}$ at which only two values of $\sqrt{\omega'}$ used for 15 experimental runs in the study of Ohmi et al. (1982). In the same manner, the flow dynamics at the end of transition should be investigated and compared with those in literature.

3. The designed program, *TDFC.vi* and the used methodology in the present study has an ability to trigger the MFC unit and control the measurement devices, to acquire and acquire the data from the measurement devices, to process, analyze and post-process the data, to plot the necessary charts and graphs and to save all data and their corresponding results as processed data, charts and graphs into the specified file. The program has also been developed in order to detect the onset of transition to turbulence in pulsatile pipe flows, due to the difficulty for detection of the turbulent bursts by visual observation in velocity waveforms.

In this manner, the end of transition should be detected by means of a well-controlled program devised in a software program similar to the devised program in LabView environment in the present study.

4. The experimental data in the range of $2.72 \leq \sqrt{\omega'} \leq 32.21$ provide a contribution to the literature filling the gap in $\sqrt{\omega'}$ range.

The maximum $Re_{ta,crit} = 4817$ at the onset of transition is obtained at $\sqrt{\omega'} = 3.85$ ($f = 0.2$ Hz). The variation of $Re_{ta,crit}$ with A_1 at $\sqrt{\omega'} = 2.72$ at the onset of transition to turbulence is seen to be sinusoidal. The variations of $Re_{ta,crit}$ with A_1 are observed to become slightly sinusoidal at $\sqrt{\omega'} = 7.70$ and $\sqrt{\omega'} = 8.61$ when compared with those at $\sqrt{\omega'} \leq 6.67$. The effect of A_1 on $Re_{ta,crit}$ begins to disappear at $\sqrt{\omega'} = 12.17$. The values of $Re_{ta,crit}$ at each A_1 are seen to be very close to each other for $\sqrt{\omega'} \geq 12.17$ ($f \geq 2$ Hz).

As an overall observation, the value of $Re_{ta,crit}$ tends to increase when $\sqrt{\omega'}$ increases in the range of $2.72 \leq \sqrt{\omega'} \leq 3.85$. After $\sqrt{\omega'} = 3.85$, the value of $Re_{ta,crit}$ decreases up to $\sqrt{\omega'} = 12.17$, and maintains almost at constant value between $\sqrt{\omega'} = 12.17$ and $\sqrt{\omega'} = 17.22$. Then, it begins to increase up to $\sqrt{\omega'} = 27.22$ and again decreases up to $\sqrt{\omega'} = 32.21$. However, as a result of the detailed investigation, it is observed that the value of $Re_{ta,crit}$ is almost independent on $\sqrt{\omega'}$ at $A_1 = 0.10$ and $A_1 = 0.20$ with maximum deviation of $\pm 4\%$. The sinusoidal variation between $Re_{ta,crit}$ and $\sqrt{\omega'}$ begins at $A_1 = 0.30$. The variations between $Re_{ta,crit}$ and $\sqrt{\omega'}$ at $A_1 > 0.30$ are found to be completely different in shape when compared with those at $A_1 \leq 0.30$. The value of $Re_{ta,crit}$ increases suddenly up to $\sqrt{\omega'} = 3.85$ and then begins to decrease $\sqrt{\omega'} > 3.85$ at $A_1 > 0.30$. The value of $Re_{ta,crit}$ decreases sharply for $3.85 \leq \sqrt{\omega'} \leq 8.61$, however its value is nearly maintained constant for $\sqrt{\omega'} > 8.61$ at $A_1 > 0.30$.

These detailed analyses on the flow dynamics should also be performed in oscillating and transient pipe flows.

5. The effects of the time-dependent flow characteristics such as Re_{ta} , Re_{os} , $\sqrt{\omega'}$ and A_1 on the development length for fully developed laminar and turbulent time dependent pipe flows should be studied.
6. The studies on the time dependent pipe flow dynamics should also be carried out in rough pipes in the future.
7. The onset and the end of transition to turbulence should be studied in both oscillating and transient pipe flows.
8. Heat enhancement should also be studied at the onset and the end of transition in time dependent pipe flows in the future.

9. The physical nature of the pneumatic conveying systems is similar to the time dependent flows. Hence two-phase time dependent pipe flows should be studied for improvements and contributions in pneumatic conveying systems.

REFERENCES

- Akashi, K., Watanabe, H. and Koga, K. (1978). Flow rate measurement in pipe line with many bends. *Mit Heavy Ind*, **15**, 87-96.
- Akhavan, R., Kamm, R.D. and Shapiro, A.H. (1991). An investigation of transition to turbulence in bounded oscillatory Stokes flows Part 1. Experiments. *J. Fluid Mech.*, **225**, 395-422.
- Al-Garni, A.M. (2007). Low speed calibration of hot-wire anemometers. *Flow Meas. Instrum.*, **18**, 95-98.
- Anderson, J.D. (1991). *Fundamentals of Aerodynamics*. McGraw-Hill Inc., New York.
- Aydın, M. and Leutheusser, H.J. (1980). Very low velocity calibration and application of hot-wire probes. *DISA Information*, **25**, 17-18.
- Barnes, H.T. and Coker E.G. (1905). The flow of water through pipes. *Proc R Soc London*, **74**, 341-356.
- Bradshaw, P. and Pankhurst, R.C. (1964). The design of low-speed wind tunnels. *J. Progress in Aero. Sci.*, **5**: 1-69.
- Bhatia, J.C., Durst, F. and Jovanovic, J. (1982). Corrections of hot-wire anemometer measurements near walls. *J. Fluid Mech.*, **122**, 411-431.
- Bruun, H.H. (1995). *Hot-wire anemometry, principles and signal analysis*. New York. Oxford University Press.
- Bruun, H.H., Farrar, B. and Watson, I. (1989). A swinging arm calibration method for low velocity hot-wire probe calibration. *Exp. Fluids*, **7**, 400-404.

Bruun, H.H., Khan, M.A., Al-Kayiem, H.H. and Fardad, A.A. (1988). Velocity calibration relationships for hot-wire anemometry. *J. Phys. E: Sci. Instrum.*, **21**, 225-232.

Clamen, M. and Minton, P. (1977). An experimental investigation of flow in an oscillating pipe. *J. Fluid Mech.*, **81**, 421-431.

Christman, P.J. and Podzimek, J. (1981). Hot-wire anemometer behaviour in low velocity air flow. *J. Phys. E: Sci. Instrum.*, **14**, 46-51.

Chua, L.P., Li, H.S. and Zhang, H. (2000). Calibration of hot-wire for low speed measurements. *Int. Commun. Heat Mass Transfer*, **27**, 507-516.

Clancy, L.J. (1975). *Aerodynamics*. John Wiley&Sons, New York.

Collis, D.C. and Williams, M.J. (1959). Two-dimensional convection from heated wires at low Reynolds numbers. *J. Fluid Mech.*, **6**, 357-384.

Çarpınlioğlu, M.Ö. (2003). An approach for transition correlation of laminar pulsatile pipe flows via frictional field characteristics. *Flow Meas. Instrum.*, **14**, 233-242.

Çarpınlioğlu, M.Ö. and Gündoğdu, M.Y. (2001). A critical review on pulsatile pipe flow studies directing towards future research topics. *Flow Meas. Instrum.*, **12**, 163-174.

Çarpınlioğlu, M.Ö. and Gündoğdu, M.Y. (2001). Presentation of a test system in terms of generated pulsatile flow characteristics. *Flow Meas. Instrum.*, **12**, 181-190.

Çarpınlioğlu, M.Ö. and Özahi, E. (2011). Laminar flow control via utilization of pipe entrance inserts (a comment on entrance length concept). *Flow Meas. Instrum.*, **22**, 165-174.

Das, D. and Arakeri, J.H. (1998). Transition of unsteady velocity profiles with reverse flow. *J. Fluid Mech.*, **374**, 251-283.

Durst, F., Haddad, K., Al-Salaymeh, A., Eid, S. and Ünsal, B. (2008). Mass flow-rate control unit to calibrate hot-wire sensors. *Exp. Fluids*, **44**, 189-197.

Durst, F., Heim, U., Ünsal, B. and Kullik, G. (2003). Mass flow rate control system for time-dependent laminar and turbulent flow investigations. *Meas. Sci. Technol.*, **14**, 893-902.

Durst, F., Ismailov, M. and Trimis, D. (1996). Measurement of instantaneous flow rates in periodically operating injection system. *Exp. Fluids*, **20**, 178-188.

Durst, F., Ray, S., Ünsal, B. and Bayoumi, O.A. (2005). The development lengths of laminar pipe and channel flows. *J. Fluids Eng.*, **127**, 1154-1160.

Durst, F. and Ünsal, B. (2006). Forced laminar-to-turbulent transition of pipe flows. *J. Fluid Mech.*, **506**, 449-464.

Durst, F., Ünsal, B., Ray, S. and Trimis, D. (2007). Method for defined mass flow variations in time and its application to test a mass flow rate meter for pulsating flows. *Meas. Sci. Technol.*, **18**, 790-802.

Durst, F. and Zanoun, E.S. (2002). Experimental investigation of near-wall effects on hot-wire measurements. *Exp. Fluids*, **33**, 210-218.

Durst, F., Zanoun, E.S. and Pashtrapanska, M. (2001). In situ calibration of hot wires close to highly heat-conducting walls. *Exp. Fluids*, **31**, 103-110.

Eckmann, D.M. and Grotberg, J.B. (1991). Experiments on transition to turbulence in oscillatory pipe flow. *J. Fluid Mech.*, **222**, 329-350.

Einav, S. and Sokolov, M. (1993). An experimental study of pulsatile pipe flow in the transition range. *Trans. of the ASME*, **115**, 404-411.

Ekman, V.W. (1883). On the change from steady to turbulent motion of liquids. *Ark. f. Math. A*, **174**, 1-12.

Emmons, H.W. (1951). The laminar-turbulent transition in a boundary layer, Part 1. *J Aero Sci.*, **18**, 490-498.

Erdal, A. (1997). A numerical investigation of different parameters that affect the performance of a flow conditioner. *Flow Meas Instrum.*, **8**, 93-102.

Erdal, A., Lindholm, D. and Thomassen, D. (1994). Development of a flow conditioner. *North Sea Flow Meas Workshop*, Scotland.

- Ertunç, Ö., Ünsal, B., Ray, S. and Durst, F. (2003). Application of a mass flow controller to time-dependent laminar and transitional pipe flows. *740th Eurotherm Seminar, Proceedings*, 165-176.
- Farell, C. and Youssef, S. (1996). Experiments on turbulence management using screen and honeycombs. *Trans. ASME, J. Fluids Eng.*, **118**, 26-32.
- Fargie, D. and Martin, B.W. (1971). Developing laminar flow in a pipe of circular cross-section. *Proc. Roy. Soc. Lond.*, **A321**, 461-476.
- Fishler, L.S. and Brodkey, R.S. (1991). Transition, turbulence and oscillating flow in a pipe: a visual study. *Exp. Fluids*, **11**, 388-398.
- Florio, P.J. and Mueller, W.K. (1968). Development of a periodic flow in a rigid tube. *J. Basic Eng., Trans. ASME*, **90**, 395-399.
- Fox, A., Lessen, M. and Bhat, W.V. (1968). Experimental investigation of the stability of Hagen-Poiseuille flow. *Phys. Fluids*, **11**, 1-4.
- Frattolillo, A. and Massarotti, N. (2002). Flow conditioners efficiency a comparison based on numerical approach. *Flow Meas. Instrum.*, **13**, 1-11.
- Gerrard, J.H. (1971). An experimental investigation of the pulsating turbulent water flow in a tube. *J. Fluid Mech.*, **46**, 43-64.
- Gerrard, J.H. and Hughes, M.D. (1971). The flow due to an oscillating piston in a cylindrical tube: a comparison between experiment and a simple entrance flow theory. *J. Fluid Mech.*, **50**, 97-106.
- Gibbings, J.C., Madadnia, J. and Yousif, A.H. (1995). The wall correction of the hot-wire anemometer. *Flow Meas. Instrum.*, **6**, 127-136.
- Gilbrech, D.A. and Combs, G.D. (1963). Critical Reynolds numbers for incompressible pulsating flow in tubes. *Dev. Theo. Appl. Mech.*, **1**, 292-304.
- Groth, J. and Johansson, A.V. (1988). Turbulence reduction by screens. *J. Fluid Mech.*, **197**, 139-155.

Guellouz, M.S. and Tavoularis, S. (1995). A simple pendulum technique for the calibration of hot-wire anemometers over low-velocity ranges. *Exp. Fluids*, **18**, 199-203.

Gündoğdu, M.Y. (2000). *An experimental investigation on pulsatile pipe flows*. PhD Thesis. University of Gaziantep.

Gündoğdu, M.Y. and Çarpınlioğlu, M.Ö. (1999). Present state of art on pulsatile flow theory Part I: Laminar and transitional flow regimes. *JSME International Journal*, **42**, 384-397.

Gündoğdu, M.Y. and Çarpınlioğlu, M.Ö. (1999). Present state of art on pulsatile flow theory Part 2: Turbulent flow regime. *JSME Int. J. Series B Fluids and Therm. Eng.*, **42**, 398-410.

Hagen, G. (1839). Über die bewegung des wassers in engen zylindrischen röhren. *Pogg. Ann.*, **46**, 423-442.

Hagen, G. (1854). Über den einfluß der temperatur auf die bewegung des wassers in röhren. *Abh. Akad. Wiss.*, Berlin, 17-98.

Hama, F.R., Long, J.D. and Hegarty, J.C. (1957). On transition from laminar to turbulent flow. *J. Appl. Phys.*, **28**, 388-394.

Hama, F.R. and Nutant, J. (1963). Detailed flow field observations in the transition process in a thick boundary layer. In: *Proc. Heat Transfer and Fluid Mech. Inst.*, Stanford University Press, 77-93.

Hebbar, K.S. (1980). Wall proximity corrections for hot-wire readings in turbulent flows. *DISA Information*, **25**, 15-16.

Heikal, M., Antoniou, A. and Cowell, T.A. (1988). A rig for the static calibration of constant-temperature hot wires at very low velocities. *Experimental Thermal and Fluid Science*, **1**, 221-223.

Hershey, D. and Im, C.S. (1968). Critical Reynolds number for sinusoidal flow of water in rigid tubes. *AIChE J.*, **14**, 807-809.

Hino, M., Sawamoto, M. and Takasu, S. (1976). Experiments on transition to turbulence in an oscillatory pipe flow. *J. Fluid Mech.*, **75**, 193-207.

Hino, M. and Takasu, S. (1974). Experiments on turbulence in an oscillatory pipe flow. *Proc. 18th Conf. Hydraulic Research, Japan Soc. Civil Engng.*, 145-150.

Hutchins, N. and Choi, K-So. (2002). Accurate measurements of local skin friction coefficient using hot-wire anemometry. *Progress in Aerospace Sciences*, **38**, 421-446.

Iguchi, M. and Ohmi, M. (1982). Transition to turbulence in a pulsatile pipe flow. Part 2: Characteristics of reversing flow accompanied by relaminarization. *Bull. JSME*, **25**, 1529.

Iguchi, M. and Ohmi, M. (1984). Transition to turbulence in a pulsatile pipe flow, Part 3. *Bull. JSME*, **27**, 1873-1880.

Iguchi, M., Ohmi, M. and Fujii, Y. (1989). Behaviour of turbulent slugs in a transient pipe flow. *JSME Int. J. Ser. II*, **32**, 340-347.

Iguchi, M., Ohmi, M. and Kimura, H. (1986). Behavior of turbulent slug in a pulsatile pipe flow. *Trans. Jpn. Soc. Mech. Eng.*, (in Japanese), **52**, 2390, *Flow Control Measurement*, **2**, 951, Pergamon Press.

Iguchi, M., Urahata, I. and Ohmi, M. (1987). Turbulent slug and velocity field in the inlet region from pulsatile pipe flow. *JSME Int. J.*, **30**, 414-422.

Johnson, G.W. (1997). *LabVIEW Graphical Programming: Practical Applications in Instrumentation and Control*. (2nd ed.). McGraw-Hill.

Johnstone, A., Uddin, M. and Pollard, A. (2005). Calibration of hot-wire probes using non-uniform mean velocity profiles. *Exp. Fluids*, **39**, 525-532.

Karnik, U., Jungowski, W.M. and Botros, K.K. (1994). Effects of turbulence on orifice meter performance. *ASME J. Offshore Mech. and Arct.*, **116**, 77-85.

Kaskel, A. (1961). Experimental study of the stability of pipe flow: II. Development of disturbance generator. *Jet Propulsion Laboratory, Tech. Rep.* 32-138, Pasadena, California.

Khoo, B.C., Chew, Y.T., Lim, C.P. and Teo, C.J. (1998). Dynamic response of a hot-wire anemometer. Part I: A marginally elevated hot-wire probe for near-wall velocity measurements. *Meas. Sci. Technol.*, **9**, 751-763.

Kirmse, R.E. (1979). Investigation of pulsating turbulent pipe flow. *Trans. of ASME: J. of Fluids Engng.*, **101**, 436-442.

Klebanoff, P.S. and Tidstrom, K.D. (1959). Evolution of amplified waves leading to transition in a boundary layer with zero pressure gradient. *NACA Tech Note*, D-195.

Klebanoff, P.S., Tidstrom, K.D. and Sargent, L.M. (1962). The three-dimensional nature of boundary layer transition. *J. Fluid Mech.*, **12**, 1-34.

Kohan, S. and Schwarz, W. (1973). Low speed calibration formula for vortex shedding from cylinders. *Phys. Fluids*, **16**, 1528-1529.

Kovaszny, L.S.G., Komoda, H. and Vasudeva, B.R. (1962). Detailed flow field in transition. *In: Proc. Heat Transfer and Fluid Mech. Inst.*, Stanford University Press, 1-26.

Lange, C.F., Durst, F. and Breuer, M. (1999). Wall effects on heat losses from hot-wires. *Int. J. of Heat and Fluid Flow*, **20**, 34-47.

Lange, C.F., Durst, F. and Breuer, M. (1999). Correction of hot-wire measurements in the near-wall region. *Exp. Fluids*, **26**, 475-477.

Laws, E.M. (1990). Flow conditioning-a new development. *Flow Meas. Instrum.*, **1**, 165-170.

Laws, E.M. and Chesnoy, A. (1993). The design and development of flow conditioning devices. *devices for flow measurement and control*, ASME, FED 159.

Laws, E.M. and Quazzane A.K. (1995). Flow conditioning for orifice plate flow meters. *Fluid Flow Measurement 3rd International Symposium*, San Antonio, TX.

Lee, T. and Budwig, R. (1991). Two improved methods for low-speed hot-wire calibration. *Meas. Sci. Technol.*, **2**, 643-646.

Leite, R.J. (1959). An experimental investigation of the stability of Poiseuille flow. *J. Fluid Mech.*, **5**, 81-97.

Lekakis, I. (1996). Calibration and signal interpretation for single and multiple hot-wire/hot-film probes. *Meas. Sci. Technol.*, **7**, 1313-1333.

Ligrani, P.M. and Bradshaw, P. (1987). Spatial resolution and measurement of turbulence in the viscous sublayer using subminiature hot-wire probes. *Exp. Fluids*, **5**, 407-417.

Loehrke, R.L. and Nagib, H.M. (1976). Control of free stream turbulence by means of honeycombs: a balance between suppression and generation. *ASME J. Fluids Eng.*, **98**, 342-353.

Lumley, J.L. (1964). Passage of a turbulent stream through honeycomb of large length-to-diameter ratio. *J. Basic Eng., Trans. ASME, Series D*, **86**, 218-220.

Merkli, P. and Thomann, H. (1975). Transition to turbulence in oscillating pipe flow. *J. Fluid Mech.*, **68**, 567-575.

Mizushima, T., Maruyama, T. and Shiozaki, Y. (1973). Pulsating turbulent flow in a tube. *J. of Chem. Eng. of Japan*, **6**, 487-494.

Mizushima, T., Maruyama, T. and Hirasawa, H. (1975). Structure of the turbulence in pulsating pipe flows. *J Chem. Eng. of Japan*, **8**, 210-216.

Morrison, G.L., Hall, K.R., Holste, J.C., Ihfe, L., Gaharan, C. and DeOtte, R.E. Jr. (1997). Flow development downstream of a standard tube bundle and three different porous plate flow conditioners. *Flow Meas. Instrum.*, **8**, 61-76.

Nerem, R.M., Seed, W.A. and Wood, N.B. (1972). An experimental study of the velocity distribution and transition to turbulence in the aorta. *J. Fluid Mech.*, **52**, 137-160.

Ohmi, M. and Iguchi, M. (1980). Flow pattern and frictional losses in pulsating pipe flow Part 2 Effect of pulsating frequency on the turbulent frictional losses. *Bull. JSME*, **23**, 2021-2028.

Ohmi, M. and Iguchi, M. (1981). Flow pattern and frictional losses in pulsating pipe flow Part 6 Frictional losses in a laminar flow. *Bull. JSME*, **24**, 1756-1763.

Ohmi, M. and Iguchi, M. (1981). Flow pattern and frictional losses in pulsating pipe flow Part 7 Wall shear stress in a turbulent flow. *Bull. JSME*, **24**, 1764-1771.

Ohmi, M. and Iguchi, M. (1982). Critical Reynolds number in an oscillating pipe flow. **25**, 200, 165-172.

Ohmi, M., Iguchi, M., Kakehashi, K. and Masuda, T. (1982). Transition to turbulence and velocity distribution in an oscillating pipe flow. *Bull. JSME*, **25**, 365-371.

Ohmi, M., Iguchi, M. and Urahata, I. (1982). Flow patterns and frictional losses in an oscillating pipe flow. *Bull. JSME*, **25**, 536-543.

Ohmi, M., Iguchi, M. and Urahata, I. (1982). Transition to turbulence in a pulsatile pipe flow: Part 1; Wave forms and distribution of pulsatile velocities near transition region. *Bull. JSME*, **25**, 182-188.

Ohmi, M., Iguchi, M. and Usui, T. (1981). Flow pattern and frictional losses in pulsating pipe flow, Part 5: Wall shear stress and flow pattern in a laminar flow. *Bull. JSME*, **24**, 75-81.

Ohmi, M., et al. (1979). Preprint of Japanese hydraulics and pneumatics society (in Japanese), pp: 1, 1979-11.

Ohmi, M., Iguchi, M., Usui, T. and Minami, H. (1980). Flow pattern and frictional losses in pulsating pipe flow. Part 1: Effect of pulsating frequency on the turbulent flow pattern. *Bull. JSME*, **23**, 2013-2020.

Ohmi, M., Usui, T., Fukawa, M. and Hirasaki, S. (1976). Pressure and velocity distributions in pulsating laminar pipe flow. *Bull. JSME*, **19**, 298-306.

Oka, S. and Kostic, Z. (1972). Influence of wall proximity on hot-wire velocity measurements. *DISA Inf.*, **13**, 29-33.

Özahi, E., Çarpınlioğlu, M.Ö. and Gündoğdu, M.Y. (2010). Simple methods for low speed calibration of hot-wire anemometers. *Flow Meas. Instrum.*, **21**, 166-170.

Patel, V.C. and Head, M.R. (1974). Some observations on skin friction and velocity profiles in fully developed pipe and channel flows. *J. Fluid Mech.*, **25**, 181-201.

Peacock, J., Jones, T., Tock, C. and Lutz, R. (1998). The onset of turbulence in physiological pulsatile flow in a straight tube. *Exp. Fluids*, **24**, 1-9.

Pfenniger, W. (1961). in *Boundary Layer and Flow Control*, (G. V. Lachman ed.), Pergamon.

Poiseuille, J.L.M. (1840). Recherches experimentelles sur le mouvement des liquides dans les tubes de tres petits diameters. *Comp. Rend.*, **11**, 961-1041.

Pratt, R.L. and Bowsher, J.W. (1978). A Simple technique for the calibration of hot-wire anemometers at low air velocities. *DISA Information*, **23**, 33-34.

Ouazzane, A.K. and Barigou, M. A. (1999). Comparative study of two flow conditioners and their efficacy to reduce asymmetric swirling flow effects on orifice meter performance. *T IChemE*, **77** (Part A), 747-753.

Rae, W.H. and Pope A. (1984). *Low Speed Wind Tunnel Testing*. John Wiley&Sons, New York.

Ramaprian, B. and Tu, W.W. (1980). An experimental study of oscillatory pipe flow at transitional Reynolds numbers. *J. Fluid Mech.*, **100**, 513-544.

Reynolds, O. (1883). An experimental investigation of the circumstances which determine whether the motion of water shall be direct or sinuous and the law of resistance in parallel channels. *Phil. Trans. R. Soc.*, **174**, 935-982.

Roshko, A. (1954). On the development of turbulent wakes from vortex streets. *NACA Report 1191 (formerly TN-2913)*, 801-825.

Sarpkaya, T. (1966). Experimental determination of the critical Reynolds number for pulsating Poiseuille flow. *Trans. ASME D, J. Basic Engng.*, **88**, 589-598.

Schiller, L. (1934). Neu berichte zur turbulenzentwicklung, *Z. Angew. Math. Mech.*, **14**, 36-42.

Schlichting, H. and Gersten, K. (2000). *Boundary layer theory*. Springer-Verlag, Berlin Heidelberg.

Schubauer, G.B. (1957). *Boundary Layer Research*. Springer-Verlag.

Schubauer, G.B. and Klebanoff, P.S. (1956). Contributions on the mechanics of boundary-layer transition. *NACA Rep.*, 1289.

Seifert, G. and Graichen, K. (1982). A calibration method for hot-wire probes including the low velocity range. *DISA Information*, **27**, 8-11.

Sergeev, S.I. (1966). Fluid oscillations in pipes at moderate Reynolds numbers. *Fluid Dyn. (Mekh. Zh.)*, **1**, 21-22.

Shan, H., Ma, B., Zhang, Z. and Nieuwstadt, F.T.M. (1999). Direct numerical simulation of a puff and a slug in transitional cylindrical pipe flow. *J. Fluid Mech.*, **387**, 39-60.

Shemer, L. (1985). Laminar-turbulent transition in a slowly pulsating pipe flow. *Phys. Fluids*, **28**, 3506-3509.

Shemer, L. and Kit, E. (1984). An experimental investigation of the quasisteady turbulent pulsating flow in a pipe. *Phys Fluids*, **27**, 72-76.

Sreenivasan, K.R. and Ramshankar, R. (1986). Transition intermittency in open flows and intermittency routes to chaos. *Physica*, **23**, 246-258.

Stettler, J.C. and Hussain, K.M.F. (1986). On transition of the pulsatile pipe flow. *J. Fluid Mech.*, **170**, 169-197.

Tewari, S.S. and Jaluria, Y. (1990). Calibration of constant-temperature hot-wire anemometers for very low velocities in air. *Rev. Sci. Instrum.*, **61**, 3834-3845.

Tozzi, J.T. and von Kerczek, C.H. (1986). The stability of oscillatory Hagen-Poiseuille flow. *J. Appl. Mech.*, **53**, 187-192.

Tsanis, I.K. (1987) Calibration of hot-wire anemometers at very low velocities. *Dantec Inf.*, **4**, 13-14.

Turan, Ö. and Azad, R.S. (1989). Effect of hot-wire probe defects on a new method of evaluating turbulence dissipation. *J. Phys. E: Sci. Instrum.*, **24**, 254-261.

Turan, Ö., Azad, R.S. and Atamançuk, T.M. (1987). Wall effect on the hot-wire signal without flow. *J. Physics, E: Sci. Instrum.*, **20**, 1278-1280.

Uchida, S. (1956). The pulsating viscous flow superposed on the steady laminar motion of incompressible fluid in a circular pipe. *J. Appl. Math. Physics (ZAMP)*, **7**, 403-422.

Ünsal, B. and Durst, F. (2006). Pulsating flows: experimental equipment and its application. *Int. J. JSME Series B*, **49**, 980-987.

Ünsal, B., Ray, S., Durst, F. and Ertunç, Ö. (2005). Pulsating laminar pipe flows with sinusoidal mass flux variations. *Fluid Dyn. Res.*, **37**, 317-333.

Vagt, J.D. and Fernholz, H.H. (1979). A discussion of probe effects and improved measuring techniques in the near-wall region of an incompressible three-dimensional turbulent boundary layer. *AGARD Conf. Proc.*, **271**, 101-107.

Wenzhong, L., Khoo, B.C. and Diao, Xu. (2006). The thermal characteristics of a hot wire in a near-wall flow. *Int. J. of Heat and Mass Transfer*, **49**, 905-918.

White, F.M. (1984). *Viscous Fluid Flow*. New York: McGraw-Hill.

Wills, J.A.B. (1962). The corrections of hot-wire readings for proximity to a solid boundary. *J. Fluid Mech.*, **12**, 388-396.

Wyganski, I.J. and Champagne, F.H. (1973). On transition in a pipe. Part 1. The origin of puffs and slugs and the flow in a turbulent slug. *J. Fluid Mech.*, **59**, 281-336.

Wyganski, I, Sokolov, M. and Friedman, D. (1975). On transition in a pipe. Part 2. The equilibrium puff. *J. Fluid Mech.*, **69**, 283-304.

Xia, L., Farrell, C. and Kavanagh, P. (1990). Experimental investigation of the unsteady flow behind screens and honeycombs. *Proceedings of the 36th International Instrumentation Symposium*, Denver, CO, USA.

Xiong, W., Kalkühler, K. and Merzkirch W. (2003). Velocity and turbulence measurements downstream of flow conditioners. *Flow Meas. Instrum.*, **14**, 249-260.

Yellin, E.L. (1966). Laminar-turbulent transition process in pulsatile flow. *Circulation Research*, **19**, 791-804.

Yue, Z. and Malmström, T.G. (1998). A simple method for low-speed hot-wire anemometer calibration. *Meas. Sci. Technol.*, **9**, 1506-1510.

Zanker, K.J. (1960). The development of a flow straightener for use with orifice-plate flowmeters in disturbed flows. *Flow Meas. in Closed Conduits, NEL*.

Zanker, K.J. and Goodson, D. (2000). Qualification of a flow conditioning device according to the new API 14.3 procedure. *Flow Meas. Instrum.*, **11**, 79-87.

APPENDICES

APPENDIX 1

SUMMARY OF THE STUDIES IN LITERATURE CONDUCTED ON PULSATILE PIPE FLOWS

Author/ Article Name	Re	Period (T)	$\sqrt{\omega'}$	f	Amplitude (A_1)	Velocity Measurement	Pressure Measurement	r/R	D	Medium
									L	
Shemer, Wygnanski and Kit (1985)/ Pulsating flow in a Pipe	$2900 \leq Re_m \leq 7500$	$0.5 \text{ s} \leq T \leq 5 \text{ s}$	$4.5 \leq \sqrt{\omega'} \leq 15$	$0.2 \text{ Hz} \leq f \leq 2 \text{ Hz}$	$A_1 < 0.35$	At the exit of plane with arrays of normal hot wires	Pressure drop along the pipe with pressure transducers	0.5 mm from the wall ; $r/R=0.97$.	33 mm	air
									16.5 m	
Gündoğdu (2000) / An experimental investigation on pulsatile pipe flows	$1870 \leq Re_{ta} \leq 61200$ $109 \leq Re_{os} \leq 18650$	$0.339 \text{ s} \leq T \leq 10.64 \text{ s}$	$4.9 \leq \sqrt{\omega'} \leq 28$	$0.094 \text{ Hz} \leq f \leq 2.95 \text{ Hz}$	$0.0035 \leq A_1 \leq 0.7113$	In the pipe test section with hot wire, $X=125D$	Pressure drop along the pipe with pressure transducer		50.4 mm	air
									10 m	
Iguchi and Ohmi (1985)/ Experimental Study of Turbulence in a Pulsatile Pipe Flow	$18900 \leq Re_{ta} \leq 84500$	$0.51 \text{ s} \leq T \leq 3.21 \text{ s}$	$9.01 \leq \sqrt{\omega'} \leq 22.6$	$0.311 \text{ Hz} \leq f \leq 1.96 \text{ Hz}$	$0.248 \leq A_1 \leq 0.802$	In the pipe test section with hot wire, $X=90D$	Pressure drop along the pipe with pressure transducer	$r/R = 0.975$	49.9 mm	air
									6 m	

Ohmi, Iguchi and Urahata (1982)/ Transition to Turbulence in a Pulsatile Pipe Flow, Part 1	$0 \leq Re_{ta} \leq 24000$	$0.975 \text{ s} \leq T \leq 3.33 \text{ s}$	$8.93 \leq \sqrt{\omega'} \leq 16.5$	$0.3 \text{ Hz} \leq f \leq 1.026 \text{ Hz}$	$0.0636 \leq A_1 \leq 1.81$	In the pipe test section 2730 mm from the inlet with hot wire, hence $(X/(ReD))=0.027$	Pressure drop along the pipe with pressure transducer	$r/R = 0.975$	50.4 mm	air
									5 m	
Einav and Sokolov (1993)/ An Experimental Study of Pulsatile Pipe Flow in the Transition Range	$0 \leq Re_m \leq 100000$ $0 \leq Re_{os} \leq 4000$	$8.93 \text{ s} \leq T \leq 41.6 \text{ s}$	$9.89 \leq \sqrt{\omega'} \leq 21.2$	$0.024 \text{ Hz} \leq f \leq 0.112 \text{ Hz}$	Amplitude adjustments between 0 and 5 cm by moving the 90 cm crank in a groove on the flywheel.	In the pipe test section at 8.2 m from the entrance with a conical hot film probe.	Pressure drop with capacitance transducer at 6.2 m and 11.9 m downstream from the pipe entrance.	$r/R = 1$	25.4 mm	water
									18.3 m	
Peacock, Jones, Tock and Lutz (1998)/ The Onset of Turbulence in Physiological Pulsatile Flow in a Straight Tube	$450 \leq Re_m \leq 4200$ $1500 \leq Re_{peak}^P \leq 9500$	$0.4 \text{ s} \leq T \leq 3.33 \text{ s}$	$1.5 \leq \sqrt{\omega'} \leq 55$	$0.3 \text{ Hz} \leq f \leq 2.5 \text{ Hz}$		LDA measurement Ultrasound flow probe to measure instantaneous volumetric flow.	Hot film probe was mounted flush with the pipe wall to measure wall shear stress.		4 mm, 9 mm, 14mm, 30mm	water 50% sodium Thiocyanate+ water, 40% glycerol+water
Shemer and Kit (1984)/ An Experimental	$3600 \leq Re_m \leq 9000$	$0.55 \text{ s} \leq T \leq 5.5 \text{ s}$	$4.55 \leq \sqrt{\omega'} \leq 14.4$	$0.182 \text{ Hz} \leq f \leq 1.82 \text{ Hz}$		Nine hot wires distributed equidistantly along the	Pressure drop measurement along the pipe with a pressure	$r/R = 0.97$ at 0.5 mm from the wall.	33 mm	air

Investigation of the Quasisteady Turbulent Pulsating Flow in a Pipe						radius at the exit cross section of the pipe.	transducer		17 m	
Shemer (1985)/ Laminar-Turbulent Transition in a Slowly Pulsating Pipe Flow	Measurements at $Re_m = 4000$. Laminar was kept at $Re_m \leq 20000$.	$T = 2.7$ s	$\sqrt{\omega'} = 6.5$	$f = 0.37$ Hz		At several radial locations at the exit plane of the pipe. Also, two flush-mounted hot wires .	Pressure drop measurement along the pipe with a pressure transducer	$r/R = 0.97$	33 mm 17 m	air
Gerrard / An Experimental Investigation of Pulsating Turbulent Water Flow in a Tube	$Re_m = 3770$	$T = 12$ s	$\sqrt{\omega'} = 14.4$	$f = 0.082$ Hz		Velocity measurement by marking the fluid and taking photographs.			38.1 mm	water
Sarpkaya (1966)/ Experimental Determination of the Critical Reynolds Number for Pulsating Poiseuille Flow	Laminar up to $Re = 6500$.			$0.5 \text{ cps} \leq f \leq 3 \text{ cps}$	Piston stroke: 0.5-6 inch	Discharge was measured with an orifice meter.	Differential pressure transducer.		11.2 mm 16.46 m	Aerohydraulic oil

Stettler and Hussain (1986)/ On Transition of the Pulsatile Pipe Flow	$1100 \leq Re_m \leq 3000$	$0.204 \text{ s} \leq T$	$0 \leq \sqrt{\omega'} \leq 70$	$0 \leq f \leq 4.88 \text{ Hz}$	$A_1 \leq 1$	Measurement with LDA			25.4 mm	water
									13.97 m	
Yellin (1966)/ Laminar-Turbulent Transition Process in Pulsatile Flow	$0 \leq Re_m \leq 3500$	$3.31 \text{ s} \leq T \leq 15.72 \text{ s}$	$4 \leq \sqrt{\omega'} \leq 13$	$0.064 \text{ Hz} \leq f \leq 0.302 \text{ Hz}$		Orifice flowmeter and visually by photosensitive cells			12.7 mm	Bentonite
Hershey and Im (1968)/ Critical Reynolds Number for Sinusoidal Flow of Water in Rigid Tubes	$200 \leq Re_m \leq 4000$	$0.857 \text{ s} \leq T \leq 5.98 \text{ s}$	$0 \leq \sqrt{\omega'} \leq 4.24$	$0.167 \text{ Hz} \leq f \leq 1.167 \text{ Hz}$		The average flow rate was measured directly with a graduated cylinder and a stopwatch.	Two pressure transducers connected to pressure taps.		$2.5 \text{ mm} \leq d \leq 8 \text{ mm}$	water
									1 m	
Ramaprian and Tu (1980)/ An Experimental Study of Oscillatory Pipe Flow at Transitional Reynolds Numbers	$Re_m \approx 2100$	$0.571 \text{ s} \leq T \leq 20 \text{ s}$	$3.77 \leq \sqrt{\omega'} \leq 22.3$	$0.05 \text{ Hz} \leq f \leq 1.75 \text{ Hz}$	$0.6 \leq A_1 \leq 1.4$	Measurements with LDA	Pressure transducer		50 mm	"Eureka" oil
									8.8 m	

Clamen and Minton (1977)/ An Experimental Investigation of Flow in an Oscillating Pipe	$1275 \leq Re_m \leq 2900$	$5.68 \text{ s} \leq T \leq 32.2 \text{ s}$	$11.2 \leq \sqrt{\omega'} \leq 26.7$	$0.031 \text{ Hz} \leq f \leq 0.176 \text{ Hz}$	$0.5 \leq A_1 \leq 5.4$	Hydrogen-bubble technique (photographed by a camera to measure the velocities of pulsating flow.			51 mm	water
									6 m	

APPENDIX 2

SUMMARY OF THE STUDIES IN LITERATURE CONDUCTED ON OSCILLATING PIPE FLOWS

Author/ Article Name	Re	Period (T)	$\sqrt{\omega'}$	f	Amplitude (A_1)	Velocity Measurement	Pressure Measurement	r/R	D	Medium
									L	
Eckmann and Grotberg (1991)/ Experiments on Transition to Turbulence in Oscillatory Pipe Flow	$500 \leq Re_{\delta_s}^E \leq 854$ (Transition to turbulence detected) $0 \leq Re_m \leq 40000$	$0.0064 \text{ s} \leq T \leq 0.0854 \text{ s}$	$9 \leq \sqrt{\omega'} \leq 33$	$11.71 \text{ Hz} \leq f \leq 157 \text{ Hz}$	$2.4 \leq A_1 \leq 21.6$ A=stroke distance / tube radius	LDA and hot film anemometer measurements indicate the core flow remains stable when the B.L. becomes turbulent for Re_{δ} up to 1310.		r/R=0.95	31.8 mm	Potassium thiocyanate, water
Fishler and Brodkey (1991)/ Transition, Turbulence and Oscillating Flow in a Pipe	$7200 \leq Re_{peak}^F \leq 22000$		$7.75 \leq \sqrt{\omega'} \leq 16.4$			Flow visualization method with camera.			25.4 mm	Trichloroethylene
Hino, Sawamoto and Takasu (1976)/ Experiments on Transition to Turbulence in an Oscillatory Pipe Flow	$105 \leq Re \leq 5830$ $Re = \hat{U}D/\nu$ \hat{U} =oscillating mean velocity amplitude $19 \leq Re_{\delta} \leq 1530$ $Re_{\delta} = \hat{U} \delta/\nu$	$1 \text{ s} \leq T \leq 6.25 \text{ s}$	$1.9 \leq \sqrt{\omega'} \leq 8.75$	$0.16 \text{ Hz} \leq f \leq 1 \text{ Hz}$	$0.053 \text{ m/s} \leq \hat{U} \leq 6.03 \text{ m/s}$	Hot wire measurement in the middle of the pipe (2 m)			14,5 ; 30 mm	air
									4 m	

Ohmi, Iguchi, Kakehashi and Masuda (1982)/ Transition to Turbulence and Velocity Distribution in an Oscillating Pipe Flow	$600 \leq Re_{os} \leq 6500$ 0	$0.16 \text{ s} \leq T \leq 18.97 \text{ s}$	$2.6 \leq \sqrt{\omega'} \leq 41$	$0.0527 \text{ Hz} \leq f \leq 6.24 \text{ Hz}$		Hot wire measurement		$r/R = 0.95$	50.4 mm	air
									5 m	
Merkli and Thomann (1975)/ Transition to Turbulence in Oscillating Pipe Flow	$A_{crit} \approx 400$ for transition.	$0 \text{ s} \leq T \leq 0.0077 \text{ s}$	$0 \leq \sqrt{\omega'} \leq 140$	$0 \text{ Hz} \leq f \leq 130 \text{ Hz}$		Hot wire measurement in the middle of the pipe.	Pressure transducer for taking p-signal.		19 mm	air
									2.5 m	

APPENDIX 3

TECHNICAL SPECIFICATION OF THE SCREWED AIR COMPRESSOR

The compressor in the set-up has the following technical specifications;

Compressor Type	: Lupamat LKV 30/8 Screwed Air Compressor
Air Supply	: 4.85 m ³ /min (0.08 m ³ /s)
Operating Pressure Range	: 8 bar
Weight	: 800 kg

APPENDIX 4

TECHNICAL SPECIFICATION OF PSK TYPE PRESSURIZED AIR DRIER

The pressurized air drier has the following technical specifications;

Model	: Pnöso Type-S PSK-6000F
Condenser Cooling Type	: Air Cooling Type
Refrigerant	: R-22
Air Supply	: max. 6 m ³ /min (0.1 m ³ /s)
Air Inlet Temperature	: 35 °C
Dew Point	: 4 °C
Operating Pressure	: 7 bar
Maximum Operating Pressure	: 16 bar
Compressor Motor Power	: 1.5 HP (1.12 kW)
Weight	: 220 kg

APPENDIX 5

TECHNICAL SPECIFICATION OF PROBE TRAVERSING MECHANISM

RCP2-SA6-I-PM-6-200-P1-SBE Robocylinder has the following technical specifications;

Product	: Electro-mechanic cylinder
Stroke	: 200 mm
Product Total Length	: 450 mm
Speed	: 300 mm/max
Acceleration	: 0.3G
Motor	: 42P Pulse motor
Positioning Repeatability	: 0.02 mm
Load Capacity	: 12 kg max (Horizontal)- 2.5 kg max (Vertical)
Encoder	: Incremental
Drive System	: Ball screw Ø 10 mm, rolled C10
Backlash	: 0.1 mm or less
Guide	: Integrated with base
Allowable Load Moment	: Ma: 8.9 Nm, Mb: 12.7 Nm, Mc: 18.6 Nm
Base	: Material: Aluminum with white alumite treatment

RCP2-CGA-SA6-I-PM-O-P Robocylinder Positioning Unit has the following technical specifications;

Product	: Electro-mechanic cylinder motor-encoder driver and positioning unit
Input Power	: DC24V \pm 10 %
Power Capacity	: 2 A max.
Number of Controlled Axes	: 1 axis
Controlled Method	: Weak field-magnet vector control (patent pending)
Positioning Number	: Standard 16 points, maximum 64 points
Backup Memory	: 100,000 times rewritten ability EEPROM
PIO	: 10 dedicated inputs, 10 dedicated outputs
LED Indicators	: Ready (Green), Run (Green), Alarm (Red)
I/F Power	: External Power Supply: DC24V \pm 10 %, 0.3 A, insulated
Communication	: RS485 1 channel (terminated externally)
Encoder Interface	: Incremental specification conforming to EIA RS-422A/423A
Forced Release of Electro-magnetic Brake	: Toggle switch on front panel of enclosure
Insulation Strength	: DC500V 10 M Ω
Operating Temperature	: 0-40 °C
Operating Humidity	: 85% RH or less (non-condensing)
Protection Class	: IP20
Weight	: 300 g
Accessory	: PIO flat cable (2 m)

APPENDIX 6

TECHNICAL SPECIFICATION OF 55P11 GENERAL PURPOSE TYPE MINIATURE PROBE

The technical specification of the 55P11 general purpose type miniature probe is given as;

Sensor Material	: Pt-plated tungsten wire
Sensor Wire Dimensions	: 5 μm diameter 1.25 mm long (l/d=250)
Sensor Resistance R_{20} (approx.)	: 3.5 Ω
Temperature Coefficient of Resistance (TCR) α_{20} (approx.)	: 0.36 %/ $^{\circ}\text{C}$
Maximum Sensor Temperature	: 300 $^{\circ}\text{C}$
Maximum Ambient Temperature	: 150 $^{\circ}\text{C}$
Minimum Velocity	: 0.2 m/s (for air)
Maximum Velocity	: 500 m/s (for air)
Frequency Limit f_{cpo}	: 90 Hz
Frequency Limit f_{cmax}	: 400 kHz
Space Conditions	: Recommended for both little space and sufficient space

APPENDIX 7

TECHNICAL SPECIFICATIONS OF 56C17 CTA BRIDGE and 56N21 LINEARIZER

56C17 CTA system has the following technical specifications;

Probe Resistance Range	: 3-30 Ω
Bridge Ratio	: 1:20
Upper Frequency Limit	: 150 kHz
Maximum Probe Current	: 315 mA
Typical Output Noise Level (10 m/s, 10 kHz)	: 0.02 % Turbulence
Output Impedance	: 10 Ω
Output Voltage Range	: 0-12 V
Maximum Gain AC	: 1111
Maximum Gain DC	: 38783
Maximum Length of Transducer Cable	: 100 m
Square Wave Generator Frequency	: 1 kHz
Typical Equivalent Input Drift of Amplifier	: 3 $\mu\text{V}/^\circ\text{C}$
Typical Equivalent Input Noise of Amplifier	: 2.2 nV/Hz ^{1/2}
Module Width	: 1 Inches
Uncertainty in Resistance Measurement	: <5 %
Ambient Temperature Range	: 5-40 $^\circ\text{C}$
Ambient Humidity Range	: 20-80 %
Weight	: 0.65 kg

56N21 Linearizer has the following technical specifications;

Type of Linearization Principle	: Exponential
Accuracy of Linearity	: 0.5 % of reading +0.15 % of full scale
Upper Frequency Limit	: 300 kHz
Input Impedance	: 10^4 M Ω
Output Impedance	: 100
Input Voltage Range	: 0-12 V
Output Voltage Range	: 0-10 V
Stability	: 0.05 %/ $^{\circ}$ C
Module Width	: 1 Inches
Module Weight	: 0.39 kg

APPENDIX 8

TECHNICAL SPECIFICATION OF THE PRESSURE TRANSMITTER

The WIKA SL-1 pressure transmitter for low pressure applications has the following technical specifications;

Pressure Ranges	: ± 20 mbar (± 2 kPa)
Type of Pressure	: Relative Pressure
Wetted Parts Material	: Stainless Steel, Silicon, Aluminum, Gold
Case Materials	: Stainless Steel
Power Supply	: 14-30 VDC
Signal Output	: 0-10 V
Accuracy	: ≤ 0.5 %
Non-linearity	: ≤ 0.2 %
Non-repeatability	: ≤ 0.1 %
1-year Stability	: ≤ 0.3 %
Time Resolution	: 1 kHz
Permissible Temperature of Medium	: -30 °C.. 80 °C
Permissible Temperature of Ambient	: -20 °C.. 80 °C
Process Connection	: G1/2"
Weight	: approx. 0.3 kg

APPENDIX 9

TECHNICAL SPECIFICATION OF DATA ACQUISITION AND PROCESSING EQUIPMENT

Personal Daq/3001 USB Module has the following technical specifications;

Resolution	: 16 bit
Sample Rate	: 1 MHz
On-board Thermocouple Inputs	: 8
Analog Inputs (channels)	: 8 (differential) or 16 (single-ended)
Analog Outputs	: 4 (16 bit, 1 MHz)
Digital I/O	: 24
Counter Inputs/Timer Outputs	: 4/2
Latency	: low-latency control output capability as low as 2 μ s latency
Environment Operating Temperature	: -30 °C..70 °C
Communications	: USB 2.0 high-speed mode (480 Mbps) if available, otherwise USB 1.1 full- speed mode (12 Mbps)
Acquisition Data Buffer	: 1 MSample
Power Supply	: 6-16 VDC
Voltage Measurement Speed	: 1 μ s per channel
Output Voltage	: \pm 10 V
Weight	: 431 g

The Personal Daq/3001 USB Module supports C++[®], Visual Basic[®], LabVIEW[®], .Net[®], DASyLab[®] and MATLAB[®] softwares.

CURRICULUM VITAE

PERSONAL INFORMATION

Surname, Name: ÖZAHİ, Emrah

Nationality: Turkish (TC)

Date and Place of Birth: 3 September 1979, Gaziantep

Marital Status : Married

Phone: +90 505 684 40 06

Fax: +90 342 360 11 04

email: ozahi@gantep.edu.tr

EDUCATION

Degree	Institution	Year of Graduation
MS	University of Gaziantep, Graduate School of Natural and Applied Sciences	2006
BS	University of Gaziantep, Department of Mechanical Engineering	2002
High School	Gaziantep Super High School	1997

WORK EXPERIENCE

Year	Place	Enrollment
2005-Present	University of Gaziantep, Department of Mechanical Engineering	Research Assistant
2004-2005	Super Film Packaging Company/Turkey	Project Engineer

FOREIGN LANGUAGES

Foreign Language: English

Examination Date: March 2010

Score: 85/100

Test Field: Natural and Applied Sciences

PUBLICATIONS

International Journals

1. Çarpınlioğlu, M.Ö. and Özahi, E. (2011). Laminar Flow Control via Utilization of Pipe Entrance Inserts (A Comment on Entrance Length Concept). *Flow Meas. Instrum.*, **22**,165-174.
2. Özahi, E., Çarpınlioğlu, M.Ö. and Gündoğdu, M.Y. (2010). Simple Methods for Low Speed Calibration of Hot-Wire Anemometers. *Flow Meas. Instrum.*, **21**, 166-170.
3. Çarpınlioğlu, M.Ö., Özahi, E. and Gündoğdu, M.Y. (2009). Determination of Laminar and Turbulent Flow Ranges Through Vertical Packed Beds in Terms of Particle Friction Factors. *Adv. Powder Technol.*, **20**, 515-520.
4. Özahi E., Gündoğdu, M.Y. and Çarpınlioğlu, M.Ö. (2008). A Modification on Ergun's Correlation for Use in Cylindrical Packed Beds with Non-spherical Particles. *Adv. Powder Technol.*, 19, 369-381.
5. Çarpınlioğlu, M.Ö. and Özahi, E. (2008). A Simplified Correlation for Fixed Bed Pressure Drop. *Powder Technol.*, **187**, 94-101.

Communications Presented and Published In a Book In The International Scientific Meetings

1. Özahi, E. and Çarpınlioğlu, M.Ö. (2011). Periodic Flow as an Alternative for Pneumatic Conveying Pipelines (Presentation of an Experimental Test Case). *14th Inter. Freight Pipeline Society Symp.*, 28 June-01 July, 56-64, Madrid-Spain.
2. Çarpınlioğlu M.Ö. and Özahi E. (2011). Transitional Characteristics of Pulsatile Pipe Flows as a Control and Modelling Tool for Pneumatic Transport of Solid Particles. *14th Inter. Freight Pipeline Society Symp.*, 28 June-01 July, 47-55, Madrid-Spain.

3. Özahi E. and Çarpınlioğlu M.Ö. (2008). A Brief Review on Laminar to Turbulent Transition in Time-Dependent Pipe Flows. 1st Inter. Eng. Sci. Conf., 2-4 November , Aleppo University, Syria.

HOBBIES

Reading, discovery, tennis, chess, music.